UNIVERSITÉ DE SHERBROOKE
Faculté de génie
Département de génie mécanique

Simulation Directe du Bruit Propre de Profil à Haut Nombre de Reynolds

Direct Numerical Simulation of Airfoil Self-Noise at High Reynolds Numbers

Thèse de doctorat
Specialité: génie mécanique

Hao WU

Sherbrooke (Québec) Canada

Février 2019

JURY MEMBERS

Stéphane MOREAU

Supervisor

Richard SANDBERG

Examiner

Xiaohua WU

Examiner

Sébastien PONCET

Examiner

Gaofeng WANG

Examiner

RÉSUMÉ

Ce travail propose une étude numérique utilisant la simulation numérique directe (SND) afin d'avoir une meilleure compréhension du mécanisme de génération du bruit au bord de fuite (BF), ou bruit propre de profil. 2 SND compressibles de haute résolution de l'écoulement autour d'un profil NACA6512-63 et du profil CD, ont été effectuées, à un nombre de Reynolds $Re_c = 150\ 000$ basé sur la corde et à un nombre de Mach amont $Ma = 0\ 25$, en prenant en compte les effets d'installation de la soufflerie. Pour le profil NACA6512-63, même si ce cas est difficile à simuler à cause de l'écoulement étroit du jet de la soufflerie, grâce à des conditions limites bien choisies, les effets d'installation sont généralement bien reproduits en comparant avec les résultats d'essais. A l'intrados, la transition se produit au bord d'attaque (BA) et une couche limite totalement turbulente existe jusqu'au BF. A l'extrados, une couche limite instable et décollée au BF donne une source de bruit supplémentaire par rapport au cas trippé simulé auparavant dans lequel une couche limite turbulente attachée était présente. Il est démontré de plusieurs manières que la couche limite oscillante au BF à l'extrados du cas non-trippé change la topologie de l'écoulement à l'intrados. Des plus grosses structures sont formées au BF à l'intrados en raison de la couche limite instationnaire et la position de la transition a changé au BA. Les analogies acoustiques utilisées donnent une bonne prédiction globale pour les cas trippé et non-trippé. Pour le profil CD, les résultats de cette étude prouve que cette SND peut être considérée comme une base de données de haute fidélité. A l'intrados, l'écoulement reste laminaire jusqu'au BF où un échappement tourbillonaire se produit. A l'extrados, l'écoulement transitionne après une fine bulle de recirculation au BA et puis reste turbulent et attaché jusqu'au BF avec successivement un gradient de pression favorable (GPF), un gradient de pression nul (GPN) et finalement un gradient de pression adverse (GPA) dans la région au BF. L'effect de gradient de pression moyen sur l'écoulement à l'extrados est discuté en utilisant une analyse QR. L'évolution moyenne de la dynamique de l'invariant du tenseur de gradient de vitesse varie fortement avec les gradients de pression moyens différents (GPF, GPN et GPA). Cette évolution change aussi beaucoup en fonction de la distance à la paroi. Le couplage du Hessien de pression et le gradient de vitesse est l'élément majeur qui provoque tous les changements de la dynamique de l'invariant dans cet écoulement. Le gradient de pression donne un effet important au moins dans la zone externe et dans la zone logarithmique de cet écoulement. Le GPA favorise plus d'enroulements des trajectoires moyennes à ces deux zones et empêche l'étirement tourbillonaire. La paroi empêche aussi principalement ce régime. Du point de vue acoustique, on observe la source liée à la transition de l'écoulement dans la bulle de recirculation comme identifié précédemment à bas nombre de Reynolds, celle liée à l'interaction de la couche turbulente avec le BF, et une source supplémentaire dans le proche sillage. C'est la première fois que ce phenomène est observé pour cet écoulement. Après plusieurs vérifications numériques, y compris une nouvelle SGE (Simulation des Grandes Echelles) compressible de haute résolution, cette source de bruit supplémentaire dans cette SND apparaît bien physique.

Mots-clés : SND, Aéroacoustique, Bruit au bord de fuite, Profil

ABSTRACT

This work proposes a numerical study using direct numerical simulation (DNS) to gain a better understanding of the generation mechanisms of the trailing-edge (TE) noise, or airfoil self-noise. 2 high resolution compressible DNS, respectively of the flow over NACA6512-63 airfoil and the CD airfoil, at an airfoil chord based Reynolds number of $Re_c = 150\ 000$ and at a freestream Mach number of $Ma = 0\ 25$, are conducted taking the mean wind-tunnel installation effects into account. For NACA6512-63 airfoil, although it is a difficult case to simulate because of the narrow stream from the wind-tunnel jet, due to the proper sets of boundary conditions, the mean installation effect is generally well captured when compared with experiments. On the pressure side transition occurs at the leading-edge (LE) and a fully turbulent boundary layer exists close to the trailing edge. On the suction side, a flapping and separated boundary layer at the TE leads to an extra noise source compared with a tripped case previously simulated where an attached turbulent boundary layer is present. It is demonstrated from multiple aspects in this study that the flapping shear layer at the TE on the suction side of the untripped airfoil has changed the flow topology on the pressure side. Larger structures at the TE on the pressure side are formed due to the flapping shear layer and such an influence has even modified the transition location at LE. Acoustic analogies are used and give a good overall prediction for both the untripped and tripped cases. For the CD airfoil, the results from present study prove that this DNS can be considered as a high-fidelity database. On the pressure side, the flow stays laminar until at the TE where minor vortex shedding appears. On the suction side, the flow transitions after a short separation bubble at LE then stays turbulent and attached till the TE experiencing a mean favorable pressure gradient (FPG), zero pressure gradient (ZPG) and finally an adverse pressure gradient (APG) in the TE region. The mean pressure gradient effects on the flow on the suction side are discussed in detail through a QR analysis. The mean evolution of the velocity gradient tensor invariant dynamics is found to vary strongly for regions undergoing FPG, ZPG and APG. This evolution changes also greatly with the distance to the wall. The coupling of the pressure Hessian with the velocity gradient is the major factor that drives all the changes of the invariant dynamics in this flow. The pressure gradients have a significant impact at least in the outer-layer and log-layer of the flow. The adverse pressure gradient leads to more rolling features to the mean trajectories in these two layers and suppresses the vortical stretching regime. The wall is observed to mainly suppress the vortical stretching features of the flow. On the acoustic side, besides the previously observed noise source from the leading-edge transition bubble and the trailing-edge noise from the interaction between the convecting turbulent boundary layer and the trailing-edge, an extra noise source exists in the near wake. Such a phenomenon is found for the first time for such a flow case from a compressible DNS approach. Through multiple measures including a newly produced high resolution compressible LES (Large Eddy Simulation), the extra noise source in the DNS is proved to be actually physical.

Keywords: DNS, Aeroacoustics, TE Noise, Airfoil

ACKNOWLEDGEMENTS

It was my honor to have worked with and have learned from so many brilliant people during this PhD project. I would like to acknowledge firstly Prof. Stéphane Moreau of the excellent supervision and guidance during this PhD study. His research vision, rich experience and network made this project possible. Especially, thanks to his trust, I was able to realize a project that I was fond of with a world-leading committee. The discussions with my co-supervisor Prof. Richard D. Sandberg were of great value. His rigorous attitude and innovative opinions always guided me to a better work. His warm welcome when I visited University of Southampton helped me a lot when I started doing DNS. Stefan Schlanderer, Patrick Bechlars, Richard Pitchler, Florian Hammer and many more in Southampton were truly kind and helpful to me since we met there. I sincerely appreciate the helpful discussions with Prof. Xiahua Wu. I have really benefited from the discussions with him from time to time and improved the understanding of turbulent flows by his precious suggestions. I am very grateful to late Dr. Yannick Rozenberg, who served on my committee at the beginning of my thesis. He is a generous and patient person who always encouraged me, even before when I started considering doing a PhD. A very special thanks to Dr. Marlène Sanjosé, who not only helped me a lot when I started this project but also is a role model for me as a researcher on numerical simulations. Her expertise has inspired me a lot during this project.

I should say thanks to my friends Manqi Zhu and Gaofeng Wang, who actually led me to the world of CFD since my internship in CERFACS in 2012 and were always there to help when I needed. It was a pleasure to have met Vianney Masson, Jiaping Wu, Leila Jafari, Prateek Jaiswal, Chaofan Zhang, Thomas Léonard, Stefan Pröbsting, Carlos Pérez Arroyo, Bastien Dignou, Régis Koch, the Kholodovs and many more at Université de Sherbrooke. They were amazing in supporting, distracting, and celebrating with me for many wonderful moments during these 4 years in Sherbrooke. And of course, I was happy and lucky to have met my girlfriend Yuzhu Jiang here, who was always able to find a way to cheer me up. She has an interesting mind and often helped me consider things from different angles. Many thanks to my old friends Huan Tong, Yuanyuan Liu, Shu Wang and Cheng Hang. As friends even since childhood, it is great that we all end up in North America and are often able to hang out together. No matter in Toronto, Boston, New York or Houston, thanks to their long time support and experience sharing, I had a colorful life besides the work during these years.

Finally but most importantly, I would like to thank my parents Yayan Gong and Junlin Wu. Since high school, I have lived far away from my family. Being a single child, I was sorry that I was often not able to be around them when they needed. They showered me with their unique love and support. Both taught me to accept challenges and to respect different people, traits of great importance when working with others in science. I cannot find the right words to express the importance of my family to me and to this work.

Merci à tous.

TABLE OF CONTENTS

LIST OF FIGURES

LIST OF TABLES

LIST OF SYMBOLS

Roman Symbols	
$\boldsymbol{A}$	Velocity gradient tensor matrix
$\boldsymbol{A}_{Re}$	Reynolds stress tensor matrix
B	Constant in classical law of the wall
c	Airfoil chord length
c_f	Skin friction coefficient
c_p C_p	Pressure coefficient
f	Frequency
F_i	External force
G	Green's function
H	Shape factor
$\boldsymbol{H}$	Source term in the velocity gradient tensor dynamics equations
h	Wall normal distance
I	Identity matrix
I_1 I_2 I_3	First, second and third Reynolds stress tensor invariants
i	Subscript of a certain component
i	Imaginary number
K	Acceleration parameter
k	Wavenumber
l_z	Spanwise coherence length
L	Length
$\mathcal{L}$	Radiation integral in Amiet's model
Ma	Mach number
$\mathbf{n}$	Normal vector
P	First velocity gradient tensor invariant
p	Pressure
p_t	Total pressure
p_s	Static pressure
Pr	Prandtl number
Q	Second velocity gradient tensor invariant
R	Third velocity gradient tensor invariant
Re_c	Airfoil chord based Reynolds number
Re	Momentum thickness based Reynolds number
s	Airfoil curvilinear coordinate
r_{ij}	Reynolds stress tensor component
S	A certain surface
T	Dimensionless temperature
T_{ij}	Lighthill's tensor component
T_u	Turbulence intensity
t	Dimensionless time

Roman Symbols (Continued)	
$u\ v\ w$	Cartesian velocity components
u_e	Edge velocity
u_t	Wall parallel velocity
$x\ y\ z$	Cartesian coordinates

Greek Symbols	
	Angle of attack
$_c$	Clauser pressure-gradient parameter
	Viscous effects
	Ratio of specific heats
$_2$	Coherence function
	Boundary layer thickness
$_{99}$	Boundary layer thickness based on 99% of the edge velocity
$_{p99}$	Boundary layer thickness based on 99% of the exterior total pressure
	Boundary layer displacement thickness
	Angle in polar coordinates/Boundary layer momentum thickness
	von Kármán constant
	Wavelength
	Dynamic viscosity
	Kinematic viscosity
	Fluid density
$_w$	Wall shear stress
	Pressure-density correlation term
	Favre stress tensor
$\boldsymbol{\tau}$	Viscous stress tensor
$_{pp}$	Wall pressure spectra
	Eigenvalue of the velocity gradient tensor matrix
	Angular frequency

Other Symbols	
A_0	Reference value of A (e.g. $_0$ p_0 U_0, etc)
$A^{'}$ Fluctuation of A (e.g. $u^{'}$ $p^{'}$, etc) $\overline{A}$	Time-averaged value of A
	Kinematic viscosity
	Fluid density
$_{ref}$	Fluid reference density
	Favre-averaged terms
	Fluctuation around Favre-averaged terms
$^+$	Wall normalized terms

LIST OF ACRONYMS

Acronymes (en français)	
AdA	Angle d'attaque
BA	Bord d'attaque
BF	Bord de fuite
ECL	Ecole Centrale de Lyon
PGA	Gradient de pression adverse
PGF	Gradient de pression favorable
PGN	Gradient de pression nul
SGE	Simulation des grandes échelles
SND	Simulation numérique directe
UdeS	Université de Sherbrooke

Acronyms (in English)	
APG	Adverse pressure gradient
AoA	Angle of attack
CBC	Characteristic boundary condition
CD	Controlled-Diffusion
CFL	Courant–Friedrichs–Lewy
DES	Detached eddy simulation
DNS	Direct numerical simulation
FFM	Far-field microphone
FPG	Favorable pressure gradient
FWH	Ffowcs Williams & Hawkings
HLD	High-lift device
HVAC	Heat, ventilation and air conditioning
HWM	Hot-wire measurements
ICBC	Integrated characteristic boundary condition
LBM	Lattice Boltzmann method
LE	Leading edge
LES	Large eddy simulation
MPA	Microphone phase array
MSU	Michigan State University
NACA	National advisory committee for aeronautics
PDE	Partial differential equation
p.d.f.	Probability density function
PIV	Particle image velocimetry
PSD	Power-spectral density
RANS	Reynolds averaged Navier-Stokes
RMP	Remote microphone probes
SGS	Subgrid-scale
SPL	Sound pressure level
SPS	Static pressure sensor
TE	Trailing edge
TKE	Turbulent kinetic energy
TU-Delft	Delft University of Technology
URANS	Unsteady Reynolds averaged Navier-Stokes
ZCBC	Zonal characteristic boundary condition
ZPG	Zero pressure gradient

CHAPTER 1

Introduction

1.1 Motivation of Airfoil Aerodynamic Noise Reduction

Mankind has a long history of using rotating machines. Aside from the enormous contributions to our lives, unwanted aerodynamic sound, or aerodynamic noise, is always generated when the machines are operated in a flow in general. It is a small by-product in most cases, especially at the very beginning of its history. However, after the second world war, with the increasing demand in air transportation and the growing number of wind turbine installations in the vicinity of populated areas, the aerodynamic noise problem has become a more pressing topic of concern. Such a noise is considered as one of the major forms of the well known term "noise pollution", which may harm or even cause severe impacts on human life. People are now more frequently exposed to such scenarios. The noise problem has expanded from the aircraft industry into other domains. Manufacturers of everyday products are in strong competition. The range of products includes ventilation and climate control systems in tunnels and buildings; cooling fans in computers or vehicles; and power plant fans and turbines, among others. Quieter machines and equipments can be used as sales arguments. In addition, governmental regulations are imposed on the manufacturers for the dissemination of the technology, as is eminent, for example, in the selection of wind turbine sites. Consequently, the current situation makes aerodynamic noise reduction not only a demand but also a must for industry.

To define the source of the aerodynamic noise, a representative example of residential HVAC (heat,ventilation and air conditioning) system is presented in Fig. 1.1. This system usually contains the ventilation and air conditioning components which are all rotating machines and are the principal noise generation parts. According to the source, the aerodynamic noise could be classified in two categories:

interaction with the environment (the casing and the room);
self noise of the blades of the machine.

While the former depends on the configuration of the system, the latter, which comes from the interaction of the flow with the airfoil blade, always exists as long as the air

enters the machine. Therefore, the motivation for studying airfoil aerodynamic noise is well established.

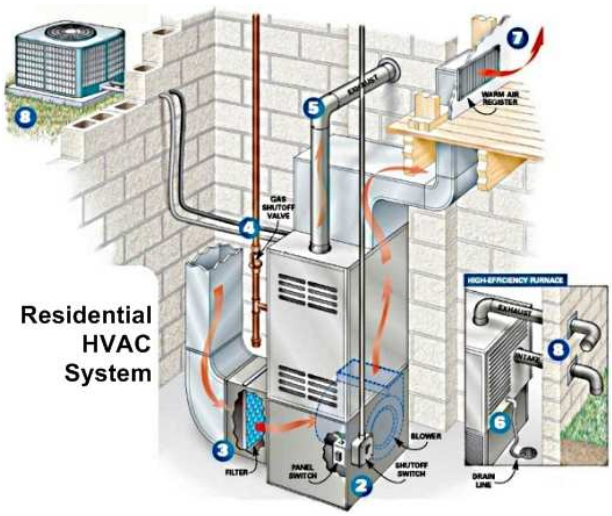

Figure 1.1 A cross-section view of a typical residence building HVAC system room.

Beginning with the pioneering work of Lighthill [Lighthill, 1952a][Lighthill, 1952c], first attempts and math basis were made in the early 1950s to explain the process of aerodynamic noise generation and thereby to develop the knowledge and physical insight that will lead to possible noise reduction methods. Even though research on aerodynamically generated sound has begun more than 60 years ago, there are many questions remaining unanswered [Morfey, 2000][Casalino, 2010], ranging from a complete understanding of certain noise mechanisms to their prediction and reduction methods.

1.2 Trailing-edge Noise

The present work concentrates on the trailing-edge (TE) noise, or airfoil self-noise. When other airfoil noise sources can be reduced or avoided by a careful design, the TE noise is the only remaining noise source when an airfoil encounters a homogeneous stationary flow. Hence TE noise is the minimum achievable noise. Such a noise is generated by the interaction between the TE with pressure fluctuations convected in the boundary layer. If the boundary layer is laminar, which is observed frequently in low-speed turbomachinaries such as automotive cooling fans or small wind turbines, tonal noise may be observed; if the boundary layer is turbulent, pressure fluctuations are present over a wide range of frequencies, which leads to broadband noise radiation and is a dominant contributor to

noise produced in many engineering applications of lifting surfaces such as wings and rotating blades. It is the canonical noise problem for wall bounded problems.

As airfoils produce tonal and broadband noise at low to moderate Reynolds number (typically from 5 10^3 to 2 10^5), at which many important engineering applications operate, to understand and to reduce the TE noise have become an inevitable objective for industry. Although various explanations have been proposed by researchers for TE noise, due to its complex generation mechanism, its physical nature has not been understood thoroughly. This is the original motivation of the present work.

In the following sections, theories on tonal an broadband noise are briefly presented.

1.2.1 Tonal Noise

The tonal noise refers to the noise radiated by airfoils in certain flow conditions as a distinct whistle which is at a discrete frequency, typically between 20 and 30 dB higher than the broadband noise. This is also called laminar instability noise as it is often observed for flows that undergo transition to turbulence for low to transitional Reynolds number because of instabilities.

The discrete tonal noise of an airfoil with sharp TE was firstly noticed experimentally by Clarke [1966] but without detailed analysis. Hersh *et al.* [1974] also observed the similar phenomenon. A thorough experimental investigation of the tonal noise was carried out by Paterson *et al.* [1973]. They found that the frequency of the noise behaves like $f \quad U_0^{1\,5}$ by relating the Strouhal number with the thickness of the boundary layer over a flat plate, where U_0 stands for the reference free-stream velocity. This result was on the assumption that the Strouhal number was constant if the airfoil was considered as a bluff body. They then concluded that the noise field was governed by vortex shedding through correlation analysis of their hot-wire measurements (HWM). One year after, Tam [1972] on the other hand cast doubt on Paterson's theory because an airfoil was streamlined and thus the bluff body assumption by Paterson was poor and he then proposed instead a self-feedback loop between the TE and a certain point in the downstream wake.

The aeroacoustic feedback loop theory proposed by Tam was developed later by Wright [1976], Longhouse [1977], Fink [1977] and Arbey and Bataille [1983], but with different feedback loop mechanisms. In general, it was believed that aerodynamic disturbances induced a fluctuating pressure on the airfoil surface interacting with the sharp TE of the airfoil, generated sound and the sound waves propagating upstream reinforced the original disturbance, thus completing the feedback loop. The latter was maintained if the sound

had appropriate phase and magnitude to couple with the boundary layer waves at the source point, where the boundary layer wave became unstable.

With the development of the calculation capacity on super computers, some exciting results from numerical work, including the direct numerical simulation (DNS), have provided more flow details on this subject, especially on several NACA airfoils [Jones, 2008] [Sandberg *et al.*, 2009] [Desquesnes *et al.*, 2007]. They suggest that suction side feedback as well as pressure side feedback are involved in the noise generation. The multiple-peak structure in the frequency spectrum is a consequence of the simultaneous participation of those two feedback loops. These numerical works have offered new thoughts aside from that from the traditional experimental work. Most recently, Sanjosé *et al.* [2017, 2018] showed that a transition mechanism is clearly involved for such a noise. The detailed presentation of the associated research will be introduced in *Chapter 2*.

It could be seen that most of these studies on tonal noise confirm the presence of a feedback-loop mechanism and is responsible for the frequency selection resulting in tonal noise. While on the other hand, new ones often do not support the results and claims made in the past. This is a topic still under active discussion. A comprehensive understanding of the tonal noise requires more accurate and systematic studies in the future.

1.2.2 Broadband Noise

When the boundary layer is turbulent and attached at TE, broadband noise will be generated. Turbulent flow consists of a random number of eddies of various scales and thus creates a broadband fluctuating surface pressure near the airfoil TE (Fig. 1.2). This broadband surface pressure is scattered by the TE [Amiet, 1976] and creates broadband acoustic waves that in some cases could be intense and very annoying to the human ear. This form of TE noise is responsible for most of the aerodynamic noise from wind turbines as well as significant amounts of noise from air plane wings propellers and rotors [Caro and Moreau, 2000; Glegg *et al.*, 1987; Hubbard and Shepherd, 1991; Wright, 1976].

Unlike the tonal noise the generation mechanism of which is still an active debate, broadband noise is better understood. From the late 1970s, various experiments were performed [Brooks and Hodgson, 1981; Brooks *et al.*, 1989; Fink, 1975] over NACA0012 airfoils. These experiments were conducted through the use of airfoils immersed in open-jet wind tunnel facilities. The experimental studies have focused on incident velocity fluctuations, wall pressure fluctuations, and far field sound. Several models were proposed during that time to predict such a noise according to experimental results. Howe [1978] has classified these models in 3 types based on their derivation approaches:

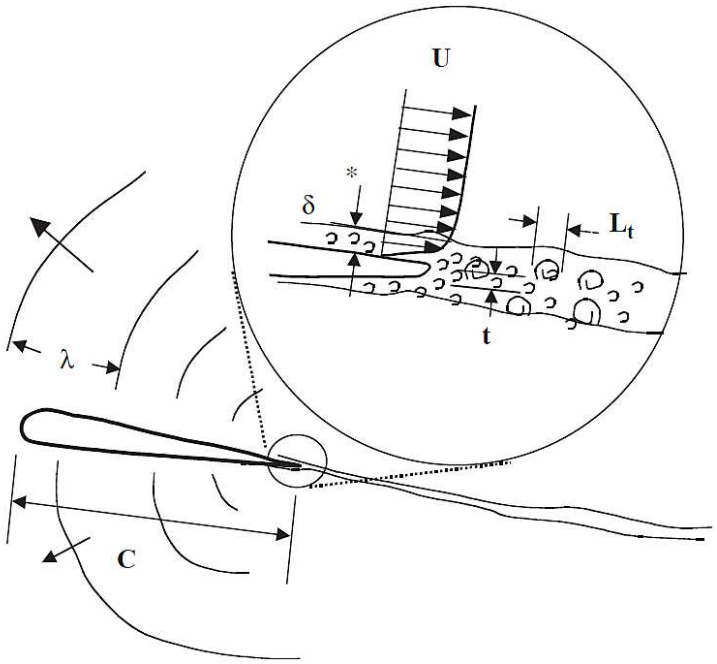

Figure 1.2 Broadband noise radiation from airfoil TE [Colonius and Lele, 2004].

1) Models based on Lighthill's acoustic analogy;

2) Models based on linearized hydroacoustic problems;

3) Models using ad-hoc approach.

Since then more models have been proposed which can take into account the effect of Reynolds number, pressure gradient, etc. However, the effects due to the airfoil geometry and the angle of attack are rarely considered. In general, these models are derived for low to moderate cambered airfoils. Another limitation is that the effects of airfoil thickness is usually neglected and small or zero angle of attack is assumed. As a result, it could be concluded that most of these models are able to explain the broadband noise but in certain limited flow conditions over flat plates. Hence it could be said that the generation mechanism on such a noise is established, but is constrained to limited flow conditions: fully established attached turbulent flows, which is questionable, for its applications on airfoils. Because the flow over airfoils are essentially spatially developing flows and the flow conditions can be quite different from one to another because of different airfoil geometries and angles of attack.

Compared with tonal noise, an important difference worth noticing is that the broadband noise is induced by the small scale, less organized turbulent boundary layers. This is quite challenging to be measured properly from experiments and make the study of such a noise relies greatly on highly resolved simulations (both in space and in time) such as LES

(Large Eddy Simulation) and DNS. Theoretically, DNS resolves all scales and is ideal as a numerical tool for such a noise study. However, due to the Reynolds number constraints [Chapman, 1979; Choi and Moin, 2012; Pope, 2000], most of the reliable DNS databases were at low Reynolds numbers in previous studies [Jones, 2008; Jones *et al.*, 2008] as a compromise to computational costs. LES was usually employed for higher Reynolds number cases yet most of the cases are on canonical flows: flow over the symmetrical thick NACA0012 airfoils [Wolf and Lele, 2012]. In both the LES and DNS cases, the installation effects [Moreau *et al.*, 2003], which describes the actual airfoil loading and wake deviation based on experimental setup, in contrast to the ideally free-field, were rarely considered in previous studies. This lack of consistency makes the results from these simulations hard to be compared with experiments as such effects can dramatically change the aerodynamics and thus the associated aeroacoustics. In all, DNS of a more realistic flow at high Reynolds number taking the installation effects into account should bring knowledge to the generation mechanisms of such a noise.

1.3 Research Tools on TE Noise Study

As partly mentioned in the section above, TE noise was firstly studied through experimental approaches and the experiments continue being a fundamental tool for the research. Later the analytical and numerical studies came out and have played important roles in the domain. Unfortunately, the measured results differ substantially from each other due to diverse experimental setups and the analytical methods always have limitations which will be discussed in detail later in *Chapter 2*. Thus the state-of-the-art numerical approach DNS will be employed in this dissertation to gain a more comprehensive understanding of TE noise taking the installation effects into account. Apart from the higher accuracy in the simulation, one crucial advantage of DNS is that there is no background wind tunnel noise which is almost inevitable in the experiments. When properly carried out, the DNS is able to provide an environment in which airfoil self noise is truly the only noise source present.

1.4 Objectives and Outline of the Thesis

This PhD project thus uses DNS of the flow over an airfoil to achieve 2 main desired objectives:

To better understand the TE noise generation mechanism;

To validate and to discuss the limitations of analytical approaches through DNS results.

To that end, 2 DNS cases on a NACA6512-63 airfoil and on a Controlled-Diffusion (CD) airfoil respectively at a high Reynolds number based on the chord length of 1 5 10^5 are realized in this thesis. In both cases, the airfoil are untripped. Various comparisons and analysis with experimental and other numerical methods are made and discussed. In the following, a literature review concerning the airfoil TE noise from different approaches are presented in *Chapter 2* to show the current research progress. A detailed discussion on the assumptions of analytical approach and on numerical methods with emphasis on the DNS are presented. In *Chapter 3*, the details of the numerical code used for both simulations and the associated post-processings are introduced. In *Chapter 4* and *Chapter 5*, numerical setups and results for the 2 DNS cases are shown and discussed. And at the very end, a summary of the main results of the thesis and the possible perspectives are given.

CHAPTER 2

State-of-the-Art

2.1 Experimental Methods

Understanding and predicting TE noise have been an on-going challenge for researchers and engineers over the last 40 years. Experimental studies on airfoil TE noise were firstly carried out in the 70 80s ([Brooks and Hodgson, 1981] [Fink, 1975] [Brooks *et al.*, 1989], etc) to quantify the parameters of the noise source related to the airfoil boundary layer. Brooks proposed the following definition for the airfoil self-noise [Brooks *et al.*, 1989]: "The total noise produced when an airfoil encounters smooth non turbulent inflow". Such a notion is widely accepted for the TE noise studies, particularly to distinguish from the other airfoil related noise namely the turbulence-interaction noise or leading-edge noise. Measurements of the velocity of the hydrodynamic field in the vicinity of the TE or the wake have been reported using hot-wire [Finez *et al.*, 2010] [Moreau *et al.*, 2006b] [Padois *et al.*, 2015]. Pressure sensors are used to measure surface pressure spectra near TE [Herr and Dobrzynski, 2005] [Moreau and Roger, 2005] [Moreau and Roger, 2009] [Padois *et al.*, 2015] (Fig. 2.1). More recently, the spatial and time resolved PIV (Particle image velocimetry, Fig. 2.2) measurements [Schröder *et al.*, 2004] [Ghaemi *et al.*, 2012] [Pröbsting *et al.*, 2013] [Pröbsting *et al.*, 2015] have been conducted to get directly the velocity fluctuations of the boundary layer near TE thus to reconstruct surface pressure fluctuations. These experimental methods can provide validations of the simulations and analytical models.

The experimental methods vary from hot-wire measurements (HWM), particle image velocimetry (PIV) measurements, remote microphone probes (RMP) measurements, static pressure sensor (SPS) measurements, microphone phase array (MPA) measurements and far field microphone (FFM) measurements. They are summarized in Tab. 2.1.

However, in an experimental setup in general, it is challenging to separate the TE noise from other noise sources, such as the noise from the shear layer of an open jet or noise from the separation and reattachement of the boundary layer. Besides, only low speed flow cases could be employed as the noise from the wind tunnel ventilation system (part of the background noise) will increase as the flow speed goes up. And even with the state-of-the-art experimental method PIV, several aspects are limited:

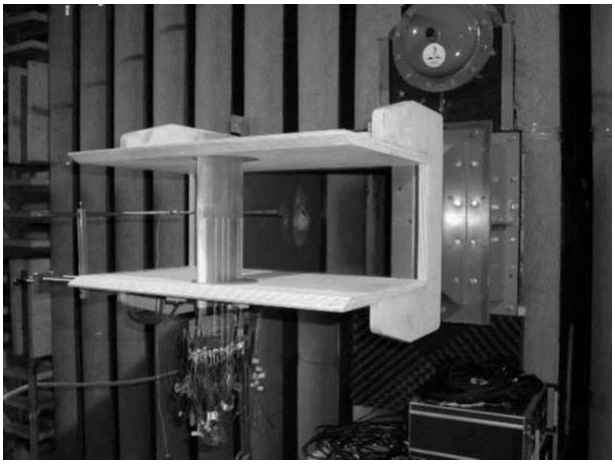

Figure 2.1 Pressure sensors on the Controlled-Diffusion airfoil in the ECL large wind tunnel [Moreau and Roger, 2005].

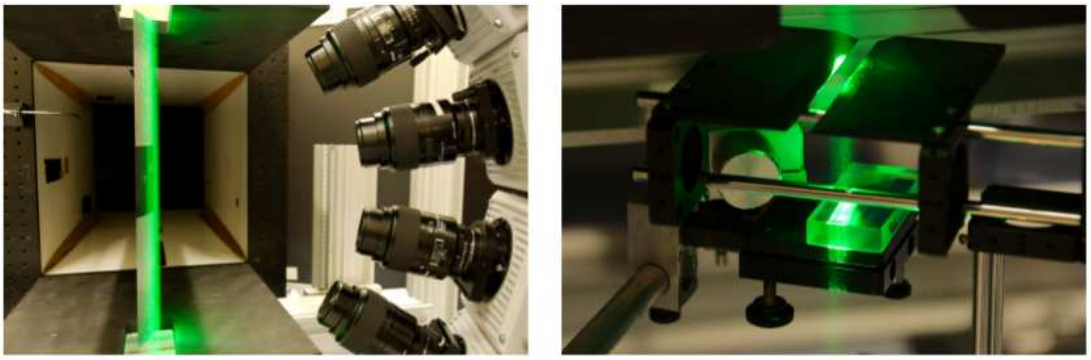

Figure 2.2 A typical tomographic PIV set-up for imaging the flow over a trailing edge (left). Details of the multi-pass illumination arrangement (right) [Pröbsting, 2015].

Experimental Methods	Target Parameter	Comments
HWM	Velocity	BL and near wake velocity profiles
PIV	Velocity field	Entire velocity field near TE and near wake
RMP	Wall-pressure fluctuations	Airfoil TE noise source
SPS	Wall static pressure	Airfoil loading
MPA	Acoustic pressure	Identification of the noise source near airfoil surface
FFM	Acoustic pressure	Far field sound

BL: Boundary Layer

In Amiet's based theories [Amiet, 1976] [Moreau and Roger, 2009]

Table 2.1 Experimental measurements.

The resolution is limited due to the current camera capture capacity and the mock-up size [Adrian and Westerweel, 2011]. Usually, the range of the flow speed and the range of the turbulence scales have to be chosen before the experiments, which means certain flow details may not be observed from a single set of PIV measurements;

The field of view is limited due to the mock-up and to the performance of the camera and the lens;

The attenuation of the laser power may introduce uncertainties to the high frequency phenomenon;

Reflections from the metal surface of the airfoil mock-up (when it is illuminated by the laser beam) add uncertainties of the flow details near the wall.

These drawbacks make the analytical and numerical methods, especially the latter one, essential to get a more comprehensive understanding of such a noise mechanism.

2.2 Analytical Methods

The analytical method aims at providing approximate but very fast and cheap results to predict noise radiated at TE. This is quite useful in engineering or industrial field during the design or test stage of a certain turbomachinery product for example. It is dedicated to an isolated, previously identified mechanism and needs considerable simplifications and assumptions on the flow features or on the geometry [Camussi, 2013]. The analytical method can also be used in the post-processing progress of a simulation result to deduce the far field sound.

Most airfoil TE noise models are based on acoustic analogies and Lighthill's pioneering work [Lighthill, 1952b]. By suitably arranging and combining the Navier-Stokes equations (continuity and momentum equations), a wave equation is obtained. Lighthill's approach

is to compare the real flow with those in an ideal quiescent medium at rest, i.e., outside the turbulent flow field. A Lighthill stress tensor T_{ij} is introduced which acts as a source of sound in Lighthill's wave equation:

$$(\frac{^2}{t^2} \quad c_0^2 \frac{^2}{x_j^2}) \ ' = \frac{^2 T_{ij}}{x_i \ x_j} \tag{2.1}$$

Thus the sound propagation and noise source are presented on the left-hand and right hand sides respectively. Because no simplifications have been introduced in the derivation process of Eq. (2.1), it is clear that Lighthill's equation takes into account not just the sound generation, but also its reflection and scattering effects. To solve this equation, Green's function technique can be applied. This however, assumes that the right-hand side of Eq. (2.1) is decoupled from the left-hand side. This is true when the listener's position is in the far field. The so-called far field is satisfied when the distance between the noise source and the listener are orders of magnitude larger than the wavelength of the source defined as $= c_0 \ f$. A more general solution of Eq. (2.1) was derived by Ffowcs Williams & Hawkings [Williams and Hawkings, 1969] for surfaces in arbitrary motion in free space. Before that, Curle [1955] considered the solution for a stationary surface in a turbulent flow, which is applicable for our TE noise prediction. The integral solution to Eq. (2.1) for the acoustic pressure p in presence of a solid body of surface S is given by [Goldstein, 1976]:

$$\begin{aligned} p^{'}(\mathbf{x} \ t) = & \int_V \frac{^2 G}{y_i \ y_j}(\mathbf{x} \ \mathbf{y} \ t \quad) T_{ij}(\mathbf{y} \quad) d^3\mathbf{y} d \\ & + \int_S \frac{G}{y_i}(\mathbf{x} \ \mathbf{y} \ t \quad) p^{'}_{ij}(\mathbf{y} \quad) n_j d^2\mathbf{y} d \\ & + \int_S \frac{G}{}(\mathbf{x} \ \mathbf{y} \ t \quad) \ _0 u_n(\mathbf{y} \quad) d^2\mathbf{y} d \end{aligned} \tag{2.2}$$

with the surface normal vector $\mathbf{n}$ being directed into the fluid. Eq. (2.2) states that sound is generated:

- by the turbulent stresses T_{ij} distributed throughout the fluid (quadrupole source);
- by the unsteady forces $p^{'}_{ij} n_j$ exerted from S on the fluid (dipole source);
- by the rate of variation of local mass outflow from S (monopole source).

For a rigid airfoil, the wall-normal velocity u_n is zero, and this last term vanishes.

To seek a proper Green's function G, which represents the causal solution of the wave equation (Eq. (2.1)) and satisfies the proper boundary conditions on the surface S, is thus the target of the diffraction theories. The Green's function G is a function of the source

location $\mathbf{y}$, the observer location $\mathbf{x}$, and sources radiated at emission time and heard at t. Here and afterwards, these notions are used. Exact analytical Green's functions are known only for simple geometries (such as half planes, spheres, or circular cylinders for instance). However, it is possible to find approximate Green's functions such as compact Green's functions [Howe, 2001], which are valid for solid bodies that produce sound of wavelengths that are relative large compared to the dimension of the body. For more complex geometries, the Green's function needs to be computed numerically by finite-element method [Caro *et al.*, 2004] [Escobar, 2007] or alternative techniques. Several TE noise models were reported in the literature. The difference between different theories is essentially how to treat and choose Green's function G.

A review from Howe [Howe, 1978] has classified the models as 3 categories: Lighthill's [Lighthill, 1952b] acoustic analogy based models [Williams and Hawkings, 1969] [Williams and Hall, 1970] [Crighton, 1975]; Amiet's (or similar) theory based on the solution of special problems approximated by the linearized hydroacoustic equations [Amiet, 1976] [Chase, 1972] [Curle, 1955]; and ad hoc models [Tam and Yu, 1975] [Hayden *et al.*, 1976]. The last type involves postulated source distributions whose strength and mulitpole types are generally determined empirically as they were proposed at the early stage of the development of the domain. In this last type, the so-called "BPM" (Brooks, Pope, and Marcolini) model [Brooks *et al.*, 1989] based empirical correlations from airfoils over a large range of conditions serves often as a prediction tool for industrial applications. It will rather be the first two types that will be discussed in this section.

2.2.1 Ffowcs Williams & Hall Analogy

Ffowcs Williams & Hall analogy [Williams and Hall, 1970] uses the volumetric sources in the vicinity of the TE. It uses half-plane Green's functions (which indicates that the airfoil is considered as a semi-infinite half plane) with zero thickness to count for the sound scattering and then the compressibility of the air to deduce sound propagation. The velocity fluctuations around TE are the noise sources of the model. It should be noticed that such an analogy originally is limited to thin airfoils and can be used with incompressible acoustic sources. Wang *et al.* [2009] has generalized this analogy to finite-chord length when deducing far field sound from LES (large eddy simulation) computation. According to the change of coordinate system introduced by Wang *et al.* [2009], the far

field acoustic pressure p_a is given by

$$p_a(\mathbf{x}\quad) = \quad {}_0\frac{2e^{\ i\ \ 4}}{1\ 2}k^2 sin(\quad 2)\quad {}_V\frac{e^{ikR}}{4\ \ R}\frac{sin^{1\ 2}(\ \ )}{(2kr_0)^{3\ 2}} \\ [u^2\quad u_r^2 sin(\ {}_0\ 2)]\quad 2u_r u\ cos(\ {}_0\ 2)\ d^3\mathbf{y} \tag{2.3}$$

where is a correction factor multiplied to the original source terms in [Williams and Hall, 1970] (details in Appendix in [Wang *et al.*, 2009] taking the finite-chord effects into account). It can be seen that such an analogy requires velocities (3D) from the time and space resolved volume from the noise source, i.e., near the airfoil TE. It should be noticed that recording such a volume data during the simulation is expensive. Moreover, the size of the volume is a priori unknown and need to be evaluated for each case. The Ffowcs Williams & Hall analogy is applicable for noise prediction from numerical simulations but normally not for experimental data [Pröbsting, 2015] as a volume integral of the velocity field is required with high spatial resolution.

2.2.2 Curle/Amiet's Analogy

Curle's analogy [Curle, 1955] considers noise radiated from stationary surface. Compared with Ffowcs Williams & Hall analogy, it involves compressibility effects (density fluctuations) in the source terms and that makes the use of such an analogy suitable for compressible simulations. For incompressible simulations, its application will be restricted to compact source region, i.e., l 1. Here the l for airfoil case will be the chord length c. That means only low frequency source can be considered. The far-field acoustic pressure in Curle's analogy is

$$p'(\mathbf{x}\ t) = \frac{^2}{x_i\ \ x_j}\qquad {}_V[\frac{T_{ij}}{4\ \ c_0^2\ \mathbf{x}\quad \mathbf{y}}]d^3\mathbf{y}\qquad {}_V[\frac{p' n_i}{4\ \ c_0^2\ \mathbf{x}\quad \mathbf{y}}]d^2\mathbf{y} \tag{2.4}$$

At low speed the volume integral in Eq. (2.4) can be neglected. Thus, in the DNS, the pressure fluctuations on the airfoil surface needs to be recorded.

Amiet's diffraction theory provides a simpler way to compute the wall-pressure fluctuation p'. The linearized Euler equations are recast into a wave equation that is transformed into a Helmholtz equation by a time-Fourier transform. This equation with the proper boundary condition in two half-planes can be solved by the Schwarzchild method borrowed from diffraction problems in electromagnetism []. As the broadband noise is a random process, a statistical treatment of the far-field acoustic pressure is needed to yild the following

power spectral density (PSD)

$$S_{pp}(\mathbf{x} \quad) = (\frac{sin}{2 \ R})^2 (kC)^2 d \ \mathcal{L}^{\ 2} \quad _{pp}(\quad) l_z(\quad) \tag{2.5}$$

where $\mathcal{L}$ is an analytical radiation integral, $\quad_{pp}$ is the PSD of the wall-pressure fluctuations near the TE and l_z is the spanwise coherence length of these wall-pressure fluctuations near the TE. Both $\mathcal{L}$ and l_z depend on some turbulent convection speed u_c. The assumption of such a theory includes a frozen boundary layer (status of points inside the boundary layer is similar) at TE and a thin or flat plate TE. Recent extensions by Roger & Moreau [Roger and Moreau, 2005] [Moreau and Roger, 2009] [Roger *et al.*, 2006] has introduced leading edge back-scattering effect and vortex shedding effects, which makes Amiet's analogy possible to include finite-chord length and airfoil thickness influence. Yet because of the camber, the adverse pressure gradient effect is one aspect to be addressed by the DNS. Besides, the spanwise correlation length is normally based on Corcos' model [Corcos, 1964]. From DNS such a parameter can be obtained directly.

Amiet's theory for TE noise [Amiet, 1976] requires the wall-pressure spectrum near the TE. For modeling it, empirical models were firstly proposed in late 60's from experiments data base for the flat plate TE noise in which no pressure gradient was considered. Willmarth and Roos [1965] have collected experimental wall-pressure measurements beneath a turbulent boundary layer. Based on those measurements, Amiet [Amiet, 1976] proposed an analytical formulation using outer boundary-layer variables:

$$\frac{_{pp}}{u_e^3} = 2 \ 10^{\ 5} \frac{F(\quad)}{2} \tag{2.6}$$

with F function of $\quad = \quad u_e$ where $\quad$ and u_e represent the boundary layer displacement thickness and the external velocity. The model showed a good agreement with available experimental results [Keith *et al.*, 1992] at high frequencies for zero-pressure gradient flows. Chase [Chase, 1980] proposed a formulation for the wall-pressure spectrum based on mixed variables, which takes into account both the inner and outer boundary layer variables:

$$\frac{_{pp} u_e}{^2_w} = \frac{2(\quad u_e)^2}{[(\quad u_e)^2 + 0 \ 0144]^{3 \ 2}} \tag{2.7}$$

where $_w$ stands for the wall shear stress. The use of mixed variables has become more popular after this model as it presents more physical information. Goody [Goody, 2004] has improved this model to take into account the ^{5} spectral decay which has been measured at high frequencies, and above all, the Reynolds dependence of the high-frequency

roll-off. However, the normalized wall-pressure spectra can be increased by up to 10 dB in the case of adverse pressure gradient, as observed experimentally by Schloemer [Schloemer, 1967] and numerically by Na [Na, 1997]. Recently, Rozenberg [Rozenberg, 2007] [Rozenberg *et al.*, 2010] [Rozenberg *et al.*, 2012] has proposed a model to include the adverse pressure gradient effects as shown in Eq. (2.8), which makes the model more adapted to the TE noise prediction on real airfoil cases where pressure gradients are observed because of angle of attack (AoA) and camber:

$$\frac{{}^{pp}u_e}{{}^{2}_{w}} = \frac{0\ 78(1\ 8\quad {}_{c} + 6)(\frac{}{u_e})^2}{[(\frac{}{u_e})^{0\ 75} + C1]^{3\ 7} + [C_3(\frac{}{u_e})]^7} \tag{2.8}$$

It is considered as a better model among other empirical models [Christophe, 2011; Lee, 2018; Lee and Villaescusa, 2017; Node-Langlois *et al.*, 2014; Volkmer and Carolus, 2018] because it is computationally inexpensive and account for adverse pressure gradient based on several airfoil experimental datasets, which consequently gives more robust results. Yet Catlett *et al.* [2014] has argued that unfavorable results from this model was observed for a different airfoil (not cambered) at relatively higher AoA of which the boundary layer was under higher adverse pressure gradient. He has proposed another empirical model called NSWCCD based on improvement of Goody's [Goody, 2004] model. However, the new model for V2 and Controlled Diffusion (CD) airfoil on which Rozenberg's model was established, ended up with a poor prediction. Most recently, Lee and Villaescusa [2017] compared 5 existing empirical models: Goody's [Goody, 2004], Rozenberg's [Rozenberg *et al.*, 2012], Catlett's [Catlett *et al.*, 2014], Kamruzamman's [Kamruzzaman *et al.*, 2015] and Hu & Herr's [Hu and Herr, 2016] models. They found that there is not a single model that provides consistently accurate results for different test cases. However, for zero pressure gradient flows, Goody's model [Goody, 2004] and Hu & Herr's model [Hu and Herr, 2016] are the most accurate. For a adverse pressure gradient on airfoils, Rozenberg's model [Rozenberg *et al.*, 2012] and Kamruzzaman's model [Kamruzzaman *et al.*, 2015] are the most accurate. Catlett's model [Catlett *et al.*, 2014] results in inaccurate results in most cases. They proposed further an improved model [Lee, 2018; Lee and Villaescusa, 2017] based on the Rozenberg's model [Rozenberg *et al.*, 2012], which extends the validity of the original Rozenberg's model to zero pressure gradient flows as well. This is, according to the knowledge of the author, the most advanced empirical models up to now. In general, as the coefficients of the empirical models depend partly on the associated experiments who differ from case to case in terms of flow condition and airfoil geometry, it is logical to apply such models according to reference cases. These limitations coming from empiricism and the consequent uncertainties in different models can be avoided by applying direct

numerical simulations as the acoustics and fluid dynamics are computed at the same time without any turbulence modeling.

From a different point of view, a set of models based on the velocity statistics from turbulent boundary layers are developed. An important difference between these models and the empirical models such as shown in Eqs. (2.7) and (2.8) is that the empirical models are purely local and rarely take the boundary layer statistics into account except for the wall surfaces whereas these models based on velocity statistics do. These models are developed from Kraichnan's work [Kraichnan, 1956] on a model which relates the spectrum and correlation function of the surface pressure distribution to the corresponding functions for a homogeneous turbulent flow to reconstruct the turbulent flow on a flat plate. Two branches of models based on [Kraichnan, 1956] were then developed. One branch is the the so-called "Blake-TNO" models by Blake [1986], Parchen [1998] and most recently by Moriarty *et al.* [2005], Bertagnolio *et al.* [2014] and Fischer *et al.* [2017]. The name "TNO" comes from the name "TNO Institute of Applied Physics" in the Netherlands. These models impose some simplifications on the 5 integrals of the model from Panton and Linebarger [Panton and Linebarger, 1974] in order to reach a single integral in their final forms to calculate the wall spectra.

Recently, another branch of models [Grasso *et al.*, 2018; Remmler *et al.*, 2010] dedicated in the application of Panton and Linebarger's model use Monte-Carlo methods to calculate the whole 5 integrals in [Panton and Linebarger, 1974]. In this way, the computation is more expensive than the Blake-TNO models. Yet the result relies on less restrictive assumptions (only the frozen turbulence assumption was taken) on the characteristics of the turbulent boundary layer. Remmler *et al.* [2010]'s work is taken here as an example. The model is based on the reformulation of the incompressible Navier-Stokes equation into the form of a Poisson equation for the pressure. Hypothesis is made that the flow is statistically stationary and homogeneous in the streamwise and spanwise directions (which is a questionable assumption as the physical process depends on the flow features as well as the airfoil geometry near TE), and the Poisson equation is solved with a Green's function. The pressure spectrum is then integrated over the planes parallel to the wall and over the spanwise wave number k_3. The final expression of the wall-pressure spectrum is:

$$_{pp}(\ \ ) = 8\ ^2 \qquad _0 \quad \frac{k_1(\ \ )^2}{k\ (\ \ )^2} e^{\ \ k\ (\ \ )(y+y)} S_{22}(y\ \ y\ \ \ \ ) \frac{U_1}{y} \frac{U_1}{y} dy dy k_3 \tag{2.9}$$

where S_{22} stands for the energy spectrum of the vertical velocity fluctuations given by:

$$S_{22}(y\ y\quad) = \frac{\overline{u_2}(y)\overline{u_2}(y)}{2}\ \ ^2 \qquad _0 \ R_{22}cos(\ \ k_1(\ \ )r_1)cos(\ \ k_3r_3)dr_1r_3 \tag{2.10}$$

The model uses actually the streamwise mean velocity profile U_1 and the crosswise velocity fluctuation profile $u_2(y)$. The velocity correlation function R_{22} and the scale anisotropy factor [Amiet, 1976; Paterson *et al.*, 1973] need to be modeled [Panton and Linebarger, 1974]. In [Remmler *et al.*, 2010], RANS simulation input was fed to this model and the comparisons with experimental data showed an acceptable prediction. This model together with Rozenberg's model [Rozenberg, 2007] [Rozenberg *et al.*, 2010], is reported in [Christophe, 2011] to have a good overall prediction for the pressure spectrum at the TE of the CD airfoil (Fig. 2.3). Yet both methods have limitations on the frequency ranges. Rozenberg's model [Rozenberg *et al.*, 2012] may have difficulties in precisely predicting the high frequency noise sources as the wall shear stress is one key parameter which depends highly on the quality of the simulation or experiments. For Remmler et al.'s model [Remmler *et al.*, 2010], uncertainties appear at low frequencies due to the convergence of Monte-Carlo methods.

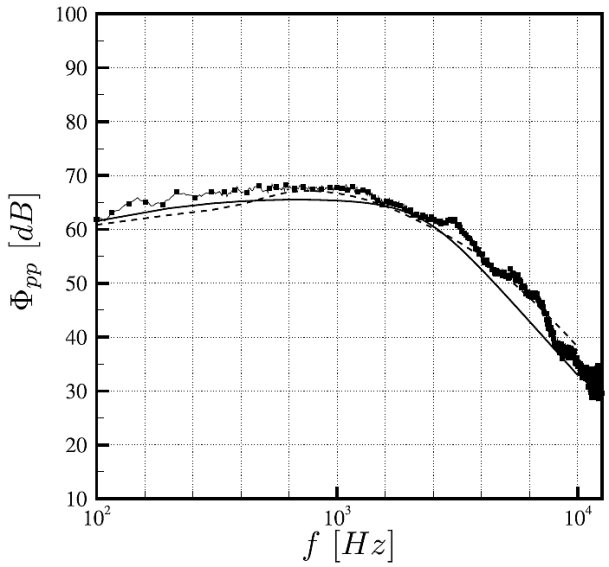

Figure 2.3 Comparison of experimental spectrum (plain-squares) and corresponding modelling using RANS inputs near the TE ($x\ c = \ \ 0\ 02$)of the Controlled Diffusion airfoil: (plain) Rozenberg's model [Rozenberg, 2007] and (dashed) Panton's model [Panton and Linebarger, 1974].

Nevertheless, all the models developed after the work of Kraichnan [Kraichnan, 1956] have several common and imposed assumptions:

Flow considered as incompressible (Poisson's equation applied);

Turbulence intensity and mean shear null outside the boundary layer;

Frozen turbulence near the TE (explained in [Panton and Linebarger, 1974], [Bertagnolio *et al.*, 2014] and [Fischer *et al.*, 2017]);

Flow considered as homogeneous parallel to the wall and isotropic within the parallel planes.

These assumptions, however, are not always established in a real turbulent boundary layer over an airfoil and can consequently affect the related noise. With highly time and space resolved simulations as DNS, these assumptions can be further verified and analyzed.

2.2.3 Limitations of Models

In summary, the analytical methods are quick and relatively accurate solutions to certain flow cases and are useful for quick estimation purposes, but they involve several aspects limiting the application of such methods, which, can be addressed by the current DNS study:

Airfoil TE Shape effects (which can lead to possible vortex shedding and can challenge the Kutta condition in the models);

Pressure gradient effects;

Spanwise correlation effects;

Anisotropic turbulence effects;

Possible compressibility effects;

These aspects will be further discussed with the DNS data in *Chapter 4* and *Chapter 5*.

2.3 Numerical Methods

The numerical methods are relatively new compared with the experimental and analytical methods on flow generated noise. The recently called CAA (Computational Aero-Acoustics) regroups all methods involving numerical computations to produce acoustical information of aerodynamic phenomena. Typically, the CAA could be classified into two types:

Hybrid methods decouple the computation of the flow from the computation of the sound. So normally, the flow field is obtained from an unsteady computation near the noise source and then the acoustic source radiation is computed in the far field using an acoustic propagation method [Christophe, 2011] [Wang and Moin, 2000] [Salas and Moreau, 2015]. Such methods are established on one assumption: the flow has an influence on the sound generation and propagation but not the

other way around. Such methods have an obvious advantage on the computational cost as incompressible flow computations could be used for low Mach numbers flows and only a relatively small area around the acoustic source needs to be taken into account and fully resolved. Therefore, for an estimation purpose or verification of certain analytical theory, the hybrid methods are apposite.

Direct methods compute the flow and sound fields altogether by solving the compressible flow equations. Time dependent simulations as DNS, LES (Large Eddy Simulation), URANS (Unsteady Reynolds Averaged Navier-Stokes) and DES (Detached Eddy Simulations) can be employed. Especially the DNS, which will be addressed later in this chapter, attracts extreme interest of the academic world because of its capacity of capturing the flow and acoustic field details which leads to the understanding of the real noise generation mechanism [Wang *et al.*, 2006] [Jones, 2008] [Winkler *et al.*, 2012]. However, aside from the requirements on the numerical methods, compared to other simulations, direct computation of sound generated aerodynamically requires larger simulation domain due to the extent of acoustic field and the compressible flow needs higher level of time steps for stability reasons. Moreover, in high Reynolds number and low Mach number cases, the disparities between the hydrodynamic and acoustic amplitudes on the one hand, and the disparities between the turbulent scales and the acoustic wavelengths on the other hand, makes the methods hard to apply. That is why till today, the airfoil TE noise study using such methods has been limited to moderate Reynolds numbers and still open for further progress.

Traditional CFD (Computational Fluid Dynamics) tools solve Navier-Stokes equations (eqs. (2.11) (2.12) (2.13)). According to the descending order of the modelled turbulence (Fig. 2.4) (which is normally the increasing order of computational cost), CAA studies on TE noise can be categorized as URANS, LES and DNS.

For a compressible flow, the governing Navier-Stokes equations are:

$$\frac{}{t} + \frac{(\ u_k)}{x_k} = 0 \tag{2.11}$$

$$\frac{(\ u_i)}{t} + \frac{[\ u_i u_k + p\ _{ik} \quad _{ik}]}{x_k} = 0 \tag{2.12}$$

$$\frac{(\ E)}{t} + \frac{[\ u_k(E + \frac{p}{}) \quad u_i\ _{ik} + q_k]}{x_k} = 0 \tag{2.13}$$

where is the density, u_i stands for the velocity component i, p the pressure, $_{ik}$ is the Kronecker symbol and the total energy is defined as $E = T\ [\ (\quad 1)Ma^2] + 0\ 5u_i u_i$ The

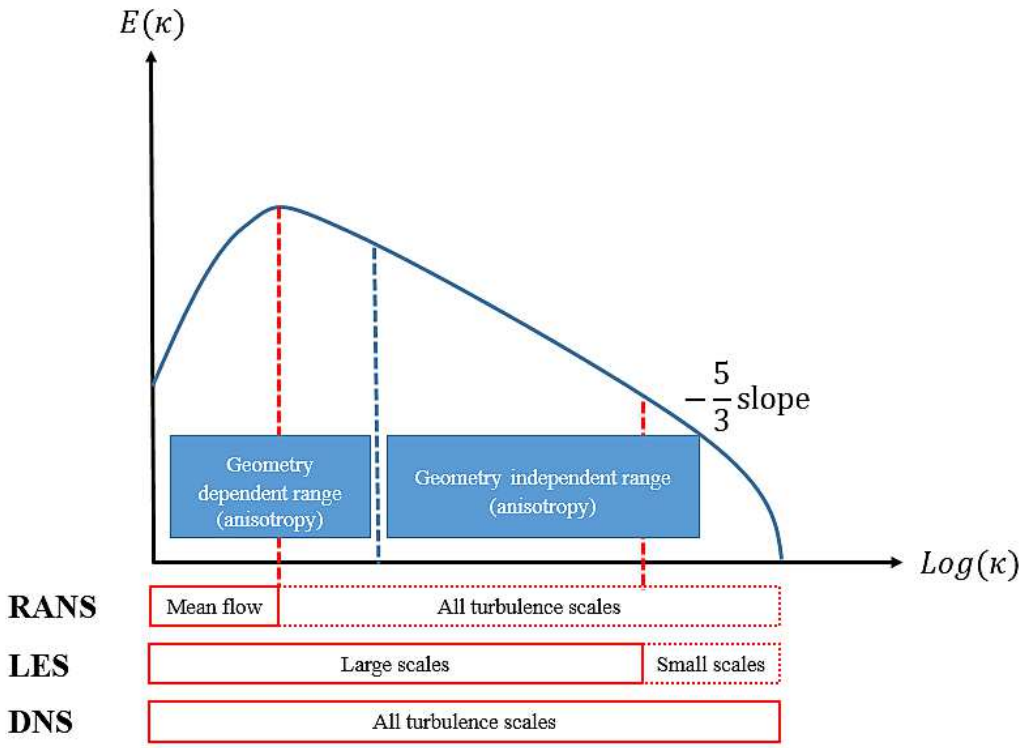

Figure 2.4 RANS, LES and DNS in the turbulent energy spectrum.

stress tensor and the heat-flux vector are computed as

$$u_i \;_{ik} = \frac{}{Re_c}\left(\frac{^i}{x_k} + \frac{^k}{x_i} \quad \frac{2}{3}\frac{^j}{x_j}\;_{ik}\right) \qquad \text{and} \qquad \mathrm{q_k} = \frac{}{(\quad 1)\mathrm{Ma^2PrRe_c}}\frac{\mathrm{T}}{\mathrm{x_k}} \tag{2.14}$$

respectively.

2.3.1 URANS, LES and Hybrid Simulations

As the sound production is essentially an unsteady phenomenon, unsteady solvers (URANS, or what will be mentioned later LES and DNS) are usually employed to compute the noise source. URANS (Unsteady Reynolds Averaged Navier-Stokes) simulations are based on the hypothesis that any instantaneous flow field can be decomposed in two separate components, namely a mean time-averaged flow component and a fluctuation component (eq. (2.3.1)) [Pope, 2000].

$$u_k(\mathbf{x}\;\; t) = \overline{u_k}(\mathbf{x}\;\; t) + u_k(\mathbf{x}\;\; t) \tag{2.15}$$

Alternatively, the sources of sound can be computed from steady RANS, which consumes least computational source and can get rather quickly the aerodynamic field. The volumetric acoustic source can be obtained by means of stochastic methods [Remmler *et al.*,

2010] [Golliard *et al.*, 2006], reconstructing the unsteady turbulent field from the RANS flow quantities, or, using statistical methods as mentionned in *Section 2.2.2*, which provide spectral information depending on RANS inputs, as the wall-pressure spectrum from the distribution of the turbulent kinetic energy (TKE) in a boundary-layer solving linearised vorticity equation [Glegg *et al.*, 2008] or from turbulent boundary-layer profiles solving the Poisson's equation [Panton and Linebarger, 1974] [Remmler *et al.*, 2010]. However, Eq. (2.3.1) results in an open equation system, as the so-called Reynolds stress tensor $r_{ij} = \overline{u_i u_j}$ being created by the fluctuating flow components cannot be obtained directly and is only created as a result of modelling the flow components into mean and instantaneous flow fields. Turbulence models are used to close the system and to define the Reynolds stress, thus allowing to solve the flow field. This modelling comes with a price, as turbulence models are manifold and are often based on empirical studies and are often tuned to particular flow solutions, thus including an additional uncertainty in the resulting flow field calculations.

LES calculations on the other hand are based upon the idea that the larger scales of turbulence in a flow are the main source of energy and must be resolved through the filtered Navier-Stokes equations as they are dependent on the modeled geometry and the overall nature of the flow. The effects of the smaller scale motions are modelled and are considered to have homogeneous and isotropic behaviour. LES offers the promise between the DNS and RANS based simulations, especially, it can be realized for Reynolds number of practical or industrial interests. It copes with the Reynolds number limitation of DNS (which will be presented in *Section 2.3.4*) by only explicitly representing the large turbulence scales in the flow and models the effect of the smaller scales. The mathematical formalism for LES is established through a spatial filtering operation applied to the Navier-Stokes equations, which results in unclosed subgrid-scale (SGS) stress terms. Because the small-scale motions are more universal than the large-scale motions, SGS modeling is expected to be more robust than turbulence modeling in the RANS context [Wang *et al.*, 2006]. Such a closure methodology is based on the Smagorinsky [Smagorinsky, 1963] eddy viscosity model. In the early 1990s, a dynamic procedure for computing the model coefficient from the resolved velocity field was developed, which requires no adjustable constant and near-wall damping functions ([Germano *et al.*, 1991] [Lilly, 1992]), and is thus considered as a major improvement in the robustness and accuracy of LES. In compressible flows, SGS flux terms are also present in the continuity and energy equations, which can be modeled in an anologous way [Moin *et al.*, 1991]. For instance, many more SGS models can be refered in [Bardino *et al.*, 1983] [Stolz and Adams, 1999] [Hughes *et al.*, 2001].

LES simulations are in essence time dependant, as opposed to the time-averaging performed in RANS calculations. It has been a popular tool during the last decade for the TE noise simulations considering that it is a tradeoff between accuracy and computational cost. Wang and Moin [2000] applied incompressible LES together with Ffowcs Williams & Hall's theory to simulate the TE noise of the flow at a Reynolds number based on the chord of 2 1^6 over a slanted flat plate experimentally studied by Blake [Blake, 1975] with an asymmetric TE at Reynolds number of 2 1 10^6. Reasonable agreement with experimental data [Blake, 1975] was obtained for velocity statistics, frequency spectra of surface pressure fluctuations and the far-field sound spectra. The fact that this LES did not take into account the installation effects explains the poor pressure distribution prediction compared with experiments. Later Wang *et al.* [2004] further validated the LES approach for computing the spatio-temporal characteristics of unsteady pressure on the CD airfoil at a Reynolds number at 1 5 10^5. Other incompressible LES simulations on airfoil TE noise can be found in [Oberai *et al.*, 2002] [Christophe *et al.*, 2009] [Christophe, 2011] [Winkler *et al.*, 2010]. All these simulations used either Amiet's model or the Ffowcs Williams and Hall analogy to compute the far-field sound. In these studies, the LES yield acceptable results for flows both with boundary layer separation (caused by higher angle of attack, for instance in [Christophe *et al.*, 2009]) and without. Winkler *et al.* [2010] and Christophe [2011] have argued that the mesh refinement in the spanwise direction is critical in order to better reproduce the aerodynamics in the corresponding experiments because this aspect can affect both the wall-pressure level and the spanwise correlation length at high frequencies, which are two major parameters in Amiet based models. Recently, compressible LES were reported [Wolf *et al.*, 2012a] [Salas and Moreau, 2015]. Wolf *et al.* [2012a] conducted the 3D compressible LES (0.1 chord length in the spanwise direction) of the flow over a NACA0012 airfoil with a rounded TE at Reynolds number of 4 08 10^5 at 5 AoA for two flow configurations with different freestream Mach numbers. The acoustic predictions are performed by the Ffowcs Williams & Hawkings (FWH) acoustic analogy formulation and incorporate convective effects. Salas and Moreau [2015] has conducted a first 3D compressible LES on a high-lift device (HLD) taking into account the installation effect of the jet nozzle [Moreau *et al.*, 2003]. It captures interaction between the shear layer of the nozzle and the airfoil without simplification. It was reported that the numerical schemes have great impact on accuracy on the same wall-resolved grid.

Despite the growing interest in LES on TE noise studies, little attention has been paid to the impact of SGS models on simulation accuracy. Using the Lighthill [Lighthill, 1952a] [Lighthill, 1952c] framework for discussion, the effect of SGS modeling can be illuminated

by the following decomposition of the Lighthill stress tensor in Eq. (2.16).

$$T_{ij} \quad {}_0u_iu_j = T_{ij}^{LES} + T_{ij}^{SGS} + T_{ij}^{other} = \ {}_0\overline{u_iu_j} + \ {}_0(\overline{u_iu_j} \quad \overline{u_i}\,\overline{u_j}) + \ {}_0(u_iu_j \quad \overline{u_iu_j}) \quad (2.16)$$

T_{ij}^{LES} represents the Lighthill stress evaluated from the resolved velocity field; T_{ij}^{SGS} is the subgrid-scale contribution to the Lighthill stress at resolved scales. These two terms represent all the information that can be obtained from a LES source field. T_{ij}^{SGS} however, is generally inaccurate and not fully available from the proposed SGS models such as the Smagorinsky-type [Smagorinsky, 1963], in which the trace of the SGS stress tensor is absorbed into pressure. In addition, T_{ij}^{other} represents the unresolved part of the Lighthill stress, which can only be modeled. All these lead to the fact that in today's Lighthill-based calculations, only T_{ij}^{LES} is used to represent the sound source.

Despite the missing scales (T_{ij}^{other}) effect, SGS model effect (T_{ij}^{SGS}) can be important for noise prediction. Seror [Seror *et al.*, 2000] performed a priori and a posteriori tests of the contributions of the 3 terms in Eq. (2.16) to sound production for decaying and forced isotropic turbulence. The missing-scale contribution was found negligible with typical cut-off wave numbers used in LES, whereas the SGS contribution was not. He [He *et al.*, 2002] [He *et al.*, 2004] examined the SGS modeling effect on the velocity space-time correlations, which are related to the radiated sound intensity by statistical formulation of Lighthill's theory. For decaying isotropic turbulence, he indicated that the accuracy of space-time correlations was determined by that of the instantaneous energy spectra. The performance of several SGS models was evaluated in terms of space-time correlations, and the dynamic model in conjunction with the multi-scale LES procedure was the most accurate. Note that these analyses are all for homogeneous and isotropic turbulence, which is very different from realistic noisy flows such as TE noise in which shear and other effects have to be considered. To the author's knowledge, the effects of SGS modeling is not clearly known for wall-bounded problems on noise study, which makes SGS noise modeling a remaining open area for progress. These uncertainties make LES simulations still lack of reliability on the understanding of TE noise generation.

For most of the URANS and LES simulations, the hydrodynamic near field is computed and the results are then used as input data for an acoustic solver. For the computation of acoustic field, solvers are based on the analytical models mentioned in Section 2.2 ([Oberai *et al.*, 2002],[Winkler *et al.*, 2010], [Wolf and Lele, 2012], [Wang and Moin, 2000]). Through the decoupling of the acoustic and aerodynamic fields, the feedback of acoustic waves on the fluid motion is ignored. RANS on the other hand, can provide initial field and boundary conditions for LES simulations as a practical way to reduce largely the computational

domain and as well to keep the installation effects [Moreau *et al.*, 2003] as used often by Wang *et al.* [2009], Christophe and Moreau [2008] and Winkler *et al.* [2012] in their studies as shown in Fig. 2.5. This idea tested first by [Deniau *et al.*, 2011] for a compressible LES on a NACA651210 airfoil can also be employed for future DNS study. However, due to the modeling limitations which lead to uncertainties to define the noise source when applying acoustic analogies, such methods are not enough to get an comprehensive understanding of the TE noise generation mechanism.

Compressible DNS thus appears to be the most reliable numerical approach that aims at exploring the essential physical phenomena of both aerodynamic and acoustic aspects simultaneously ([Jones and Sandberg, 2012], [Ikeda *et al.*, 2012]).

2.3.2 DNS

In DNS calculations, all scales of the flow field are resolved through the Navier-Stokes equations, including all turbulence scales. This principle enables researchers to employ the "numerical experiment", which, if taken out properly, is the most accurate and detailed way to present the flow field. Compared with the most state-of-the-art experimental method PIV, the spatial resolution of DNS is even higher. Typically, in a DNS simulation the dimensionless wall distance y^+ can be easily smaller than 1 yet in the PIV measurements, it depends on the mock-up and the camera [Adrian and Westerweel, 2011]: given the same PIV system, if the airfoil is bigger the resolution will be better yet the wind tunnel nozzle will have to be redesigned according to the airfoil and the wind tunnel power has to be increased, which is not very feasible if not impossible. For instance, to the author's knowledge, the planar PIV system installed at University of Sherbrooke can achieve a $y^+ = 9$ at most. On the other hand, it is the only computational method that does not require turbulence modeling and thus costs more computational resources than LES, and of course than URANS. Quantitatively speaking, for DNS of turbulent boundary layers, the required number of grid points is estimated as $Re_c^{9\ 4}$ (2.28) [Pope, 2000]; for a wall-resolved LES, this number is $Re_c^{13\ 7}$ [Choi and Moin, 2012] and for a wall-modeled LES, this number is about $Re_c^{2\ 5}$ [Chapman, 1979]. DNS is driven at the beginning by researchers on turbulence study [Moin, 1998]. At that time the flow cases were simple such as flow on a flat plate or in a channel. But with the development of the super calculators and the enhancement of code efficiency, various codes are now dealing with much more complex flows and geometries. As a consequence, it is now feasible to investigate airfoil TE noise using DNS.

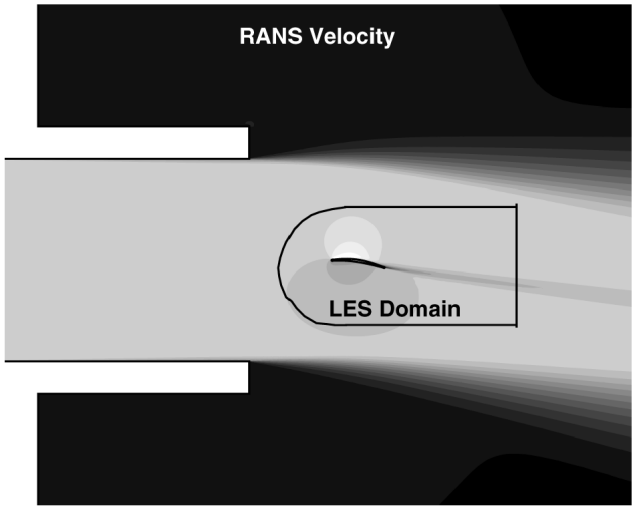

Figure 2.5 LES domain embedded in a RANS solution field [Wang *et al.*, 2009].

For tonal noise study, an acoustic feedback mechanism firstly found from experiments [Arbey and Bataille, 1983; Nash *et al.*, 1999] involving boundary layer instabilities was recently confirmed by direct numerical simulations (DNS) [Desquesnes *et al.*, 2007; Jones and Sandberg, 2011; Sandberg *et al.*, 2009]. These DNS were 2D simulations or used very limited span and at relatively lower Reynolds numbers. Sandberg *et al.* [2009] confined their work to a NACA0012 aerofoil at 0 , 5 and 7 angles of attack. The flow Mach number was 0.4 and the Reynolds number was 5 10^4. No tone was found at 0 AoA. At 5 AoA, a separation bubble formed on the suction side of the aerofoil. At 7 AoA, flow separation took place. Later, Jones and Sandberg [2011] repeated a similar computation at a slightly higher Reynolds number of 1 10^5. The angles of attack in this work were 0 , 0 5 , 1 and 2 . They performed instability wave analysis of the airfoil boundary layer. They reported that the feedback loop is found only when an flow instability is present, which then yields prominent tonal noise. It is also found to self-select a frequency almost identical to that of the tonal self-noise. The constituent mechanisms of the acoustic feedback loop are considered, which appear to explain why the preferred frequency is lower than that of the most convectively amplified instability wave.

Comparing with analytical methods, Sandberg *et al.* [2007] have noticed that viscosity affects the behaviour of the flow at low to moderate Reynolds number when comparing the DNS data against the results from Amiet's theory (2D). Moreover, TE noise models based on Amiet's theory cannot account for additional noise sources such as reattaching laminar separation bubbles or quadrupole source in the wake. Later their continuous studies [Jones, 2008] [Jones and Sandberg, 2009] shows that laminar separation bubbles during the transition process is a significant noise source at this low Reynolds number

(5 10^4). Other DNS studies such as Tam and Ju [2006] at higher Reynolds number claims that the vortex shedding causes the emitted tones. Yet, Tam and Ju [2006]'s work was constrained to 2D simulations and could not account for the actual turbulence development for the considered Reynolds number.

2.3.3 LBM

Aside from the traditional CFD tools based on the discretization of the Navier-Stokes equations on TE noise study, LBM (lattice-Boltzmann method) simulations have also provided some interesting results in the field. The development of such method for aeroacoustic applications can be found in Marie's thesis [Marié, 2008].

The LBM relies on the statistical physics by considering an ensemble of particles described by a distribution function (a probability density function) $f(\mathbf{x}\ \mathbf{c}\ t)$, which represents the probability of molecules with a velocity $\mathbf{c}$ at the location $\mathbf{x}$ and at the time t. The evolution of $f(\mathbf{x}\ \mathbf{c}\ t)$ is given by the Boltzmann equation (1872) [Succi, 2001]:

$$\frac{f}{t} + c_i \frac{f}{x_i} + \frac{F_i}{m} \frac{f}{c_i} = \quad \frac{f}{t}_{collision} \tag{2.17}$$

in which, m is the molecular mass of the gas. It describes the advection of f at the velocities c_i exposed to an external force F_i with an additional source term named the "collision operator" at the right hand side of Eq. (2.17). This source term represents the effect of the particle collision. Bhatnagar *et al.* [1954] introduced a simplified model for this source term, called the BGK model:

$$\frac{f}{t}_{collision} = \quad \frac{1}{}(f \quad f^{eq}) \tag{2.18}$$

where is a relaxation time. One can relate the fluid kinematic viscosity to the relaxation time by

$$= (\quad 1\ 2)T \tag{2.19}$$

The BGK model describes a relaxation process to an equilibrium state defined by the Maxwell-Boltzmann velocity distribution:

$$f^{eq}(\mathbf{x}\ \mathbf{c}\ t) = \quad \frac{m}{2\ k_B T}^{\frac{3}{2}} \quad e^{\ \frac{m}{2\pi k_B T}(\mathbf{c}\ \ \mathbf{u})} \tag{2.20}$$

By neglecting the external forces and by combining Eqs. (2.17) and (2.18), the Boltzmann equation writes:

$$\frac{f}{t} + c_i \frac{f}{x_i} + \frac{F_i}{m} \frac{f}{c_i} = \quad \frac{1}{}(f \quad f^{eq}) \tag{2.21}$$

This Boltzman-BGK equation is the basic equation that the LBM based solvers use. Its expansion allows to recover the Navier-Stokes equations. It can be rewritten as a differential equation form:

$$\frac{\mathrm{d}f}{\mathrm{d}t} + \frac{1}{}f = \quad \frac{1}{}f^{eq} \tag{2.22}$$

with

$$\frac{\mathrm{d}}{\mathrm{d}t} = \frac{}{t} + c_i \frac{}{x_i} \tag{2.23}$$

The integration over timestep t gives the discrete form [He and Luo, 1997]:

$$f(x_i + c_i \quad t \;\; c_i \;\; t + \quad t) \quad f(x_i \;\; c_i \;\; t) = \quad \frac{1}{}\left[f(x_i \;\; c_i \;\; t) \quad f^{eq}(x_i \;\; c_i \;\; t)\right] \tag{2.24}$$

To solve the Boltzmann-BGK equation (Eq. (2.21)) over all possible velocities is impossible in numerical simulations. The velocity space (infinite dimensions for infinite velocity directions in theory) has to be reduced to a fixed discrete number of velocity directions. The chosen discrete velocities must verify a set of symmetry conditions in order to ensure an enough lattice isotropy to correctly recover the macroscopic partial differential equations [Latt, 2007]. A possible discretization is the D3Q19 model. D3 stands for 3 dimensional and Q19 for the number of the considered velocity directions. Obviously, the more velocities are involved, the better the accuracy can be achieved to describe the flow but more velocities end up with higher computational cost. For the D3Q19 model, the equilibrium function up to 2^{nd} order in terms of Hermite polynomials gives the equilibrium distribution function f^{eq} as

$$f^{eq} = \quad _i \quad 1 + \frac{\mathbf{u} \quad \mathbf{c}_i}{rT} + \frac{(\mathbf{u} \quad \mathbf{c}_i)^2}{2r^2T^2} + \frac{\mathbf{u}^{\,2}}{2rT} \quad + \mathcal{O}(\ ^3) \tag{2.25}$$

where $_i$ the weight function related to the velocity discretization model and is an infinitesimal. Through Eq. (2.25), macroscopic quantities and $\mathbf{u}$ can be computed by summing the discrete momentum of the particle distribution. This discretization has been shown to be enough to recover the Navier-Stokes equations in low-Mach number isothermal flows.

The LBM is naturally transient and compressible which can lead to a direct insight on aerodynamics mechanisms responsible for TE noise sources. It could be used in LES [Lew

et al., 2010] or DNS [Sanjosé *et al.*, 2017, 2014b, 2011] depending on the Reynolds numbers considered. For the LES cases, smaller scales are modeled based on RANS equations. In addition, as it possesses from its nature the advantages in terms of integration time and scalability due to simpler partial differential equations and a very compact stencil. On each voxel, the CFL number (Eq. (2.29)) is 1. It is thus a much faster approach for low Mach number cases compared with traditional explicit Navier-Stokes methods. This aspect leads to a faster statistical convergence and makes more and smaller voxels (volume cells) in the simulation possible for a certain flow case, which is vital for aerocoustic applications.

Recently, Sanjosé [Sanjosé *et al.*, 2017, 2011] performed DNS simulations with the LBM method on the CD airfoil at a Reynolds number of 1 5 10^5 and a Mach number of 0.2 for broadband (8 AoA) and tonal noise (5 AoA) respectively, in order to try and reproduce the flow properties and noise mechanisms observed in experiments run at École Centrale de Lyon, Michigan State University, Delft University of Technology and Université de Sherbrooke. These simulations used the low-Mach number LBM solver Powerflow developed by Dassault Systems, as originally suggested by Frisch *et al.* [1987] for gas hydrodynamics. For the broadband (8 AoA) noise case, the far-field simulated sound pressure levels are in close agreement with experimental data in the 200-2000 Hz; results at lower frequency were perturbed by the jet shear layer noise whereas at higher frequencies the experimental data reaches the background noise threshold of the experimental setup. It was mentionned that the 3D setup with more than 11% chord in span was able to capture the vortex stretching in the spanwise direction and the boundary layer was very accurately captured especially at the last location near the TE. This is a key point to precisely capture the TE noise mechanism. This spanwise length was firstly set by experiment [Moreau and Roger, 2005; Roger and Moreau, 2004], and later verified by simulations according to previous incompressible LES for the same flow case indicating that for such a flow case the spanwise extent should be at least 10% chord [Christophe, 2011; Christophe *et al.*, 2008, 2009; Wang *et al.*, 2009]. Because of the high Reynolds number and the low Mach number of such a flow case, this was the first attempt to compute directly the TE noise for a 3D setup. It will be interesting to compare such results with a DNS from a Navier-Stokes solver in this PhD study. For the tonal (5 AoA) noise case, the simulation compares favorably with experimental measurements of wall-pressure, wake statistics, and far-field sound. The temporal evolution of wall-pressure fluctuations shows significant unsteadiness especially in the aft region of the suction side. This is the aspect that such kind of simulation is really capable of because for a traditional DNS for such a flow case, the simulation time would be much more expensive if possible to capture these low frequency and intermittent phenomena.

2.3.4 Brief Summary on Airfoil TE Noise Flow Cases of Existing DNS

Compared to URANS or LES, the significant advantage from DNS that all scales in the flow are resolved directly by DNS, theoretically makes it a method that can automatically handle all phenomena from flow instabilities, transition to turbulence, energy exchanges between the different turbulent scales, to sound production. However, even with today's most powerful computers, DNS is limited to low to moderate Reynolds numbers cases. For the clarity of discussion hereafter, for airfoil TE noise problem, the airfoil chord length based Reynolds number and Mach number are defined as

$$Re_c = \frac{U_0 c}{} \tag{2.26}$$

$$Ma = \frac{U_0}{c_0} \tag{2.27}$$

where U_0 stands for the free stream velocity, c the airfoil chord length, c_0 the sound velocity and the conventional kinematic viscosity of air, which is the ratio of dynamic viscosity and fluid density . It can be shown from an order of magnitude relation that for homogeneous isotropic turbulence the computational cost scales as Eq. (2.28) [Pope, 2000]

$$N^3 \quad Re_c^{9\ 4} \quad \text{and} \quad N_t \quad Re_c^{1\ 2} \tag{2.28}$$

where N is the number of grid points in one spatial direction and N_t is the number of time steps required. Hence, the computational cost strongly depends upon the Reynolds number of the flow. Another constraint comes from the Mach number. As mentioned by Powell [Powell, 1959], the TE noise radiated by a dipole (represented by p) scales as $p \quad Ma^{4\ 6}$, which means, the smaller the Mach number is, the more intense the simulation will be because if p has similar level or is even smaller than the numerical error, due to the finite order of the numerical scheme, p from the simulation can be purely the numerical error. Additionally, from a CFL (Courant–Friedrichs–Lewy) number (which is defined in Eq. (2.29), where c_0 is the velocity of sound, u the velocity of flow, Ma the Mach number as defined in Eq. (2.27) and x the minimum grid cell distance) point of view, by keeping the same CFL number which represents the accuracy level using the same temporal time marching scheme, the augmentation of the number of grid points or loss of temporal resolution will occur if the Mach number is smaller. That's the reason why DNS

suffers from low Mach number cases.

$$CFL = \frac{U \quad t}{x} = \frac{(c_0 + u) \quad t}{x} = \frac{c_0(1 + Ma) \quad t}{x} \tag{2.29}$$

Since direct numerical simulations have such constraints, only a few flow cases have been reported related to TE noise. Tab. 2.2 summarizes flow cases that have been conducted according to the chosen airfoil and associated chord based Reynolds number, Mach number, angle of attack and spanwise length.

Most of the DNS results on TE noise are conducted for the NACA0012 airfoil as there exists a relatively large experimental data base (on aerodynamics and aeroacoustics) since the experiments conducted by Blake [1975]. Moreover, the parameters to produce such an airfoil are easily accessible. It should be noticed however, that due to the variations in the LE and TE radii, and different angles of attack, all these simulations can be hardly compared.

Airfoil	Numerical Method (Year of Publication)	Re_c	Ma	l_{span} c
NACA0012	DNS(2007)	1 10^5/2 10^5	0.05/0.1	5 /2 0
	DNS(2008)	5 10^4	0.4	5 /7 0.2
	DNS(2009)	5 10^4	0.4	0 5 /7 0
	DNS(2009)	5 10^4	0.4	5 0.2
	DNS(2010)	1 10^5	0.4	0 /0 5 /1 /2 0.2
	DNS(2012)	2 5 10^5	0 09 0 21	0 0
NACA0006	DNS(2010)	5 10^4	0.4	7 0.2
NACA0018	DNS(2012)	1 6 10^5	0.09	0 /3 /6 /9 0
NACA6512-63 Tripped	DNS(2012)	**1 5 10^5**	0.25	0 0.15
NACA6512-63 Untripped	DNS(2017)	**1 5 10^5**	0.25	0 0.15
CD	LBM(2011 & 2014)	**1 5 10^5**	0.2	8 0.11
	LBM(2017)	**1 5 10^5**	0.2	5 0.12
	DNS(2018)	**1 5 10^5**	0.25	8 0.12

Table 2.2 Summary of existing DNS on TE noise [Desquesnes *et al.*, 2007] [Sandberg *et al.*, 2008] [Sandberg *et al.*, 2009] [Jones and Sandberg, 2009] [Sandberg and Jones, 2010] [Tam and Ju, 2012] [Jiang *et al.*, 2012] [Winkler *et al.*, 2012] [Wu *et al.*, 2017a] [Sanjosé *et al.*, 2011] [Sanjosé *et al.*, 2014b] [Sanjosé *et al.*, 2017] [Wu *et al.*, 2018] .

Tab. 2.2 shows that the state-of-the-art Reynolds number is 10^5 for direct noise studies. This value is thus considered as a high Reynolds number for a direct simulation. For such a Reynolds number, the flow is often in a transition state to turbulence, which is often observed in engineering applications. In this PhD, we focus on this Reynolds number range. The cases with the superscript " " are the 2 cases achieved in this PhD project. The low to moderate Reynolds numbers for DNS cases on the other hand have been thoroughly reported [Sandberg, 2015]. As mentioned previously, Tam and Ju [2012] have realized simulations with a relatively higher Reynolds number. Yet, their simulation was 2D, the results are not reliable because they do not represent the actual turbulent flow and therefore the mechanisms of TE noise generation. The spanwise length l_{span} is an important parameter on top of Re_c, Ma and . It has a direct impact on the dissipation of the turbulence because of the 3D characteristics of turbulence [Pope, 2000]. Especially if a separation bubble or other recirculation process is present on the airfoil surface, the spanwise length has to be large enough to enable any turbulent eddy to stretch in the spanwise direction. Besides, as partly mentioned in *Section 2.2*, the analytical methods suffer from the spanwise correlation models which can be improved by a high resolution simulation like a DNS. It is thus necessary to do a simulation that has a proper dimension in the spanwise direction. To determine the spanwise length in the simulation, experimental data on the transition process (bubble, recirculation) are usually used and cross correlation techniques are usually employed for the signals in the spanwise direction [Sanjosé *et al.*, 2011] [Sandberg *et al.*, 2008] for the purpose of verification.

2.4 Numerical Considerations of DNS Code

Special features of noise generated by flow motion have demanded special numerical considerations, most of which stem from the very low energy content of the radiated noise relative to the unsteady flow. Because of this energy mismatch, small errors in the unsteady flow have the potential to ruin predictions of the radiated sound [Tam, 2004]. A "clean" acoustic field is important for associated simulations. Particularly, for DNS simulations, several aspects have to be carefully studied to guarantee the accuracy and the performance. This section presents the progress on numerical techniques used in DNS codes.

2.4.1 Numerical Schemes

Navier-Stokes equations are solved directly in DNS simulations through spatial and temperal discretization (Fig. 2.6) on a given mesh. Different spatial discretization methods are

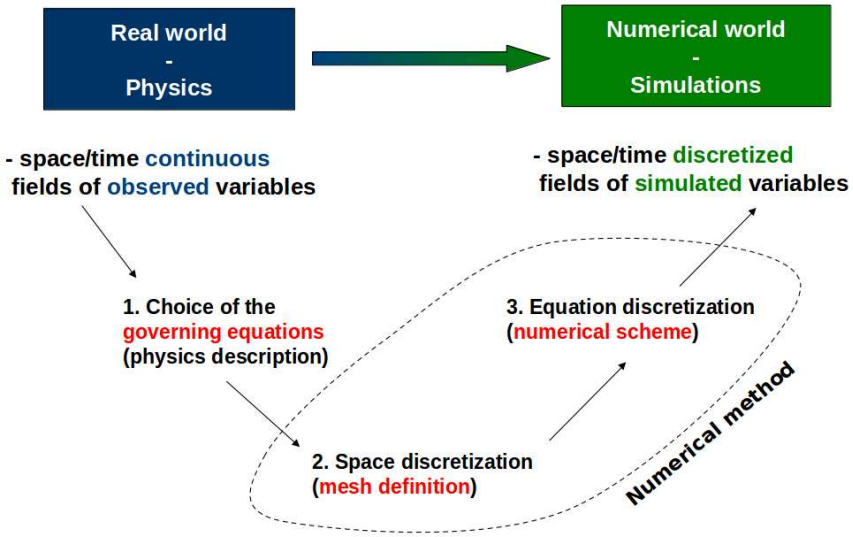

Figure 2.6 Illustration of discretization in numerical studies.

proposed among which finite-volume, finite-element, finite-difference and spectral methods are the major ones. Their particular characteristics are summarized in Tab. 2.3. The application of the spatial schemes depends on the target problem and the associated fluid solver. For an unstructured mesh based solver (typically the choice of RANS or LES) which is normally designed to tackle complex geometries, finite-element or finite-volume method can be employed; for a structured mesh based solver (which, to the author's knowledge, is the case for most high-order accurate DNS solvers), finite-difference schemes are widely used as they can be easily implemented (especially to impose boundary conditions [Tam, 2004]), and its accuracy which will be presented shortly can be easily increased; a spectral method is most accurate and particularly suited to periodic domains and flow phenomena.

Spatial Discretization

In general, DNS for a CAA study is very sensitive to the choice of numerical scheme as the error introduced by the schemes differs from case to case. Finite-difference and spectral methods are presented here in detail due to their suitability to DNS codes. The term "Finite-Difference Scheme" comes from the fact that this method estimates the discretized differential operator using Taylor expansions:

$$u(x + \quad x) = u(x) + \quad x\frac{u}{x} + \frac{^2x}{2!}\frac{^2u}{x^2} + \quad + \frac{^nx}{n!}\frac{^nu}{x^n} \tag{2.30}$$

The order of accuracy of the finite-difference scheme depends on the number of points considered in the stencil around a certain point as shown in Fig. 2.7. In CAA, an estimation of the error introduced by such a scheme can be shown through the example of a 1D linear

Spatial Discretization	General	Applications
Finite-Element	Discretization of the weak form of the conservation laws	Discretized by elements of arbitrary shape and size; A mass matrix must be inverted to solve the problem; The order of accuracy can be increased without changing the stencil; Easy to use with complex geometries.
Finite-Volume	Discretization of the integral formulation of the conservation laws	Discretized by elements of arbitrary mesh; Control volumes must be properly defined (normals of surfaces); Easy to use with complex geometries.
Finite-Difference	Discretization of the Navier-Stokes partial differential equations using node values and Taylor expansions	Easy to develop high order schemes by increasing the stencil; The grid is not necessary regular but must be structured; Also applicable for time discretization.
Spectral Method	Discretization of the Fourier transforms of the Navier-Stokes partial differential equations	Very suited for homogeneous turbulence and periodic problems; Easy to achieve low error level; Not applicable to complex geometry.

Table 2.3 Spatial discretisation methods and their characteristics.

advection/wave problem as follows:

$$\frac{u}{t} + c\frac{u}{x} = 0 \tag{2.31}$$

where c is the constant wave speed, with an initial condition:

$$u(x\ 0) = u^0(x) \tag{2.32}$$

If a 2^{nd} order accurate centered scheme is used as shown in Fig. 2.7 ($x_{i+1} = x_i +\ \ x$):

$$\frac{u}{x}_{\ i} = u_i^{'} \quad \frac{u_{i+1} \quad u_{i\ 1}}{2\ \ x} \tag{2.33}$$

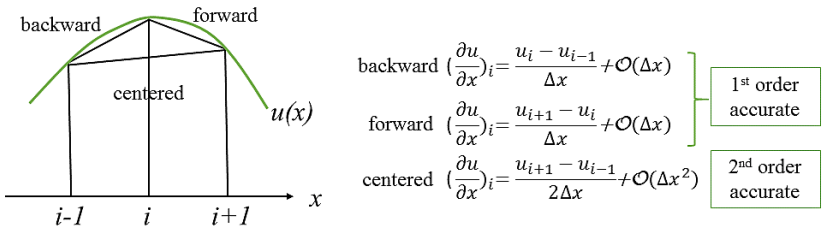

Figure 2.7 Illustration of accuracy of different spatial scheme.

This procedure however introduces important errors for wave related studies (acoustic). If the an initial solution $u(x\ 0)$ is $u^k(x) = \exp(\ \ ikx)$, the exact spatial derivative is

$$\frac{u^k(x_i)}{x} = \ \ i\frac{}{h}u^k(x_i) \qquad \text{with} \qquad = k \ \ x \tag{2.34}$$

Yet the numerical approximation is

$$\frac{u^k(x_i)}{x} \quad \frac{\exp(\ \ ik(x_i + \ \ x) \quad \exp(\ \ ik(x_i \qquad x)))}{2 \ \ x} = \ \ i\frac{}{h}u^k(x_i)\frac{\sin(\ \ )}{} \tag{2.35}$$

From the last equation (Eq. (2.35)), such a numerical scheme has introduced a modified wavenumber sin( ) compared with the exact solution. This effect is referred as *dispersion*. It presents the phase error introduced by the discretization. This error cannot be solved by increasing the grid resolution. It has been reported [Kim and Lee, 1996] [Colonius and Lele, 2004] that dispersion effect can be reduced by applying higher-order schemes (which normally require more points in the stencil). As a result, high-order finite-difference methods for DNS have become increasingly popular, especially for compressible turbulence and CAA.

Compact difference schemes [Lele, 1992] [Kim and Lee, 1996] [Kim, 2007] in contrast to standard difference schemes use the first derivative of the neighbouring points to compute the second derivative and thus the system is implicit. This is more computationally expensive than in case of standard difference schemes but it also has a higher accuracy. DRP(Dispersion-Relation-Preserving) finite-difference schemes [Tam and Webb, 1993] also controls better the dispersion problem and can be employed for unsteady sound generation

problems such as TE noise. Colonius and Lele [2004] has provided a chart for selecting a finite-difference method from some available schemes to minimize computational expense given an accuracy target.

In the 70's and 80's, Orszag and Patterson Jr [1972] and Kim *et al.* [1987] began to employ spectral methods to account for spatial variations. Spatial derivatives are evaluated with the help of Fourier series or one of their generalizations. For a periodic function specified at uniformly spaced set of points, it is possible to express it by a discrete Fourier series:

$$f(x_i) = \sum_{q=\ N\ 2}^{(N\ 2)\ \ 1} F(k_q) \exp^{\mathrm{i}k_q x_i} \tag{2.36}$$

where $x_i = \mathrm{i}\ \ x$ and $k_q = 2\ \ q\ \ \ \ xN$. Eq. (2.36) can be inverted in a simple way by using the formula for the summation of geometric series:

$$F(k_q) = \frac{1}{N} \sum_{i=1}^{N} f(x_i) \exp^{\ \mathrm{i}k_q x_i} \tag{2.37}$$

The most important thing is that Eq. (2.36) can be used to interpolate a continuous function $f(x)$. The choice of the range of q is important. Different sets of q produce different interpolants. The best choice will be the one that gives the smoothest interpolant. Having defined the interpolant, $f(x)$ can then be differentiated as:

$$\frac{df}{dx} = \sum_{q=\ N\ 2}^{(N\ 2)\ \ 1} \mathrm{i}k_q F(k_q) \exp^{\mathrm{i}k_q x} \tag{2.38}$$

which shows that the Fourier coefficients of $df\ \ dx$ is $\mathrm{i}k_q F(k_q)$. This gives such a method several characteristics:

The method is easily generalized to higher derivatives. For example, the Fourier coefficient of $d^2 f\ \ dx^2$ is $\ \ k_q^2 F(k_q)$;

The error in the computed derivative decreases exponentially with N when the number of grid points N is large;

The cost of computing the Fourier coefficients using Eq. (2.37) scales as N^2. The method is made practical by the existence of a fast method of computing Fourier transform (FFT) for which the cost is proportional to $N \log_2 N$.

These characteristics give spectral methods some remarkable advantages. The most important one is that if the range of q is well chosen (normally it means big enough, say infinity mathematically), the error decreases faster than any power of 1 N [Gottlieb and Orszag,

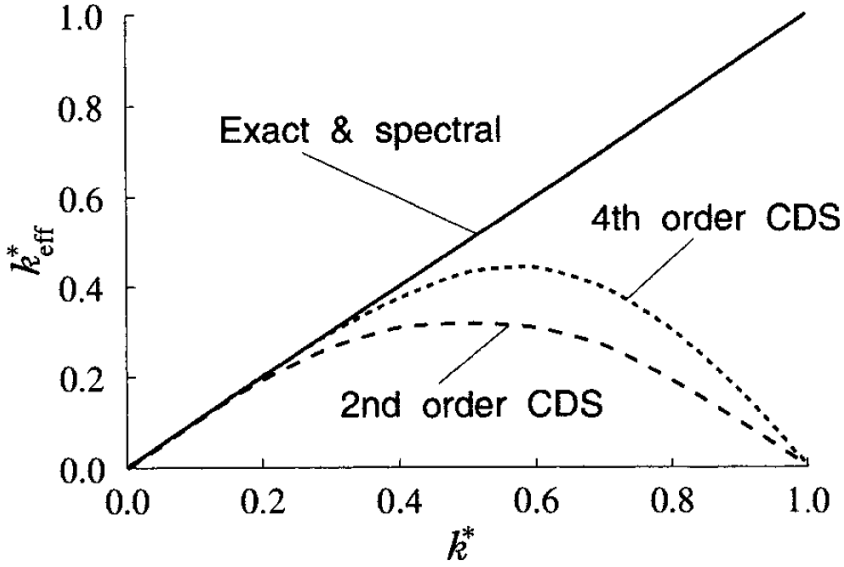

Figure 2.8 Effective wavenumber for the second and fourth order central-difference approximation for the first derivative in the Taylor expansion compared with spectral method [Ferziger and Peric, 2012].

1977]. Therefore, compared to a nth order finite-difference approximation, of which the error is proportional to ($x)^n$ (1 $N)^n$, a spectral method converges with exponential or "infinite-order" accuracy (Fig. 2.8). This method is particularly useful when computing TE noise in the spanwise direction since the periodic nature of such methods will give a faster convergence than discretizing Navier-Stokes by finite-difference.

The disadvantages of spectral methods include the inability to consider complex flow geometries and the special treatment required to enforce inflow/outflow boundary conditions. Due to their use of global basis functions, and the need to access the entire domain in each direction (if it is applied to an entire 3D simulation), spectral methods tend not to perfom well on large distributed-memory parallel systems. Moreover, they cannot accurately represent flow discontinuities, and therefore are not well suited for shock wave study for example.

In summary, spectral methods have their limitations yet very efficient in terms of precision and convergence speed for a suitable case. As in CAA study most of the geometries considered are periodic (especially for academic study cases) in the spanwise direction and flow discontinuities (such as shock wave) are rarely considered, such a method is well suited for simulating the present fluid motion around an airfoil.

Temporal Discretization

For temporal discretisation, two general classifications of time discretization can be found:

Implicit methods, where the spatial derivatives are approximated using information at the new time step.

Explicit methods, where all spatial derivatives needed to advance the solution in time are evaluated at an earlier time step;

Besides these two typical methods, a combination of the two approaches have been used for example, explicit applied to the convective terms and implicit to the viscous terms. Accuracy and stability are tightly connected. Generally speaking, implicit schemes are naturally stable, but at the risk of having lower order of accuracy, because implicit schemes are usually solved with iterative or approximate factorization methods. Such methods will enable the application of a significantly larger timestep, yet at the same time, will introduce a relaxation factor that influences the accuracy [Blazek, 2015].

For explicit schemes, their time-integration can be devised with n-th order of accuracy, which is similar to optimization of spatial finite-difference schemes. The time advancement schemes can also be optimized for frequency resolution [Hu *et al.*, 1996]. The error introduced by the temporal scheme will cause a so-called "dissipation effect". This effect is assessed by studying the ratio u_i^{n+1} u_i^n where n stands for the number of timesteps. Such an effect will damp the amplitude of certain waves in the acoustic field. The derivation is similar to the dispersion effect presented in the section *Spatial Discretization*. High order (4^{th} or more) Runge-Kutta methods are usually the choice of explicit scheme for DNS since they offer a good compromise between accuracy and stability [Colonius and Lele, 2004]. For more details about the stability issue, Kennedy *et al.* [2000]'s work can be referred to.

2.4.2 Initial Conditions

In order to solve the governing Navier-Stokes equations mentioned above, initial and boundary conditions are required. The quality of the initial conditions needed by a DNS varies widely. For stationary flows, the only benefit of specifying a fully physical turbulent initial condition is to minimise the time it takes to overcome an initial transient. Normally, for a high-level resolution simulation such as DNS, the initialization field is given by RANS or a coarser grid DNS or LES to provide the averaged flow field. Such an efficient approach was mentioned in the simulations done by Winkler *et al.* [2012]. This PhD project will use similar procedure to generate the initial conditions for the DNS calculation.

2.4.3 Boundary and Interface Conditions

One of the most challenging aspects of CAA is to impose robust and accurate boundary conditions. For direct noise simulation, the computational domain is chosen to correctly

represent the noise sources (i.e., the TE of the airfoil in this project). At the boundaries of the domain, however, the governing equations cannot be solved since they rely on the flow outside of the chosen domain. Hence, the physical information has to be prescribed in form of special boundary conditions. How to dissipate the disturbances at the boundary and to how to transmit the acoustic wave through the boundaries without reflections are the major challenges of the boundary conditions. Additionally, the boundary conditions should be able to control target main flow features (flow rate, pressure...) and to avoid spurious noise generation. To tackle these problems at computational domain boundaries, 3 representative numerical techniques are employed:

Characteristic based boundary conditions;

Euler or Navier-Stokes characteristic boundary conditions (CBC) aims at tackling small perturbations which are locally one dimensional and inviscid. A description of the mathematical background of boundary conditions based on characteristic wave analysis can be found in [Kreiss, 1970] [Higdon, 1986] [Thompson, 1987] [Poinsot and Lele, 1992]. In Navier-Stokes CBC (NSCBC), the Navier–Stokes equations are written in their characteristic forms to make explicit their dependency on the acoustic waves traveling across the boundary. Characteristic waves are represented by their amplitude time variations $\mathcal{L}_i$. The waves propagate in such a way that some of them leave the domain, while the others enter from outside. If the wave is outcoming, it will be computed using an upwind scheme using interior values; if the wave is incoming, it will be computed using targeted values according to the type of boundary conditions (Fig. 2.9).

Because the CBC of Thompson [1987] and Poinsot and Lele [1992] have been proven to be robust in practice, the CBC has been widely used for almost all types conditions including inlet, outlet, wall or block interface conditions. Some useful extensions have been made. Thompson [Thompson, 1990] extended his original work to conditions for walls (inviscid and no-slip), constant pressure and a force-free boundary condition. Kim [Kim and Lee, 2000] describe techniques for implementing CBC in generalized

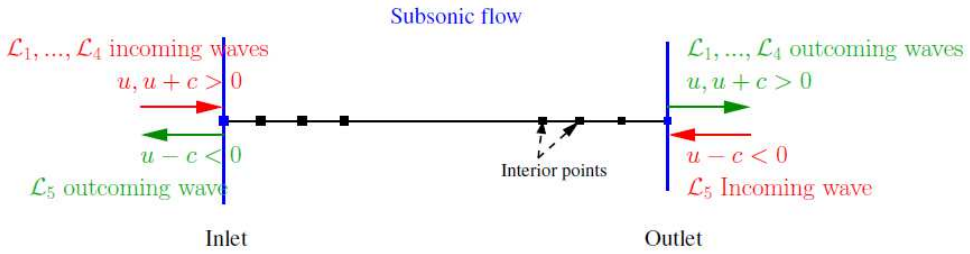

Figure 2.9 Illustration of CBC at inlet and outlet.

coordinates which is often used in the latest codes. Most recently, such a boundary condition has been successfully extended that is suitable for more complex flows such as the flow in a turbomachinery [Odier *et al.*, 2019].

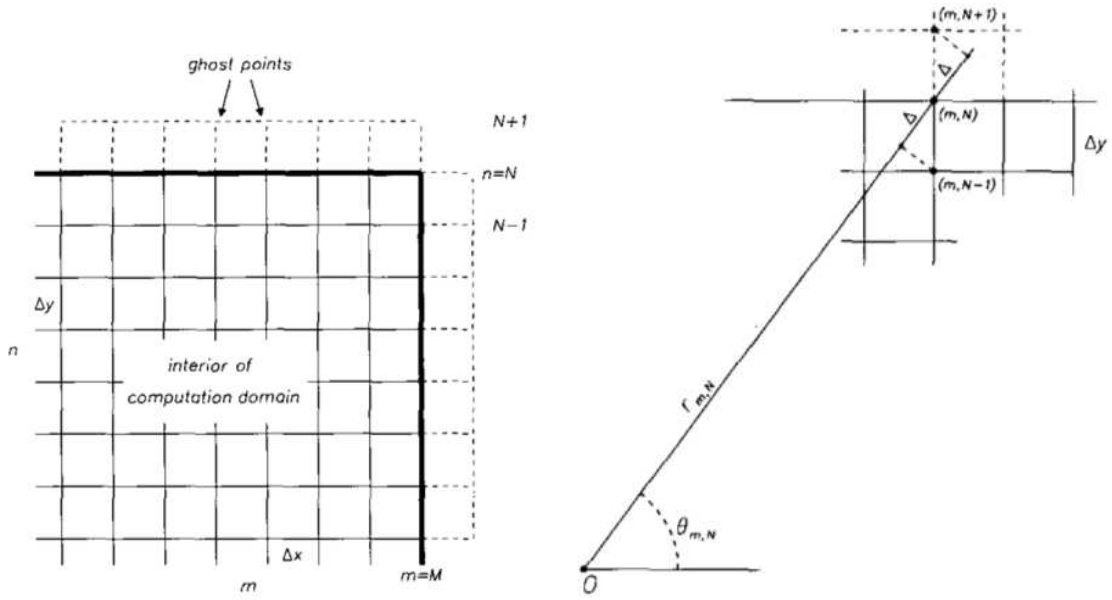

(a) (b)

Figure 2.10 (a) Illustration of the ghost points near boundary; (b) Geometrical relations of the ghost points and interior points at boundary. [Tam and Webb, 1994]

Radiation boundary conditions;

Another alternative developed almost in the same period as the CBC is the radiation boundaries. The technique was originally developed by Bayliss and Turkel [Bayliss and Turkel, 1980] [Bayliss and Turkel, 1982]. Such a method uses asymptotic solutions for the propagation of outwardly propagating disturbances at large distance from their source. Tam [Tam and Webb, 1994] suggested a strategy to implement radiation boundary conditions for finite-difference calculations. He used rows of"ghost" points outside the computational domain. One-sided optimized finite-difference schemes are used to compute derivatives normal to the boundary at the ghost points and the boundary is used to advance the solution at the ghost points (Figs. 2.10(a) and 2.10(b)).

Sponge/buffer zone; In situations where there is a significant nonuniform flow crossing the boundary or where large amplitude disturbances are propagating out of the boundary, a single CBC performs poorly. An example will be the case of airfoil TE noise study in the wake downstream of the boundary layer which possibly involves

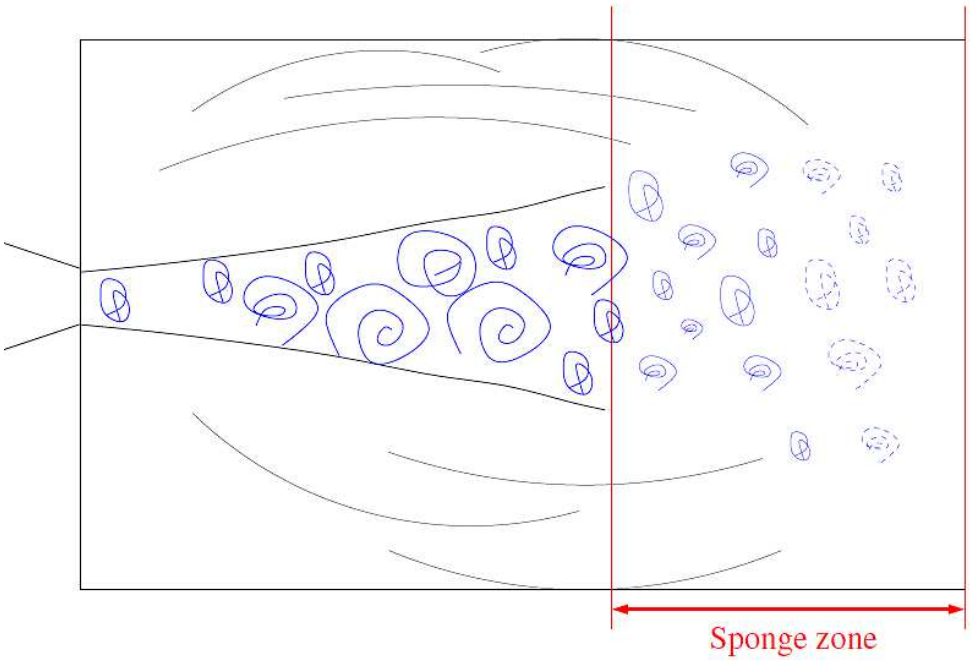

Figure 2.11 Illustration of sponge zone.

vortex shedding and other larger disturbances than acoustic waves. A sponge or buffer zone is needed to attenuate these disturbances before the flow leaves the domain outlet.

Some methods are proposed to realize the damping such as adding a relaxation term [Freund, 1997], applying a higher order filter [Karni, 1996], grid stretching [Rai and Moin, 1991] [Colonius *et al.*, 1993] and fringe/windowing methods [Nordström *et al.*, 1999] [Guo *et al.*, 1994] [Schlatter *et al.*, 2005]. Recent development also combines the CBC with sponge like zonal CBC [Sandberg and Sandham, 2006]. The difference of a zonal CBC with a regular CBC is that the treatment is not only applied to the last point but also to a certain number of points, where a ramping function is defined as in Eq. (2.39) where x_s and x_{out} mean the starting point of the buffer zone and the outlet. Fig. 2.12 shows the difference between a zonal CBC and a classical CBC when a vortex approaches the CBC outlet. A comparison between a (stretching grid+CBC) and a (zonal CBC+CBC) strategy for TE dilatation field is shown in Fig. 2.13. Yet there is no reason at this stage, to assess which sponge method is more adapted for TE noise study. It depends on the flow case and as well their availability in each code.

$$g(x) = 0\ 5\ \ 1 + cos[\frac{(x \quad x_s)}{x_{out} \quad x_s}] \tag{2.39}$$

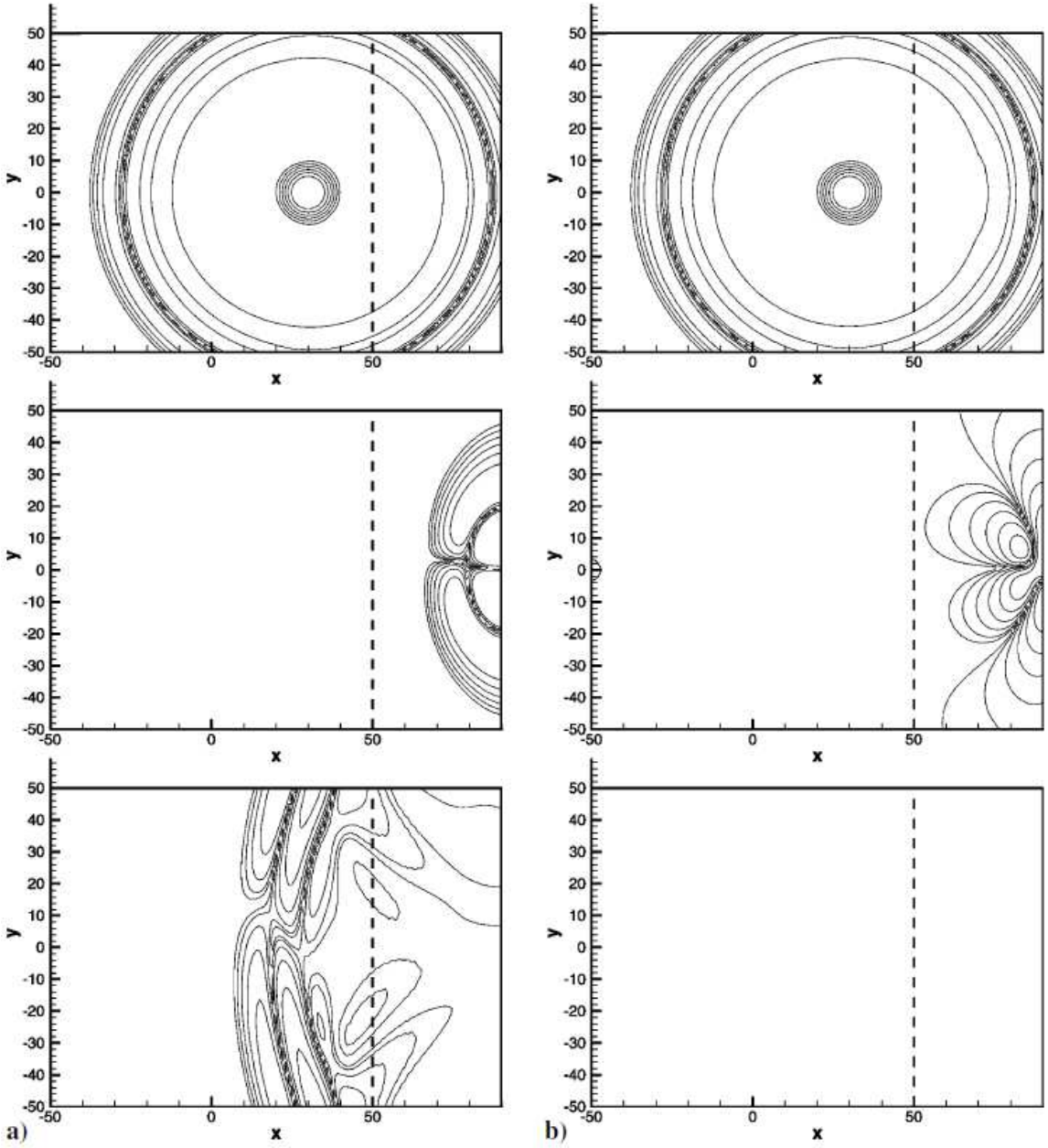

Figure 2.12 Contours of normalized disturbance pressure for single vortex problem: a)typical CBC; b) zonal CBC at t=30,100,and 160 (from top to bottom) [Sandberg and Sandham, 2006].

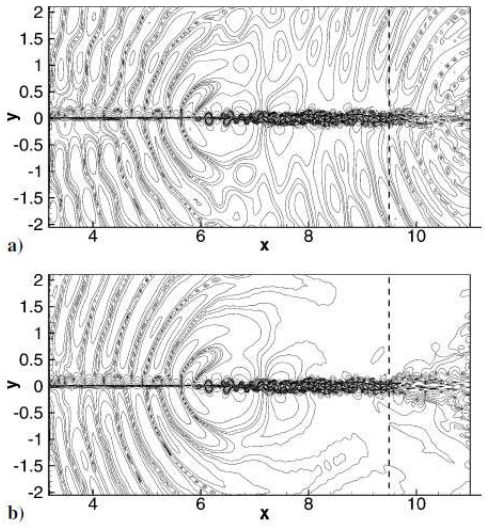

Figure 2.13 Contours of magnitude of dilatation for TE simulations: a) using a typical CBC combined with low-pass filtering and strong grid-streching; b) using zonal CBC [Sandberg and Sandham, 2006].

Besides the boundary conditions, interface conditions are also vital to a high resolution DNS for acoustic purposes (or DNS in general). Multi-block structured grids are often used to allow for higher flexibility in grid generation. Actually, for each airfoil case (sharp, blunt or round TE), a most optimized grid topology exists according to its geometry characteristics. This is true especially for structured grids where the form of the cells are less flexible compared with unstructured or hybrid grids. For parallel computation, each block is calculated independently and communicates between them. Between the blocks, there are interfaces and in classical approaches the numerical schemes are applied across these boundaries and thus grids, in particular the metric terms, have to be smoothed across them. Kim [Kim and Lee, 2003] developed an approach where a characteristic form treatment like what is introduced in section *Boundary Conditions* for domain boundaries is applied at interfaces. Such an interface, referred as CIC, is employed when structured grids have difficulties to ensure the orthogonality at block borders [Kim and Lee, 2003] (Fig. 2.14). Another more trivial method of interface is the so called "halo exchange". For blocks connected smoothly from the orthogonality point of view, each connected subdomain (block) can be extended in each direction by two grid-points. These extra cells are denoted "halo" cells and are filled with data from the first and second grid-points of adjacent processor subdomain before evaluating derivatives, as illustrated in Fig. 2.15. Generally, "halo exchange" can be chosen as an interface condition if the orthogonality can be ensured at block interfaces. For grids of complex geometry which are sensitive to connections and hard to ensure the orthogonality, such as grids of compressor blade or

cambered airfoil, the CIC is the first choice. When using CIC however, it is necessary during the grid topology design to avoid flow parallel to the interfaces.

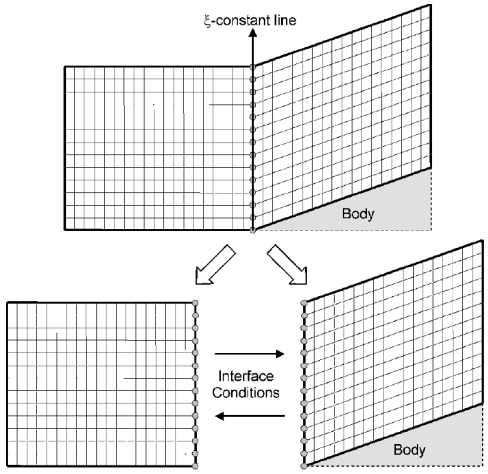

Figure 2.14 Block connection using CIC [Kim and Lee, 2003].

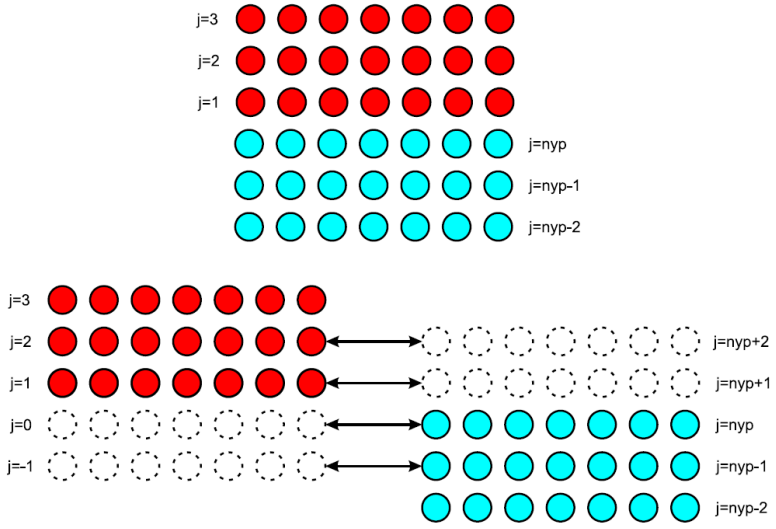

Figure 2.15 Illustration of "halo" exchange [Jones, 2008].

2.5 Seleted DNS Cases: NACA6512-63 and CD Airfoils

With the above context, from both research interests and computational feasibility, 2 airfoils cases are chosen for this PhD project: a NACA6512-63 airfoil with an airfoil chord based Reynolds number of $Re_c = 1\ 5 \quad 10^5$ and a Mach number of $M = 0\ 25$ at $0 \quad$ AoA

and the CD airfoil with $Re_c = 1\ 5 \quad 10^5$ and $Ma = 0\ 25$ at 8 AoA. Because firstly, both of the chosen airfoils possess a solid experimental data base and already some simulations at the Reynolds number of interest. This project can thus draw a conclusion on the former studies. Secondly, because of their representative geometric shapes, these simulations can give useful information for airfoil TE noise studies in general.

2.5.1 NACA6512-63 Airfoil

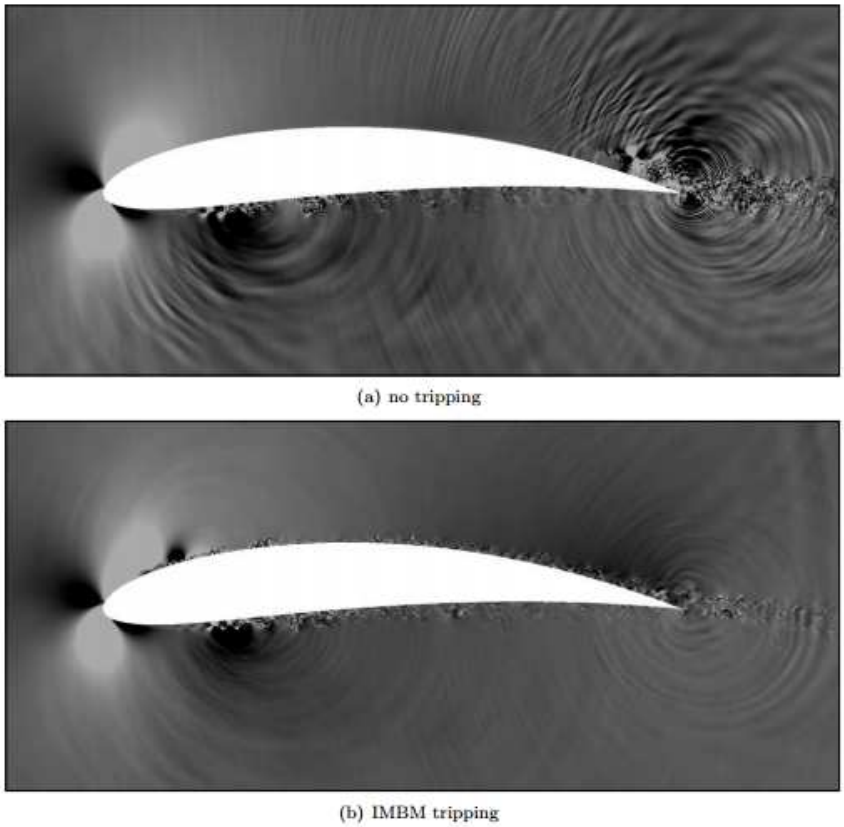

(a) no tripping

(b) IMBM tripping

Figure 2.16 Comparison of dilatation field on the NACA6512-63 airfoil: (a) untripped case; (b) tripped case. [Winkler *et al.*, 2012]

For the NACA6512-63 airfoil, the tripped case has been thoroughly studied from incompressible LES [Winkler and Moreau, 2008] [Winkler *et al.*, 2009] [Winkler *et al.*, 2010] and recently compressible DNS [Winkler *et al.*, 2012] (Fig. 2.16). The LES cases have employed several geometrical shapes of the tripping device and the Reynolds number and Mach number were chosen to be the same as in experiments. The DNS including installation effects at $Re_c = 1\ 5 \quad 10^5$ has been carried out using suction side tripping [Winkler *et al.*, 2012]. The tripping using IMBM (Immersed-Boundary Method) method was not activated until the flow field was fully developed. The effect of the tripping is to produce a fully attached turbulent boundary layer.

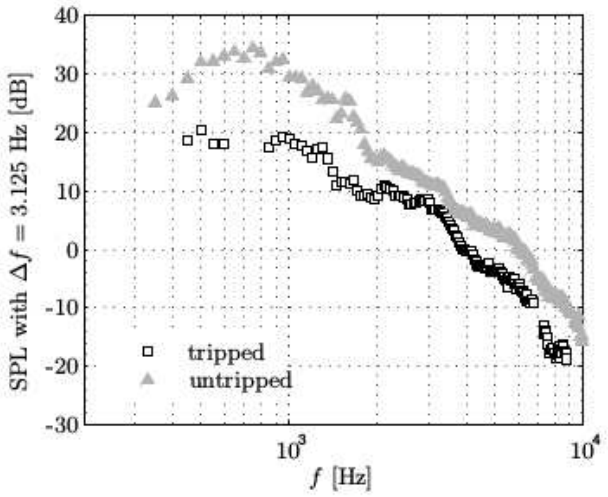

Figure 2.17 Acoustic far-field measurements [Winkler and Carolus, 2009] of the airfoil with and without boundary-layer tripping at 1.2 m downstream from the trailing edge in the midspan plane at 90 with respect to the airfoil chord.

On the experimental side, measurements for both the tripped and untripped airfoils were conducted [Winkler and Carolus, 2009]. Results from acoustic far-field measurements for this flow condition and airfoil profile are shown in Fig. 4.27 [Winkler and Carolus, 2009]. For the untripped case, no tonal noise components are seen in the data. This suggests that any feedback loop that may be present and amplified by the existence of the separation bubble is actually weak. The flapping shear layer itself is expected to be responsible for the large broadband noise increase noticed in the experimental data. In fact, slowly increasing the trip thickness in the experiments leads to a reduction in the broadband noise hump, until it reached the minimum noise level given by the fully tripped airfoil. In that case the boundary layer on the suction side was fully turbulent and attached [Winkler and Carolus, 2009]. The scattering of the pressure disturbances produced by the turbulent bubble at the trailing edge is therefore responsible for the large broadband noise increase.

As a continuation work, a DNS without the tripping is achieved in this PhD project. In this untripped case, the boundary layer separates on the suction side and then starts flapping close to the TE. As shown in Fig. 2.16, extra noise is produced in the untripped case in contrast to the attached turbulent boundary layer in the tripped case. Such an extra noise source seems to be a stronger noise source than the turbulence sweeping over the edge close to the wall. Besides, a turbulent boundary layer is developing on the pressure side from the reattachment of the laminar separation bubble at the leading edge up to the trailing edge. This laminar separation bubble also produces additional acoustic waves. The suction-pressure side coupling is possible as well. It would be interesting to evaluate these

effects on TE noise generation. On the numerical side, in [Winkler *et al.*, 2012], only the tripped airfoil simulation was reported because for the non-tripped case, the airfoil loading was drifting after a certain time. This current study is meant to solve this problem and to find a more optimized boundary condition option for such a narrow calculation domain for acoustic study. Compared with other airfoil noise cases, this calculation domain is especially small due to the narrow wind tunnel jet width at University of Siegen (in order to exclude the shear layer effects of the jet). Several 2D tests have been conducted during the first year of PhD for this case to find the effect and proper boundary conditions. The details are reported in the following in *Chapter 4*.

2.5.2 CD Airfoil

A Brief History on CD Airfoil Cases

The CD airfoil as mentioned in several publications before ([Christophe, 2011] [Wang *et al.*, 2006] [Moreau and Roger, 2005] [Roger and Moreau, 2004] [Sanjosé *et al.*, 2011], etc) was designed by Valeo which was used in their preliminary design process. The so-called "CD" (Controlled Diffusion) refers to a class of cambered airfoils that employ specific characteristics to carefully control the flow and the losses around the airfoil surface by controlling and mitigating the boundary layer growth. The profile has a 4% thickness to chord ratio and a camber angle of 12.554 . Such a profile that reduces drag has been used for turboengine compressor blades, automotive engine cooling fan systems, aerospace Heat and Ventilation Air-Conditioning (HVAC) systems and turbofans. This airfoil has been systematically studied during the last decade and there is a solid experimental and numerical data base established by researchers all over the world both on aerodynamics and on aeroacoustics.

The experiments of the flow over the CD airfoil in open-jet wind tunnels have been performed respectively at ECL (École Centrale de Lyon, anechoic wind tunnels), at MSU (Michigan State University, non-anechoic chamber) and more recently at TU-Delft (Delft University of Technology, non-anechoic chamber) and at UdeS (Université de Sherbrooke, anechoic chamber, Fig. 2.20). The improved anechoic level in the chamber at UdeS compared with that at ECL is shown in Fig. 2.19. The flow conditions are set by varying the AoA (through rotating the airfoil in sliding disks embedded in the side plates holding the mock-up at the nozzle exit) and the flow velocity U_0 through the nozzle of the wind tunnel (changing the power of the tunnel blower). As the airfoil has a camber angle of 12 554 , it should be noticed that here the AoA refers to the geometrical AoA that is between the airfoil chord line and the free stream velocity (U_0) direction. In [Moreau *et al.*,

2003] [Moreau and Roger, 2005], this was expressed as $_w$. Such an angle is shown in Fig. 2.18 for the 8 case. In [Roger and Moreau, 2004], an $_g$ was introduced which is the AoA with respect to the camber line at the leading edge. The relationship between these two is

$$:= \quad _w = \quad _g + 12\ 554 \tag{2.40}$$

From now on, only will be used.

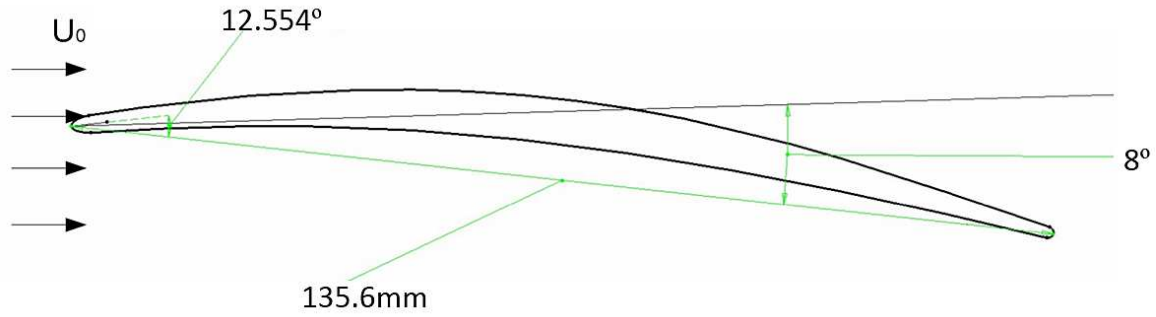

Figure 2.18 Illustration of the CD geometry AoA for = 8 case.

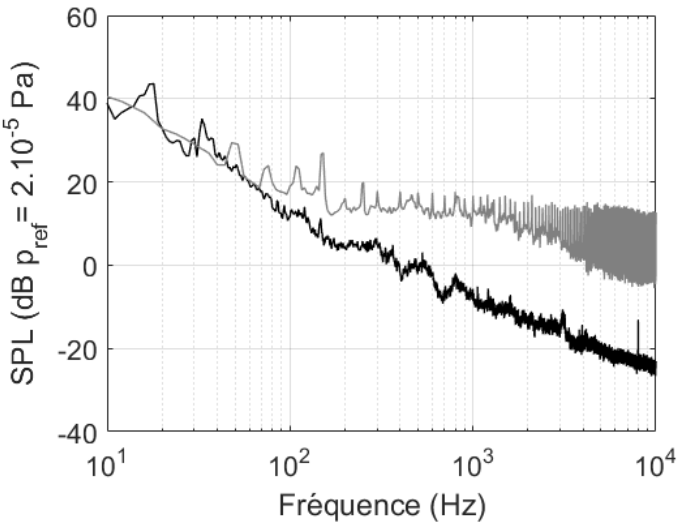

Figure 2.19 Background noise comparison of anechoic wind tunnels at ECL (gray) and at UdeS (black) with 50cm jet width at $U_0 = 16$ m/s.

The experimental cases are listed in Tab. 2.4 according to , U_0, the airfoil chord based Reynolds number Re_c (Eq. (2.26)), the Mach number Ma (Eq. (2.27)) and wind tunnel jet width (which determines the installation effects [Moreau *et al.*, 2003]). This table is made as an inclusive summary according to all published results. The terms in *Available Data* column in Tab. 2.4 are explained in Tab. 2.1. Similarly, the simulation cases are

listed in Tab. 2.5. The RANS simulations are 2D which represents the mid-span of the experimental setups. For 3D DES, LES and DNS, their respective spanwise extent are listed in the last column.

Facility Location	Jet Width (cm)		U_0 (m/s)	Re_c	Ma	Available Data
ECL (Anechoic)	50	8	16 30	1 5 2 9 10^5	0.05/0.09	HWM,RMP,FFM
		12	16	1 5 10^5	0.05	RMP
		14	16	1 5 10^5	0.05	RMP
		15	16 30	1 5 2 9 10^5	0.05/0.09	HWM,RMP,FFM
		16	16	1 5 10^5	0.05	RMP
		18	16	1 5 10^5	0.05	RMP
		27	16	1 5 10^5	0.05	RMP
	13	8	16	1 5 10^5	0.05	RMP,FFM
		15	16 30	1 5 2 9 10^5	0.05/0.09	RMP,FFM
		18	16	1 5 10^5	0.05	RMP
		27	16	1 5 10^5	0.05	RMP
UdeS (Improved Anechoic)	50	5	16	1 5 10^5	0.05	HWM,PIV,RMP, SPS,MPA,FFM
		8	16	1 5 10^5	0.05	HWM,PIV,RMP, SPS,MPA,FFM
	30	0	8 16 20 28	7 10^4 2 5 10^5	0 02 0 09	HWM,RMP,SPS, MPA,FFM
		1	16 20	1 5 10^5	0.05/0.06	HWM,SPS, RMP,MPA
		2	16 20	1 5 10^5	0.05/0.06	HWM,SPS,RMP
		8	16	1 5 10^5	0.05	HWM,PIV,RMP, SPS,MPA,FFM
		10	8 16 20 28	7 10^4 2 5 10^5	0 02 0 09	HWM,RMP,SPS, MPA,FFM
		16	8 16 20 28	7 10^4 2 5 10^5	0 02 0 09	HWM,RMP,SPS, MPA,FFM
MSU (Non-anechoic)	50	8	16	1 5 10^5	0.05	HWM,PIV, RMP,SPS
TU-Delft (Non-anechoic)	50	8	16	1 5 10^5	0.05	PIV,SPS

Short terms are from Tab. 2.1. Acoustic data RMP and FFM are available for the 30 cm jet width at UdeS at = 0 15 (every 2) and at $U_0 = 10$ 40 m/s (every 2 m/s) [Laffay, 2014][Idier, 2014]. Wall-pressure fluctuation data measured by RMP is available for the cases of 13 cm jet width ($U_0 = 16$ 30 m/s, which gives $Re_c = 1\,4$ $3\,5$ 10^5). Not published. PIV data in the table refers to data obtained from planar/stereo space-resolved system.

[Moreau *et al.*, 2003][Moreau and Roger, 2005][Moreau *et al.*, 2006b]; [Roger and Moreau, 2004]; [Sanjosé *et al.*, 2017][Wu *et al.*, 2018] [Laffay, 2014][Idier, 2014][Padois *et al.*, 2015][Wu *et al.*, 2016][Moreau *et al.*, 2016]; [Neal, 2010][Cawood, 2012][Hower, 2012]; [Wu *et al.*, 2018]

Table 2.4 Summary on flow conditions of experiments over CD airfoil.

Jet Width (cm)	Simulation Type		U_0 (m/s)	Re_c	Ma	l_{span} c
50	RANS/URANS	8	16	1 5 10^5	0.05	0
		6 10	16	1 5 10^5	0.05	0
		12	16	1 5 10^5	0.05	0
		14	16	1 5 10^5	0.05	0
		15	16	1 5 10^5	0.05	0
		16	16	1 5 10^5	0.05	0
		18	16	1 5 10^5	0.05	0
		27	16	1 5 10^5	0.05	0
	DES	8	16	1 5 10^5	0.05	0.05/0.1
	LES	8	16	1 5 10^5	0.05	0.1/0.3
		6 10	16	1 5 10^5	0.05	0.1
		15	16	1 5 10^5	0.05	0.1
	LBM-DNS	5	16	1 5 10^5	0.2	0.12
		8	16	1 5 10^5	0.2	0.05/0.12
30	RANS/URANS	0	20	1 5 10^5	0.06	0
		1	20	1 5 10^5	0.06	0
		4	20	1 5 10^5	0.06	0
		8	16	1 5 10^5	0.05	0
		10	16	1 5 10^5	0.05	0
		15	16	1 5 10^5	0.05	0
13	RANS/URANS	8	16	1 5 10^5	0.05	0
		15	16	1 5 10^5	0.05	0

a. 9 calculation cases respectively in RANS (2D) and LES (3D) have been conducted by varying around 8 ([2 2]) for the purpose of uncertainty quantification [Christophe *et al.*, 2010][Christophe *et al.*, 2014].

b. The published LES simulations are based on incompressible solvers. Ongoing unpublished work includes compressible LES. [Wang *et al.*, 2004][Moreau *et al.*, 2004][Moreau *et al.*, 2006a][Christophe and Moreau, 2008] [Christophe *et al.*, 2010] [Wang *et al.*, 2009][Christophe *et al.*, 2009][Sanjosé *et al.*, 2011][Christophe *et al.*, 2014] [Sanjosé *et al.*, 2017]

Results from ($U_0 = 20$ m/s, $= 1$ and U_0=16m/s, $= 8$) cases are published in [Padois *et al.*, 2015][Wu *et al.*, 2016] [Moreau *et al.*, 2003][Moreau and Roger, 2005]

Table 2.5 Summary on flow conditions of simulations over CD airfoil.

50 cm Jet Width Cases

For the larger (50 cm) jet width cases [Moreau *et al.*, 2003] [Moreau and Roger, 2005], various angles of attack were tested to assess the airfoil loading. At $= 12$, the flow is still attached at the TE and a laminar separation bubble appears earlier than the design flow condition ($= 12$) at the leading-edge. At $= 14$, the flow starts to separate near the TE. This regime corresponds to turbulent vortex shedding with no mean backflow. Increasing the AoA to 16 leads to a large laminar recirculation zone near the leading edge. At much larger incidence ($= 27$), the airfoil seems to be in stall condition with a flow detachment from the leading-edge bubble at the leading edge. For aeroacoustic aspects, for $8 < < 14$, the boundary layer stays turbulent and attached at the airfoil TE thus only broadband noise is considered.

The 8 and 15 cases have been studied more in detail by varying the Re_c from 1 5 10^5 to 2 9 10^5 in [Moreau and Roger, 2005] to give an insight into the Reynolds-number effect on such an airfoil and into the two previously investigated flow regimes, which correspond to the turbulent boundary layer initiated by a leading-edge laminar separation bubble with vortex shedding at the TE (8) and the turbulent boundary layer with severe separation (15). It is reported that larger jet width induces more coherent large structures in the vortex-shedding regime.

For the 8 case, the transition to turbulence is triggered by a laminar recirculation bubble at the leading edge and the spectra of wall-pressure fluctuations at TE is similar to a flat plate under adverse pressure gradient. On the simulation side, Wang *et al.* [2004] achieved the first incompressible LES by deducing the far field noise with a modified (finite-chord taken into account) Ffowcs Williams & Hall [Williams and Hall, 1970] analogy. The prediction has a reasonable agreement with the far field acoustic microphone. Subsequent attempts to reduce the computational costs included the use of non-boundary-conforming methods such as the Lattice Boltzmann method (LBM) and immersed boundary method [Moreau *et al.*, 2004], as well as hybrid solution methods such detached eddy simulations (DES) [Moreau *et al.*, 2005]. Yet these techniques yielded less accurate mean wall-pressure distributions (larger laminar recirculation bubble near the leading edge and possibly turbulent flow separation near the trailing edge) and frequency spectra near the trailing edge than those obtained by [Wang *et al.*, 2004]. Later, hot-wire measurements [Moreau *et al.*, 2006b] were realized and it was shown that simulation (LES, RANS) seemed to overpredict the velocity deficit in the wake. Later Neal [Neal, 2010] realized the hot-wire measurements in the MSU facility for the same case and emphasized that the single hot-wire tended to underestimate the actual wake-velocity deficit. In 2011, Sanjosé conducted

the first DNS [Sanjosé *et al.*, 2011] using LBM method in which both TE noise and fully resolved turbulent flow were obtained at a Reynolds number of $Re_c = 1\,5 \quad 10^5$ including the wind tunnel geometry environment. It was mentioned that the 3D setup was able to properly capture the vortex stretching in the spanwise direction. Another aspect worth mentioning is that such an airfoil is very sensitive to the angle of attacks. Christophe *et al.* (2010; 2014) conducted uncertainty analysis on the LES of the 8 case by slightly varying the inlet flow angle around 8 and found that at larger angles of attack, the recirculation bubble at leading edge increases but the flow remains attached at the trailing edge; for the lowest angles of attack, the laminar recirculation bubble has disappeared at the leading edge but a new one has formed after mid-chord. This is a significant departure from the corresponding RANS solutions, which shows no variations.

In 2008, Christophe [Christophe and Moreau, 2008] achieved an incompressible LES simulation for the $= 15$ case. It was reported that the spanwise extent $l_{span} \quad c = 0\,1$ seemed to be too small to well represent the detached boundary layer. Moreover, there were not enough points in the spanwise direction either for that LES. The wall-pressure fluctuations were well captured for frequencies higher than 1kHz and for frequencies below 1kHz, the LES resulted in an overestimation.

Most recently, the 5 case has been thoroughly studied by DNS using the LBM method [Sanjosé *et al.*, 2017]. The simulation compares favorably with experimental measurements of wall-pressure, wake statistics, and far-field sound. The temporal evolution of wall-pressure fluctuations shows significant unsteadiness especially in the aft region of the suction side. Time periods of quiet and intense events have been detected and compared. A linear stability analysis performed on the mean flow of the simulation has demonstrated that the recirculation bubble close to the trailing-edge is the inception of the tonal mechanism.

30 cm Jet Width Cases

For cases from medium nozzle jet width (30 cm) [Padois *et al.*, 2015] (Fig. 2.20), three distinct flow regimes were also observed. At high AoA and high velocity the usual broadband noise signature found in the 50 cm jet width case is recovered. At low AoA, the power spectral density of the microphone signal is dominated by a primary tone with secondary tones, typical of boundary layer instability noise (previously termed T-S noise) radiation due to unstable laminar boundary layer. It was reported in [Laffay, 2014] that stable tonal noise is observed for the case of $= 0 \quad 1 \quad 2 \quad 8$ at $U_0 = 16$ m/s and instable tonal noise is in the cases of $= 0 \quad 1 \quad 2$ at $U_0 = 20$ m/s. Recently, Wu *et al.* [2016] has found that the

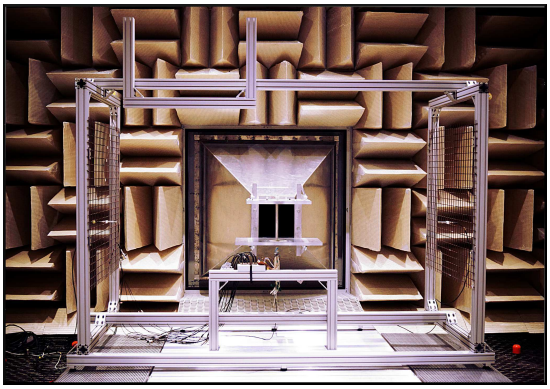

Figure 2.20 Illustration of the experimental setup at UdeS.

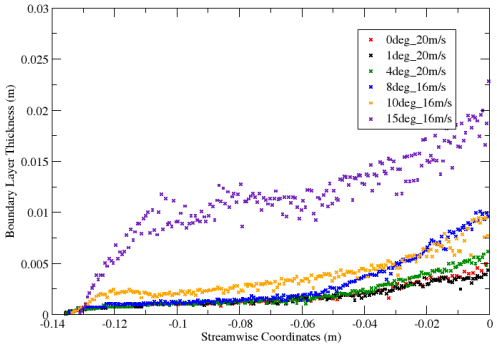

Figure 2.21 Boundary layer thickness from URANS for 30 cm jet width at UdeS.

transition process is modified because of the installation effects for the 8 reference case. The laminar separation bubble at the leading edge of the 50cm case has been replaced by a thinner recirculation bubble near the TE for the 30cm jet with case. A parallel URANS study at the beginning of the PhD has been conducted and showed that the boundary layer thickness changes dramatically with different AoA as shown in Fig. 2.21. Moreau *et al.* [2016] showed multiple noise reduction techniques on this airfoil: serrations, porous media and blowing. All control devices yield significant noise reduction of the tonal noise and the broadband noise over a large frequency range for certain flow conditions.

13 cm Jet Width Cases

For cases of the most confined nozzle jet (13 cm), experimental and analytical studies (based on Amiet's and Howe's theory) were reported in [Roger and Moreau, 2004]. Three distinct regimes are:

For small angles of attack (typically = 0 3), a quasi-laminar boundary layer along the entire airfoil is observed with the existence of T-S wave;
For medium angles of attack (= 8 18), an attached turbulent boundary layer exists at TE which generates broadband noise;
For high AoA, (= 27), the boundary layer is detached at TE.

In summary, except for the stall case at high AoA, for 8 < < 16 , the noise radiation is broadband from an attached turbulent boundary layer at the TE. For < 8 , the instabilities in the boundary layer exist and some tonal noise is possibly created. It should be noticed that, these same 3 regimes exist for all the jet widths but over different AoA.

Chosen Case for the DNS on the CD Airfoil

The flow condition of (= 8 U_0 = 16 m/s) has been intensively studied both experimentally (Tab. 2.4) and numerically ([Moreau *et al.*, 2003][Moreau *et al.*, 2004][Moreau *et al.*, 2006a][Addad *et al.*, 2008][Christophe and Moreau, 2008][Wang *et al.*, 2009][Sanjosé *et al.*, 2011][Sanjosé *et al.*, 2014b]). The flow is attached over most of the chord length and has a laminar separation bubble which triggers the transition at the LE. This flow regime corresponds to an attached turbulent boundary layer with adverse pressure gradient that radiates broadband noise. Such a boundary layer status on the suction side at the TE satisfies most of the application condition of the TE noise models and consequently the results from it can be representative to validate the limitations of these models. Besides, as the CD airfoil has a thick and round TE, it would be interesting to compare the results with other DNS simulations in which usually a sharp TE geometry is present. For the case with a 50 cm jet width, data from both experiments and simulations is the most abundant. The comparison with them will be interesting from both physical and technical points of view. Regarding the computational cost, as the transition process appears at the LE, less spanwise extent is required compared to the case where laminar separation bubble appears at the TE (the 30 cm jet width case). It is thus the first case for the DNS simulation for this PhD project and will give a conclusive understanding from the numerical side.

As a summary, the DNS simulations for both of the airfoils are operated at $Re_c = 1\ 5 \quad 10^5$, which is the state-of-the-art Reynolds number for DNS TE noise studies, and they include both the installation effects. The different airfoil geometries and flow regimes on these airfoils will give a more comprehensive information for such a transitional flow on TE noise generation.

CHAPTER 3

Numerical Codes

The DNS and post-processing codes involved in this PhD project are briefly presented here. RANS and LES simulations are also involved in this project yet they are mainly for the purpose of flow initialization and comparison. The RANS and LES solver information are summarized in Tabs. 3.1 and 3.2. The detailed numerical setups for these simulations will be introduced in the following chapters together with the DNS ones.

3.1 DNS

As stated in the previous chapter, special numerical considerations need to be taken into account when dealing with noise problems generated by turbulent flow. According to those considerations, in this PhD project, HiPSTAR (**Hi**gh **P**erformance **S**olver for **T**urbulence and **A**eroacoustic **R**esearch) is chosen to be the DNS solver for the 2 chosen airfoil flow cases. It is multi-block structured Navier-Stokes DNS solver originally from University of Southampton by R.D. Sandberg, designed for parallel computing, with a state-of-the-art scaling in performance [Sandberg, 2009; Sandberg *et al.*, 2015].

The flow under consideration is governed by the full compressible Navier–Stokes equations (as shown in eqs. (2.11), (2.12) and (2.13) in *Chapter 2*). The fluid is assumed to be an ideal gas with constant specific heat coefficients. All quantities are made dimensionless. The Prandtl number is assumed to be constant with $Pr = 0\ 72$ and $= 1\ 4$. The molecular viscosity is computed using Sutherland's law [White and Corfield, 2006], setting the ratio of the Sutherland constant over freestream temperature to 0 36867. To close the system of equations, the pressure is obtained from the non-dimensional equation of state, i.e., $p = (\ T)\ (\ Ma^2)$.

RANS Solver	Flow Case	Compressibility
ANSYS CFX V11	NACA6512-63 airfoil	No
ANSYS FLUENT V15	CD airfoil	No

tripping not included in RANS. Served for both tripped and untripped LES/DNS flow initialization
Served for DNS flow initialization (50cm jet width) and turbulence model test (30cm jet width)

Table 3.1 RANS solvers involved in this PhD project.

LES Solver	Flow Case	Compressibility
ANSYS CFX V11	NACA6512-63 untripped airfoil	No
AVBP V7.0	CD airfoil	Yes

Served for NACA6512-63 untripped and "unsufficiently" tripped airfoil cases
ANSYS FLUENT V6.3 also used for LES simulations for tripped airfoil with different shapes of trips
LES simulations including the wind-tunnel open-jet geometry

Table 3.2 LES solvers involved in this PhD project.

It has 4^{th} order accuracy both in space and in time. For large-scale DNS of turbulent flow problems, the amount of memory used for the simulation exceeds the available cache of the CPUs and the slower RAM has to be accessed, which is a bottleneck from a performance point of view. To keep this performance degrading way of accessing large amounts of data from RAM at a minimum and increase the performance, one should try to reduce the memory needed by the algorithm. To achieve this an ultra low storage Runge-Kutta scheme is chosen for the discretization in time. This five-step fourth-order Runge-Kutta explicit scheme was developed by [Kennedy *et al.*, 1999] and achieved fourth-order accuracy with only two registers of memory. In space a five-point 4^{th}-order central standard-difference scheme with Carpenter boundary stencils [Carpenter *et al.*, 1999] is applied for the spatial discretization in the streamwise and crosswise directions. Compact schemes can also be chosen as an option for this code yet it is not used for the current study. In the spanwise direction, a spectral method, which has a even higher accuracy, using the FFTW3 library is used. These spatial and temporal schemes guarantee a low level of dispersion and dissipation error, which is an essential aspect for noise studies. In order to increase stability of the numerical scheme a stabilizing method is applied [Kennedy and Gruber, 2008]. This method employs skew-symmetric splitting of the non-linear terms. A sixth-order accurate high-wavenumber cut-off filter [Bogey *et al.*, 2009] with a weighting to be named can also be employed after every full Runge–Kutta cycle.

Unphysical numerical reflections at the computational boundaries are avoided by the choice of appropriate boundary conditions. Characteristic based boundary conditions [Jones *et al.*, 2008; Kim and Lee, 2003; Sandberg and Sandham, 2006] are used for this simulation on domain boundaries and sub-domain interfaces. Other boundary conditions including turbulent inlet and fixed inlet with sponge zones are also optional yet not used for the current study. At the airfoil surface, an adiabatic, no-slip condition is applied.

3.2 Post-processing

The DNS code HiPSTAR described above outputs instantaneous primitive flow variables including density, the velocity vector and temperature and statistics as standard (the output for statistics can also be chosen to be turned off). Pressure can also be chosen to be the output if needed (for instance wall surfaces). The statistics recorded on-the-fly for the two DNS cases on NACA6512-63 airfoil and CD airfoil was chosen to be Favre-averaged. HiPSTAR is able to record more complicated statistics by activating a series of specific pre-compiler flags yet it is a more expensive choice both in terms of computational time and of storage for the current study. Because unlike some basic flows such as turbulent channel flows or turbulent boundary layer flows, the DNS domain as will be presented in the following chapters for both airfoil noise studies comprise not only the boundary layer but also the areas close to the boundary layer to let the boundary conditions work efficiently. These areas however, are not of interest for statistics. Consequently, besides the instantaneous primitive flow fields and Favre-averaged statistics, some volumes of the primitive flow fields were recorded during the DNS run and further processing is needed. To handle the large time series in order to calculate gradients, spectra and probability density functions, a parallel post-processing tool possessing the same operators as in HiPSTAR, called Flow Analysis Tool (FAT) was developed. FAT is basically a tool that can read the volumes comprising primitive flow fields recorded as Plot3D Subspaces format. It calculates and outputs the flow fields and/or extended statistics to be named by .dat files. The extended statistics are calculated when the $NON\_LOCAL\_STATISTICS$ pre-compiler is activated. The p.d.f sampling for velocity gradient tensor invariant dynamics can also be activated under the $LOCAL\_STATISTICS$ paradigm (and $LOCAL\_COND\_MOM$ when conditional averages are required). More details of the code can be found through [Bechlars, 2015].

Another post-processing tool that was used intensively for this work is a python based code ANTARES, developed at CERFACS. This tool was developed initially for the purpose of comparing results from different numerical codes when they have different output formats. The basic principle of the code is to put whatever a field in time, into an object called *base* and to realize the operations (or *treatment* as called in the code) needed and finally to output a certain format as named. Details can be found in *http* : $www\ cerfacs\ fr\ antares$. For the present work, version 1 8 2 has been used.

CHAPTER 4

DNS of NACA6512-63 Untripped Airfoil at 0 AoA

As mentioned in *Chapter 2*, the DNS of NACA6512-63 untripped airfoil is a continuous work of the experimental, LES and DNS studies before. Extra noise is produced due to the flow separating and flapping near the airfoil TE on the suction side in the untripped case in contrast to the attached turbulent boundary layer in the tripping case.

However, on the numerical side, this untripped DNS case has to tackle more difficulties. Firstly, due to the fact that the airfoil is immersed in a narrow stream from the wind tunnel facility at University of Siegen, in order to exclude the shear layer effects from the wind tunnel exit, the DNS domain has to be close to the airfoil. Yet this means minor changes in the boundary conditions can have effects on the main flow. This is already difficult for the tripped case yet for the untripped case it is even more challenging as bigger structures and consequently the associated noise can be more difficult for the boundary conditions to deal with compared with the tripped case. Actually, using the same DNS setup as in the tripped case led to the loading on the airfoil to drift. In order to solve this problem, a series of 2D simulations for the untripped airfoil has been conducted in the first place to get the best boundary conditions for the 3D simulation. Although normally the 2D flow field is different from 3D flow field, testing directly on 3D simulations is much more expensive. This procedure will be firstly presented in the following section. Then the results from the 3D simulation are detailed.

4.1 Numerical Setup

As mentioned before, in order to account for the installation effects, firstly a 2D RANS computation of the flow around the airfoil was conducted, taking into account the nozzle shape and geometrical configuration that were used in the experiments (Fig. 4.1(a)). The nozzle outlet velocity profile was known from hot-wire measurements and this velocity data was used to define the steady inflow conditions to the domain. In a second step, a truncated airfoil grid was extracted from the whole simulation domain (Fig. 4.1(b)). The velocity distribution around the extended C-contour was taken from the full wind-tunnel simulation solution. This data was then used to define a steady 2D inlet velocity profile.

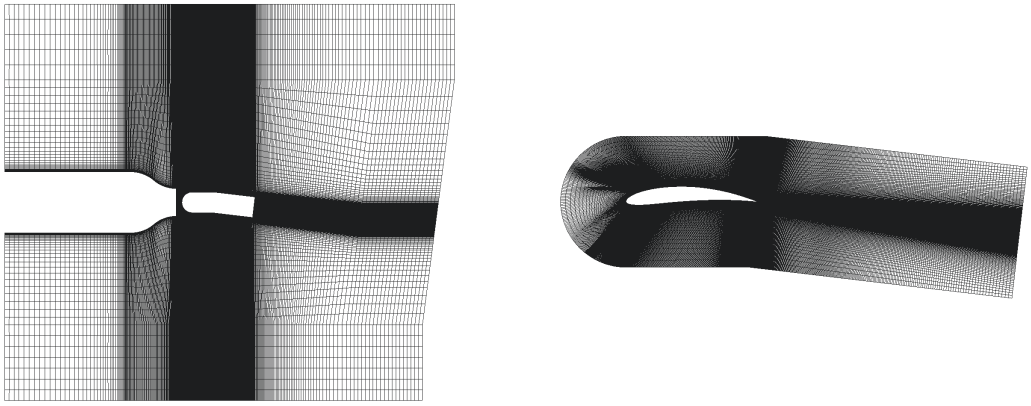

(a) (b)

Figure 4.1 (a) Grid topology of the wind-tunnel setup for initial RANS computations. (b) Truncated domain, extracted from the full wind-tunnel setup.

This profile mimics the influence of the wind tunnel (with a rectangular nozzle) on the flow field around the airfoil. In particular, it accounts for the mean effects of flow deflection. The truncated simulation domain used for the DNS study is outlined in Fig. 4.2. It comprises two regions and three blocks: the region around the airfoil (Block 2), plus the wake region. The latter is split into a pressure side (Block 1) and a suction side (Block 3) block domain. The wake blocks are aligned such that they are approximately parallel to the wake deflection slope, which is known from hot-wire measurements.

4.1.1 Evaluation of Boundary Conditions from 2D Simulations

HiPSTAR offers several inlet & outlet conditions that can be used for the airfoil TE noise cases:

Inlet

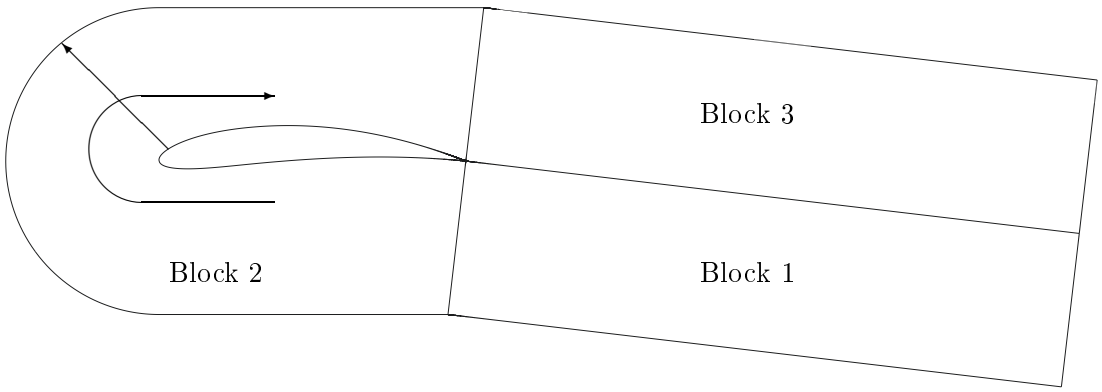

Figure 4.2 Computational domain for the NACA6512-63 untripped airfoil DNS study.

Block No.			Block 1			Block 2			Block 3		
L	L	L	2 0	0 5	0 1	1 5	0 5	0 1	2 0	0 5	0 1
n	n	n	1 200	240	194	3 200	240	194	1 200	240	194

Table 4.1 Computational domain size with respect to the airfoil chord length (L L L), and number of grid points (n n n) per block.

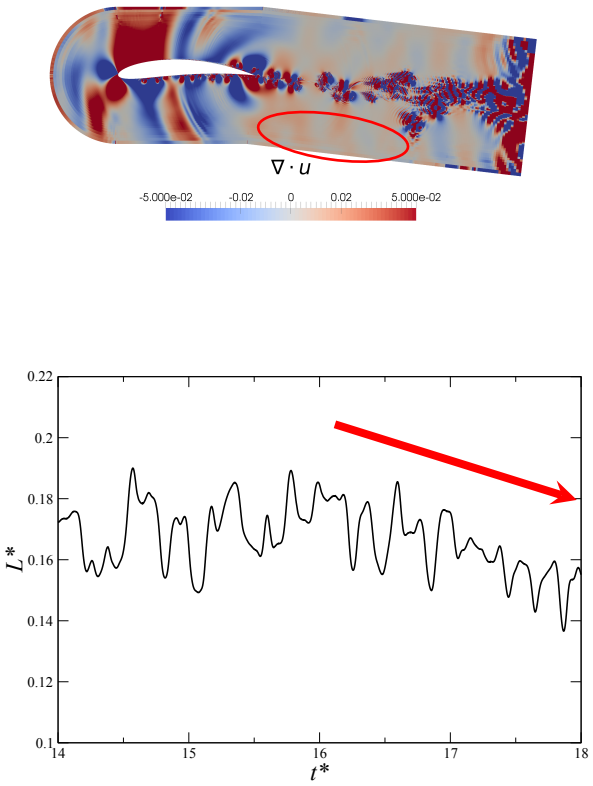

(b)

Figure 4.3 ICBC at inlet with 30 ZCBC points at outlet: (a) Instantaneous dilatation field at t = 16 and (b) airfoil loading at t = 14 18

For inlet, *Fixed Inlet with Sponge* and *ICBC (Integrated CBC)* can be employed. The *Fixed Inlet with Sponge* is used to damp out the fluctuations approaching the inlet in order to prevent reflections while holding the inlet profile such as velocity and density. The fluctuations of a variable are damped using Eq. 4.1 where c_{sponge} and f_{sponge} are respectively the sponge strength and the sponge function as shown in Eq. 4.2. x_s and x_e represent the starting and end points along the normal line to the boundary and the reference value q_0 is the specified boundary inlet profile. When using such an inlet boundary, the sponge width and strength should be carefully tuned in order

not to lose significant physical phenomena (as in most part of the sponge zone, the "physical" values obtained are not physical due to numerical damping according to Eq. 4.1). If the strength of the sponge layer is too strong, reflection will be observed already at the starting point of the zone.

$$q_{sponge}(x\ t) = q(x\ t) \quad c_{sponge} f_{sponge}(q(x\ t) \quad q_0(x\ t)) \tag{4.1}$$

$$f_{sponge} = 0\ 5\ \ 1 + \cos\ \ 2\ \frac{x \quad x_s}{x \quad x_e} \tag{4.2}$$

The latter, *ICBC* [Sandhu and Sandham, 1994] is used to avoid unphysical numerical reflections at the domain boundaries. It follows the same method as for the local characteristic boundary method except for the formulation of the modified normal Euler fluxes. At this point, the derivatives of the normal Euler fluxes are integrated with respect to time using the fourth order Runge-Kutta scheme The time-integrated normal derivatives are then subtracted from freestream values of the conservative variables to enforce the freestream conditions on the boundary.

Outlet

In HiPSTAR, at the outlet a zonal CBC (ZCBC) is optional [Sandberg and Sandham, 2006] to damp the disturbances together with CBC.

Several 2D cases are tested to see the effects of different boundary conditions. As can be seen from Fig. 4.3, 2D simulation for the untripped airfoil using the same numerical setup as in the tripped case leads to minor reflections (Fig. 4.3(a)) as marked by the red ellipse in the dilatation field and the airfoil loading drifted in the end (Fig. 4.3(b), indicated by the red arrow), as mentioned before. The purpose is to find a proper boundary condition in order to get a respectively clean acoustic field while holding the airfoil loading. The tested cases are listed in Tab. 4.2. Fixed Inlet without sponge layer has obvious reflections and such a phenomenon has polluted the dilatation field as well as the airfoil loading as could

Fixed Inlet	ICBC
Sponge Point (keeping strength 0.01): 2,5,10,20,30,40	Zonal CBC points at outlet: 0,30,100
Sponge Strength (keeping 20 points): 0.00001,0.0001(0.0005),0.001(0.005), 0.01,0.1,1	

For 2 and 5 point cases, the strength is set to be 0.0005/0.001.

Table 4.2 Tested 2D DNS cases on the untripped NACA6512-63 airfoil for different boundary conditions.

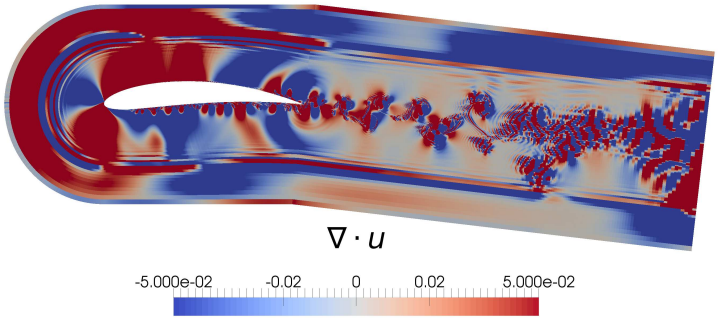

(a)

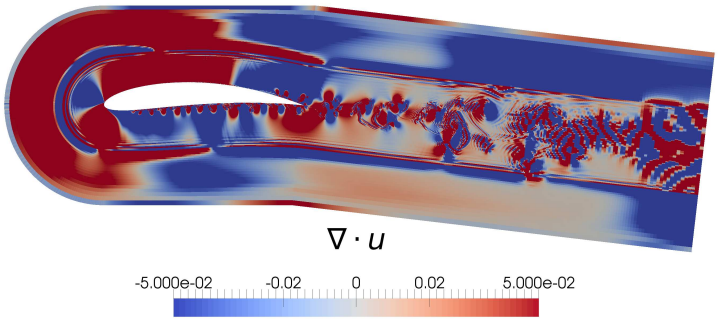

(b)

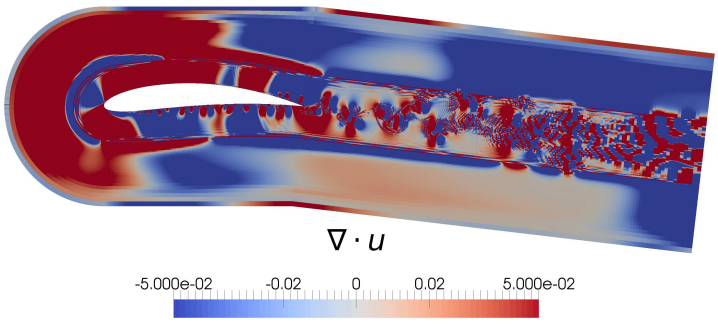

(c)

Figure 4.4 Instantaneous dilatation field using Fixed Inlet with $c_{sponge} = 0\ 01$ at $t = 16$: (a) 10-point sponge; (b) 20-point sponge and (c) 30-point sponge.

be seen from the amplitude of the oscillation; the ICBC case has indeed the problem of airfoil loading decreasing with time.

To improve the Fixed Inlet cases, several sponges are added. Given that the points used in the sponge zone cannot be used for physical considerations, for such a boundary condition, besides the main purpose that the sponge should attenuate the flow near boundary, it needs to be set by satisfying 2 requirements:

Sponge strength not too strong to cause reflections at the beginning of the sponge;
Reasonable sponge width in order not to sacrifice too many grid points.

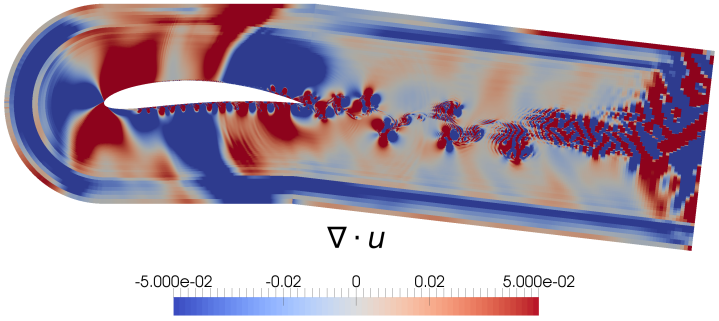

(a)

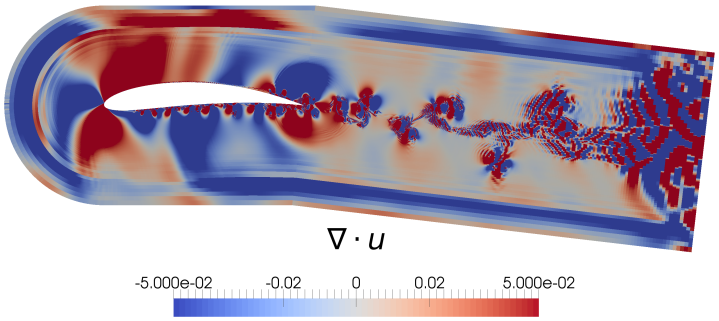

(b)

Figure 4.5 Instantaneous dilatation field of 5-point sponge cases at $t = 18$.

As the mesh cells have a high aspect-ratio near the inlet boundary, the number of points used for the sponge is quite limited. This limitation is shown in Fig. 4.4. For the tested case, the 20 or 30 points for the sponge for this airfoil case are obviously too much. Finally, it is found that the sponge width should be limited to less than 10 points and the 5 points sponge with 0.001 sponge strength is shown to be the best Fixed Inlet conditions among others (Figs. 4.5 and 4.6). But still, minor reflections are observed. The ICBC boundary on the other hand has always a cleaner acoustic field around the extended C-boundary. It can be seen in Fig. 4.7 that except for the pure CBC case (in Fig. 4.7(a)), ICBC with the ZCBC at outlet generally controls the reflection well. The minor reflection with 30

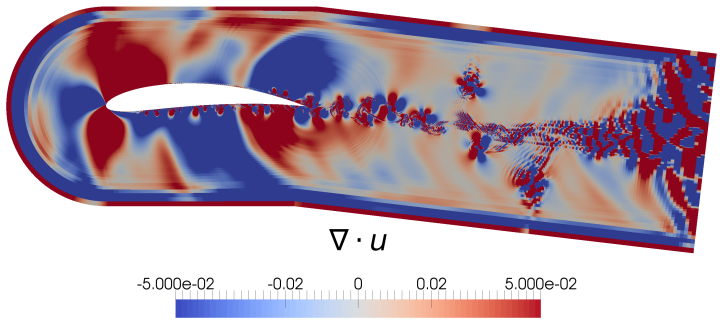

(a)

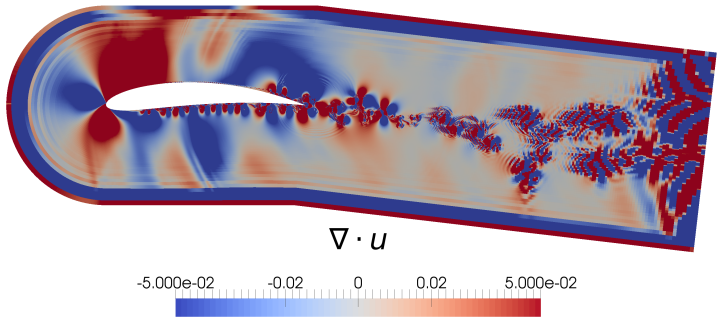

(b)

Figure 4.6 Instantaneous dilatation field of 2-point sponge cases at $t = 18$.

ZCBC points marked by the red ellipse in Fig. 4.7(b) has been improved in the 100 ZCBC points case in Fig. 4.7(c). The airfoil loading drift issue for the 30 ZCBC case (black line in Fig. 4.8) is essentially shown to be part of the low frequency oscillation which is caused by the reflection from outlet. Fig. 4.9 shows the comparison of the dilatation field between the 30 ZCBC case and 100 ZCBC case at the last timestep at $t = 26$. The low frequency reflection with an opposite propagation orientation to the noise radiated by the airfoil (marked by the red circle in Fig. 4.9) is continuously observed for several flow-through times. Such a low frequency fluctuation is hard to attenuate as it will take too much time to converge. Although for a 3D simulation such variations can be presumed to be less as the structures are less coherent because of the spanwise extent, it is better to use more ZCBC points at the outlet to avoid using too much time for the convergence. In addition, the calculation time for the 100 ZCBC point case and for the 30 ZCBC point case is of the same order. As a conclusion, the ICBC with 100 ZCBC points at outlet is the best solution to this case.

In summary, for an acoustic study, the ICBC with proper ZCBC points at outlet is the best choice for boundary conditions, even for a narrow stream. The Fixed Inlet can be employed with proper sponge layer but is quite limited by the grid stretching.

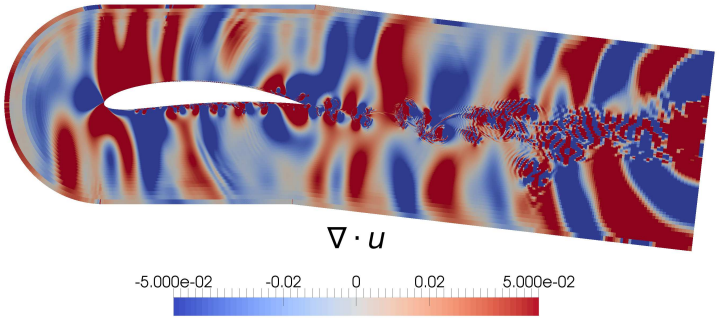

(a)

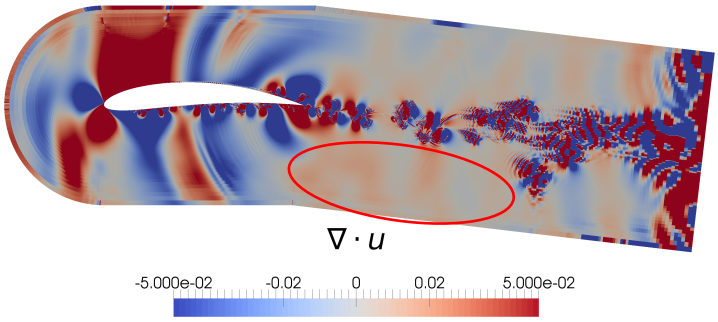

(b)

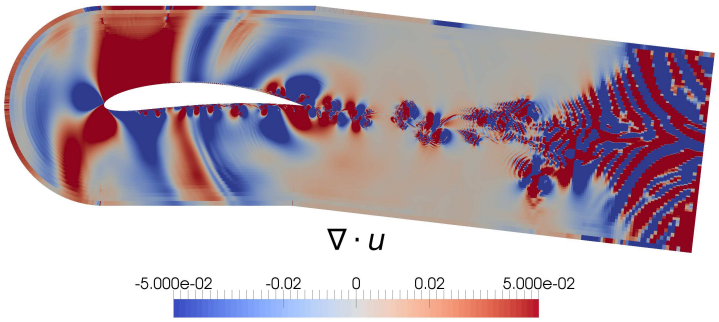

(c)

Figure 4.7 Effects of ZCBC at outlet on dilatation field at $t = 16$.

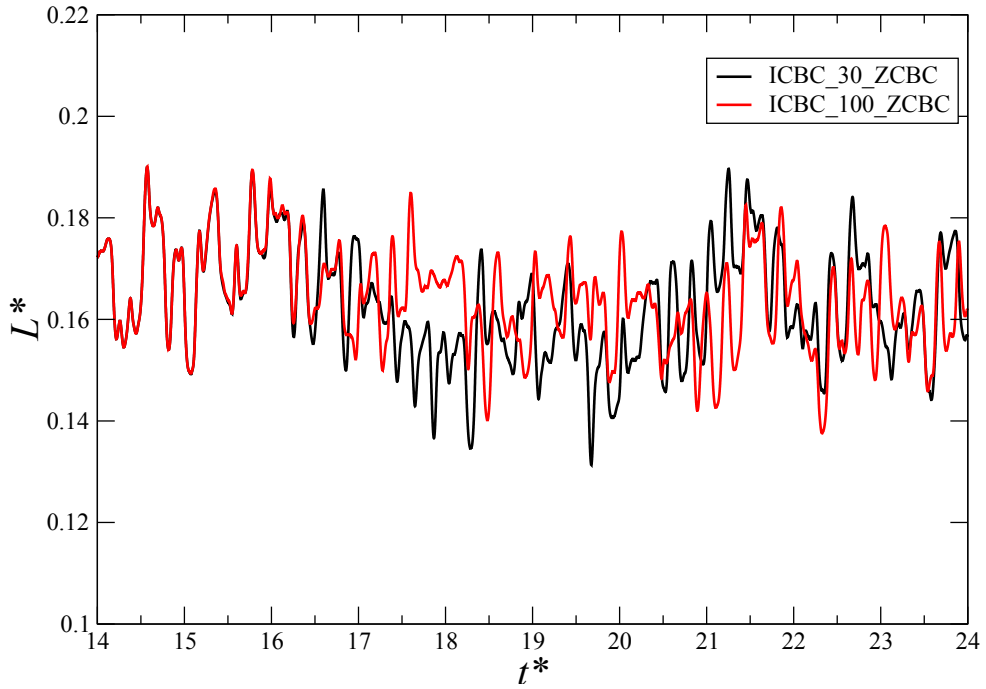

Figure 4.8 Effects of ZCBC at outlet on airfoil loading at $t = 14 \quad 24$.

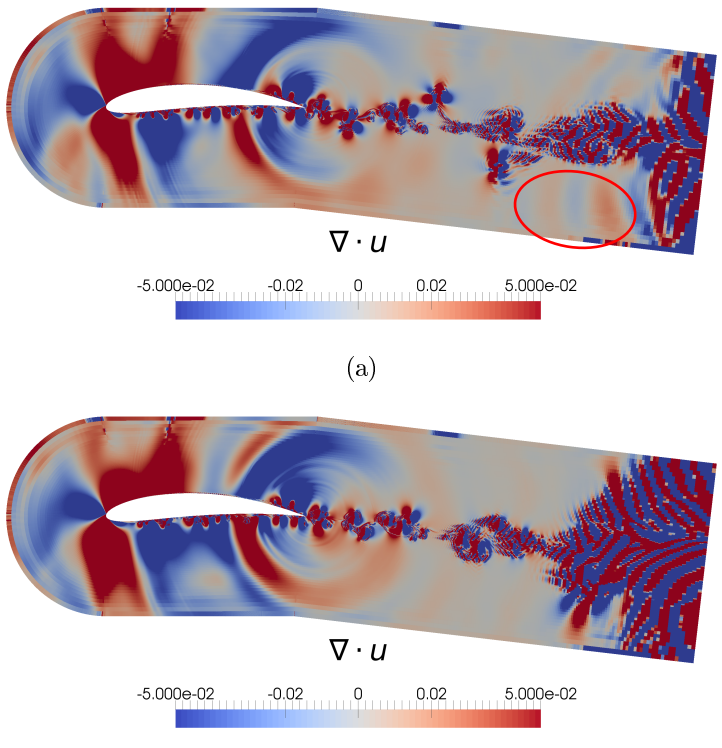

(a)

(b)

Figure 4.9 Effects of ZCBC at outlet on dilatation field at $t = 24$.

4.1.2 3D Simulation Setup

With the optimized boundary conditions from 2D simulations, the 2D simulation was extruded to 3D. In the spanwise direction, firstly 32 Fourier modes were used and then to 64, 96 and 128. Finally 96 Fourier modes are employed with 100% de-aliasing, which corresponds to 194 collocation points in physical space. This number of points was found to be sufficient to resolve down to the Kolmogorov scale [Winkler *et al.*, 2012] as shown in Figs. 4.10 and 4.11. These points are distributed over a spanwise width of 0.15 chord lengths. This length was determined to be sufficient to resolve all turbulent lengthscales in the flow field. [Winkler *et al.*, 2012]. The total number of grid points is 261 10^6.

In addition to the DNS, a series of LES studies were performed [Winkler and Moreau, 2008; Winkler *et al.*, 2009, 2012]. The LES were based on the spatially filtered, incompressible Navier-Stokes equations with the dynamic subgrid-scale model. Two different commercial numerical codes were used : Fluent V6.3 and Ansys CFX V11. For both codes, solutions were second-order accurate in space and time. The domain size is the same as in the DNS studies yet the mesh resolution was coarser. The current DNS then can verify the accuracy of the LES studies thanks to the higher order schemes both in space and time.

While the experimental [Winkler and Carolus, 2009] and LES [Winkler and Moreau, 2008; Winkler *et al.*, 2009, 2012] conditions were $Re_c = 190\ 000$ and $M = 0\,063$, the DNS was conducted (due to constraints in computational resources) at $Re_c = 150\ 000$ and $Ma = 0\ 25$. Results obtained for the tripped case study [Winkler *et al.*, 2012] indicate that the difference in Mach number and Reynolds number is practically irrelevant and the DNS simulation data can be scaled directly to the reference conditions of the experiment and LES simulation. This was also consistently observed in the context of acoustic predictions. According to these past studies, this approach is then taken for the current DNS on the untripped case.

4.2 Hydrodynamic Field

4.2.1 Grid Resolution

The resolution of the DNS cases was checked before further processing was performed. The grid spacing (time- and spanwise-averaged) in wall-units (x^+, y^+ and z^+) was checked and is shown in Figs. 4.12(a)-4.12(c). The values shown compare well with data found to be adequate in previous airfoil DNS studies [Jones *et al.*, 2008].

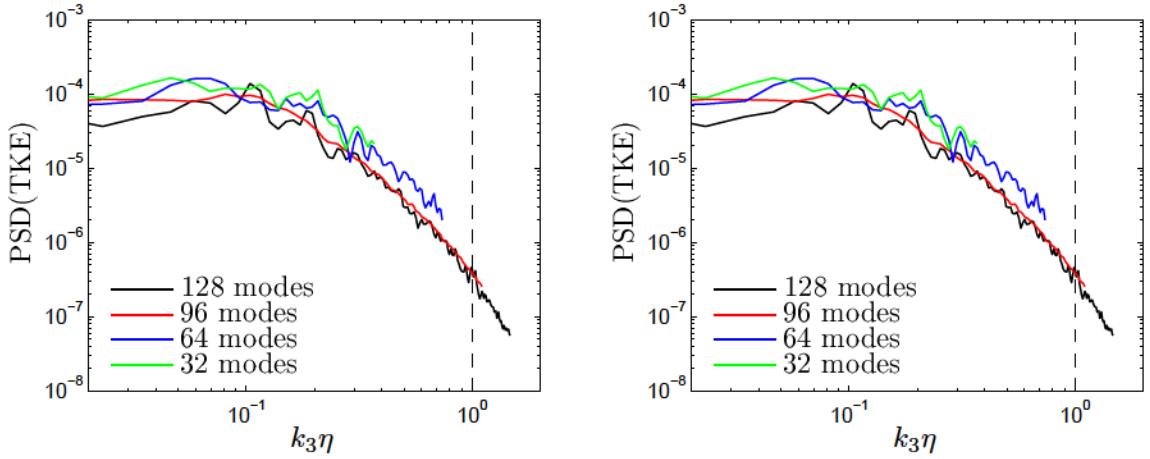

(a) pressure side (b) suction side

Figure 4.10 Time-averaged spanwise spectra of turbulent kinetic energy in the boundary layers at $x/c = 0.98$ for the tripped case.

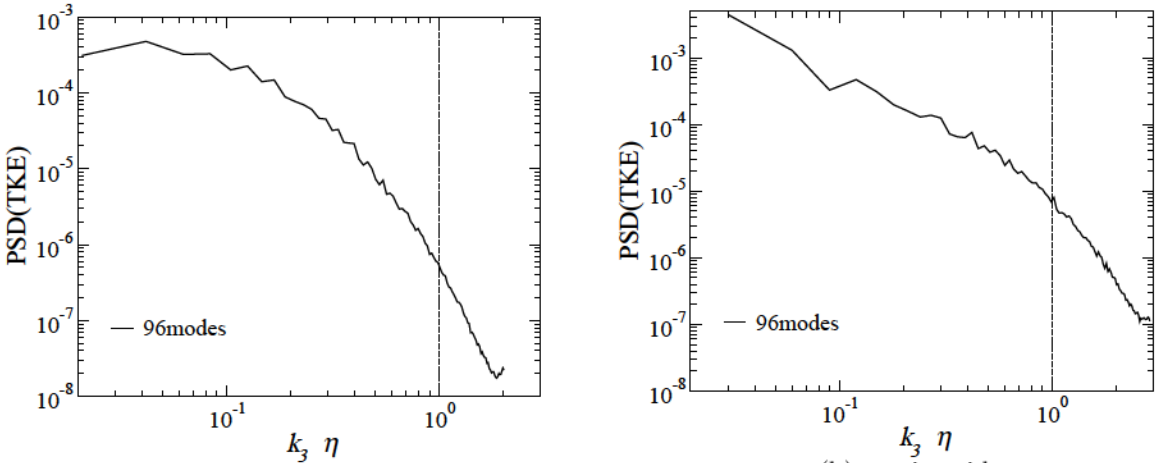

(a) pressure side (b) suction side

Figure 4.11 Time-averaged spanwise spectra of turbulent kinetic energy in the boundary layers at $x/c = 0.98$ for the untripped case.

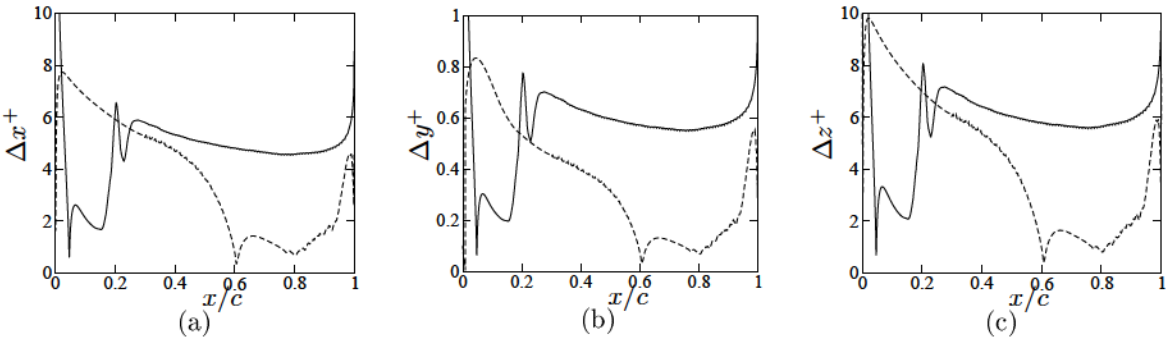

(a) (b) (c)

Figure 4.12 DNS grid resolution around the airfoil for the untripped case(---- suction side; —— pressure side).

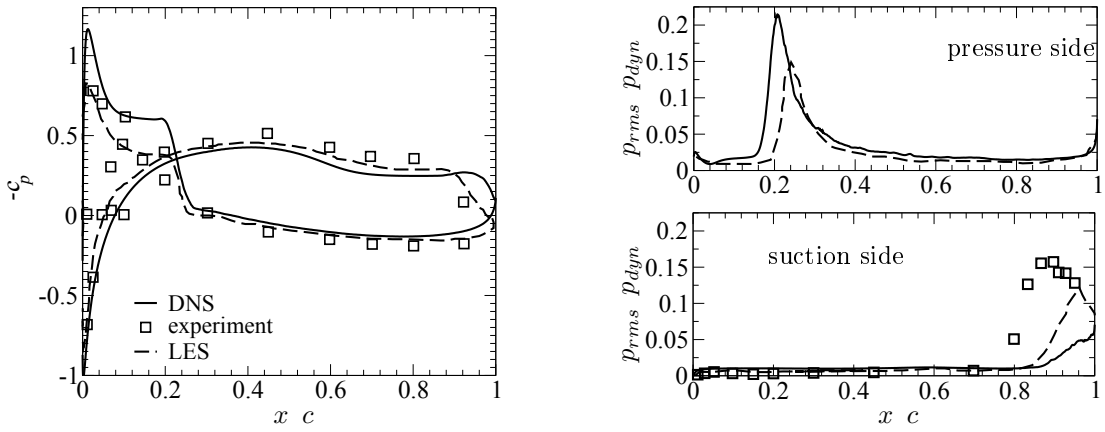

Figure 4.13 (a) Static lift distribution on the untripped airfoil, and (b) chordwise RMS pressure trace (—— DNS;---- LES [Winkler *et al.*, 2012]).

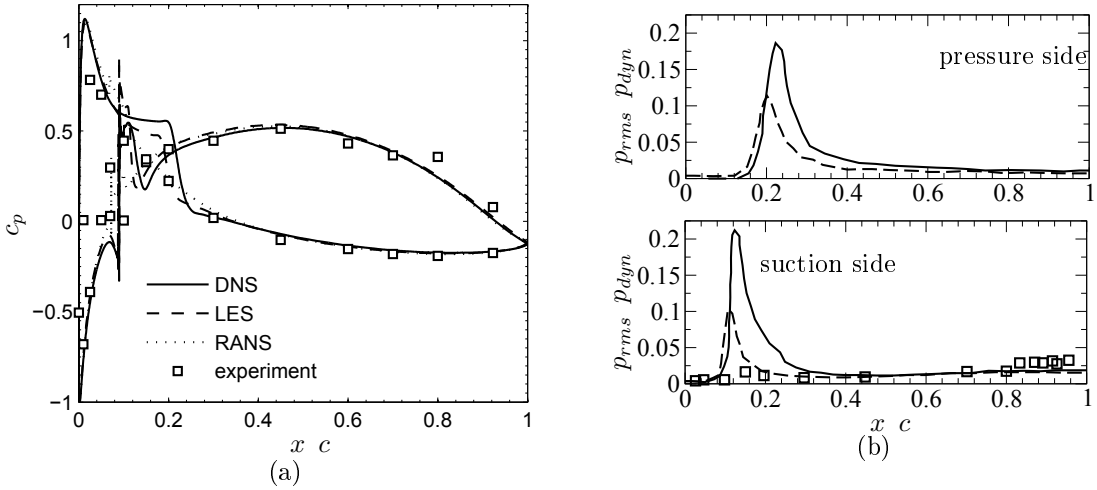

Figure 4.14 (a) Static lift distribution on the tripped airfoil, and (b) chordwise RMS pressure trace (—— DNS [Winkler *et al.*, 2012]; ---- LES [Winkler *et al.*, 2012]).

4.2.2 Mean Flow Field

As a first step in the flow field analysis, it was checked whether the inflow conditions were posed correctly. Indeed the jet width of the wind-tunnel can significantly modify the loading distribution on the airfoil. The importance of accounting for these installations effects has been discussed previously [Moreau *et al.*, 2003]. The mean static pressure distribution from the DNS run is compared with available wind-tunnel measurements, previous simulation data using a RANS and LES results. As shown in Figs. 5.6(a), 4.14(a) for the untripped and tripped cases respectively, the current DNS results generally give a correct prediction of the distribution of the mean wall-pressure coefficient c_p, which is

defined as

$$c_p = \frac{\overline{p} \quad p_0}{\frac{1}{2} \ {}_0 U_0^2} \tag{4.3}$$

Yet some differences exist.

For the untripped case, in Fig. 4.13(a), where p_0, $\ {}_0$ and U_o stand for the reference pressure, density and free-stream velocity, the location and length of the separation bubble on the suction side can be seen to be slightly different between the DNS and experimental data. On the pressure side, the results from the DNS agree closely with experiment and LES data except very close to the trailing edge. This is a direct consequence from the difference observed on the suction side. When the flow exhibits a separation/reattachment on the suction side at the trailing edge, the pressure side will deviate in order to keep the flow alignment at the trailing edge, i.e. satisfy the Kutta condition.

For the tripped case, the slight separation observed in the experimental data on the suction side comes from the difference of triggering the transition in the boundary layer trip compared to simulations. In the experiments, the trip thickness was increased in small increments until a 'reasonable' turbulent flow near the trailing edge was established. The criterion of 'reasonable' turbulent flow was when the far-field noise was reduced considerably and was checked with a stethoscope which confirmed that the transition had occurred. This procedure gives a minimum tripping height by only considering the acoustic effects. However, due to the minimum trip thickness chosen, the transition took place downstream of the trip and the flow condition near the trailing edge may therefore not have been perfectly defined. In the LES or DNS, the numerical trip thickness was increased by roughly 50% to ensure a fully turbulent boundary layer at the trailing edge. For this tripped case, the differences in Mach number and Reynolds number between DNS/LES and experiment have no effect on the c_p level and distribution. The RMS pressure distributions of the DNS are plotted in Figs. 4.14(b) and 4.13(b) and compared with LES data. Before further discussion, it should be mentioned that in both LES and DNS, no inlet turbulence was introduced whereas in experiments, the maximum inlet turbulence intensity is around 0.2% with recent improvements.

For the untripped case, the DNS shows much stronger pressure peak at the transition location on the pressure side at the leading-edge and further downstream it is quite similar to the LES results. These stronger RMS pressure peaks from DNS compared to LES is expected for two reasons: firstly, as the wall-pressure fluctuation contains the integral information from the boundary layer, the subgrid-scale modeling in LES can lead to possible errors in representing correctly the boundary layer flow. Secondly, the fact that the

DNS code uses a fourth-order accuracy scheme in time while the LES uses a second order scheme can lead to an amplitude difference. The lower the accuracy of the scheme is, the more damped the pressure signal is. The difference of RMS pressure distribution on the suction side however is most possibly due to the different freestream turbulence intensity that exists between the simulations and experiment. For a transition that is caused by a separation bubble, the external conditions, i.e., the background turbulence intensity [Jones *et al.*, 2008; Sanjosé *et al.*, 2016; Spalart and Strelets, 2000] can have a significant influence on the instabilities which then contribute to the transition to turbulence. In a recent study [Sanjosé *et al.*, 2017, 2016], flow with a separation bubble on the airfoil at the trailing edge was observed to be very sensitive to external conditions. This is further proved in a recent study by Istvan et al. [Istvan *et al.*, 2017]. This study shows that for transitional airfoil cases at moderate chord Reynolds numbers ($Re_c = 1\,0 \quad 10^5 \quad 2\,0 \quad 10^5$), increasing freestream turbulence intensity results in earlier flow transition and reattachement on the suction side. In their experiments on a NACA0018 airfoil, the background turbulence intensities were varied from 0.09% to 2.03%. These flow conditions are quite similar to the experimental setup for the current airfoil. This can explain the difference between the simulations and experiment shown in Fig. 4.13(b). Furthermore, in this study [Istvan *et al.*, 2017], it was concluded that the degree of the influence of freestream turbulence intensity on the separation bubble decreases as the chord Reynolds number is increased. As the current DNS has a lower Reynolds number ($Re_c = 1\,5 \quad 10^5$) than experiment ($Re_c = 1\,9 \quad 10^5$), this means that the flow can transition later and that such an effect from background turbulence intensity can be more pronounced. Note that the DNS is the last one to transition. The more dissipative LES transition before. In addition, as the current airfoil is immersed in a narrow stream, although the mean installation effects are considered in the simulation, the unsteady effects from the interaction from the jet shear layer and the airfoil can have effects on the airfoil flow topology. This aspect however, needs much more numerical resources to be confirmed.

For the tripped case on both sides of the airfoil, similar to the pressure side of the untripped case, DNS shows stronger pressure peaks at the transition location. When this transition process has faded out further downstream where the boundary layer turbulence is fully developed, the RMS pressure trace attains very comparable levels, especially close to the trailing edge. The transition mechanism itself does not appear to influence the turbulent pressure amplitudes further downstream. Therefore, the IMBM in the DNS works just like the actual tripping step does, and the different forced transition approaches in both numerical approaches lead to practically identical pressure fluctuation amplitudes close to the trailing edge. The difference between the RMS pressure distribution on the pressure

side from the untripped (Fig. 4.13(b)) and tripped DNS (Fig. 4.14(b)), i.e., the amplitude and position of the RMS peak, constitutes further evidence that the need to satisfy the Kutta condition at the trailing edge can influence the global flow behavior up to the leading edge leading to a minor difference in the transition process. This will be further explained in *Section* 4.3 from the correlation functions.

It is hypothesized that the flapping and separated boundary layer gives an additional noise source at the trailing edge and thus this area on the suction side is studied here in more details. Time averaged skin friction coefficient c_f on the airfoil is plotted in Fig. 4.15. It

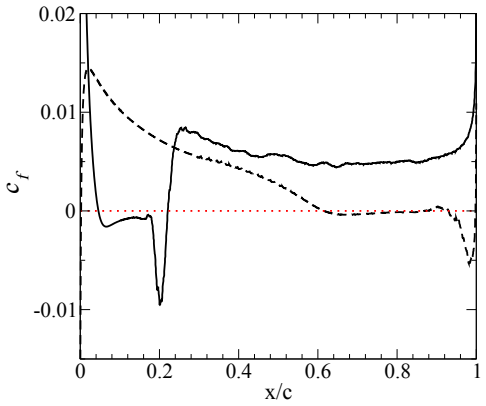

Figure 4.15 The mean skin friction coefficient over the airfoil (—— pressure side; ---- suction side).

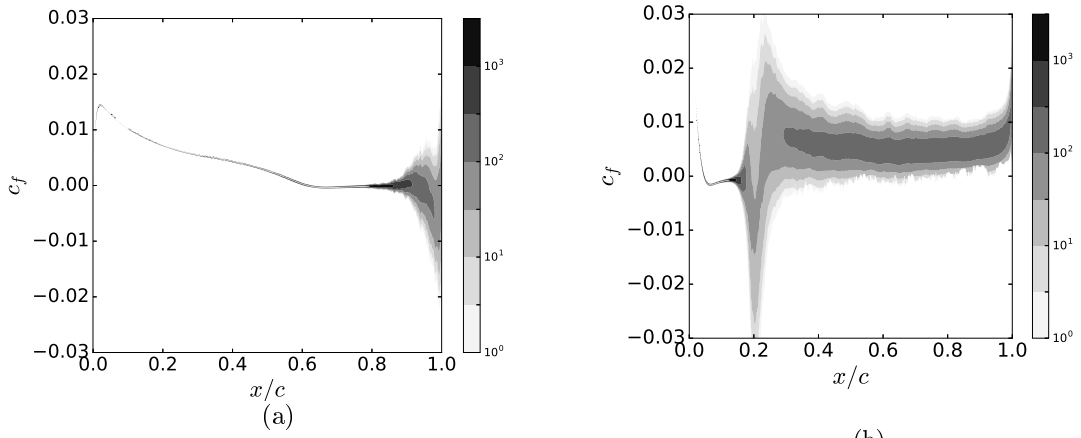

Figure 4.16 Iso-contours of the normalized c_f p.d.f. using 7 levels exponentially distributed over the range 1 to 3000: (a) on suction side and (b) on pressure side.

gives a quantitative measure of the separated region on the suction side and the bubble region on the pressure side. It can be seen that the separation on the suction side starts

after mid-chord around $x\ c = 0\ 6$ and reattaches just before the trailing edge due to the separated shear layer transitioning to turbulence. On the pressure side, the transition is triggered by the bubble on the leading edge around $x\ c = 0\ 04$ and the flow reattaches at $x\ c = 0\ 22$.

The time-dependent nature of separation can be investigated by computing the probability density functions (p.d.f.s) of c_f. As the c_f value varies along the airfoil, it is inconvenient to use an ordinary p.d.f. function in which the mean value and number of 'bins' are fixed [Jones *et al.*, 2008]. Instead, the c_f time series for each point on the airfoil is extracted and the p.d.f. is constructed using 30 bins equally spaced over 3 standard deviations about the mean c_f value. In Fig. 4.16, for each location on the airfoil, if the contours are thin, it means that the flow shows little variation over time and if the contours are wide, c_f varies strongly. The colors shows how frequent the same c_f value occurs in time.

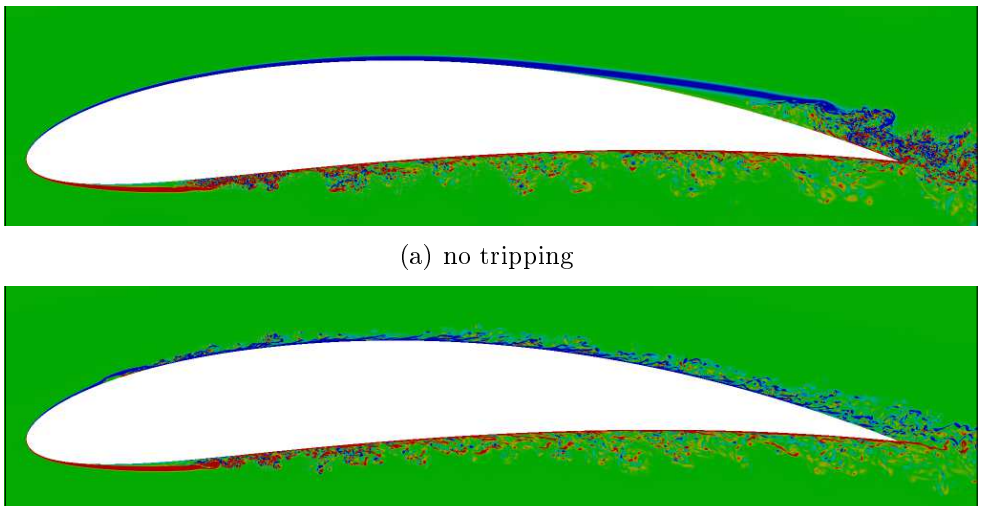

(a) no tripping

(b) IMBM tripping [Winkler *et al.*, 2012]

Figure 4.17 Instantaneous spanwise vorticity, ranging from 100 (blue) to +100 (red).

On the suction side, upstream of the separation, c_f displays nearly no variations which means the flow in this area is nearly steady. Downstream of the separation point, the c_f still varies little until at $x\ c = 0\ 9$, the flow starts to oscillate due to the transition to turbulence. Although the mean c_f in Fig. 4.15 shows all negative values at the trailing edge, the p.d.f. contours in Fig. 4.16(a) show that this reverse flow is unstable and varies considerably with time. This time dependent behavior can be the major contribution to the extra noise from the trailing edge.

On the pressure side, an even larger temporal variation exists. This larger variation seems to be caused by the roller structures generated by the leading edge separation bubble

that then have a stronger effects on the c_f downstream. Considering that the flow on the pressure side has a smaller local Reynolds number due to the lower speed, this phenomenon is coherent with the observations obtained by [Jones *et al.*, 2008] for similar cases with a lower Reynolds number.

4.2.3 Instantaneous Flow Field

As this cambered airfoil is situated in the narrow stream of a wind tunnel nozzle, the flow conditions are such that the boundary layer transition occurs naturally on both airfoil sides. On the pressure side transition occurs early on and a fully turbulent boundary layer exists close to the trailing edge. This transition is a result of flow separation and reattachment resulting in a small leading edge separation bubble. On the suction side the transition process starts further downstream and results in a long separated shear layer with turbulent reattachment close to the trailing edge. This process is visualized using contours of the spanwise vorticity in Fig. 4.17(a). The tripped DNS results are shown in Fig. 4.17(b) for comparison purposes. In the tripped case, a fully attached and developed turbulent flow field is observed at the trailing edge while in the untripped case larger structures are formed due to the flapping shear layer on the suction side. The details of the flow structures at the leading and the trailing edge for the untripped case are presented through iso-surfaces of the $_{ci}$-criterion [Wu *et al.*, 2017b; Zhou *et al.*, 1999] and colored by the streamwise velocity component in Fig. 4.18. It should be noticed that there exists a variety of vortex identification methods that can be applied to the current flow case to show the flow structures. The discussion on different vortex identification methods including the $_{ci}$-criterion can be found in *Appendix*. The value of $_{ci}$ is chosen such that it is around 3% of its maximum value for the current flow data around the airfoil, similar to what has previously been suggested [Zhou *et al.*, 1999]. On the pressure side, some spanwise roller structures are generated then lead to a short recirculation bubble that triggers the transition. On the suction side, the flapping shear layer at the trailing edge leads to larger spanwise coherent structures. These structures on the suction side close to the trailing edge are quite similar the DNS case on CD airfoil at 5 AoA [Sanjosé *et al.*, 2017, 2016], which is at the same Re_c and similar Ma ($Ma = 0\ 2$ in [Sanjosé *et al.*, 2017, 2016]). However, this untripped airfoil shows also some large structures on the pressure side. This is observed by some hump structures near the trailing edge on the pressure side in Fig. 4.17(a) compared with the tripped case (Fig. 4.17(b)). Furthermore, in Fig. 4.18(c), a roller structure very close to the trailing edge is formed on the pressure side. This roller is quite similar to the one formed on the suction side at almost the same streamwise location

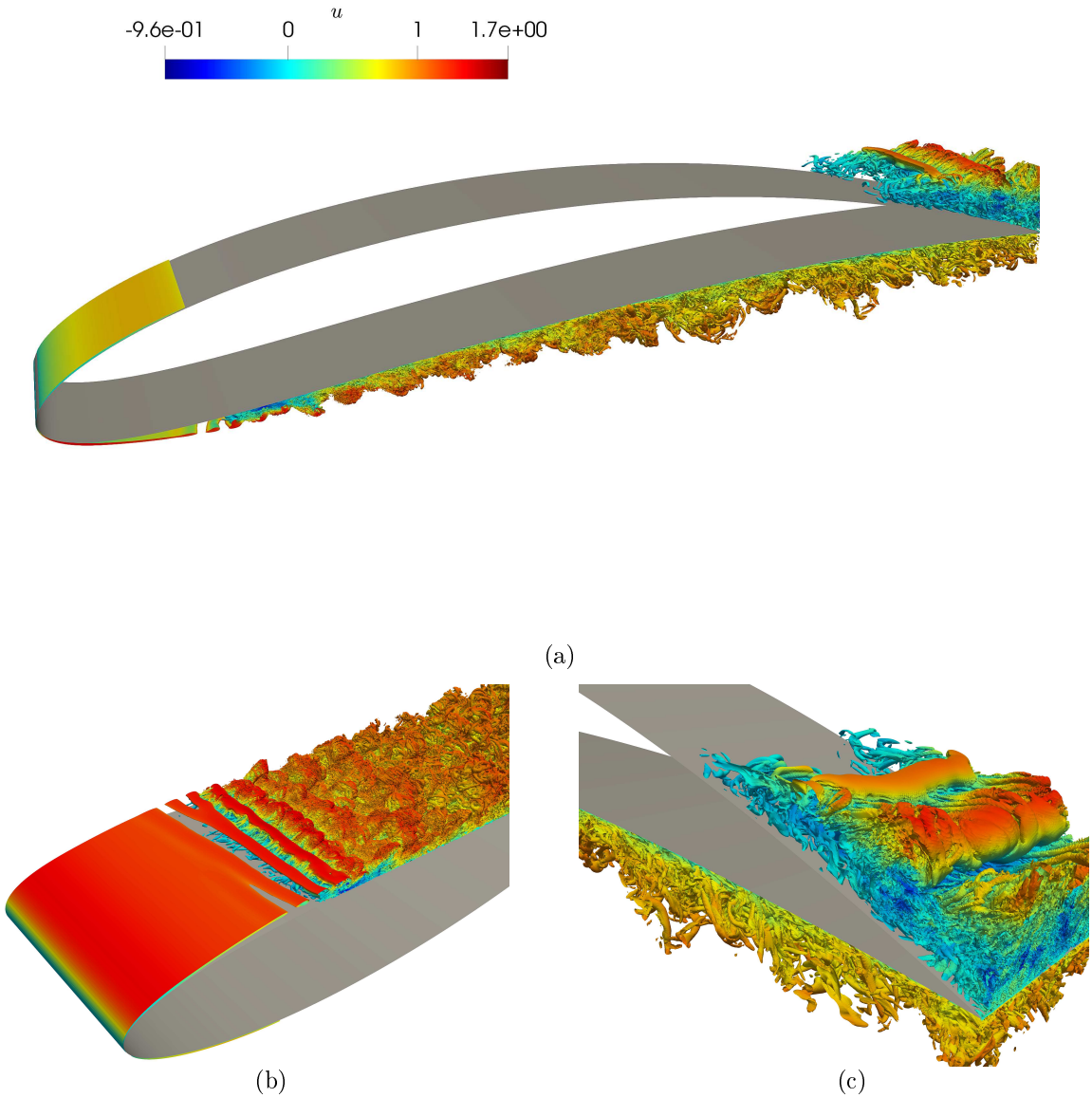

Figure 4.18 Swirling strength criterion $_{ci} = 30$ iso-contours of the NACA6512-63 untripped airfoil colored by streamwise velocity: (a) Airfoil global view; (b) Zoom view at the LE on the pressure side; (c) Zoom view at the TE and near wake.

caused by the flapping shear layer. This detail will be further quantified in the following section.

4.3 Spectra, Correlation and Coherence

Pressure signals were recorded for 7 flow-through times, based on airfoil chord length and the reference velocity, for the acoustic analysis after the simulation was statistically steady.

The analysis of the pressure amplitudes alone does not say anything about the spectral distribution of those fluctuations. To retrieve such information, surface pressure spectra were extracted from the unsteady simulations for a location close to the trailing edge ($x\ \ c = 0\ 95$). The power-spectral density (PSD) $\ \ _{pp}(\ \ )$ of the wall-pressure fluctuations p at a given angular frequency $\ \ $ is obtained from the wall-pressure cross-spectral density

$$(x\ \ z\ \ \ \ x\ \ \ \ z\ \ \ \ ) = \frac{1}{2} \quad ^{+} \quad p\,(x\ \ z\ \ t)p\,(x+\ \ \ \ x\ \ z+\ \ \ \ z\ \ t+\ \ )\ \exp\ ^{i}\ \ \ d \qquad (4.4)$$

by setting the streamwise and spanwise space-separations $\ \ x$ and $\ \ z$ between two points

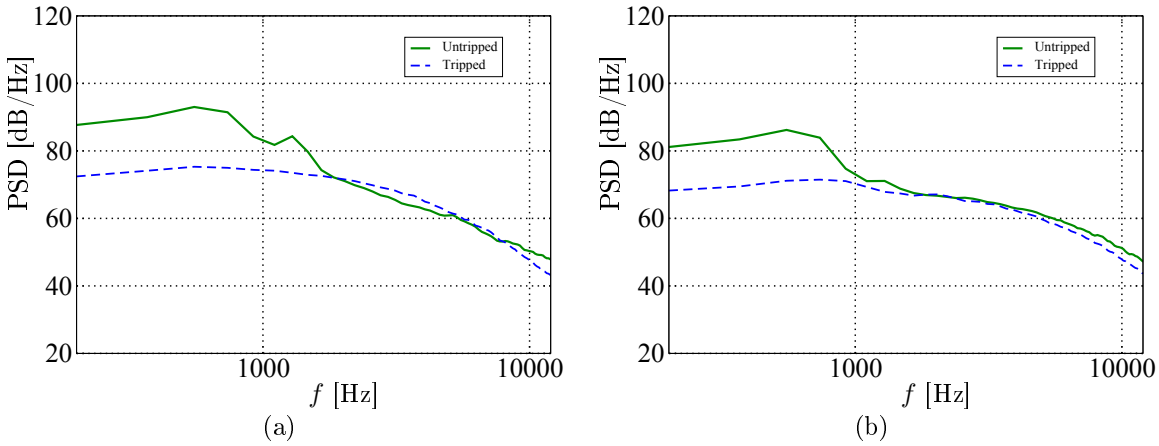

Figure 4.19 Wall-pressure fluctuation PSD at $x\ \ c = 0\ 95$ (a) suction side; (b) pressure side.

on the airfoil to zero. The DNS data was scaled to obtain dimensional quantities. This was achieved by multiplying the dimensionless pressure from the simulation by $\ _0U_0^2$, where the reference values were $\ _0 = 1\ 225$ kg/m^3 and $U_0 = 21$ m/s. These values correspond closely to the experimental conditions and the LES simulation parameters. The suction side and pressure side spectra are shown in Figs. 4.19(a) and 4.19(b), respectively, and compared with the tripped case for the same location. The untripped case is shown to exhibit higher pressure fluctuations over low frequency ranges on both sides. On the suction side, it is dominated by a hump centered at 600-700 Hz and a less dominant peak at 1300 Hz while

on the pressure side the hump around 600-700 Hz is observed with a slight lower level and at 1300 Hz a weaker hump is observed. These humps (and a peak) are believed to be related to the large structures shown in Fig. 4.18(c). As shown by the mean field in Figs. 4.13(a) and 4.13(b), the flapping shear layer on the suction side starts approximately from $x\ c = 0\ 8$. This flapping area of length $0\ 2c$ close to the trailing edge corresponds to a frequency of $f = U_0\ 0\ 2c = 778$ Hz, which is related to the low frequency hump showed in Figs. 4.19(a) and 4.19(b). For the peak or weak hump at higher frequency present in Figs. 4.19(a) and 4.19(b), it is most likely related to the rollers structures from caused by the Kelvin-Helmholtz instabilities [Desquesnes *et al.*, 2007; Sanjosé *et al.*, 2018]. The recirculation bubble at the leading edge on the pressure side should be responsible for the weakened levels on the pressure side in Fig. 4.19(b) compared with the levels on the suction side in Fig. 4.19(a) as the noise radiated by this bubble has an opposite propagation direction to that radiated from the trailing edge which as a consequence, leads to a cancellation effects. In both cases the spectra were averaged over all spanwise points. The reason for such an average is that for this flow case, the spanwise variation of the pressure fluctuations is noticeable. Figs. 4.20(a) – 4.20(d) show this spanwise variation for location $x\ c = 95\%$ on both sides of the airfoil for the untripped and tripped case.

As the flow field near the trailing edge is turbulent on both the suction and pressure sides, it is important to check the spanwise correlation or coherence to make sure the turbulent flow is sufficiently developed in the spanwise direction close to the trailing edge. It has been pointed out in previous numerical studies that the spanwise extent for such a flow case should be at least $0.074c$. In this DNS simulation, the spanwise extent is set to be $0.15c$ which is intended to account for the flapping shear layer and separation behaviour which possibly might nurture instabilities with a larger spanwise wave length than an attached turbulent boundary layer. The spanwise coherence ^{2} between two points on the airfoil surface separated by z is computed as follows

$$^2(z \quad z \quad) = \frac{_{pp}(z \quad z \quad)^2}{_{pp}(z\ 0 \quad) \quad _{pp}(z + \quad z\ 0 \quad)} \tag{4.5}$$

Spectra of the spanwise coherence function were calculated for half the span size ($z\ c$ (0 0 075)) for spanwise points 1 through 96, 2 through 97, etc. in the DNS and then averaged. The plots shown in Figs. 4.21(a) and 4.21(b) demonstrate that the domain size is sufficiently large to capture all flow features. The time data available for averaging is not yet sufficient to obtain a smoother estimate at low frequencies. Compared with the tripped case [Winkler *et al.*, 2012], the untripped airfoil has a stronger correlation on

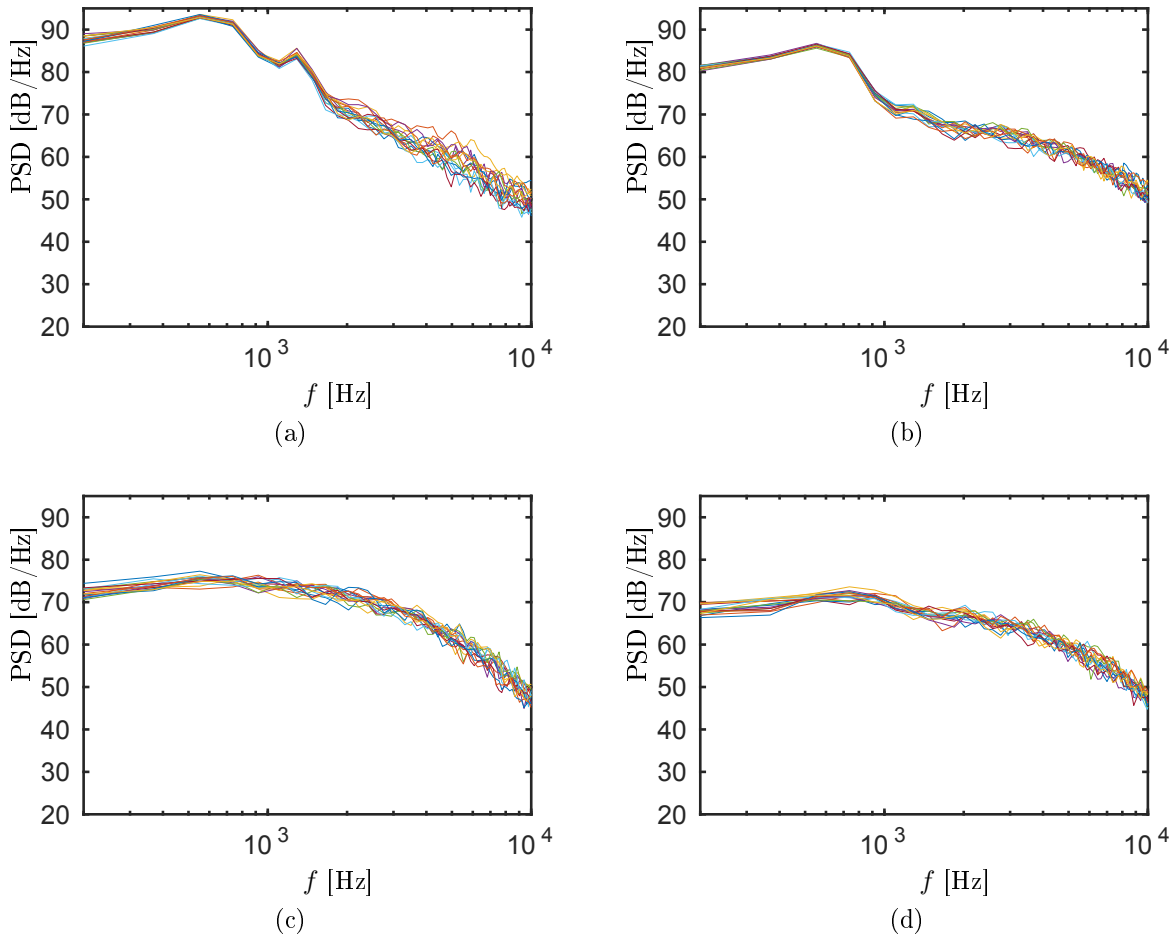

Figure 4.20 Spanwise variation of wall-pressure fluctuation at $x\ c = 0\ 95$ for $z\ c$ 0 01 (a) untripped, suction side; (b) untripped pressure side; (c) tripped, suction side; (d) tripped pressure side.

the suction side up to 1200 Hz due to the presence of larger structures. Nevertheless, it appears that a spanwise width of 0 12c would be sufficient for this flow configuration.

Spanwise correlation length of the pressure fluctuation signals is shown in Figs. 4.22(a) and 4.22(b). This is an important length scale in Amiet's model for farfield noise prediction. It can be seen that for the sensor location at $x\ c = 95\%$, the untripped case has a much larger correlation length for low frequencies on both sides of the airfoil. The frequencies where $l_z\ c$ shows its maximum values for the untripped case are coherent with what has been discussed in Figs. 4.19(a) and 4.19(b): they are related to the large structures shown in Fig. 4.18(c). The second peak of $l_z\ c$ around 1300 Hz is due to the rollers generated by Kelvin-Helmholtz instabilities.

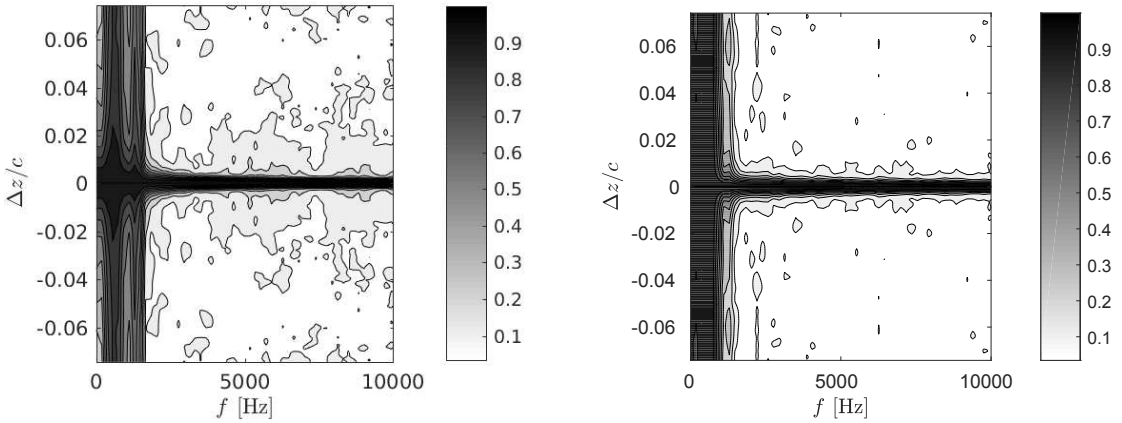

(a) suction side (b) pressure side

Figure 4.21 Spanwise coherence of surface pressure data obtained from the untripped airfoil DNS results at $x\ c = 0\ 95$.

In Figs. 4.23(a) and 4.23(b), the pressure side of the untripped case has a larger correlation length in the low frequency range compared with the tripped airfoil. This is a direct consequence of the shear layer flapping on the suction side as the pressure fluctuation signals on the pressure side is quite correlated with the suction side in the untripped case as can be seen in Figs. 4.24(a) – 4.24(d) from 4 locations near the TE. This correlation however is not observed in the tripped case in Figs. 4.25(a) – 4.25(d). Figs. 4.24(a) – 4.25(d) quantitatively explain the origin of the larger structures at TE on the pressure side of the untripped airfoil shown in Fig. 4.17(a): the flapping shear layer on the suction side. Furthermore, the peaks at higher frequencies in these coherence plots indicate that some acoustics is making both sides of the airfoil communicate.

4.4 Acoustic Field

4.4.1 Near Field

The separating shear layer without tripping exhibits a flapping motion and is inherently unstable as clearly shown by the c_f p.d.f. plots in Fig. 4.16. It ultimately generates rollers and interacts with the trailing edge and produces much stronger noise radiation than a fully tripped and turbulent boundary layer on the suction side. This is shown in Figs. 4.26(a) and 4.26(b), where the instantaneous dilatation fields are plotted with the same contour levels for the untripped and tripped DNS cases. A stronger radiation in the presence of the separating shear layer is seen. Furthermore, additional noise sources exist in this case and the propagation of acoustic waves upstream is affected by the refraction

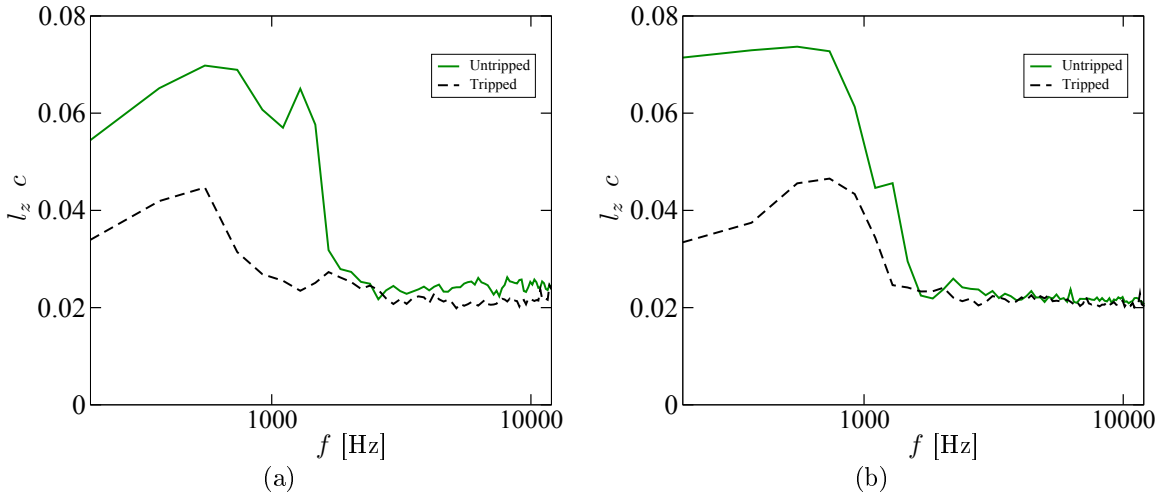

Figure 4.22 Spanwise correlation length at $x\ c = 0\,95$ (a) suction side; (b) pressure side.

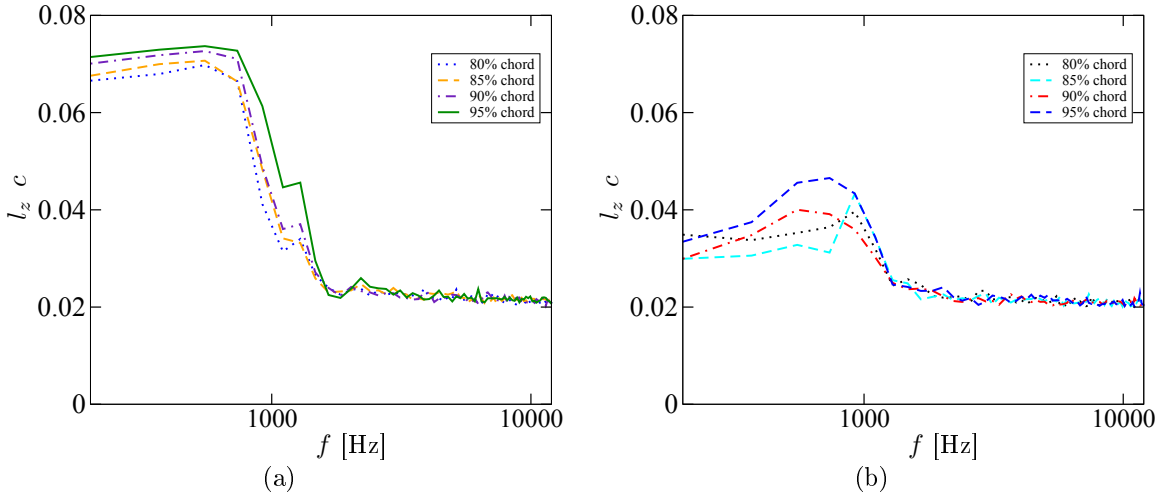

Figure 4.23 Spanwise correlation length on the pressure side near TE (a) untripped case; (b) tripped case.

through the separated shear layer. It has been hypothesized in the past that the existence of such a separation bubble constitutes a prerequisite to the occurrence of an efficient acoustic feedback loop, which leads to a single tone or multiple tones to be radiated from the airfoil.

4.4.2 Far Field

Results from acoustic far-field measurements for this flow condition and airfoil profile are shown in Fig. 4.27 [Winkler and Carolus, 2009]. For the flow conditions considered in this study, no tonal noise components are seen in the data. This suggests that any

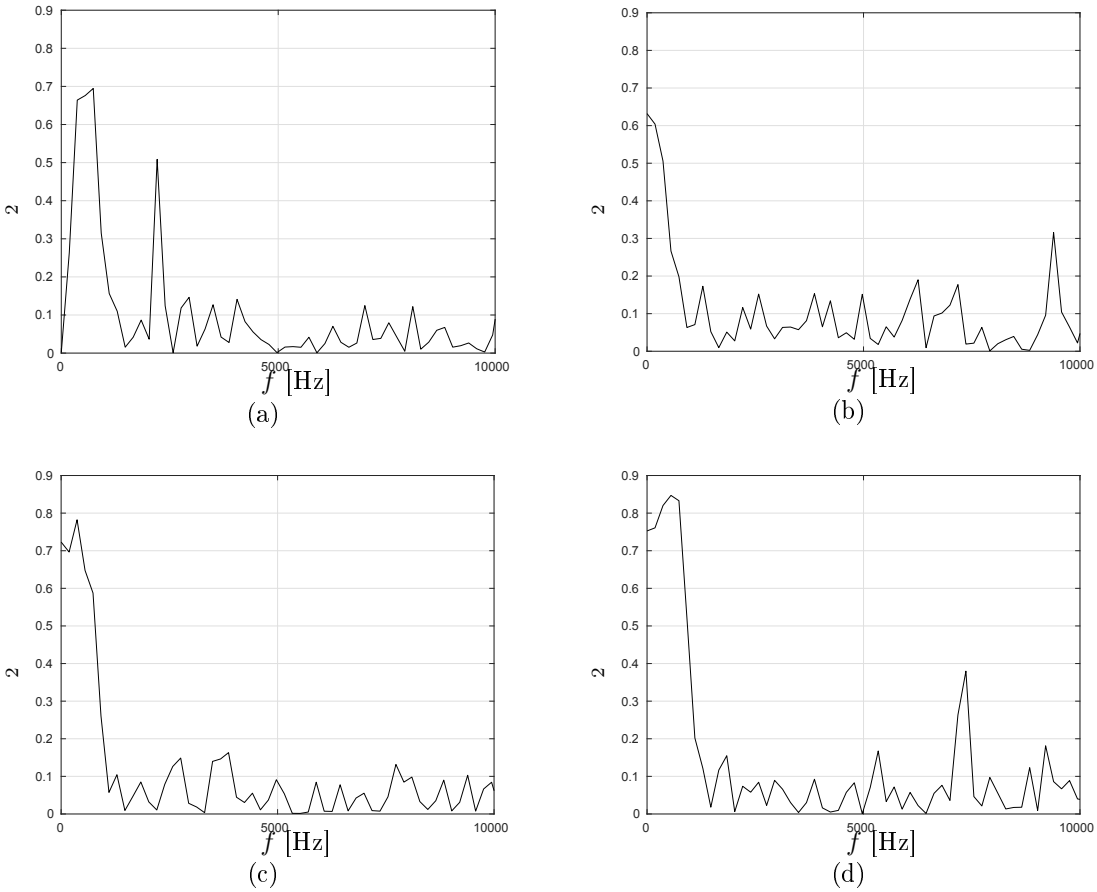

Figure 4.24 Coherence of pressure fluctuations from 2 points respectively from suction and pressure side of the untripped airfoil at (a) 80% chord; (b) 85% chord; (c) 90% chord and (d) 95% chord.

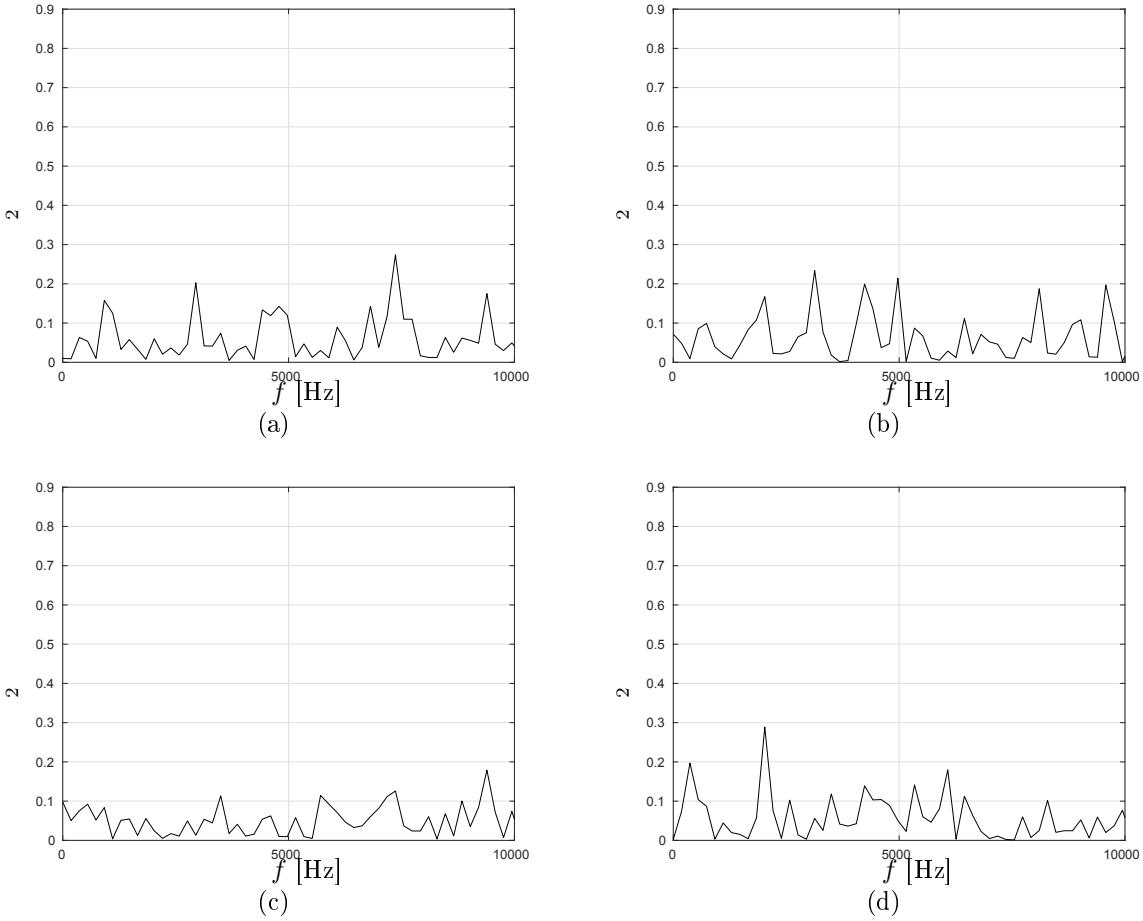

Figure 4.25 Coherence of pressure fluctuations from 2 points respectively from suction and pressure side of the tripped airfoil at (a) 80% chord; (b) 85% chord; (c) 90% chord and (d) 95% chord.

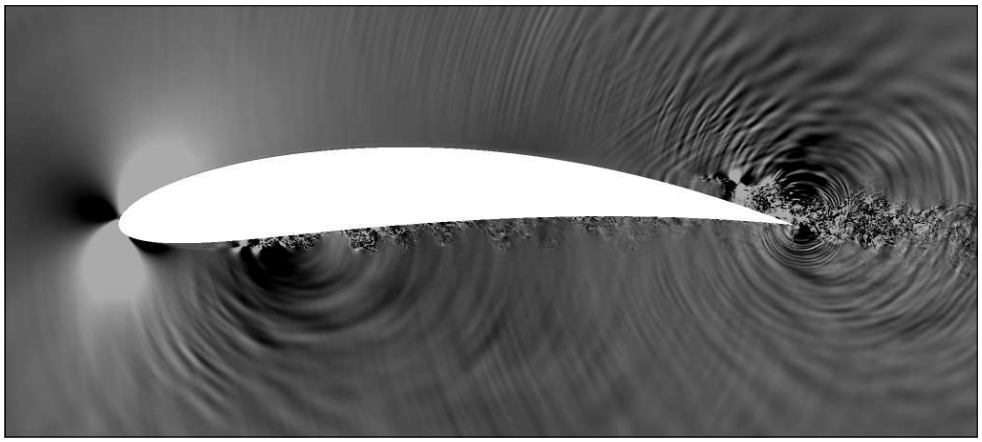

(a) no tripping

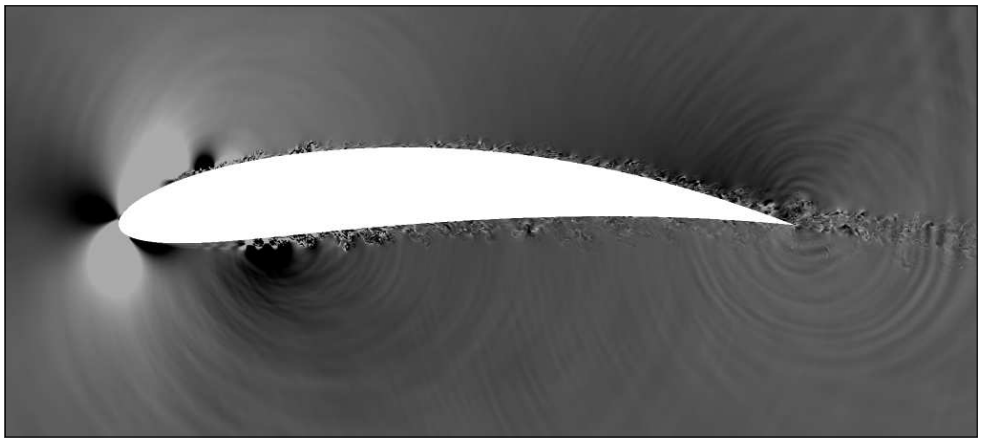

(b) IMBM tripping [Winkler *et al.*, 2012]

Figure 4.26 Dilatation field, displayed from 0 1 (white) to +0 1 (black).

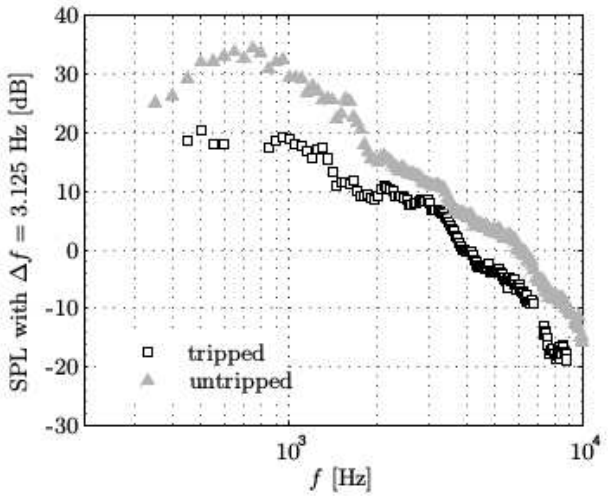

Figure 4.27 Acoustic far-field measurements [Winkler and Carolus, 2009] of the airfoil with and without boundary-layer tripping at $1.2m$ downstream from trailing edge in the midspan plane at 90 with respect to the airfoil chord.

feedback loop that may be present and amplified by the existence of the separation bubble is actually weak. The flapping shear layer itself is expected to be responsible for the large broadband noise increase noticed in the experimental data. In fact, slowly increasing the trip thickness in the experiments leads to a reduction in the broadband noise hump, until it reached the minimum noise level given by the fully tripped airfoil. In that case the boundary layer on the suction side was fully turbulent and attached [Winkler *et al.*, 2012]. The scattering of the pressure disturbances produced by the turbulent bubble at the trailing edge is therefore responsible for the large broadband noise increase.

In order to investigate the acoustic radiation from the airfoil trailing edge, the simulation is coupled with an existing Ffowcs Williams and Hawkings (FWH) propagator to compute the acoustic far-field from information on the domain boundaries. A porous FWH formulation and a solid-wall FWH formulation are used and here are referred to as Porous-FWH and Solid-FWH. Care has been taken to place the porous control surface as close as possible to the airfoil where the mesh has a high resolution, while still including all dominant sources in the flow field. The Porous-FWH surfaces are illustrated in Fig. 4.28: a C-contour shape surface around the airfoil and an end-cap surface in the wake where the turbulence intensity is lower than 10%. The contribution from the end-cap can be ignored in this case as the results for Porous-FWH surfaces with and without the end-cap show nearly no difference. Finally the results from the Porous-FWH with the end-cap are presented here.

The Porous-FWH and Solid-FWH surfaces are recorded as instantaneous shots during the simulation and then are fed to the FWH solver. Finally, in order to compare with the experimental data, the predicted far-field PSD for an airfoil of actual span L is calculated from the computational slice by

$$S_{pp\,FWH} = \frac{L}{L_{DNS}} \quad S_{pp\,DNS} \tag{4.6}$$

This is valid whenever the computational domain size is acoustically compact in the spanwise direction [Wang and Moin, 2000] and the source regions of each spanwise slice can be assumed to be statistically independent, which has been confirmed to be true from the coherence plots shown in Figs. 4.21(a) and 4.21(b).

Fig. 4.29 shows the results from the FWH predicted farfield noise level compared with the experimental data. The two FWH surfaces give significantly different results. This implies that using just the pressure fluctuations over the solid surfaces do not capture all acoustic sources for this flapping and separated boundary layer, and that the porous-FWH

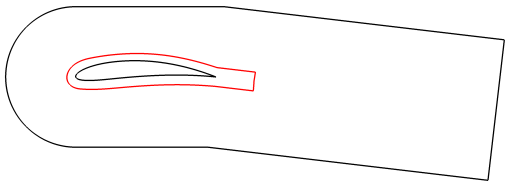

Figure 4.28 Illustration of the location of the Porous-FWH surfaces (red solid lines).

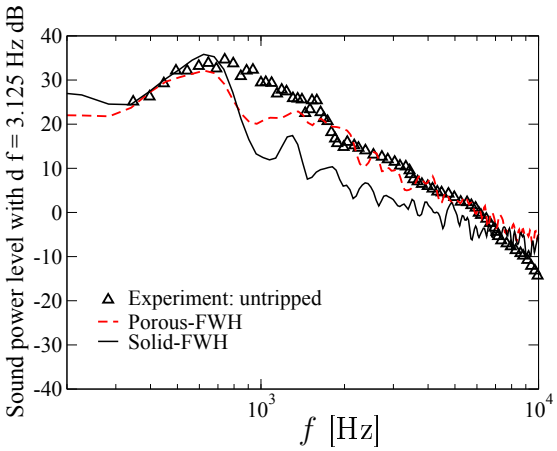

Figure 4.29 Acoustic far-field prediction using porous and solid Ffowcs Williams and Hawkings surfaces of the airfoil without boundary-layer tripping at $1.2m$ above trailing edge in the midspan plane at 90 with respect to the airfoil chord.

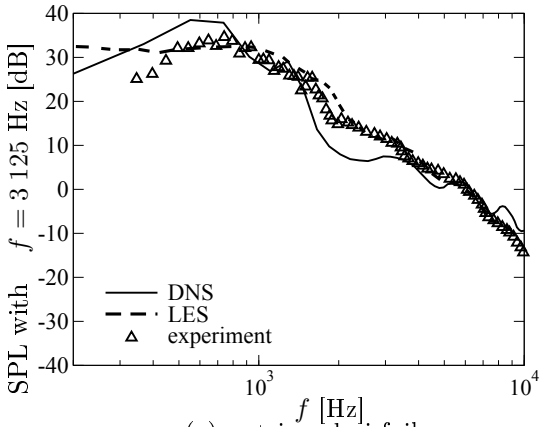

(a) untripped airfoil

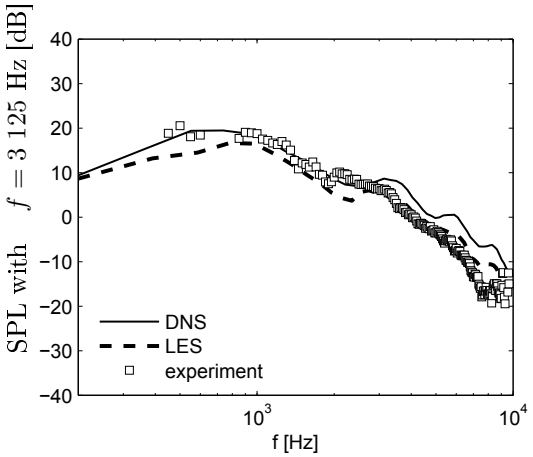

(b) tripped airfoil

Figure 4.30 Acoustic far-field prediction with DNS and LES [Winkler *et al.*, 2009] using Amiet's analogy of the airfoil with and without boundary-layer tripping at $1.2m$ above trailing edge in the midspan plane at 90 with respect to the airfoil chord compared with experiments [Winkler and Carolus, 2009].

enclosing more acoustic sources yields a better representation of the far-field noise. In the Porous-FWH case, results were also compared to the case of an open C-contour surface where the end-cap surfaces were removed and nearly no difference were presented. Both the Porous-FWH and the Solid-FWH surfaces have a dip around 1 kHz which is different from experimental results. The shape of the wall-pressure PSD also shows the dip at the

same location in the frequency domain which indicates that this difference is essentially from the wall-pressure fluctuations in the simulation as shown in Fig. 4.19(a). Although as observed by Sanjosé et al. [Sanjosé *et al.*, 2016] for a similar flow case over CD airfoil at 5 angle of attack, the pressure signals for a flow case where transition bubble exists near the TE on the suction side show very low frequency patterns which requires much longer time to be observed. In their studies, 40 flow-through time data were recorded and the flow has quite different behaviour in the so-called *quiet* and *intense* windows. This suggests that the current flow case may require much longer computational time to confirm whether the dip is due to the relatively short time compared with experiments. Otherwise, the porous-FWH formulation gives a good match with the experimental data.

On the other hand, the farfield PSD is also derived using Amiet's model with the correction considering back-scattering effects [Roger and Moreau, 2005, 2010]. In Amiet's model, the wall-pressure coherence, convection speed and spanwise correlation length are needed as inputs and these quantities are obtained from a chosen streamwise point $x \ c = 0\,95$ on both the suction and pressure sides close to the trailing edge.

In Amiet's model, the far-field acoustic PSD for a given observer location $\mathbf{x} = (x_1 \ x_2 \ x_3)$ (streamwise, crosswise, spanwise), and for a given angular frequency is computed via the following relation:

$$S_{pp\,Amiet}(\mathbf{x} \quad) \qquad \frac{kcx_2}{4 \ S_0^2}^{\ 2} \ \frac{L}{2} \ \mathcal{I} \ \ \overline{\ } \ k\frac{x_3}{S_0}^{\ 2} \ _{pp\,0} \ \ \overline{\ } \ k\frac{x_3}{S_0} \tag{4.7}$$

In this formulation, only parallel gusts to the scattering edge are considered; $k = \quad c_0$ is the acoustic wavenumber, u_c the convection speed of the turbulent structures in the boundary layer assimilated to gusts, S_0 with $S_0^2 = x_1^2 + \ ^2(x_2^2 + x_3^2)$ is the convection-corrected far-field observer position, and $\mathcal{I}$ is the analytical radiation integral that involves the aerodynamic response of a flat plate to the incident pressure gust, including the back-scattering effect from the leading edge (see [Roger and Moreau, 2005, 2010] for details). The overbar denotes quantities that are made dimensionless by the half-chord length $c \ 2$. $_{pp\,0}$ is the streamwise-integrated incident wall-pressure wavenumber-frequency spectrum for frozen turbulence, which can be approximated as follows (see Roger and Moreau [Roger and Moreau, 2005] for details):

$$_{pp\,0} \ \ \overline{\ } \ k\frac{x_3}{S_0} \qquad \overline{\ _{pp}(\ \ )}\, l_z \qquad k\frac{x_3}{S_0} \tag{4.8}$$

where l_z is the spanwise correlation length near the trailing edge, which can be calculated from the coherence function by

$$l_z \quad k\frac{x_3}{S_0} \quad = \quad {}_0 \quad \overline{{}^2(\quad z \quad)}\cos \quad k\frac{x_3}{S_0} \quad d(\quad z) \tag{4.9}$$

In Fig. 4.30, a comparison is made using Amiet's analogy between the untripped and tripped airfoil. In both cases, Amiet's analogy gives a good overall prediction on the farfield noise, at least for the given observer location. For the untripped airfoil, Amiet's prediction shows a dip around 1.5-3 KHz which is thought to be due to the weaker amplitude of pressure fluctuations shown in Fig. 4.13(b). Moreover, in Amiet's model for the untripped case, the streamwise location of the representative point near the trailing edge may not be as well defined as in the tripped case. Because in Amiet's model, a well developed turbulent boundary layer is assumed yet in the untripped DNS, the laminar to turbulence transition is predicted just before the trailing edge. On the tripped airfoil, an over-prediction above 3 kHz exists. This is due to the fact that l_z is overpredicted at high frequencies because the coherence does not completely drop to zero with the domain and the small remaining coherence level adds up in the integration.

4.5 Conclusion

A DNS of the untripped NACA6512-63 airfoil in a narrow stream was performed including installation effects at a high Reynolds number based on the airfoil chord length of 1.5 10^5. Airfoil surface, porous FWH surface and boundary layer volume around the airfoil were recorded for 7 flow-through times based on the airfoil chord and reference velocity for a sampling frequency of 47 kHz after the flow is statistically steady. A flapping and separated boundary layer at the trailing edge previously observed in experiments [Winkler and Carolus, 2009] was captured which led to an extra noise source compared with a tripped case previously simulated where an attached turbulent boundary layer was present [Winkler *et al.*, 2012]. The results are systematically compared with the tripped airfoil DNS [Winkler *et al.*, 2012], available LES data base [Winkler *et al.*, 2009] and experimental results [Winkler and Carolus, 2009]. Compared to the previous LES simulations [Winkler *et al.*, 2009], improved resolution both in space and time was achieved which enables a more detailed discussion on flow from the noise sources regions. Both porous and solid surface FWH formulations were employed for this untripped case for deducing the farfield noise and compared with the tripped DNS and the available experimental data .

For the hydrodynamic field, although it is a difficult case to simulate because of the narrow stream from the wind-tunnel jet, due to the proper sets of boundary conditions chosen for the untripped airfoil, the mean installation is generally well captured for such a flow case when compared with experimental data. The comparison of the mean and RMS values with LES and experimental results supports the conclusion made by Istvan *et al.* [2017]: the transition location is very sensitive to the background turbulence level. Also, the higher order of the present numerical scheme gives generally a higher mean pressure RMS peak at transition locations near LE than the previous lower-order LES. As the current airfoil is immersed in a narrow stream, although the mean installation effects are considered in the simulation, the unsteady effects from the interaction from the jet shear layer and the airfoil can have effects on the transition process and therefore on the airfoil flow topology. This aspect however, needs much more numerical resources to be confirmed.

The wall-pressure spectra at TE show that the flapping shear layer gives higher wall-pressure fluctuations on both sides of the airfoil compared with the tripped case. The spanwise correlation length becomes bigger in the low frequency range even on the pressure side.

The influence on the flow topology from the Kutta condition is significant when the flow on the pressure side of the untripped airfoil is compared with the tripped airfoil. It is demonstrated from multiple aspects in this study that the flapping shear layer at the TE on the suction side of the untripped airfoil has changed the flow topology on the pressure side. Larger structures at the TE on the pressure side are formed due to the flapping shear layer and such an influence has even modified the transition location at LE.

For the acoustic field, the porous FWH surface shows a better agreement with experimental data for the untripped case. A dip around 1 kHz in the farfield noise from the DNS may require much longer time signals to be filled. Amiet's model was also used for both the untripped and tripped airfoil to predict the farfield noise. It gives a good overall prediction for both the untripped and tripped cases.

Compared with a similar flow case [Deniau *et al.*, 2011] ($Re_c = 6\ 5 \quad 10^5$ and $Ma = 0\ 17$) using compressible LES on a thick and cambered NACA651210 airfoil, where the flow also transitions near the trailing edge on the suction side and turbulent on the pressure side, both the current DNS of the untripped airfoil and the NACA651210 airfoil shows an extra noise radiation from the late transition of the suction side flow close to the trailing edge. However, no frequency shift mentioned in [Deniau *et al.*, 2011] is observed for the current untripped NACA651263 airfoil for the far-field noise prediction. This can related to the

higher order explicit temporal scheme which guarantees the accuracy of the noise source computation.

CHAPTER 5

DNS of CD Airfoil at 8 AoA

As mentioned in *Chapter 2*, the CD airfoil at 8 AoA is an excellent case for airfoil noise study as the most extensive database available has been established both from experiments and simulations during the last decades. However, due to the constraints from the high Reynolds number and the low Mach number, no DNS has been achieved before using a traditional Navier-Stokes solver for this case. The present study is therefore the first attempt at computing the flow field around the airfoil and the near field noise at the same time using such an approach. In this way, the noise sources purely from the airfoil can be obtained, which can lead to a better understanding of the noise generation mechanism.

5.1 Numerical Setup

Similar to the previous NACA6512-63 cases, in order to account for the installation effects, firstly a 2D RANS computation of the flow around the airfoil was conducted, taking into account the complete nozzle shape and geometrical configuration that were used in the experiments (Fig. 5.1(a)). Considering the low Mach number in the experiments, incompressible flow solutions were used in RANS. The nozzle outlet velocity profile was known from hot-wire measurements and this velocity data was used to define the steady inflow conditions to the RANS domain.

The k SST model was found to predict better global behaviour considering the velocity and turbulence kinetic energy profiles when the results are systematically compared with experimental data. In a second step, a truncated domain comprising 6 blocks as shown by the black lines in Fig. 5.1(a) was used for the DNS solver. The initial field in the DNS is directly interpolated from the RANS solution on the DNS grid as shown in Fig. 5.1(b). The velocity profiles for the inlets of the DNS domain come from the RANS that mimic the influence of the wind tunnel on the flow field around the airfoil [Christophe *et al.*, 2009; Moreau *et al.*, 2009; Wang *et al.*, 2009; Winkler *et al.*, 2009]. In particular, it accounts for the mean effects of the flow deflection. As also mentioned by [Deniau *et al.*, 2011] using a similar procedure for a LES on a NACA651210 airfoil, it should be noted that the truncated DNS domain boundaries are made so that firstly these boundaries do not touch the shear layer from the wind tunnel exit to exclude extra computational efforts to resolve these shear layers; secondly, the velocity vectors from RANS are checked so that these

vectors are real inlets to the DNS domain to avoid possible recirculations or outflow for those boundaries in the DNS; and thirdly and most importantly, these domain boundaries should be far enough from the airfoil to allow the boundary condition to damp both turbulent structures and acoustic waves efficiently to avoid possible spurious reflections that might compromise the acoustic field.

As the CD airfoil has round LE and TE, an O-grid is used around the airfoil and the refinement in the boundary layer is carefully done according to the known data from experiment. The grid transition from TE to near wake is realized so that the skewness is well controlled and the maximum skewness is smaller than 0.2. In the wake region, the refinement is centered along the wake deviation line which is known from velocity profiles by hot-wire (HW) measurements and particle image velocimetry (PIV) measurements. These details are shown in Fig. 5.2. In the spanwise direction, 96 Fourier modes are used with 100% de-aliasing, which corresponds to 194 collocation points in physical space. This number of points was found to be sufficient to resolve down to the Kolmogorov scale for a similar flow case [Winkler *et al.*, 2012]. These points are distributed over a spanwise width L_{span} of 0.12 chord length. This length was determined to be sufficient to resolve all turbulent lengthscales in the flow field by previous incompressible studies [Christophe, 2011; Christophe *et al.*, 2008, 2009; Wang *et al.*, 2009] and compressible studies [Sanjosé *et al.*, 2011]. The total number of grid points is 345 10^6.

Unphysical numerical reflections at the computational boundaries are avoided by the choice of appropriate boundary conditions. An integral characteristic boundary condition (ICBC) is used on the C shape contour inlet (see [Jones, 2008] for details). To damp the non-linear disturbances caused by convected turbulence out of the domain, a zonal characteristic boundary condition (ZCBC) is applied in the wake [Sandberg and Sandham, 2006]. At the outlet, minor reflections can pollute the dilation field and then finally change the loading on the airfoil. 50 streamwise points are used as ZCBC in this case which have been found to be sufficient for this case. At the block interfaces characteristic interface conditions are used to avoid spurious oscillations due to discontinuities in the grid metrics [Kim and Lee, 2003]. At the two 5-block junction points above and under the TE shown in Fig. 5.27(b), the flow quantities are averaged. Finally, a hard-wall adiabatic, no-slip condition is applied on the airfoil surface.

While the experimental [Moreau *et al.*, 2006b; Neal, 2010] and previous incompressible LES [Christophe, 2011; Christophe *et al.*, 2008, 2009; Wang *et al.*, 2009] conditions were $Re_c = 150\ 000$, and $M = 0\ 05$, the DNS is conducted (due to constraints in computational resources) at $Re_c = 150\ 000$ and $M = 0\ 25$. The compressibility effects were firstly checked

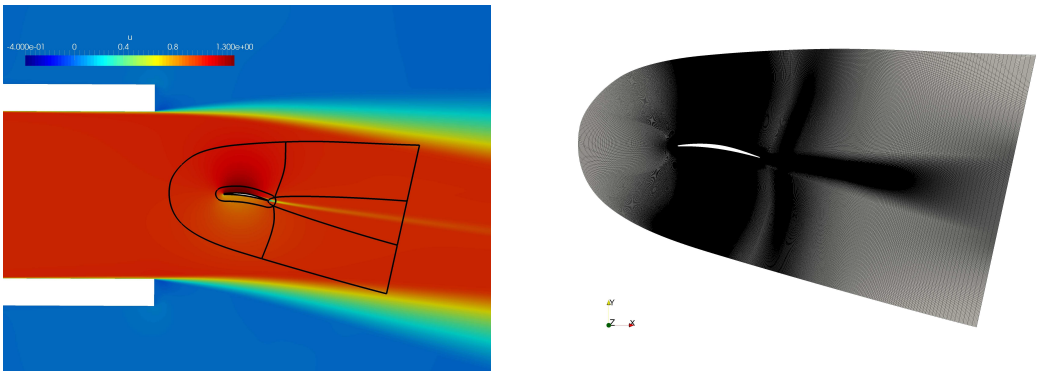

(a) (b)

Figure 5.1 (a) Wind-tunnel setup for initial RANS computations and the DNS computational domain. (b) Grid in the truncated domain, extracted from the full wind-tunnel setup.

in RANS which proved to be weak. Results obtained for flow cases at the same Reynolds number and similar Mach number [Winkler *et al.*, 2012] using the same code and from a DNS using the LBM [Sanjosé *et al.*, 2011] indicate that the difference in Mach number is practically irrelevant and the DNS simulation data can be scaled directly to the reference conditions of the experiment and LES simulation. This was also consistently observed in the context of acoustic predictions for broadband noise except when tonal noise was present. Following the past study, this approach is then taken for the current DNS.

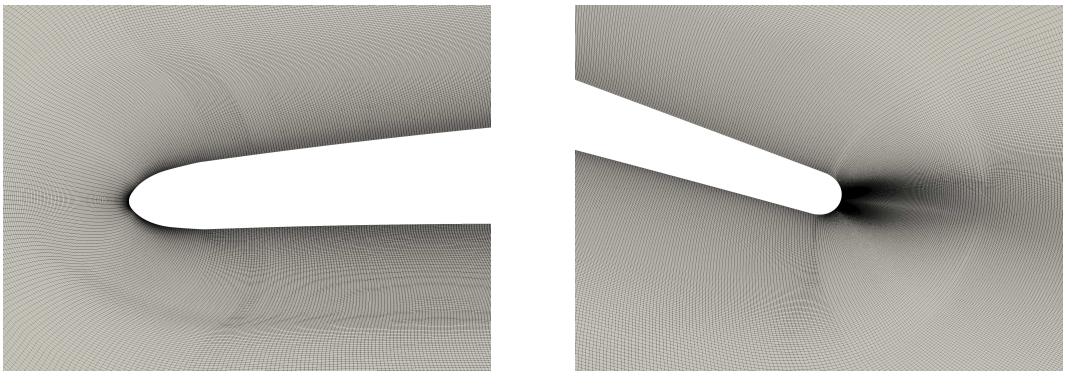

(a) (b)

Figure 5.2 DNS mesh details: (a)LE; (b)TE and near wake.

5.2 Hydrodynamic Field

5.2.1 Grid Resolution

The resolution of the DNS case is checked before further processing is performed. The time-averaged grid spacing in wall-units (x^+, y^+ and z^+) is shown in Figs. 5.3(a)-5.3(c). x^+ and y^+ values are also averaged along the span. The values compare well with data found to be adequate in previous airfoil DNS studies [Jones *et al.*, 2008; Sandberg and Sandham, 2008; Winkler *et al.*, 2012].

In addition, the proper decay of the power-spectral density (PSD) of the tubulent kinetic energy (TKE) is checked as a function of the number of spanwise spectral points N_{mode}. Two points in the boundary layer on the suction side very close to the trailing-edge where the flow is fully turbulent and attached were chosen as monitor points. Figures 5.4(a) and 5.4(b) show the spectra for the TKE for these 2 points. All spectra drop off by several orders of magnitude, and the dissipation range is also resolved properly. Here, the Kolmogorov lengthscale [Pope, 2000], has been computed as

$$= \quad \frac{3}{} \quad ^{1\,4} \qquad \text{with} \quad = 2 \quad s_{ij}s_{ij} \quad \text{and} \; s_{ij} = \frac{1}{2} \quad \frac{u_i}{x_j} + \frac{u_j}{x_i} \tag{5.1}$$

where is the dissipation rate of turbulent kinetic energy, and s_{ij} is the fluctuating rate of strain. The spanwise wavenumber k_3 has been calculated by

$$k_3 = \frac{2 \;\; N_{mode}}{L_{span}} \tag{5.2}$$

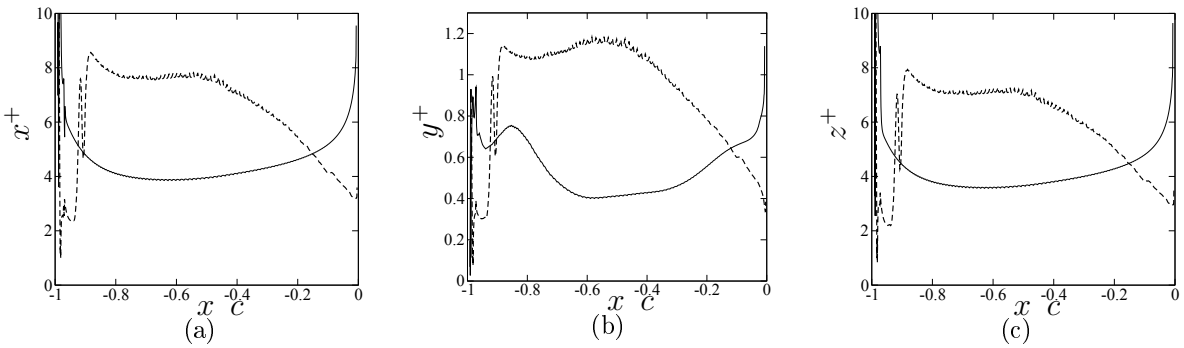

Figure 5.3 DNS grid resolution around the CD airfoil (---- suction side; —— pressure side).

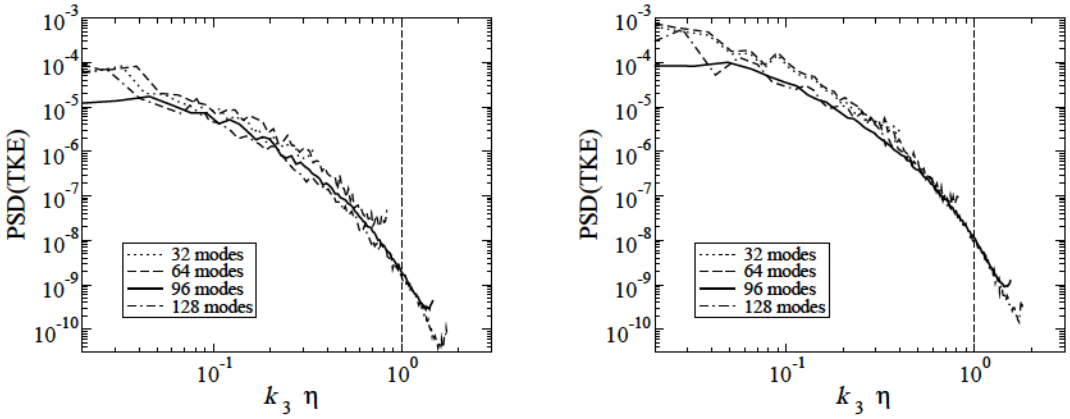

Figure 5.4 Time-averaged spanwise spectra of turbulent kinetic energy of monitor points in the boundary layers on the suction side around $x/c = 0.98$.

As indicated by the vertical dotted lines in Figs. 5.4(a) and 5.4(b), 96 modes are sufficient to resolve the smallest scales in the flow. Hence, 96 modes were used for this DNS study.

Furthermore, the mean wall normal profiles of the TKE budgets are shown together with the balance value in Fig. 5.5. The energy budgets terms are normalized by a density weighted factor of $Re_0\rho^2 u_\tau^4/T$, where T is the temperature. The TKE budgets terms in the Fig. 5.5 are defined as:

$$< \sigma, \overline{\boldsymbol{S}} >_F \;:=\; trace(\sigma\overline{\boldsymbol{S}}) \quad \text{(Turbulence production)}, \tag{5.3a}$$

$$\nabla\cdot\boldsymbol{\chi} \;:=\; \frac{\nabla\cdot\overline{(\rho\boldsymbol{u}''\boldsymbol{u}''^2)}}{2} \quad \text{(Triple momentum transport)}, \tag{5.3b}$$

$$\nabla\cdot\boldsymbol{c}_{\boldsymbol{\tau}-\boldsymbol{u}} \;:=\; \nabla\cdot\overline{\boldsymbol{\tau}''\cdot\boldsymbol{u}''} \quad \text{(Viscous transport)}, \tag{5.3c}$$

$$\varepsilon \;:=\; \overline{trace(\boldsymbol{\tau}''(\nabla\boldsymbol{u}'')^T)} \quad \text{(Dissipation)}, \tag{5.3d}$$

$$\vartheta \;:=\; \overline{\boldsymbol{u}''\cdot\nabla\cdot p'} \quad \text{(Pressure transport)}. \tag{5.3e}$$

In equation (5.3), σ and $\boldsymbol{\tau}$ denote the Favre stress and viscous stress tensor respectively. $\boldsymbol{S}$ is the symmetric shear stress tensor. $\widetilde{\bullet}$ stands for density averaged Favre-averaged terms, $\bullet''$ for the fluctuation around Favre-averaged quantities and the overline —— represents the mean value in time. The three chosen locations are at 18%, 40% and 92% of the airfoil chord. In general, the turbulence production and dissipation terms are the dominant terms which drive the TKE distribution, except for in the vicinity of the wall. The difference for these zones, which undergo different mean pressure gradients, will be discussed later in *Section 5.5*. The balance value, which is the sum of the TKE budget terms, is very close to 0 (maximum absolute value around 0.004) for all locations which indicates that the

current DNS correctly resolves the dissipation range for those investigated regions across the boundary layer and the statistical averaging time is sufficiently long for these statistics that are up to 3^{rd} order.

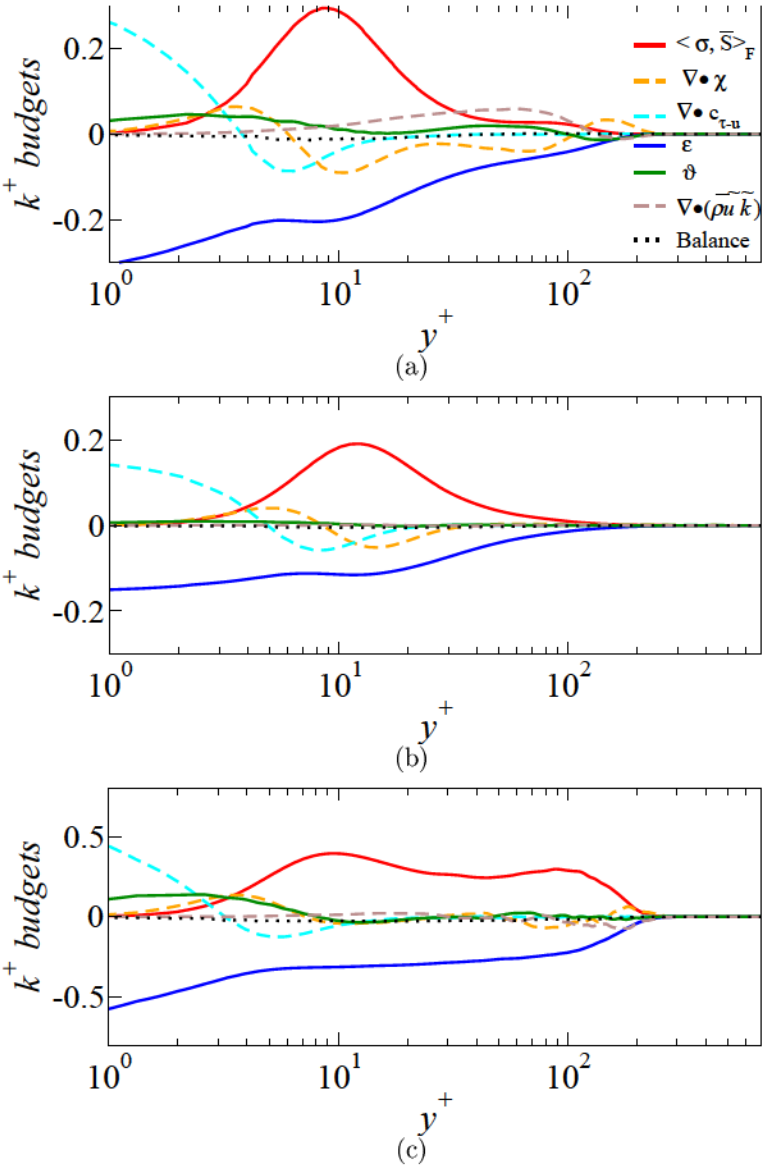

Figure 5.5 Wall normal profiles of TKE budgets. (a) $x/c = -0.82$; (b) $x/c = 0.6$ and (c) $x/c = -0.02$.

5.2.2 Mean Flow Field

To first check if the installation effects are properly accounted for [Moreau *et al.*, 2003], the mean static pressure distribution from the DNS run is compared with available wind-tunnel measurements, RANS simulation and previous LBM results [Sanjosé *et al.*, 2011].

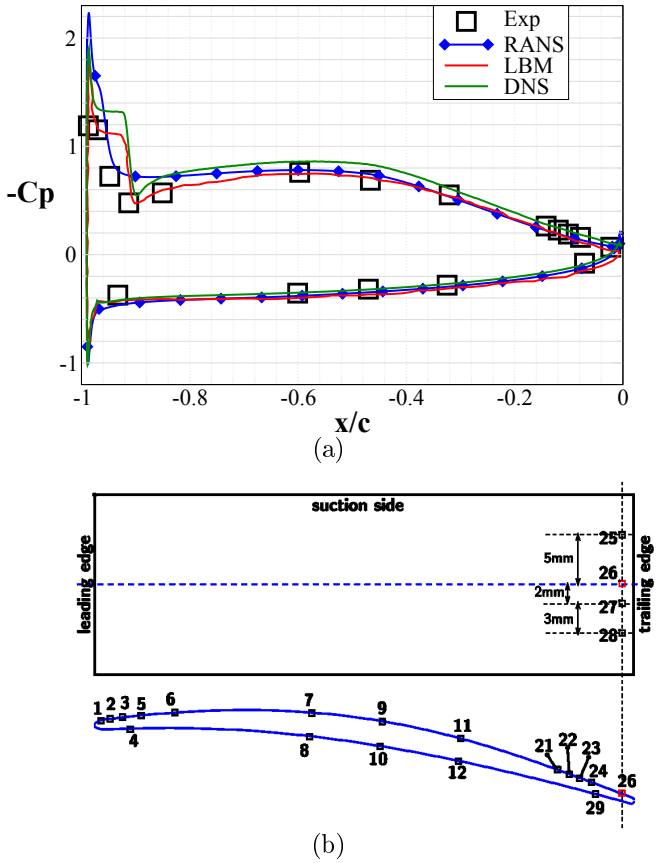

Figure 5.6 (a) Static lift distribution on the CD airfoil from experiment, RANS (k SST), LBM [Sanjosé *et al.*, 2011] and DNS; (b) Remote microphone probes (RMP) locations for the CD airfoil mock-up at ECL.

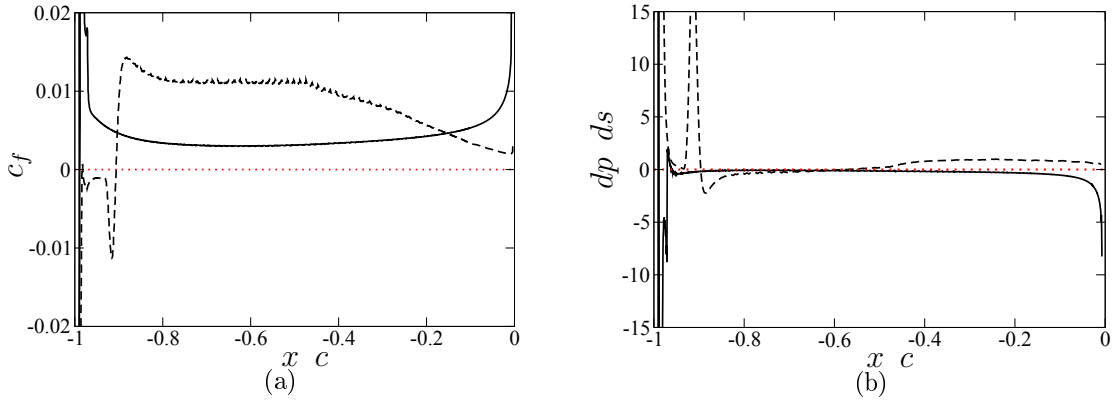

Figure 5.7 (a) Mean skin friction coefficient over the airfoil; (b) mean pressure gradient over the airfoil (—— pressure side; ---- suction side).

Two sets of experiments have been selected: measurements performed at Michigan State University (MSU) [Moreau *et al.*, 2006b; Neal, 2010] and those more recently produced at Université de Sherbrooke [Padois *et al.*, 2015] in the newly designed anechoic wind tunnel

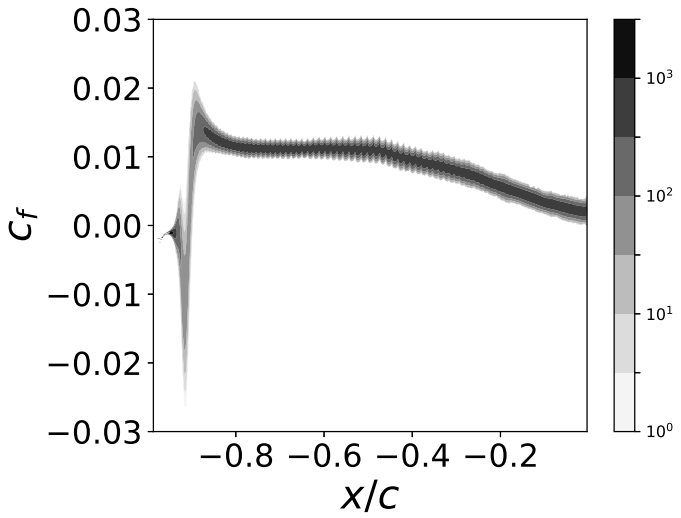

Figure 5.8 Iso-contours of the normalized c_f p.d.f. on the airfoil suction side using 7 levels exponentially distributed over the range 1 to 3000.

where a lower background turbulence intensity T_u can be achieved (T_u (0 3% 0 4%) according to the measurements) compared to the MSU data ($T_u = 0\ 5\%$).

As shown in Fig. 5.6(a), the current DNS result gives a good prediction of the distribution of the mean wall-pressure coefficient c_p defined in Eq. (4.3). However, minor differences exist. A slightly longer separation bubble is present in the current DNS, which does not account for the jet shear layers and the possible introduction of the free stream turbulence that are present in experiments [Istvan *et al.*, 2017].

Time averaged skin friction coefficient c_f on the airfoil is plotted in Fig. 5.7(a). It can be seen that the flow recirculation by separation on the suction side is around $x\ c = 0\ 9$. Similar to what has been realized before for the NACA6512-63 airfoil, the probability density functions (p.d.f.s) of c_f on the suction side is plotted in Fig. 5.8. Downstream of the separation bubble, c_f displays little variations which means the flow is rather steady in this case. The mean pressure gradient distribution is shown in Fig. 5.7(b). The flow over the airfoil suction side is submitted to a favorable pressure gradient (FPG) after the transition, then a zero pressure gradient (ZPG) around mid-chord and finally an adverse pressure gradient (APG) because of airfoil camber. Additionally, the dimensionless Clauser pressure-gradient parameter $_c$ [Clauser, 1956] is taken to quantify the distribution of the mean pressure gradients over the airfoil suction side:

$$_c = \frac{}{_w}\frac{dp}{ds} \tag{5.4}$$

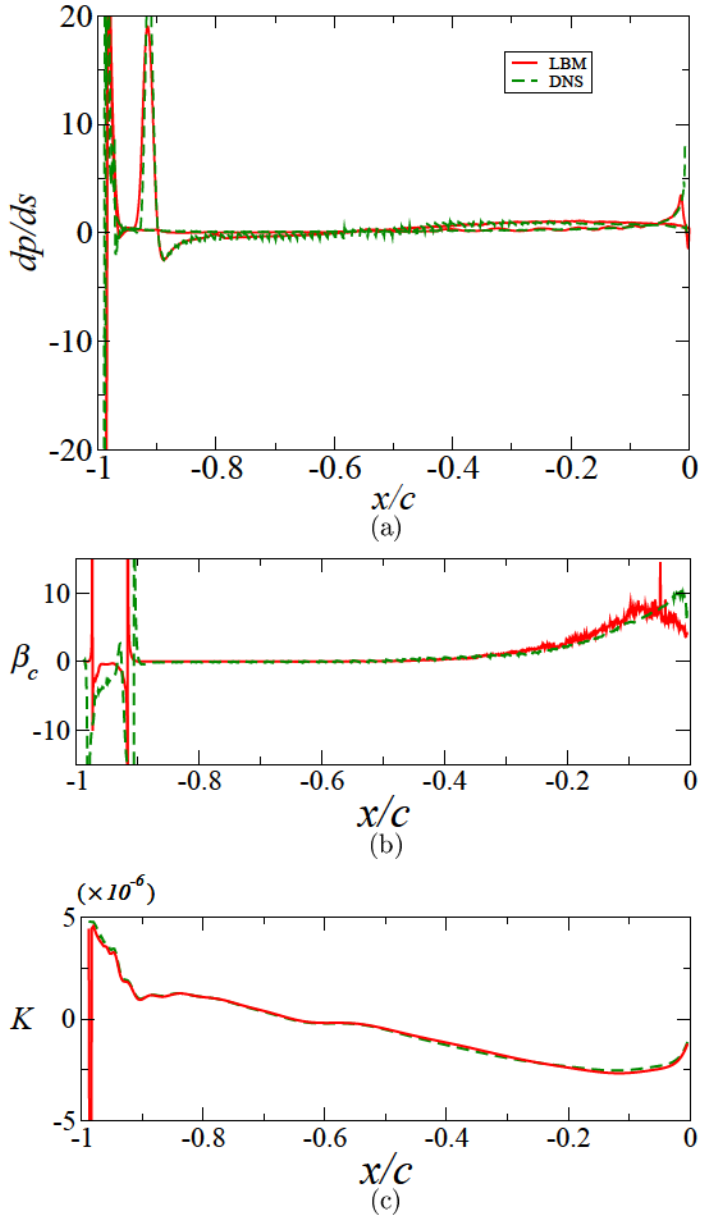

Figure 5.9 Comparisons between the current DNS and LBM [Sanjosé *et al.*, 2011] interpolated solutions on mean flow parameters (a) dp/ds, (b) β_c and (c) K.

where is the displacement thickness, $_w$ is the wall shear stress and $dp\ ds$ is the streamwise pressure gradient at the wall between two points on the surface of the airfoil suction side. The acceleration level is evaluated by the acceleration parameter K, defined as

$$K = \frac{dU_0}{U_0^2}\frac{dU_0}{ds} \tag{5.5}$$

where U_0 is the local free-stream velocity magnitude where the edge velocity is obtained from wall normal profiles and ds is the distance between two points on the surface of the airfoil suction side. It should be mentioned that in the original commonly used forms of $_c$ and K, the gradient terms are taken as the streamwise gradients $dp\ dx$ and $dU_0\ dx$. They are adapted to the airfoil case here with curvilinear forms $dU_0\ ds$ and $dp\ ds$. The $_c$ values near the TE are very similar to previously reported results from LES [Christophe *et al.*, 2014] on the same airfoil. The comparison of $dp\ ds$, $_c$ and K with the LBM solution [Sanjosé *et al.*, 2011] interpolated on the current DNS mesh is shown in Fig. 5.9. For these 3 mean flow parameter, the current DNS are very similar to the LBM solution which includes the entire jet nozzle geometry. This again proves that the current DNS has well reproduced the mean installation effects.

As a first check on the compressibility, the density weighted Favre-averaged velocity profiles from TE and near wake were extracted and compared to those extracted from Reynolds-averaged field. Fig. 5.10 shows the locations at sensor locations #24 and #26 and in the near wake with 5% and 7% chord distance to the TE. Other locations along the airfoil

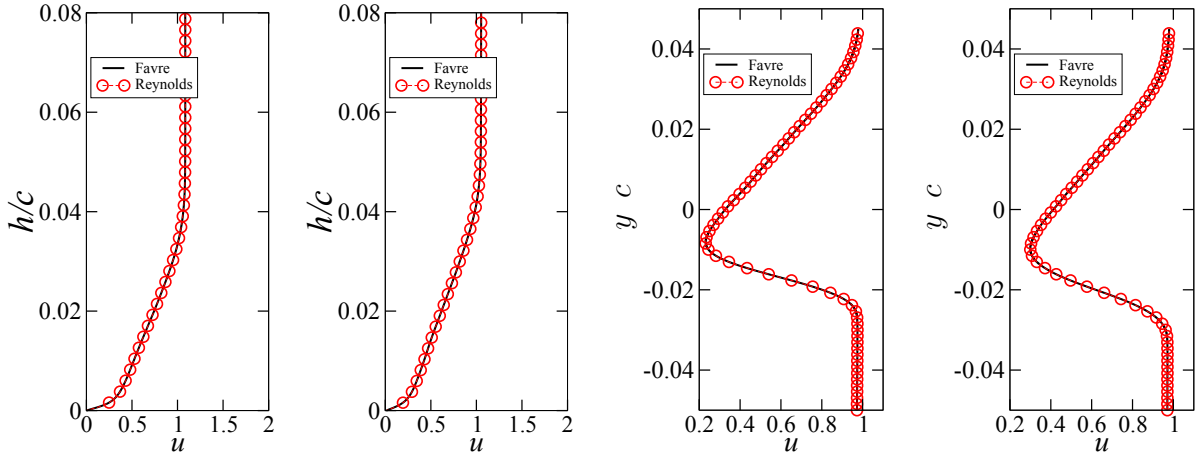

Figure 5.10 Comparison of velocity profiles extracted from Favre-averaged field and Reynolds-average field: (a) and (b) TE locations (Sensor #24 and Sensor #26); (c) and (d) near wake ($x\ c = 0\ 05$ and $x\ c = 0\ 07$).

have also been checked and no difference has been found between these two averaged fields. This indicates that the compressibility effects in this case is weak. This topic will be further proved afterwards from velocity gradient invariant analysis.

The velocity profiles are then compared with HW and PIV data from experiments and also with LBM data. In the experiment, the sensor locations for measuring the velocity profiles on the airfoil surface are illustrated in Fig. 5.6(b). For sensor locations #5 #9 #21 and #26 which represent the LE, mid chord and TE, the current DNS mean data gives a good match with the existing data sets as can be seen in Fig. 5.11. For these velocity profiles, u_t is tangential (to the airfoil surface) velocity component and u_e the edge velocity is the maximum value of u_t. h denotes the wall normal distance to the airfoil surface. The present recirculation bubble is slightly thicker than the previous DNS yielding a slightly thicker turbulent boundary layer after the recirculation bubble that triggers the transition to turbulence.

The velocity profiles in the near wake locations (Fig. 5.12) are coherent with the development of the boundary layer in Fig. 5.11. In general, the current DNS data gives an excellent match with the PIV data, which is expected as that data was acquired in the facility with the lowest T_u. Furthermore, the streamwise and vertical velocity fluctuations between the DNS and PIV data are also compared in Fig. 5.13. The vertical component shows an excellent match with PIV data. The streamwise component shows a slightly higher peak value than the PIV measurement. Yet overall, a good agreement is formed with the PIV data.

These results show that the current DNS gives a reliable hydrodynamic field which is the prerequisite to study the associated acoustics in the following sections.

5.2.3 Instantaneous Flow Field

The flow topology is shown by the iso-contours of the swirling strength criterion $_{ci}$ [Wu *et al.*, 2017b; Zhou *et al.*, 1999] and colored by the streamwise velocity component. The value of $_{ci}$ is chosen such that it is around 3% of its maximum value for the current flow data around the airfoil, as what has been used for the NACA6512-63 airfoil case. On the suction side, it can be seen that at the LE, spanwise coherent roller structures are generated due to a Kelvin-Helmholtz instability and secondary instabilities which finally lead to a short recirculation bubble that triggers the transition. The initially large structures become smaller around mid chord and then the flow further develops until the TE. Near the TE, the turbulent flow featuring hairpin structures from the suction side is mixed with the laminar flow from the pressure side in the near wake. The local Reynolds

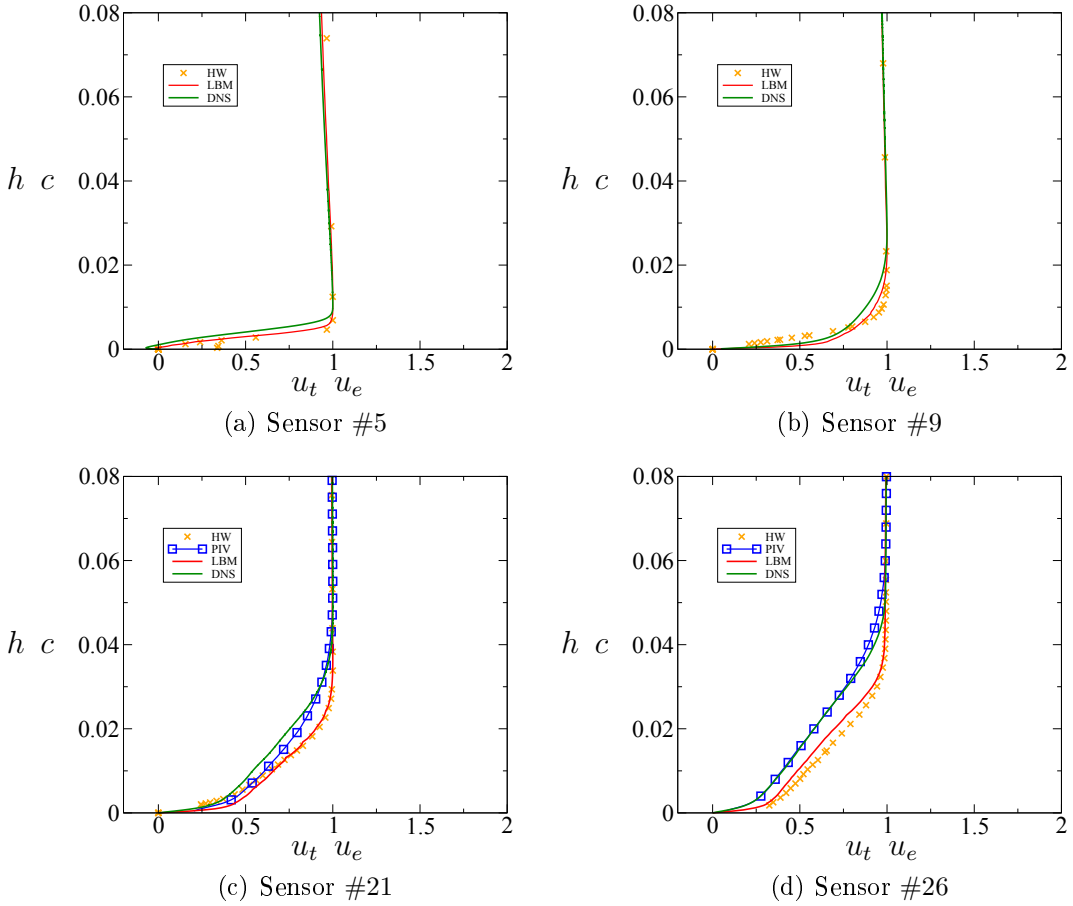

(a) Sensor #5 (b) Sensor #9

(c) Sensor #21 (d) Sensor #26

Figure 5.11 Comparison of boundary layer velocity profiles with experiments and LBM simulation [Sanjosé *et al.*, 2011].

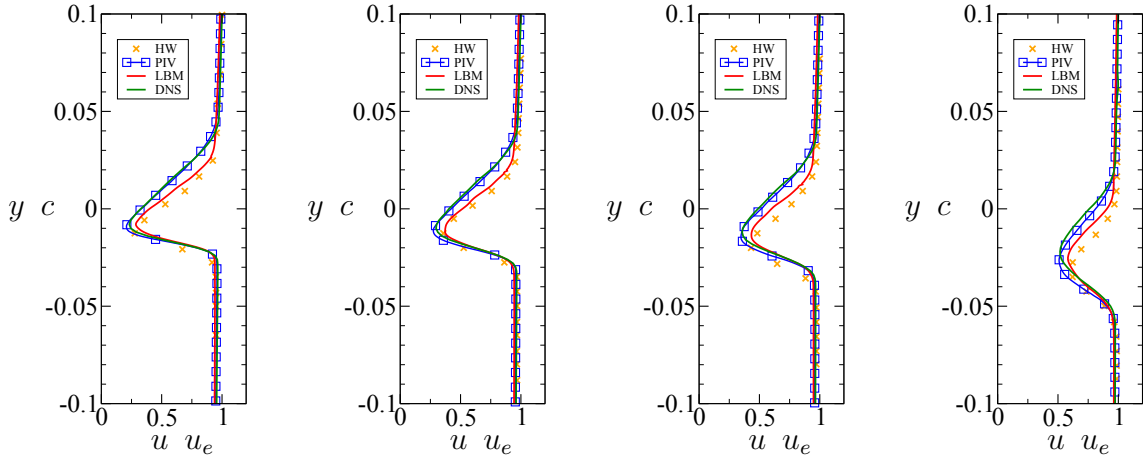

(a) $x\ c = 0\ 05$ (b) $x\ c = 0\ 07$ (c) $x\ c = 0\ 09$ (d) $x\ c = 0\ 16$

Figure 5.12 Comparison of near wake velocity profiles with experiments and LBM simulation [Sanjosé *et al.*, 2011].

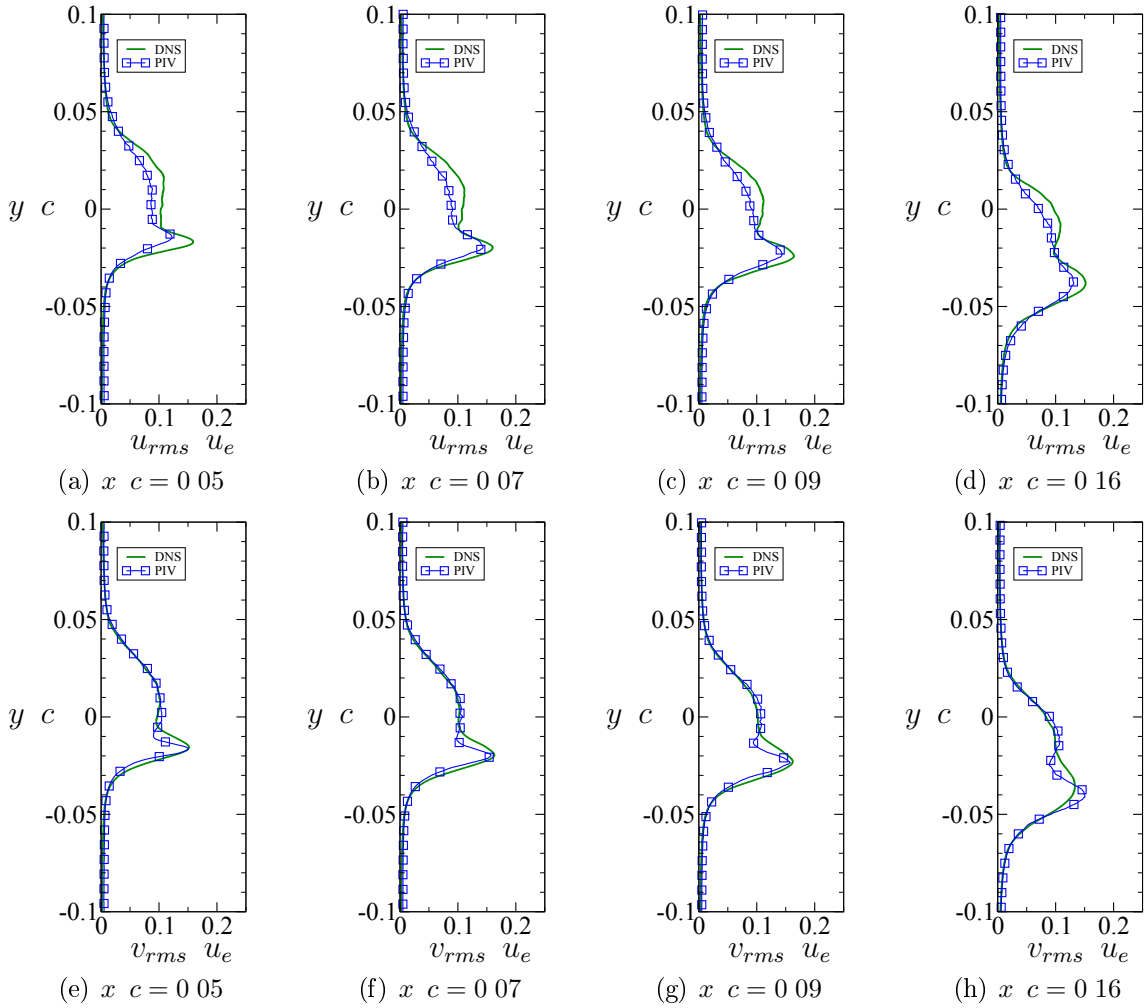

(a) $x\ c = 0\ 05$ (b) $x\ c = 0\ 07$ (c) $x\ c = 0\ 09$ (d) $x\ c = 0\ 16$

(e) $x\ c = 0\ 05$ (f) $x\ c = 0\ 07$ (g) $x\ c = 0\ 09$ (h) $x\ c = 0\ 16$

Figure 5.13 Comparison of near wake RMS velocity profiles with PIV measurements.

numbers based on the momentum thickness after the transition are Re 210 1206 with a shape factor, $H =$, range 1 51 2 14 where is the displacement thickness. On the pressure side, the laminar boundary layer stays attached, and rolls up at the TE, leading to a weak vortex shedding in the near wake. These basic flow features are qualitatively very similar to the DNS using LBM mentioned before by [Sanjosé *et al.*, 2011].

5.3 Wall Pressure Spectra, Correlation and Coherence

Pressure signals over the entire airfoil surface were recorded for 7 flow-through times at a sampling frequency of 78 kHz, based on airfoil chord length and the reference velocity, once the simulation was statistically steady.

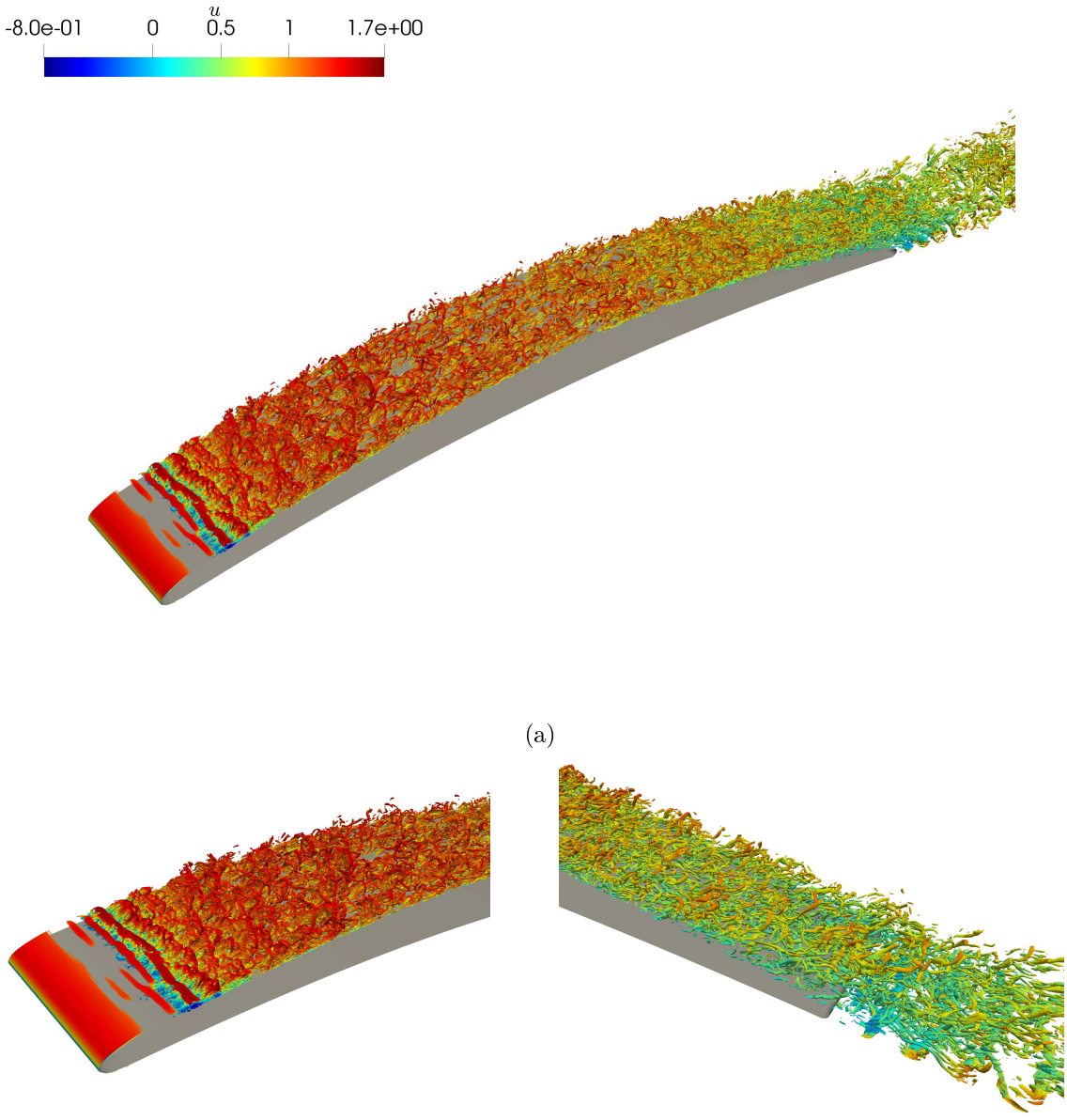

(a)

(b) (c)

Figure 5.14 Swirling strength criterion $_{ci} = 70$ iso-contours colored by streamwise velocity: (a) Aerofoil global view; (b) Zoom view at LE; (c) Zoom view at TE and near wake.

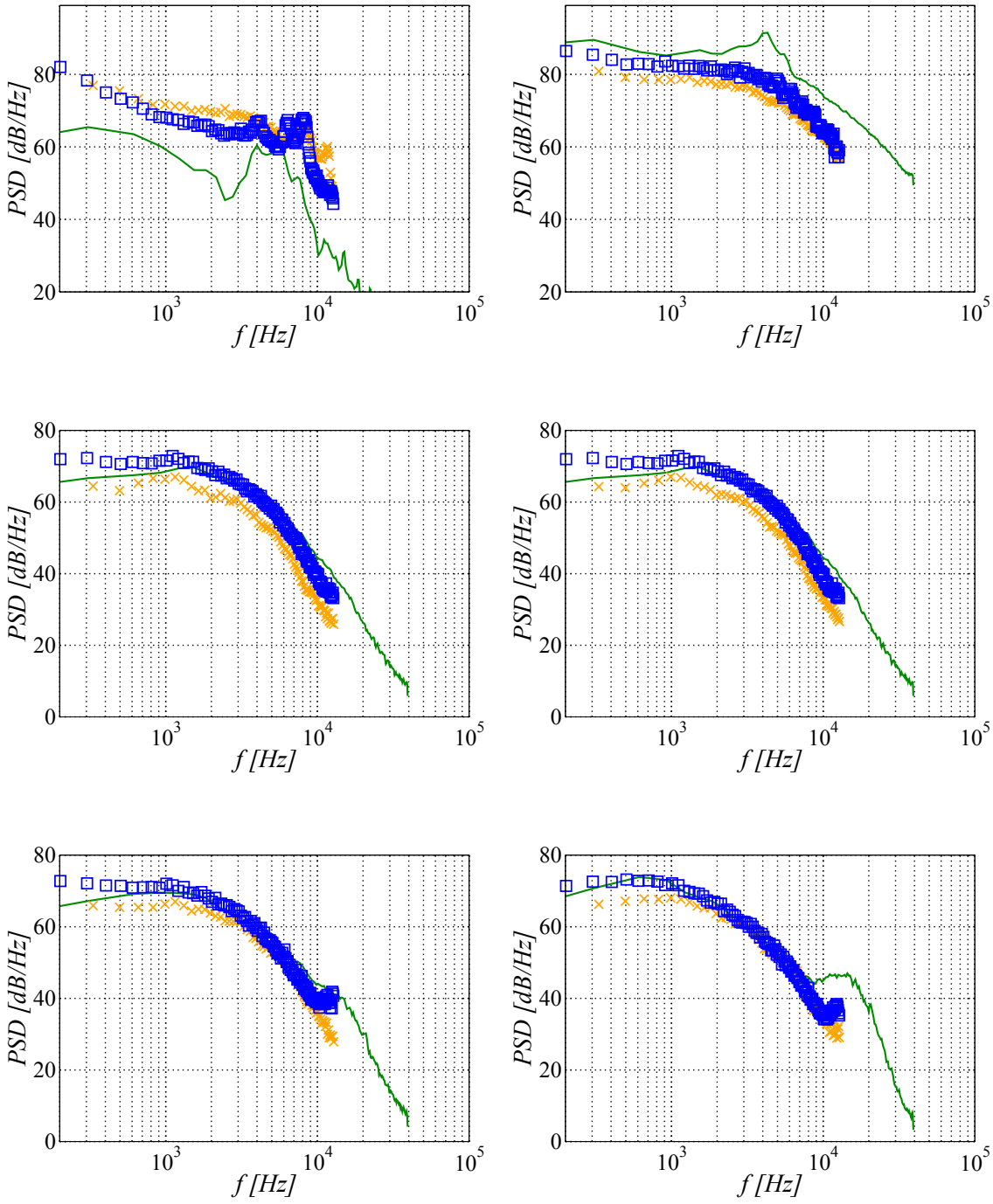

(e) Sensor #24 (f) Sensor #26

Figure 5.15 Spanwise-averaged wall-pressure spectra on the suction side for different sensor locations as shown in Fig. 5.6(b): , MSU measurements; , UdeS measurements; —— , DNS.

The PSD $_{pp}$ of the wall-pressure fluctuations $p = p \quad \overline{p}$ at a given angular frequency is obtained from the wall-pressure cross-spectral density $_{pp}(x\ z \quad x \quad z \quad)$ defined by

Eq. (4.4). The DNS data was scaled to obtain dimensional quantities. This was achieved by multiplying the dimensionless pressure from the simulation by ${}_0U_0^2$. These values correspond to the experimental conditions [Neal, 2010]. The spectra were averaged over all spanwise points. The suction side spectra for sensors #3 #5 #21 #22 #24 and #26 are shown in Fig. 5.15 and compared to the available experimental data respectively from MSU and UdeS. Sensors #3 and #5 represent respectively the locations inside the transition bubble and just after the reattachment as shown in Fig. 5.14(b). The spectral levels show a hump around 5000 Hz inside the separation and immediately following the reattachment as a result of laminar breakdown. For the TE sensors, the spectra exhibits very small variations as shown in Figs. 5.15(c) 5.15(e) for sensors #21 #22 and #24. The spectrum of sensor #26, which is the nearest to the TE, shows an extra hump at a higher frequency which is observed for the first time from a numerical approach for such a flow case. The spectrum from data at UdeS (blue squares in Fig. 5.15(f)) also shows such a hump in the high frequency range of the pressure sensors. The diffrence of PSDs between the DNS and the 2 sets of experiments is possibly due to the unsteady interaction between the shear layer and airfoil and background turbulence intensity. The latter, especially, as mentioned by [Istvan *et al.*, 2017] can have a significant influence on the transition triggered by a separation bubble on airfoil at moderate Reynolds numbers as in the current flow case. For sensors near TE, these three data sets have a very similar shape once the transition to turbulence has occured. The DNS results have an excellent agreement with the results from the newly produced UdeS experimental data. This is coherent with previous observations from the velocity profiles in Fig. 5.11 which suggest that the boundary layer at TE from the current DNS is very similar to the boundary layer from UdeS experiments. Previous numerical studies with different solvers [Christophe, 2011; Christophe *et al.*, 2008, 2009; Sanjosé *et al.*, 2011; Wang *et al.*, 2009] of the same flow condition on the CD airfoil and other studies on the NACA6512-63 airfoil [Winkler *et al.*, 2009, 2012] suggest that if the boundary conditions are properly set and that the transition is at the LE and furthermore the airfoil chord is relatively long compared to the transition bubble size, the turbulent boundary layer will show similar status for a same flow condition. This is the case for the comparison between the current DNS and UdeS measurements: although the transition process is not entirely the same, which can come from the possible pressure sensor influence around the transition region plus the shear layer interaction and the background turbulence as mentioned before is inevitable, the status of the developed turbulent boundary layer in the DNS and UdeS experiments are quite similar. The measurements from MSU however, seem to have a slightly different boundary layer along the whole chord, which again, is due to the different background turbulence level which can influence both the transition

[Istvan *et al.*, 2017] and the developed turbulence [Jiménez *et al.*, 2010; Wu and Moin, 2009]. Yet in general, these differences at the TE are small. This aspect, for TE noise sources, is critical.

The evolution of the spanwise and temporal scales can be identified by the space-time correlation of the wall-pressure fluctuation. In Fig. 5.16, this correlation is shown for 6 sensor locations as defined in Fig. 5.6(b). Near the transition region (Fig. 5.16(a)) a periodic pattern is observed in time while in space the signal is quite correlated due to the spanwise coherent rolling structures. At mid-chord (Figs. 5.16(b) and 5.16(c)), before the adverse pressure gradient zone, both the spanwise and temporal scales are small. A significant growth of the spanwise and temporal scales is seen for sensor locations further downstream due to the thickening of the boundary layer by the adverse pressure gradient as shown in Figs. 5.16(d)–5.16(f). The shapes of the isocontours are similar to those previous reference incompressible LES [Christophe, 2011; Wang *et al.*, 2009] except for lower contour levels which mainly comes from the improved spanwise resolution in the current DNS.

Another quantity that is of great importance in the simulation of turbulent flow is the spanwise coherence of the turbulence field. For the purpose of noise prediction, it represents the size of a source region which radiates independently from sources in neighboring regions in a statistical sense. It can be seen from Eqs. (2.2.2), (4.7)– (4.9), for Amiet's based noise models, the coherence level ^{2} directly determines the spanwise correlation length and thus the streamwise-integrated incident wall-pressure wavenumber-frequency spectrum and finally the predicted noise level. It has been pointed out in previous incompressible [Christophe, 2011; Christophe *et al.*, 2008, 2009; Wang *et al.*, 2009] and compressible [Sanjosé *et al.*, 2011] numerical studies of this airfoil at 8 angle of attack that the spanwise extent L_{span} should be at least 0 1c. For the current study, the spanwise extent was chosen to be 0 12c. The coherence (Eq. (4.5)) is shown in Fig. 5.17. Similar to the NACA6512-63 case, spectra were calculated for half the span size (z c (0 0 06)) for spanwise points 1 through 96, 2 through 97, etc. from the DNS. The resulting spectra were then averaged across the span. The plots shown in Fig. 5.17 demonstrate that the spanwise extent is sufficient to account for the flow development for such a flow case, for all streamwise locations from the separation bubble at the LE, to mid chord then finally to the turbulent boundary layer at the TE for most frequencies beyond 200 Hz. For lower frequencies, longer signals are required to attain better statistical convergence. The increase of coherence level in the high frequency range for sensors #24 and #26 is also observed. This is different compared with what has been observed by previous incompressible LES

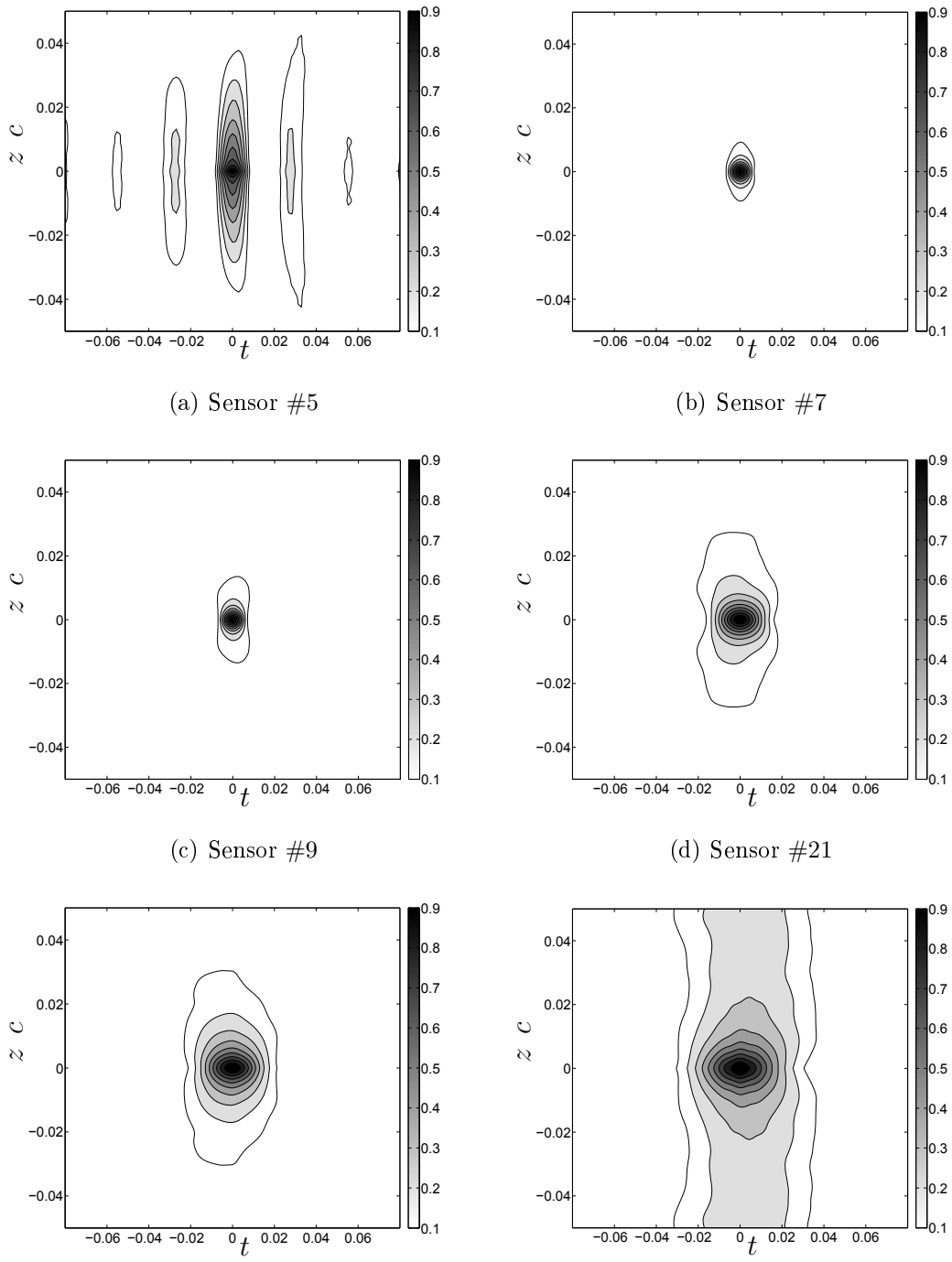

(a) Sensor #5

(b) Sensor #7

(c) Sensor #9

(d) Sensor #21

(e) Sensor #24

(f) Sensor #26

Figure 5.16 Contours of space-time correlation of the fluctuating pressure on the suction surface as a function of spanwise and temporal separations for different sensor locations as shown in Fig. 5.6(b).

[Christophe, 2011; Wang *et al.*, 2009]. On the one hand this comes from the cut-off frequency limitations of LES. On the other hand, this may indicate that the flow in the near

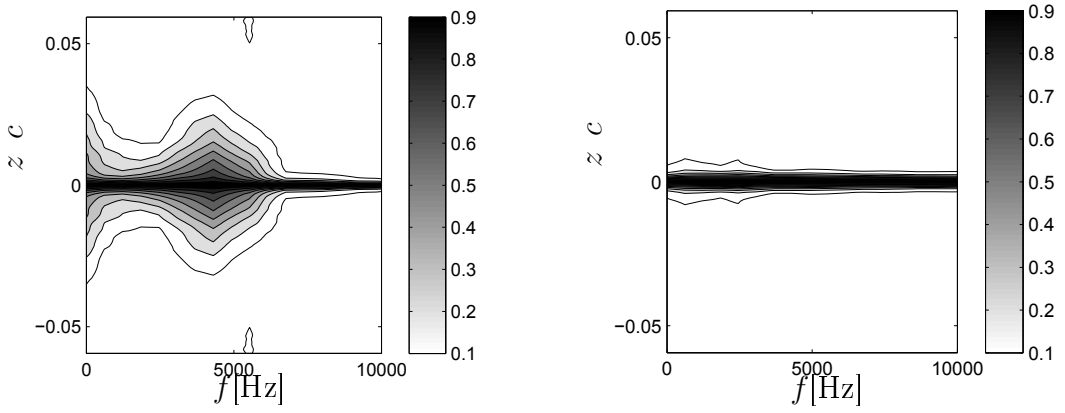

(a) Sensor #5

(b) Sensor #7

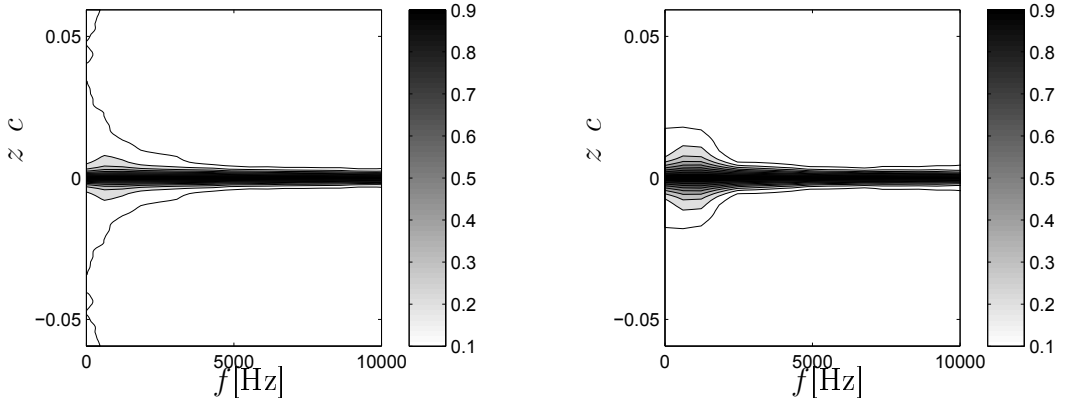

(c) Sensor #9

(d) Sensor #21

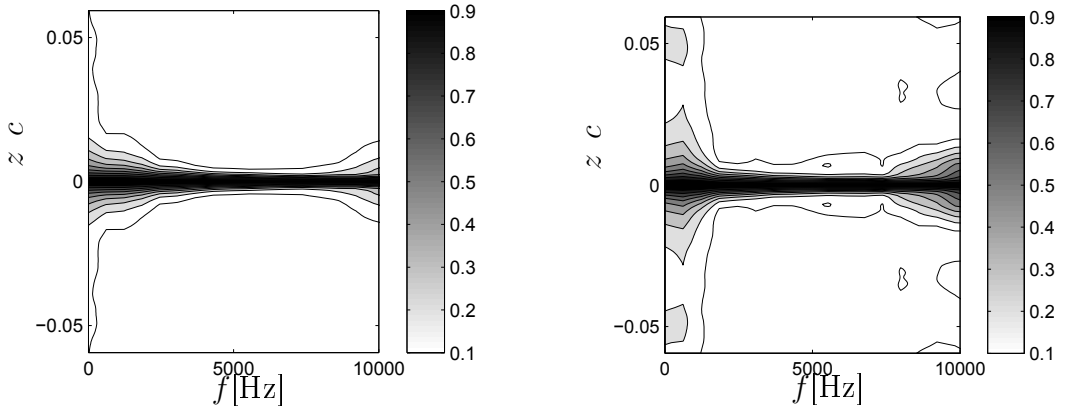

(e) Sensor #24

(f) Sensor #26

Figure 5.17 Spanwise coherence of fluctuating pressure on the suction surface for different sensor locations as shown in Fig. 5.6(b).

wake has influence on the pressure fluctuations at the TE in this frequency range as only the current DNS has the sufficient spatial (finer grid) and temporal (smaller timestep) resolution.

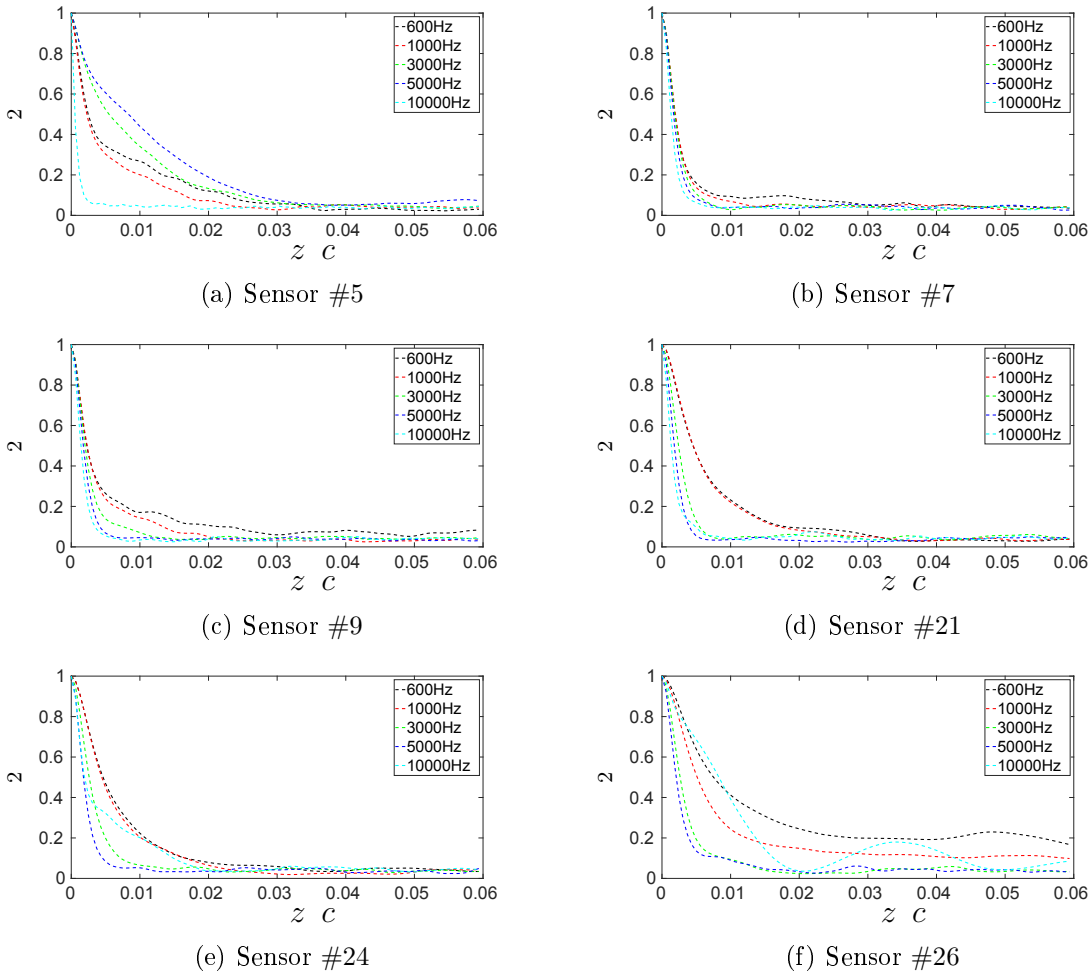

(a) Sensor #5

(b) Sensor #7

(c) Sensor #9

(d) Sensor #21

(e) Sensor #24

(f) Sensor #26

Figure 5.18 Spanwise coherence length of fluctuating pressure on the suction surface for different sensor locations as shown in Fig. 5.6(b).

The coherence level remains small after transition as shown in Figs. 5.18(a)–5.18(c). Figs. 5.18(d)–5.18(f) show that the increased spanwise correlation level near the TE is present both in the low and high frequency ranges. The low frequency range was observed before in previous incompressible LES simulations [Christophe, 2011; Christophe *et al.*, 2008, 2009; Wang *et al.*, 2009]. A high frequency correlation level increase for sensor #24 and sensor #26 however is also observed. This may indicate that the flow in the near wake has influence on the pressure fluctuations at the TE in the high frequency range.

The correlation length for different frequencies is shown in Fig. 5.18. Six frequencies are shown from 600 Hz to 10000 Hz. Their evolution of correlation length through sensor locations #5–#26 is quite interesting. At lowest chosen frequency 600 Hz, except for sensor #7, which is at mid-chord submitted to ZPG, the correlation length is relatively high for all sensors. At 1000 Hz, relatively smaller correlation length is observed at sensor

#7 and #9 around mid-chord, submitted to ZPG or mild APG. At 3000 Hz and 5000 Hz, except for sensor #5, which is the location inside the separation bubble at the LE, the correlation length exhibits an invariant character: it drops quickly after 0.01 chord length in the span for all sensors. For the highest frequency 10000 Hz, the increase of the correlation length for sensor #26 near the TE indicates that this phenomenon comes from the flow near TE, i.e., the near wake.

In Figs. 5.19(a) and 5.19(b), a comparison of spanwise coherence is made between experimental data (at ECL) and the data from the current DNS, at $x\ c =\ 0\ 02$ (sensor #26 location) for a spanwise distance of $z\ c = 0\ 02$ and $z\ c = 0\ 04$ (in the available frequency range in experiments). The current DNS shows generally a good prediction for these 2 spanwise separation distance in the frequency range of 700 2000 Hz. For lower frequencies, as argued by Christophe [2011], it is very sensitive to the sample size which requires longer signal to be confirmed. For frequencies over 2000 Hz for a spanwise separation of $z\ c = 0\ 02$, an extra hump is observed in the DNS.

5.4 Wall Pressure Filtering

A recently proposed technique base on wavenumber-frequency spectra is employed in the current study to further understand the wall-pressure fluctuations, which is one major noise source from the current DNS. Such a technique has been proposed by Arguillat and Ricot [Arguillat *et al.*, 2010] when they conducted direct measurements of the wavenumber-frequency spectra of the wall-pressure fluctuations beneath a turbulent plane channel flow using a rotative microphone array as shown in Fig. 5.20. The measurement array is obtained by placing 63 remote microphone probes along the diameter of a disk (Fig. 5.20(b)). The distance in between the holes shown in Fig. 5.20(b) ranges from $r = 2mm$ to $r = 8mm$. The measurement consists of simultaneous recording of the pressure field for a certain period of time $T_{recording}$. Then the disk was rotated by an angle of 2 9 for another set of measurement for the same time period $T_{recording}$. Such a process was repeated until the disk was rotated 360 around the center. In this way, a round "mesh" of 63 63 points with same length of pressure signal for each point was established for the wavenumber-frequency spectra analysis. Later, such a setup in the same facility (anechoic chamber with free-stream turbulence intensity T_u 1% at École Centrale de Lyon) was further used to study the aerodynamic and aeroacoustic contribution from wall-pressure fluctuations with different flow conditions including FPG, ZPG and APG [Salze *et al.*, 2014, 2015a,b]. The classical form of the wavenumber-frequency spectrum of the fluctuating wall-pressure $_{pp}(k_x\ k_y\ )$ is illustrated in Fig. 5.21(a). At a given frequency, the

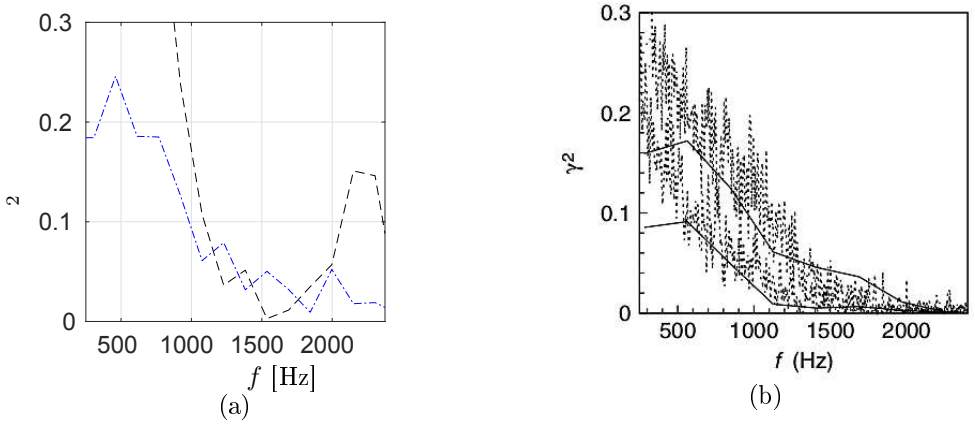

(a) (b)

Figure 5.19 Coherence between 2 spanwise points of distance $z\ c = 0\ 02$ and $z\ c = 0\ 04$ at $x\ c = 0\ 02$ (98% chord): (a) Current DNS $x\ c = 0\ 02$. – – – $z\ c = 0\ 02$ and — — $z\ c = 0\ 04$; (b) Results from —— incompressible LES [Wang *et al.*, 2009] and ····· ECL experiment.

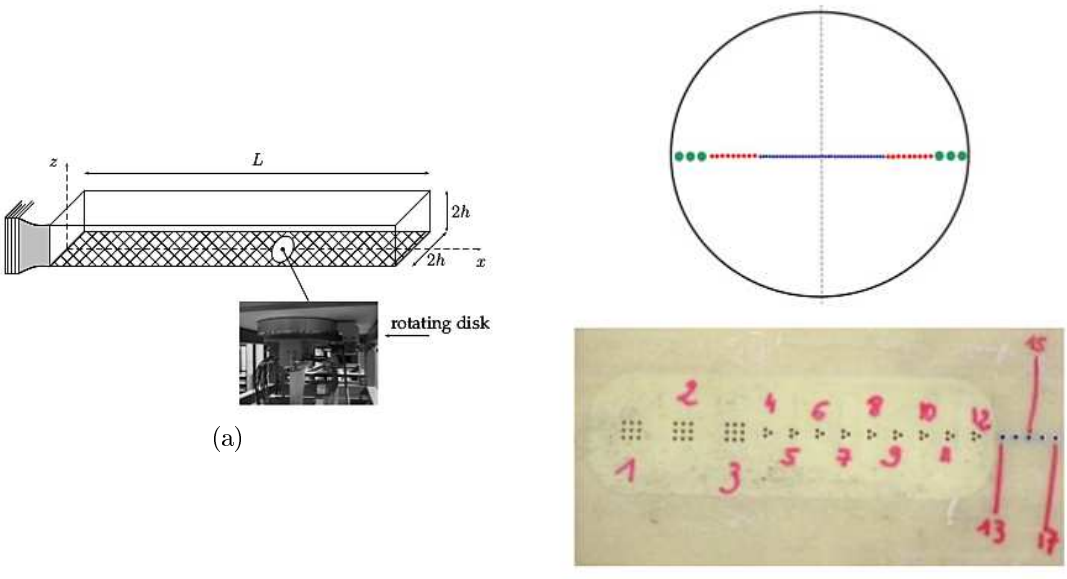

(a) (b)

Figure 5.20 Experimental setup for measuring the wavenumber-frequency spectra by Arguillat and Ricot [Arguillat *et al.*, 2010]: (a) test channel and (b) zoom view of the rotative remote microphone array disk.

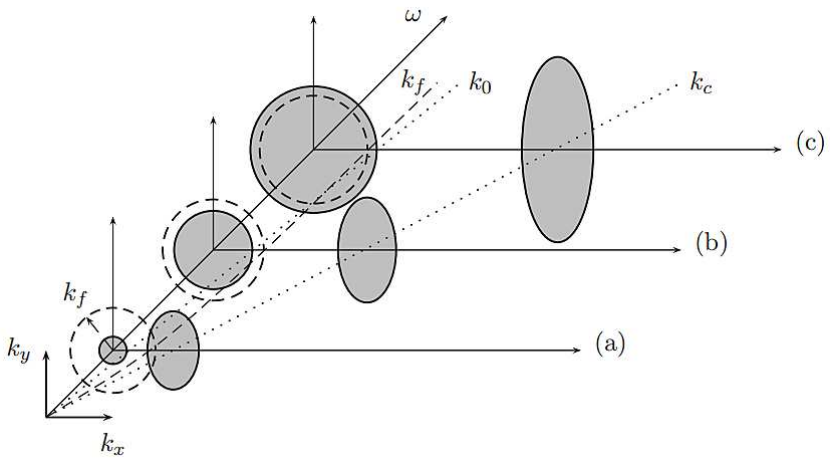

(a)

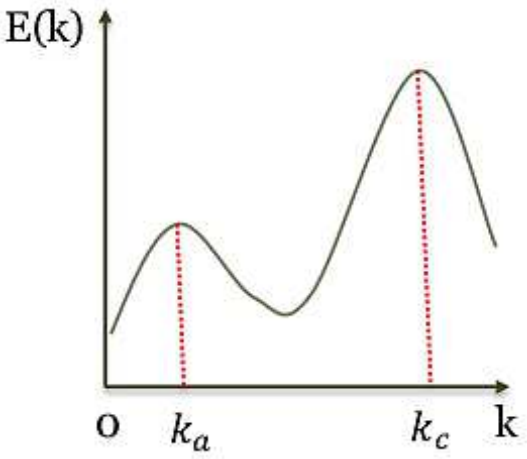

(b)

Figure 5.21 (a) Wall-pressure spectrum of a low Mach number turbulent boundary layer in the (k_x k_y) plane for a given frequency [Arguillat *et al.*, 2010]; (b) illustration of energy distribution from aerodynamic and aeroacoustic part.

energy distribution is illustrated in Fig. 5.21(b). As can be seen from these figures, $_{pp}$, which includes all the wall-pressure fluctuations, is dominated by the convective region centered on $k_x = k_c$. The acoustic contribution, is near $k_x = k_a$ 0. In Fig. 5.21(a) by Arguillat and Ricot [Arguillat *et al.*, 2010], this k_a is noted as k_0. The compressibility effects are represented by the acoustic region defined by the disk k k_a with a peak at $k = k_a$. The convective and acoustic wavenumbers are related by

$$k_a = Ma \quad k_c \tag{5.6}$$

where Ma is the free-stream Mach number.

Inspired by the previous studies on the channel flows [Arguillat *et al.*, 2010; Salze *et al.*, 2014, 2015a,b], the objective here using such a technique, is therefore to characterize 2D wavevector-frequency spectra in the TE region of the airfoil with severe APG flow condition, and to separate the aerodynamic and the acoustic contributions. According to the author's knowledge, this is the first time that such a technique is used from a high quality DNS data set from an airfoil noise study. To that end, wall-pressure fluctuations have been extracted for two chosen regions named as $Zone1$ and $Zone2$ near the TE region of the CD airfoil. The latter is closer to the TE. These two regions are shown in Figs. 5.22(a) and 5.22(b). These two regions consist of mesh points in the DNS almost uniform size of $s = 0\,08$ mm in the streamwise and spanwise direction as shown in the zoom view of the mesh in Fig. 5.22(c). The whole span of these two regions is taken which finally gives the size of the mesh for these two regions 200 194. The Fourier transforms will then be conducted in the streamwise and spanwise directions. Using the same flow directions defined from the beginning, the wavenumber-frequency spectrum $_{pp}(k_x\ k_z$) is considered.

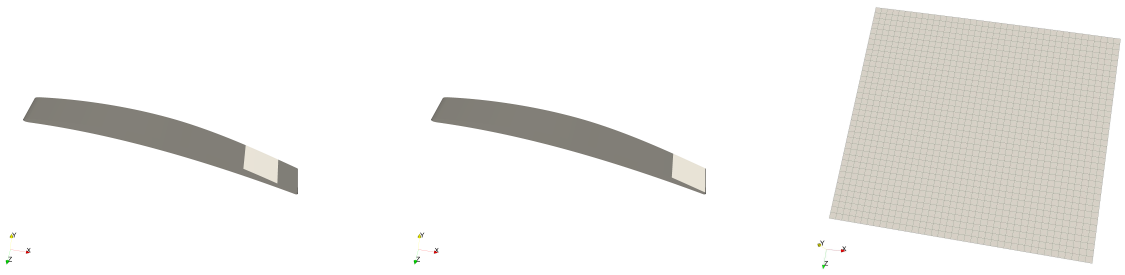

(a) (b) (c)

Figure 5.22 Investigated zones for wavenumber-frequency spectra analysis: (a) $Zone1$; (b) $Zone2$ and (c) mesh detail of $Zone1$ (skip 5 points in each direction).

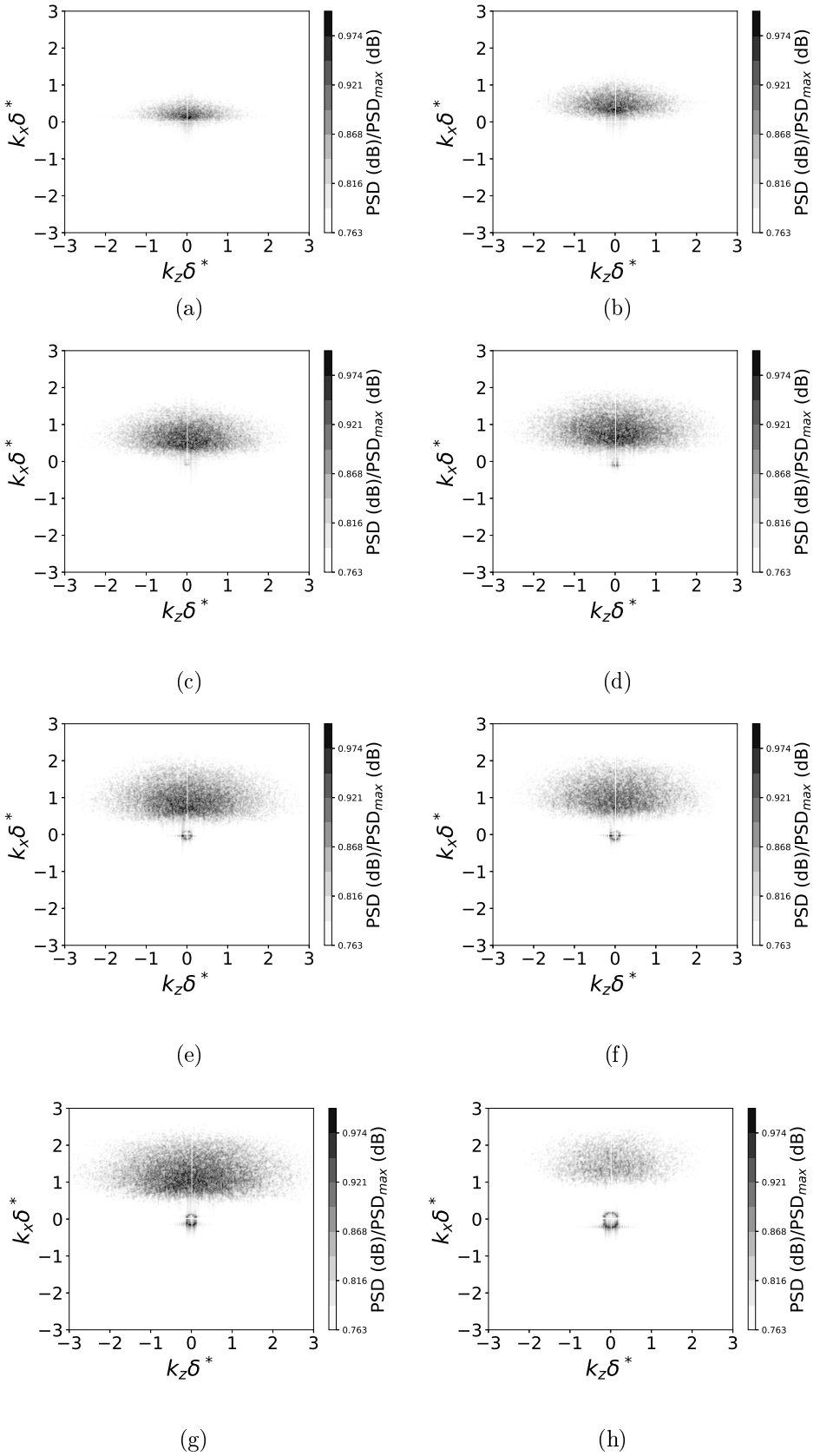

Figure 5.23 Wavenumber-frequency spectra of *Zone*1: (a) 1459 Hz; (b) 3534 Hz; (c)4993 Hz; (d) 6531 Hz; (e) 7528 Hz; (f) 8527 Hz; (g) 9987 Hz and (h) 13981 Hz.

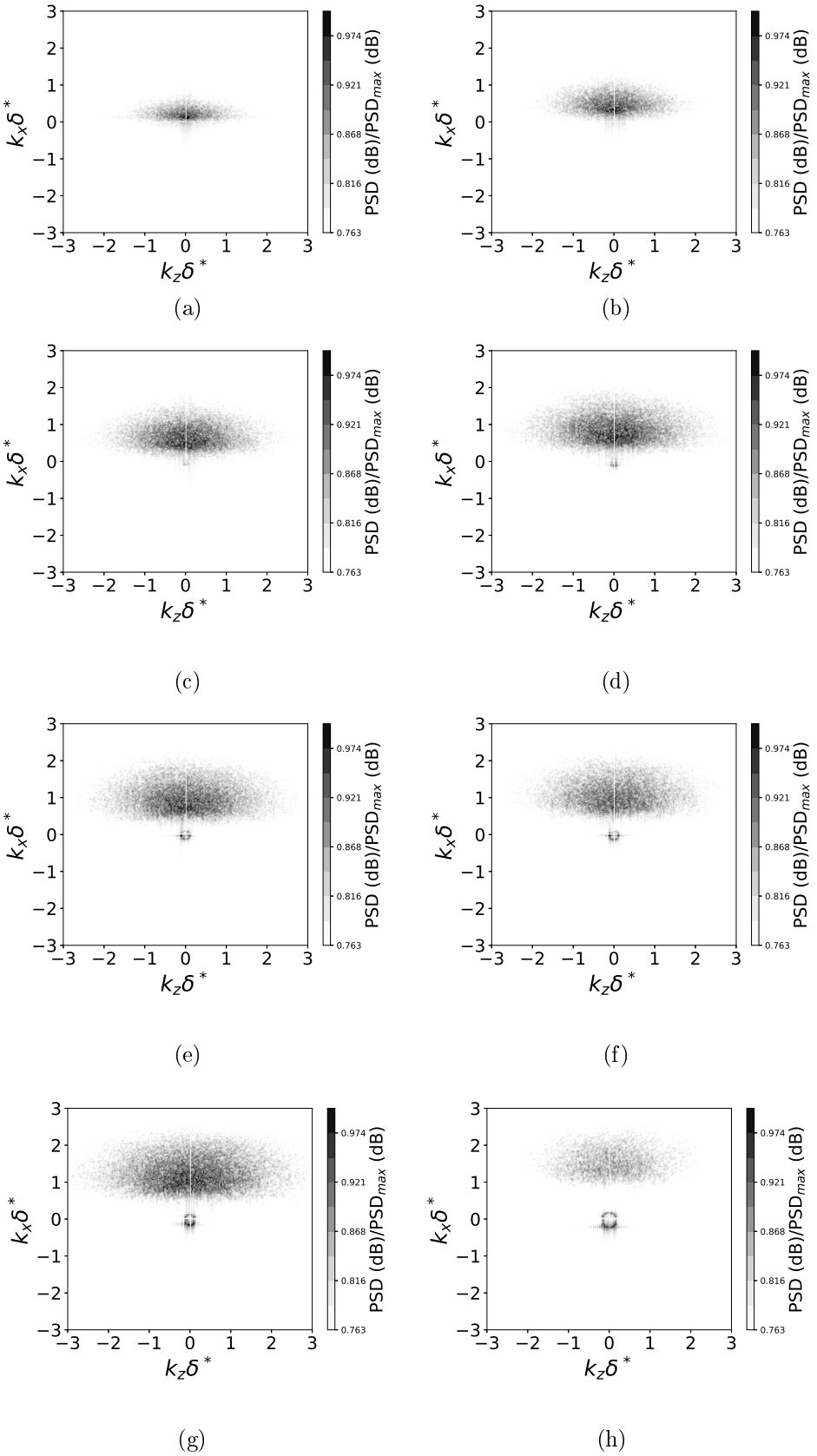

Figure 5.24 Wavenumber-frequency spectra of *Zone*2: (a) 1459 Hz; (b) 3534 Hz; (c)4993 Hz; (d) 6531 Hz; (e) 7528 Hz; (f) 8527 Hz; (g) 9987 Hz and (h) 13981 Hz.

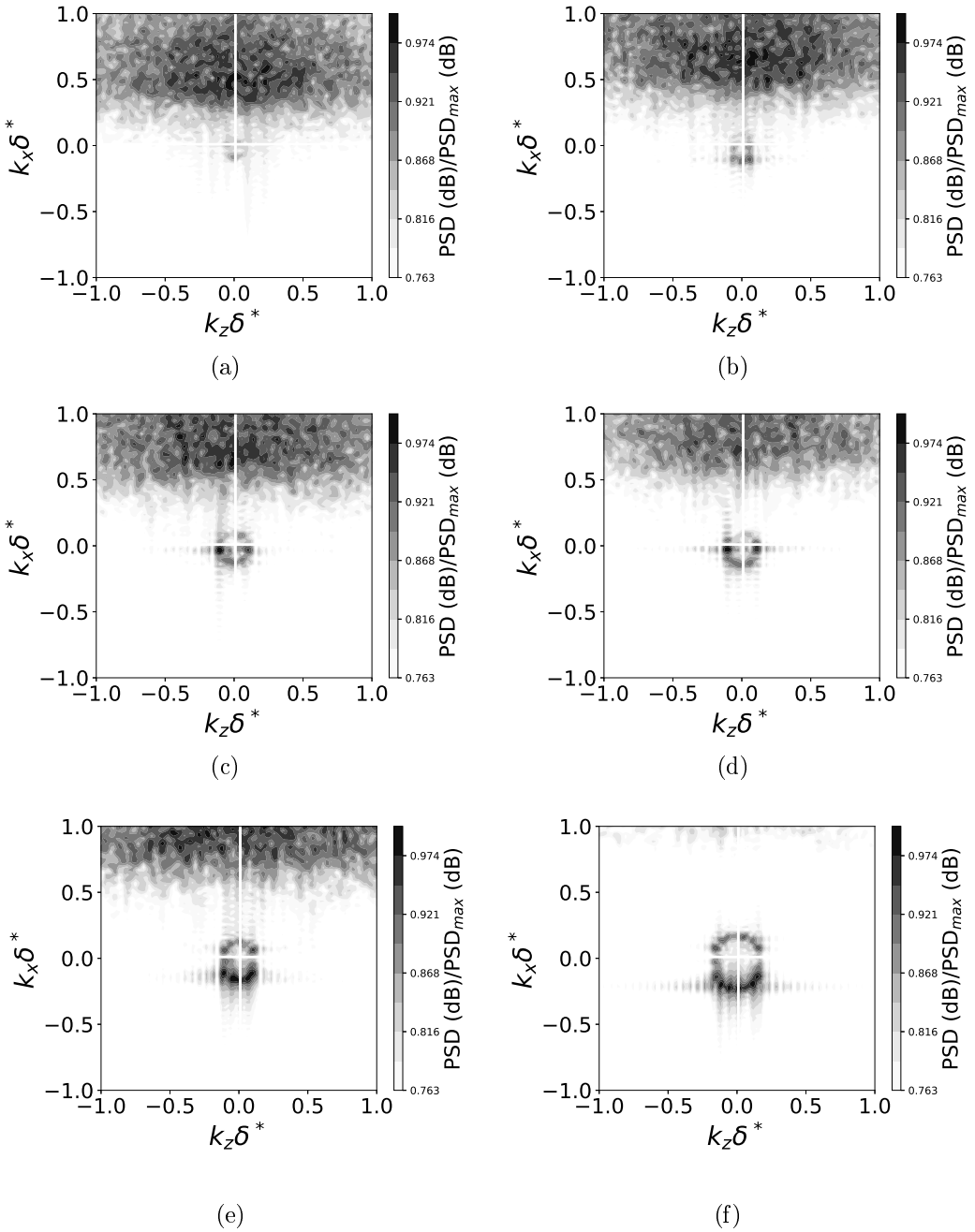

Figure 5.25 Zoom view on acoustic contribution of the wavenumber-frequency spectra of *Zone*1: (a)4993 Hz; (b) 6531 Hz; (c) 7528 Hz; (d) 8527 Hz; (e) 9987 Hz and (f) 13981 Hz.

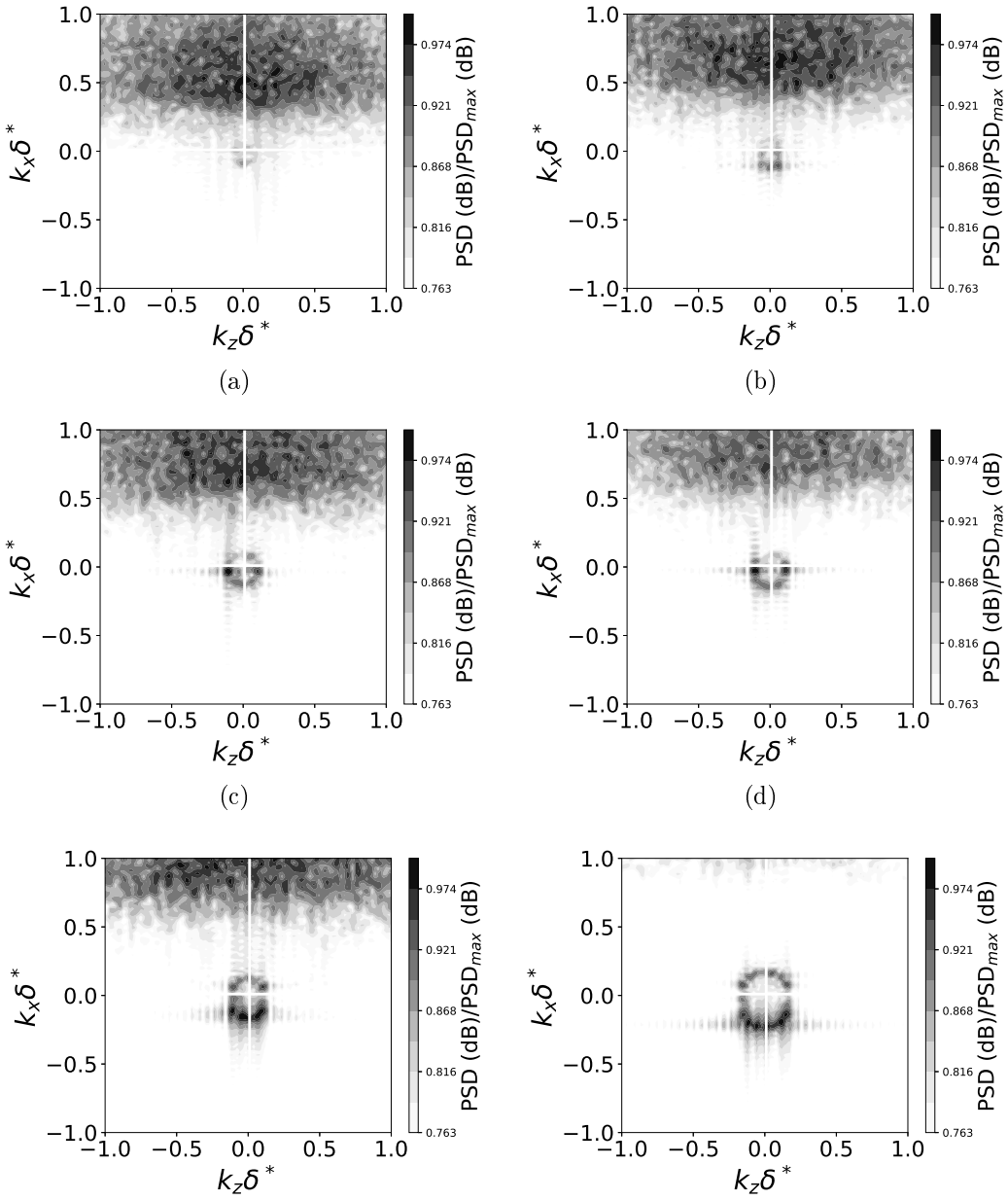

Figure 5.26 Zoom view on acoustic contribution of the wavenumber-frequency spectra of *Zone*2: (a)4993 Hz; (b) 6531 Hz; (c) 7528 Hz; (d) 8527 Hz; (e) 9987 Hz and (f) 13981 Hz.

The results of the wavenumber-frequency spectra are shown in Figs. 5.23 and 5.24 for several chosen frequencies f=1459 Hz, 3534 Hz, 4993 Hz, 6531 Hz, 7528 Hz, 8527 Hz, 9987 Hz and 13981 Hz. The horizontal and vertical axis are respectively k_z and k_x where $k_z = 2 \ f_z \ U_0$, $k_x = 2 \ f_x \ U_0$ and is the local displacement thickness at the center of the extracted planes. The isocontours are the ratio between the PSD value in dB divided by its maximum value for a given frequency f ranging from 0.5 to 1 in a linear scale. In Figs. 5.23 and 5.24, at low frequencies, the acoustic contribution is hardly seen and is mixed with the convective contribution. With the increase of frequencies (Figs. 5.23(c)–5.23(h) and 5.24(c)–5.24(h)), the acoustic and convective contributions separate. They are clearly centered respectively around the $k_x = k_a$ and $k_x = k_c$ and the convective contribution has a antisymmetric shape along k_x and an elongated shape along k_z direction. With the highest frequencies (Figs. 5.23(h) and 5.24(h)), the acoustic contribution becomes dominant as shown by the darker contours around the origin and lighter contours from the convective region. With the high wavenumber resolution thanks to the refined DNS mesh, the directivity patterns are also present in these plots. Fig. 5.25 shows the zoom view of the frequency wavenumber frequency spectra at high frequencies. With increasing frequencies, the directivity pattern changes gradually from a compact dipole shape to non-compact one with multiple lobes as shown by the darkest spots in the acoustic contribution zone (circle around origin).

The propagation seems slightly more pronounced in the upstream direction with highest frequencies (Figs. 5.25(e) and 5.25(f), k_x negative). For low frequencies, no privileged direction of propagation seems noticeable. Fig. 5.26 shows the zoom view from results of $Zone2$, no significant difference is observed from that of $Zone1$ (Fig. 5.25). From what has been observed in this section, it can be concluded that the high frequency wall-pressure fluctuations is almost purely acoustic, which, indicates that the high frequency phenomenon that have been observed in wall-pressure PSD and wall-pressure coherence, are acoustically induced phenomena.

5.5 Effects of Mean Pressure Gradients on Turbulence Development

5.5.1 Mean Flow Profiles

In Fig. 5.27, the mean wall normal velocity profiles are presented. The vertical blue lines mark the wall-normal locations that are chosen for further analysis in the following sections. These locations are respectively in the viscous sub-layer, log-layer and outer-

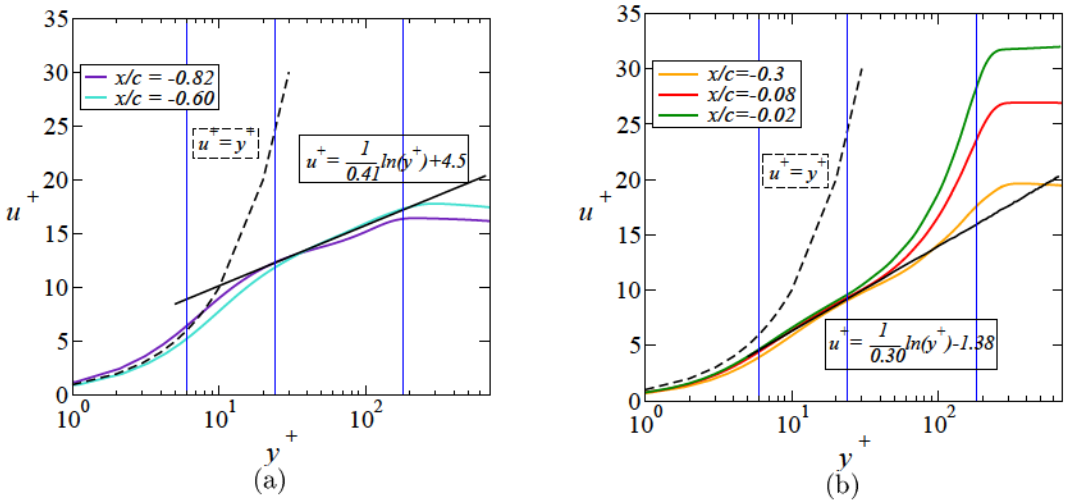

Figure 5.27 Profiles of the mean wall tangential velocity as a function of the wall normal distance: (a) FPG ($x/c = -0.82$, 18% chord) and ZPG zones ($x/c = -0.60$, 40% chord) at $Re_\theta = 210$ and 280 respectively; (b) APG zones ($x/c = -0.3$, 70% chord; $x/c = -0.08$, 92% chord; $x/c = -0.02$, 98% chord) at $Re_\theta = 621, 1009$ and 1187 respectively.

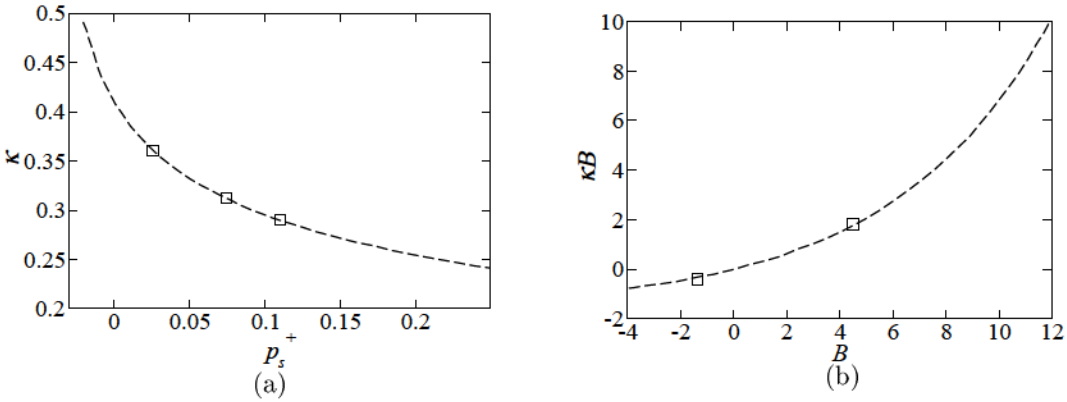

Figure 5.28 Curve fits from literature: (a) ---- curve fit obtained from Fig. 8 and equation (7.5) in [Nickels, 2004] and □ from current DNS. Values of κ and p_s^+ from APG zones ($x/c = -0.3$, 70% chord; $x/c = -0.08$, 92% chord; $x/c = -0.02$, 98% chord) in Fig. 5.27; (b) ---- curve fit from Fig. 5 in [Nagib and Chauhan, 2008] and □ from current DNS. Values of κ and B of the current DNS are from solid black lines in Fig. 5.27: ($\kappa = 0.41, B = 4.5$) and ($\kappa = 0.30, B = -1.38$).

layer spanning a range of y^+ from 6 180. The pressure gradient is seen to change the log-layer and outer-layer dramatically for these five investigated locations. The typical von Kármán constant $= 0\ 41$ for the classical law of the wall [Von Kármán, 1931]

$$u^+ = \frac{1}{-} ln(y^+) + B \tag{5.7}$$

works well in the ZPG zone. Yet, for FPG and APG zones, variations of this value have been reported. [Nagib and Chauhan, 2008] have emphasized the non-universality of the von Kármán constant through various experiments on canonical flows and showed that FPG leads to higher values of while APG gives lower . They also showed that the constant B can be negative, which is the case for the current flow. This is also consistent with the variations reported by [Nickels, 2004] (Fig. 8 in [Nickels, 2004]), which is repeated here for the present dimensionless pressure gradients $p_s^+ = (\quad u^3)(dp\ ds)$ in Fig. 5.28(a).

The values for von Kármán constant obtained from this airfoil case in APG zones are quite different from some earlier reported works of APG boundary layers from flat plates [Lee and Sung, 2008] [Knopp *et al.*, 2014]. They however correspond to quite different flow conditions. Either $_c$ is much smaller [Lee and Sung, 2008] or the local Reynolds number Re is much higher [Knopp *et al.*, 2014]. Yet they all lie on the curve fit proposed by [Nagib and Chauhan, 2008] for many FPG, ZPG and APG boundary layers as shown in Fig. 5.28(b). Moreover, as mentioned by [Lissaman, 1983] in a review of low-Reynolds-number airfoils, due to the airfoil thickness and the angle of attack, for the flow over airfoils, the turbulent boundary layer after transition can negotiate quite severe adverse pressure gradient without separation. This is in essence quite different from flow cases from flat plate for similar pressure gradients [Knopp *et al.*, 2014; Lee and Sung, 2008]. This phenomenon is actually shown in Fig. 5.9(b) as the adverse pressure gradient near the TE exhibits a high level while the flow is still attached to the airfoil surface. It is indeed one of the design objectives of the Controlled-Diffusion airfoils, to provide higher loading capacity at low Mach numbers [Hobbs and Weingold, 1984], which then gives higher pressure gradients. [Vinuesa *et al.*, 2017] compared a set of high quality DNS results for similar local Re range APG boundary layers. They for instance pinpointed that the data from a DNS [Hosseini *et al.*, 2016] over an NACA4412 airfoil at 5 angle of attack shows much severer APG measured by $_c$ for similar Re range. The strong APG over the airfoil exhibited a significant effect in the outer flow, and also noticeable in the incipient logarithmic region and all the way down to the buffer layer. Taken that the CD airfoil from the current DNS has a blade shape, which has an even higher camber and is

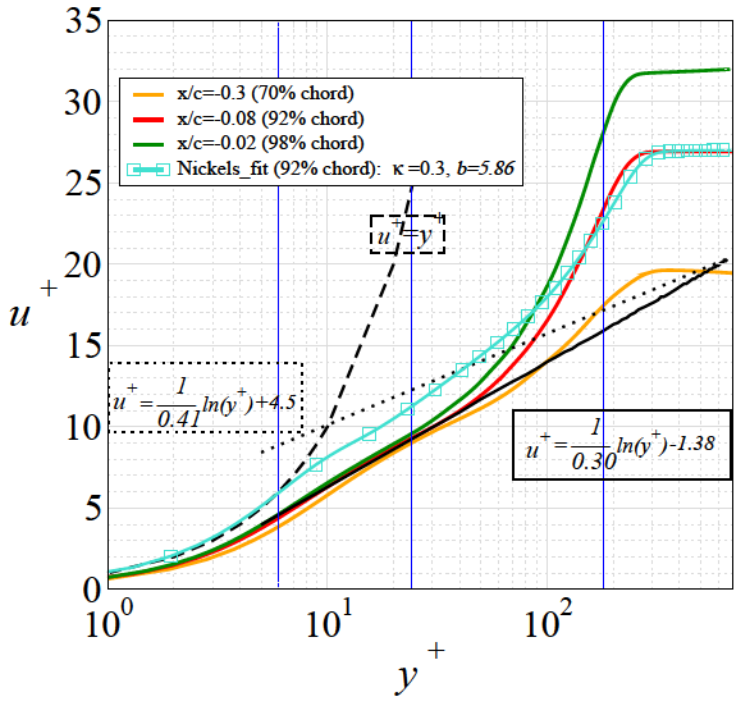

Figure 5.29 Velocity profile prediction based on equation (11.1) by Nickels [Nickels, 2004] compared with the profiles from APG zone in Fig. 5.27(b).

operated at a higher angle of attack than the case reported by [Hosseini *et al.*, 2016], the deviation of the mean velocity profiles from the standard form is therefore expected. A summary on Re_θ and β_c for APG cases is given in Tab. 5.1.

The Reynolds stress components r_{ij} are shown in Figs. 5.30 and 5.31. Here the indexes 1 and 2, which appear in the legends for r_{ij}, refer to the wall parallel and normal directions respectively. In these two figures the wall normal distance is scaled with the boundary layer thickness δ and the friction velocity u_τ respectively, to demonstrate the relative locations of the peaks. r_{ij}^+ refers to the Reynolds stress components normalized by ρu_τ^2.

Reference	Type of Data	Re_θ Range	β_c Range
Spalart and Watmuff [1993]	DNS	$640 < Re_\theta < 1600$	$0 < \beta_c < 2$
Skaare and Krogstad [1994]	Experiment	$25400 < Re_\theta < 53970$	$12 < \beta_c < 21.4$
Lee and Sung [2008]	DNS	$850 < Re_\theta < 1400$	$0.25 < \beta_c < 1.68$
Monty *et al.* [2011]	Experiment	$6100 < Re_\theta < 18700$	$0.9 < \beta_c < 4.73$
Knopp *et al.* [2014]	Experiment	$Re_\theta \approx 10000$	$\beta_c \approx 10$
Hosseini *et al.* [2016]	DNS	$750 < Re_\theta < 2800$	$0.6 < \beta_c < 85$
Kitsios *et al.* [2016]	DNS	$3500 < Re_\theta < 4800$	$\beta_c \approx 1$
TE portion of the CD airfoil	DNS	$780 < Re_\theta < 1206$	$0 < \beta_c < 10$

Table 5.1 Summary of APG boundary layer data bases.

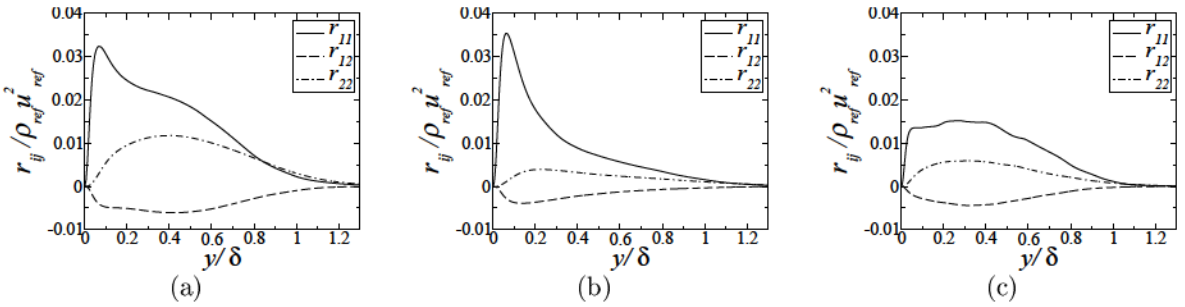

Figure 5.30 Reynolds stress components normalized with outer scales along wall normal direction. (a) FPG; (b) ZPG and (c) APG zones.

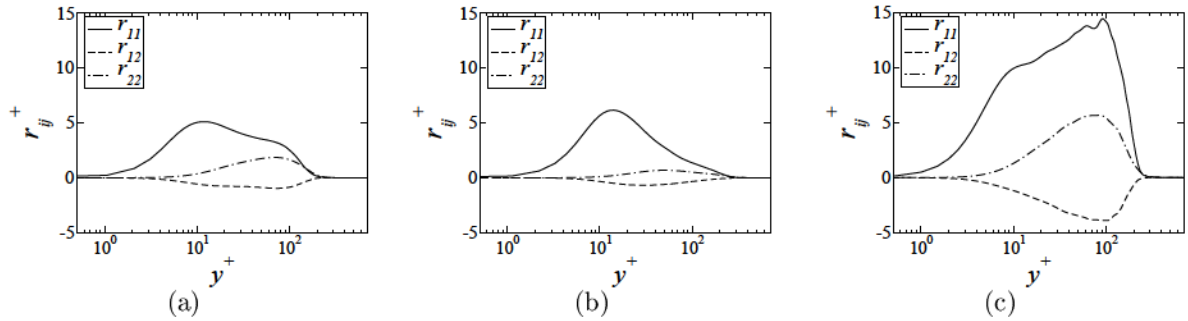

Figure 5.31 Reynolds stress components normalized with inner scales along wall normal direction. (a) FPG; (b) ZPG and (c) APG zones.

The boundary layer thickness $\delta = \delta_{p99}$ is determined by the total pressure $p_t = \frac{1}{2}\rho u^2 + p_s$ where p_s is the static pressure at a certain point. Here the flow property that the total pressure is conserved and uniform outside the boundary layer is used. The boundary layer reaches its limit when p_t reaches 99% of its maximum constant value along the wall normal direction. It is necessary to use δ_{p99} not δ_{99}, the boundary layer thickness determined by 99% of the tangential velocity maximum along a certain wall normal direction, as a reference to calculate the boundary layer thickness because for loaded airfoils, the external flow is deflected and will therefore have non-constant value. Thus, the velocity reference would give a boundary layer thickness much thicker than that obtained by using the total pressure. As shown in Figs. 5.30 and 5.31, the locations of the peak values of r_{ij}, which present the most intense momentum transfer by fluctuating velocities in a turbulent boundary layer, also exhibit a significant change due to the presence of pressure gradients. For the ZPG, the peak values are usually in the viscous sub-layer. This is the case for the data shown here in Figs. 5.30(b) and 5.31(b) for the flow at the LE and around mid-chord. Further downstream, with the increase of the adverse pressure gradient, the flow decelerates and the peak values of r_{ij} extends to the log-layer and even into the edge of the outer-layer shown as a platform shape in Figs. 5.30(c) and 5.31(c) for $8 \leq y^+ \leq 103$

which indicates that the APG acts as an additional factor to help the momentum exchange by fluctuating velocities. This platform shape is consistent with what has been reported by [Lee and Sung, 2008] at a similar Re range and by [Skaare and Krogstad, 1994] at a much higher Re for an APG flow near separation. As mentioned by [Lee and Sung, 2009] from an APG with similar Re from an incompressible DNS approach, hairpin-type vortices are the predominant structures associated with the production of Reynolds stress in the APG flows. The hairpin structures away from the wall in the TE region seen in Fig. 5.14(c) and zoomed in Fig. 5.32 support such an argument for the origin of the outer peak of the Reynolds stress in APG. These Reynolds stress profiles further confirm the information presented in Fig. 5.5: the intense turbulent mixing for APG zones exists both in the viscous sub-layer, log-layer and even extend to the outer-layer. The comparison with the flow in the mid-chord portion in Fig. 5.32 shows that the hairpin structures are predominantly forward leaning in the ZPG zone and more backward leaning ones are seen in the APG zone.

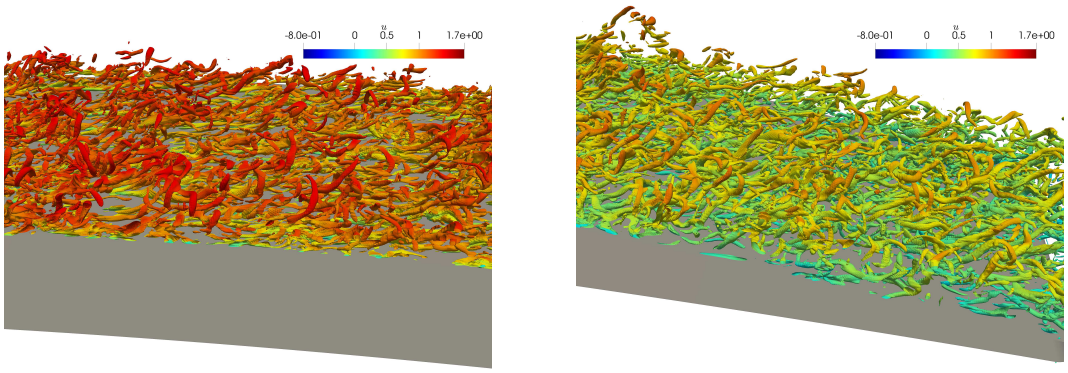

(a) (b)

Figure 5.32 Instantaneous flow details visualised by $_{ci} = 70$ iso-contours colored by streamwise velocity component: (a) Mid-chord portion (ZPG) and (b) TE portion (APG).

5.5.2 Velocity Gradient Tensor Invariants Dynamics

The character of turbulent structures, their evolution, and how they are distributed in a turbulent flow are of great importance to understand their dynamics and to drive their modeling. Besides the vortex identification methods in *Appendix*, Lagrangian dynamics offers a possibility to investigate that. In contrast to Eulerian dynamics, Lagrangian dynamics describes a flow in a reference system that is fixed with a fluid particle instead of an inertial system which is fixed with the flow domain. This allows a different perspective on the flow. However, most flow simulations, including the present direct numerical simu-

lation (DNS), rely on an Eulerian description of the considered system. In order to exploit data from an Eulerian system in the Lagrangian dynamics analysis, the velocity gradient tensor invariants are possible connections as they are invariant by rotation or translation. Furthermore, the velocity gradient tensor contains rich information about the flow and its dynamics. For instance, [Perry and Chong, 1987] summarized how local flow patterns can be characterized by the velocity gradient tensor at the locations of interest. From the point of view of a fluid particle located in a structure, it allows the distinction between four different states of the structure at the location of the particle. In detail, for incompressible or weakly compressible flow, in which P defined in equation (5.9a) equals or close to zero, the space spanned by Q and R defined in equations (5.9b) and (5.9c) respectively, can be divided into 4 sectors by the $= 0$ line and $R = 0$ line where is the discriminant of the velocity gradient tensor matrix. These 4 sectors correspond to 4 characteristic structure types: (SI) vortical structures with stretching character (> 0 R 0); (SII) vortical structures with contracting character (> 0 $R > 0$); (SIII) pure straining structures with flattening character (0 $R > 0$); and (SIV) pure straining structures with elongating character (0 R 0). Sketches of these topologies can be found in [Ooi *et al.*, 1999]. A review by [Meneveau, 2011] summarized most of the progress achieved in the field of Lagrangian dynamics of the velocity gradient tensor. More detailed explanations of the structure types can also be found in [Perry and Chong, 1987] and [Bechlars, 2015], for example. For compressible turbulence, 2 more sectors will appear in the QR-space for a given P value. Detailed explanations on the flow behaviour for these additional sectors and the characteristics of cases at relatively higher or extreme P values (both positive and negative values) from DNS results for decaying compressible isotropic turbulence can be found in [Suman and Girimaji, 2010].

The joint probability density function (joint p.d.f.) of Q and R (or the QR plot) can statistically describe the characteristic composition of turbulence for targeted regions. The isolines of this joint p.d.f for many flows have similar shape, reminiscent of a "*teardrop*" [Chong *et al.*, 1998; Martin *et al.*, 1998; Ooi *et al.*, 1999; Soria *et al.*, 1994]. Fig. 5.33 shows this "*teardrop*" shape from homogeneous isotropic turbulence [Martin *et al.*, 1998] as an example. However, variations of this QR plot shape have been found for different flows, especially for wall-bounded flows, which have a wide range of practical applications and are important to be understood. For instance from DNS of wall-bounded flows it has been found that the shapes of the QR plot at the outer-layer locations of the boundary layer has the *teardrop* shape, whereas in the buffer layer the tail of the QR plot shrinks compared to location further away from the wall. This difference has been found both from channel flows [Blackburn *et al.*, 1996] and from turbulent boundary layers flows [Chacín *et al.*,

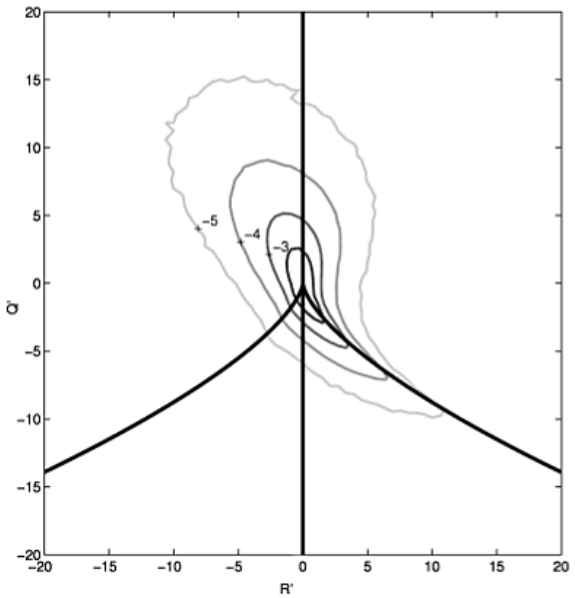

Figure 5.33 Joint p.d.f. of Q and R from homogeneous isotropic turbulence flow in [Martin *et al.*, 1998]. The contour levels are logarithmic.

1996; Wang and Lu, 2012]. Most recently, the considerable change of the QR evolution for different wall-normal locations has been studied and the wall effects have been discussed by [Bechlars and Sandberg, 2017a,b] for a zero pressure gradient turbulent boundary layer at a free stream Mach number of 0.5. The smooth changes in the outer-layers were contrasted by the strong variations in the near-wall region.

However, although a significant amount of research involving the QR analysis has been devoted to zero pressure gradient boundary layers, the same cannot be said for boundary layer flows with pressure gradient effects. These flows are usually found around surfaces with curvature, as encountered in many aerodynamic applications such as airfoils, wings and blades which have significant engineering importance. Literature [Gungor *et al.*, 2014; Lee and Sung, 2009; Yuan and Piomelli, 2015] reveals that for subsonic boundary layers that are subject to a favorable pressure gradient (FPG) or an adverse pressure gradient (APG), the flow topology and the mean statistics show significant changes compared with zero pressure gradient (ZPG) turbulent boundary layers as a results of flow acceleration and deceleration. For FPG boundary layers, the flow accelerates and the relaminarization or more accurately, quasi-laminarization [Yuan and Piomelli, 2015] is often observed when the FPG is strong enough. The turbulence kinetic energy (TKE), however, of the mean flow continues to increase as a result of the acceleration, yet the flow may become less dynamic. [Narasimha and Sreenivasan, 1973] attributes this phenomenon to the dominance of pressure forces over the slowly responding Reynolds stresses. From a flow structure point

of view, [Bourassa and Thomas, 2009] showed that the quasi-laminarization is related to the stabilizing effects of the acceleration on near-wall streaks caused by the decrease of the wall-normal and spanwise fluctuations. Recently, [Piomelli and Yuan, 2013] further extended this conclusion with help of a large eddy simulation (LES), stating that the decrease of the wall-normal and spanwise fluctuations is caused by the decrease of the magnitude of the pressure fluctuations, from a source term of the Poisson equation, which points to a redistribution of the TKE which finally leads to quasi-one-dimensional turbulence in the quasi-laminarization zones. For APG boundary layers, the flow decelerates and the boundary layer becomes thicker and if the APG is strong enough, the flow separates from the wall. It was reported that the velocity profiles of APG flows do not follow the classical law of the wall [Von Kármán, 1931], even very close to the wall [Afzal, 1983; Gungor *et al.*, 2014; Indinger *et al.*, 2006; Lee and Sung, 2008; Nagano *et al.*, 1998]. [Lee and Sung, 2008] shows that the energy redistribution is enhanced in the outer-layer of the APG flows compared to the ZPG flow using data from an incompressible flow DNS. Later [Gungor *et al.*, 2014] performed DNS of a turbulent boundary layer exposed to a strong APG and found that the mean velocity profiles do not reveal a logarithmic law and Reynolds stress peaks move to roughly the middle of the boundary layer.

In this part, a particular emphasis is put on the QR evolution caused by pressure gradients for the current flow over the CD airfoil. In order to do that, the compressible evolution system for the first three invariants of the velocity gradient tensor is briefly presented here.

The velocity gradient tensor $\boldsymbol{A} :=$ $\boldsymbol{u}$ is a 3 3 matrix. According to its characteristic polynomial p_{char},

$$p_{char}(\ ) := det(\boldsymbol{A} \quad \boldsymbol{I}) = \ ^3 + P \ ^2 + Q \ + R \tag{5.8}$$

where $\boldsymbol{I}$ is the identity matrix and the first three invariants P, Q and R can be calculated as

$$P = trace(\boldsymbol{A}) = \cdot \boldsymbol{u} \tag{5.9a}$$

$$Q = \frac{1}{2}(trace(\boldsymbol{A})^2 \quad trace(\boldsymbol{AA}) = \frac{1}{2}(P^2 \quad trace(\boldsymbol{A}^2)) \tag{5.9b}$$

$$R = det(\boldsymbol{A}) = \frac{1}{3}(P^3 \quad 3PQ + trace(\boldsymbol{A}^3)) \tag{5.9c}$$

Another invariant of the velocity gradient tensor to be used in this work is the discriminant of the characteristic polynomial p_{char}

$$:= \quad \frac{1}{4}P^2Q^2 + Q^3 + P^3R + \frac{27}{4}R^2 \quad \frac{18}{4}PQR \tag{5.10}$$

$\boldsymbol{A}$ has its own dynamics defined as

$$\frac{d\boldsymbol{A}}{dt} := \frac{\boldsymbol{A}}{t} + (\boldsymbol{u}\cdot \quad)\boldsymbol{A} = \quad \boldsymbol{A}\boldsymbol{A} + \boldsymbol{H} \tag{5.11}$$

Here the source term $\boldsymbol{H}$

$$\boldsymbol{H} := \tag{5.12}$$

is a combination of the viscous effects and the pressure-density term defined as

$$= \quad (\frac{1}{-} \quad \cdot\boldsymbol{\tau}) \tag{5.13a}$$

$$= \quad (\frac{1}{-} \quad p) \tag{5.13b}$$

With these notions set, the compressible velocity gradient tensor invariant dynamics system can be described as:

$$\frac{dP}{dt} = P^2 \quad 2Q \quad trace(\boldsymbol{H}) \tag{5.14a}$$

$$\frac{dQ}{dt} = QP \quad \frac{2}{3}Ptrace(\boldsymbol{H}) \quad 3R \quad trace(\boldsymbol{A}\boldsymbol{H}\ ) \tag{5.14b}$$

$$\frac{dR}{dt} = \quad \frac{1}{3}Qtrace(\boldsymbol{H}) + PR \quad Ptrace(\boldsymbol{A}\boldsymbol{H}\ ) \quad trace(\boldsymbol{A}^2\boldsymbol{H}\ ) \tag{5.14c}$$

where $\boldsymbol{H}$ is the traceless part from the decomposition of the pressure and viscous stress matrix $\boldsymbol{H}$

$$\boldsymbol{H} = \boldsymbol{H} \ + \frac{1}{3}trace(\boldsymbol{H})\boldsymbol{I} \tag{5.15}$$

For the following analysis, the flow data length scale is firstly rescaled from the initial chord length to the local boundary layer thickness $= {}_{p99}$. Secondly, we introduce a scaling based on the local variance of the velocity gradient tensor magnitude

$$var(\boldsymbol{A}) = \overline{trace((\boldsymbol{A} \quad \overline{\boldsymbol{A}})(\boldsymbol{A} \quad \overline{\boldsymbol{A}})^T)} \tag{5.16}$$

This is a measure of the variation of the velocity gradient tensor magnitude and it can be regarded as a gradient analogue to the turbulence kinetic energy. Consequently, the related terms in the QR-space are scaled as $\boldsymbol{A} = \boldsymbol{A} \quad \overline{var(\boldsymbol{A})}$, $\boldsymbol{Q} = \boldsymbol{Q}\ var(\boldsymbol{A})$ and $\boldsymbol{R} = \boldsymbol{R}\ var(\boldsymbol{A})^{3\ 2}$. The p.d.f. values for the QR plots in this paper are multiplied by 10 and normalized by the local maximum p.d.f. value and the color bars are plotted using a logarithmic scale from 0 to 1.

[Lozano-Durán *et al.*, 2015] state that integrating over a statistically inhomogeneous region can considerably bias the Lagrangian statistics. To avoid this bias, the investigated regions in this work are chosen so that the turbulence within the integration area is regarded as quasi-statistically homogeneous. This is achieved by following the procedure reported in [Bechlars and Sandberg, 2017a]. The mean dynamics data presented in this work were integrated in the homogeneous spanwise direction, about an extent of approximately 20 grid points in the streamwise direction and approximately 5 grid points in the wall-normal direction for each location. This results in $x^+ \quad 100$ and $y^+ \quad 6$ for the location at $y^+ = 24$. These distances are similar to the work of [Bechlars and Sandberg, 2017a].

As mentioned in previous studies, the *teardrop* shape is not a universal feature, which is always observed for homogeneous isotropic turbulent (HIT) flows. For wall bounded flows, the mean evolution of the velocity gradient tensor invariants has been found to vary strongly with the distance to the wall [Bechlars and Sandberg, 2017a]. This wall effects is observed for all investigated locations in this airfoil case.

Figure 5.34 shows the overall QR distribution, in which, each row corresponds to regions at 18%, 40% and 92% of the airfoil chord from FPG to APG zones (left to right) and each column corresponds to a certain region from $y^+ \quad 6$ to $y^+ \quad 180$ (top to bottom). The contours cover 95% of the events, which means, the black colour represents only 5% of the maximum p.d.f. value in each plot. Moreover, to obtain a more quantitative impression, the joint p.d.f is integrated over the respective sectors in QR space as mentioned in 1 to calculate the ratio of occurrence from all events in each sector. This is shown in table 5.2. The Lagrangian dynamics in these 3 zones is seen to have rather different behaviours. In the FPG zone, an oval shape is seen for the location closest to the wall (Fig. 5.34(a)). In the log-layer, the *teardrop* shape is observed (Fig. 5.34(b)). In the outer-layer, the contracting vortical mechanism is less present as can be seen from table 5.2, which then gives the QR plot a quasi-triangular shape (Fig. 5.34(c)). The shapes seen in the ZPG

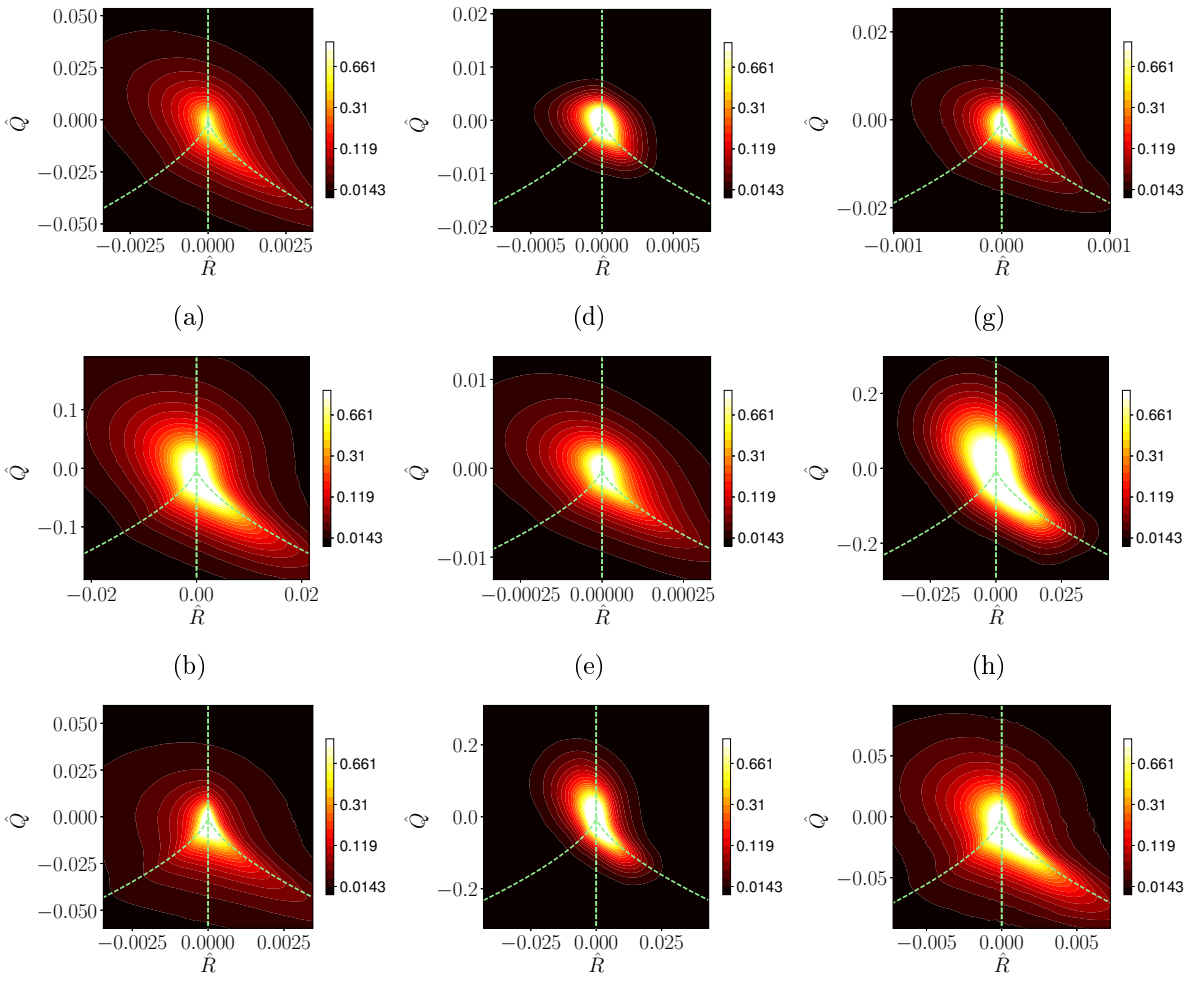

Figure 5.34 The mean QR development with distance to the wall over the CD airfoil. From left to right: FPG (18% chord), ZPG (40% chord) and APG (92% chord) zones. Three wall-normal locations are shown: (a,d,g) y^+ 6, (b,e,h) y^+ 24, (c,f,i) y^+ 180. The dashed lines divide the QR-space into 4 sectors which covers a certain flow topology respectively as mentioned in 1.

regions resemble the shapes that were reported in [Bechlars and Sandberg, 2017a]: the outer-layer matches the *teardrop* shape from HIT data in literature and becomes oval approaching the wall. The APG has the effect that the QR shape of the outer-layer becomes concentrated around $= 0$ line with positive R values which is the dividing line of sectors representing the vortical contracting manner and pure straining with flattening character. This means that the energy exchange between the mean kinetic energy and the turbulent kinetic energy is stronger than in the case of the ZPG. It is well established that vortex stretching is a major mechanism of the cascading process towards smaller scales. Figure 5.34(i) suggests that this behaviour is suppressed by the APG as there are fewer events present in the > 0 R 0 sector especially for positive Q values, as there are fewer bright areas in the SI sector compared with Fig. 5.34(f). This is also quantitatively reflected in table 5.2 when comparing the percentage in SI between APG and ZPG at y^+ 180. Closer to the wall at y^+ 24 in the log-layer, for positive R values, more flattening strain and less contracting vortical structures are present compared to the ZPG zone with the same wall normal location (Figs. 5.34(h) and 5.34(e)). The region closest to the wall produces a QR plot with similar shape to that obtained from the ZPG region (Figs. 5.34(g) and 5.34(d)). This again indicates that the APG acts as a strong mixing reinforcement in the outer-layer and log-layer for this turbulent boundary layer. In all, it can be concluded that from the QR point of view, the viscous sub-layer has an invariant character: an oval shape independent of the pressure gradient conditions. Yet the log-layer and the outer-layer strongly depend on the pressure gradient.

Component analysis: non-linearity, viscous and pressure effects

In this part, the contribution from separate terms of the compressible evolution system in equation (5.14) is studied. For this purpose, 3 groups of evolution terms are identified as suggested by [Bechlars and Sandberg, 2017a]:

(i) $\boldsymbol{H} = 0$;
(ii) $trace(\boldsymbol{H}) = = Q = R = 0$;
(iii) $trace(\boldsymbol{H}) = = Q = R = 0$.

which give the simplified invariants dynamics systems from equation (5.14):

(i)

$$\frac{dQ}{dt} = QP \quad \frac{2}{3}Ptrace(\boldsymbol{H}) \quad 3R; \tag{5.17a}$$

$$\frac{dR}{dt} = \quad \frac{1}{3}Qtrace(\boldsymbol{H}) + PR; \tag{5.17b}$$

Flow regions		(*S*I)	(*S*II)	(*S*III)	(*S*IV)
FPG at y^+	6	37%	30%	22%	11%
FPG at y^+	24	26%	25%	29%	20%
FPG at y^+	180	17%	19%	32%	32%
ZPG at y^+	6	41%	37%	12%	10%
ZPG at y^+	24	32%	31%	23%	14%
ZPG at y^+	180	31%	30%	24%	15%
APG at y^+	6	41%	30%	18%	11%
APG at y^+	24	32%	31%	23%	14%
APG at y^+	180	15%	15%	41%	29%

Table 5.2 Ratios of the characteristic flow topologies in 4 sectors as mentioned in 1 in the QR space from sampling locations over the airfoil. FPG: 18% chord; ZPG 40% chord and APG 92% chord.

(ii)

$$\frac{dQ}{dt} = trace(\boldsymbol{A}^{*}); \tag{5.18a}$$

$$\frac{dR}{dt} = trace(\boldsymbol{AA}^{*}); \tag{5.18b}$$

(iii)

$$\frac{dQ}{dt} = trace(\boldsymbol{A}^{*}); \tag{5.19a}$$

$$\frac{dR}{dt} = trace(\boldsymbol{AA}^{*}) \tag{5.19b}$$

.

where * and * are the traceless parts of and defined in equation (5.13).

Group (i) covers all the non-linear terms, except the traceless part of the source term $\boldsymbol{H}$. For incompressible flows this gives $trace(\boldsymbol{H}) = 2Q$ and the system would reduce to the restricted Euler system. For the current flow with low Mach number $Ma = 0\,25$, the compressibility effects are small. For the evolution equations restricted to the nonlinear terms (as shown in Fig. 5.36) this means that there are no significant differences with the restricted Euler system [Vieillefosse, 1984]. Data plotted in Fig. 5.36 is from 92% chord in the APG zone at y^+ 24. The trajectories (black streamlines) caused by non-linear effects are very similar to that described by [Vieillefosse, 1984]. Here only data from 92% chord in the APG zone at y^+ 24 is shown but the contribution from non-linear terms from all other investigated locations in the FPG, ZPG and APG zones shows an invariant

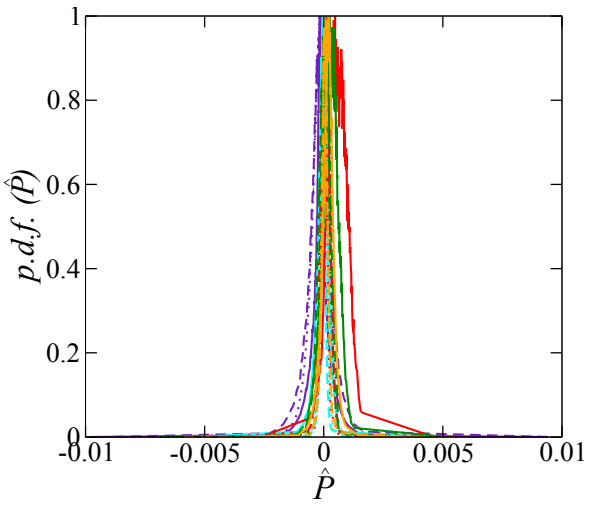

Figure 5.35 Ratios of the p.d.f of the normalized first velocity gradient invariant $\boldsymbol{P}$ divided by the maximum values for the different zones over the airfoil. Colors follow the legends in Fig. 5.27 (····· y^+ 6; ---- y^+ 24; —— y^+ 180).

character. This agreement with the incompressible reference [Vieillefosse, 1984] means that mapping the PQR-space to one of its subsets, the QR-space taking $P = 0$ for such a low Mach number case is valid. This has also been demonstrated by [Bechlars and Sandberg, 2017a] for $Ma = 0\,5$ turbulent boundary layer data. Moreover, as shown in Fig. 5.35, the p.d.f. of the normalized first velocity gradient invariant $\boldsymbol{P} = \boldsymbol{P}$ $\overline{var(\boldsymbol{A})}$, or normalized inverse dilatation, of all the investigated regions over the airfoil exhibit very low absolute $\boldsymbol{P}$ values (less than 0.002) for their maximum p.d.f. locations. This confirms that, as mentioned by [Suman and Girimaji, 2010] in terms of velocity gradient invariants analysis, at low positive or negative dilatations, the statistical behavior is similar to that of incompressible flow. In Fig. 5.36, the mean trajectories move from negative R values towards positive forming a round head when Q values increase. The evolution velocity magnitude of the restricted Euler system is small around the origin of the QR-space and increases with the distance to the origin. Together with the global QR plots shown in Fig. 5.34, the non-linear part is also seen to drive the global shape of the QR plots.

Group (ii) presents the viscous effects by neglecting all terms except the ones that link the viscous diffusion and the velocity gradient tensor. This part also shows an invariant characteristic across the boundary layer for all investigated regions. Figure 5.37 is a representative QR plot of this group. The data is extracted at 92% chord in the APG zone at y^+ 24. The trajectories are relatively straight, pointing towards the origin and only show a slight counter-clockwise spin. The evolution velocity magnitude is decreasing with decreasing distance to the origin. But overall the restricted viscous diffusion evolution has an invariant character in this turbulent flow across the airfoil regardless of the pressure

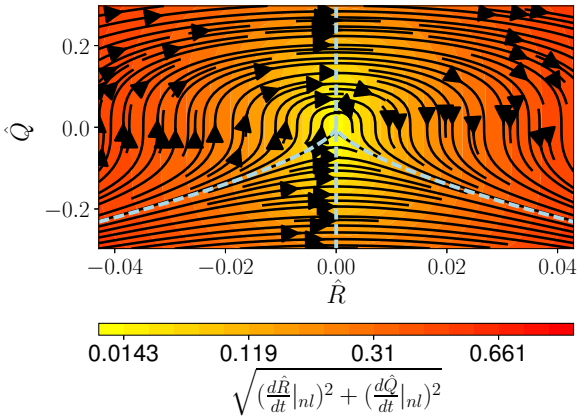

Figure 5.36 Non-linearity effects: the mean QR-phase development is shown by trajectories (black) and by the magnitude of the mean phase velocity (contours) restricted to the non-linear terms of the Navier-Stokes equations. The dashed lines divide the QR-space into 4 sectors which covers respectively a certain flow topology as mentioned in 1.

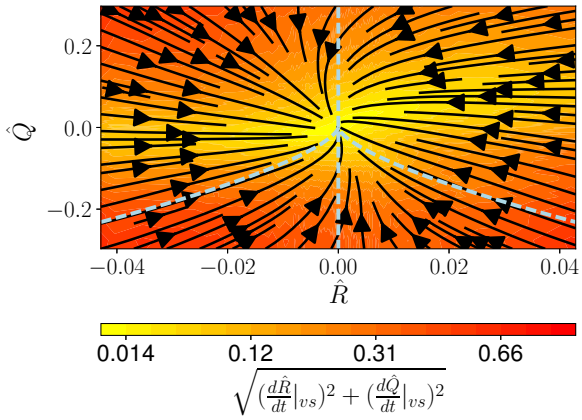

Figure 5.37 Viscous effects: the mean QR-phase development is shown by trajectories (black) and by the magnitude of the mean phase velocity (contours) restricted to the viscous terms of the Navier-Stokes equations. The dashed lines divide the QR-space into 4 sectors which covers respectively a certain flow topology as mentioned in 1.

gradient conditions. The non-linear terms and viscous terms are thus not the major reasons for the change of overall QR distribution in these investigated zones.

Group (iii) presents the pressure effects by neglecting all terms except the terms that link the pressure with the velocity gradient tensor. This is the part that is most influenced by the pressure gradient. This is shown in Fig. 5.38, in which, each row corresponds to regions at 18%, 40% and 92% of the airfoil chord from FPG to APG zones (left to right) and each column corresponds to a certain region from y^+ 6 to y^+ 180 (top to bottom). For the same wall normal location in terms of wall unit, the FPG, ZPG and APG zones have rather different behaviours. Furthermore, the contribution of the pressure term varies strongly with the wall normal location. For FPG zones, the outer-layer results show that the pressure terms totally counteract the non-linear terms (Fig. 5.36) and the mean trajectories show an "unrolling" feature (Fig. 5.38(c)). In the log region (Fig. 5.38(b)), a swirl for positive R and Q values is formed in the contracting vortical structures regime sector. More closely to the wall (Fig. 5.38(a)), two distinct mechanisms, divided by a bow-shaped line, are present. On the left side of this line the pressure also counteracts the non-linear terms whereas it supports them on the right side. These features are assumed to be related to the rolling structures of the flow reattachment after transition as shown in Fig. 5.14(b). As mentioned by [Joshi *et al.*, 2014] from PIV measurements of the flow with an acceleration parameter (defined in equation (5.5)), K 1 28 10 ^{6}, similar to the investigated FPG region of the current DNS, hairpin packets often form in the FPG boundary layer, but confines to the near-wall region and the outer-layer frequently consists of extended regions of low turbulence. This is consistent with the current observed trend as the FPG gives the trajectories away from the wall more "unrolling" behaviour. For ZPG zones, the outer-layer results (Fig. 5.38(f)) show that the pressure terms counteract the non-linear terms (Fig. 5.36) except that a swirl for positive R and Q values is formed in the contracting vortical structures regime. The evolution for this swirl is relatively small across the various locations. Approaching the wall, the swirl becomes "unrolling" and two distinct mechanisms, as for region y^+ 6 in the FPG zones, are present. These results for the ZPG zones qualitatively match the results from the zero pressure gradient turbulent boundary layer data of [Bechlars and Sandberg, 2017a]. In the APG zones, both the log-layer (Fig. 5.38(h)) and outer-layer (Fig. 5.38(i)) show strong rolling features in the contracting vortical regime sector as shown by the strong curvature of the mean trajectories. For the location closest to the wall (y^+ 6, Fig. 5.38(g)), the "unrolling" appears and is similar to FPG and ZPG regions. Therefore, at locations closest to the wall, the pressure term contribution in the QR plots is quite invariant. Yet, further from the wall, this contribution varies strongly with the local mean pressure gradient.

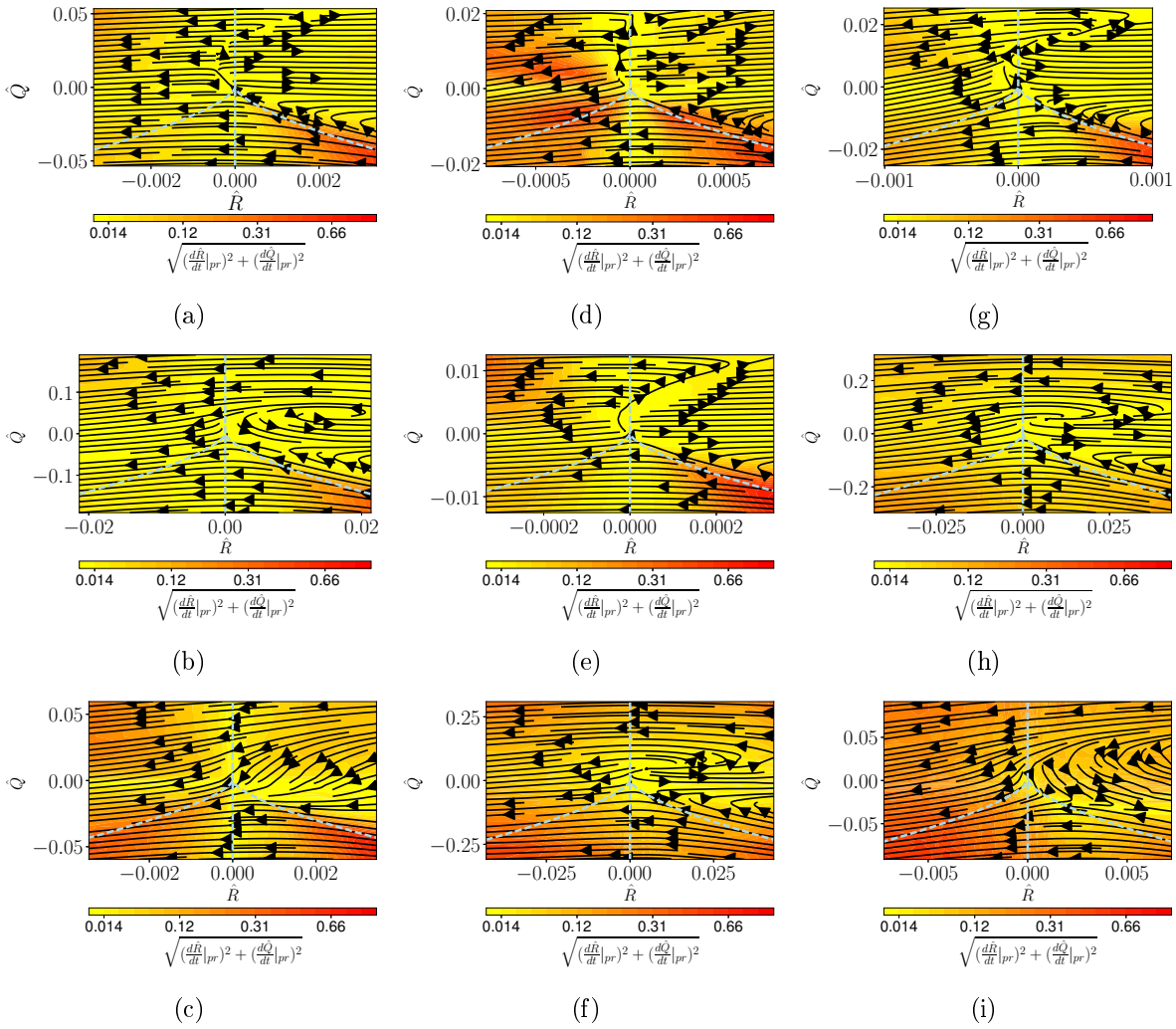

Figure 5.38 Pressure effects: the mean QR-phase development is shown by trajectories (black) and by the magnitude of the mean phase velocity (contours) restricted to the pressure term of the Navier-Stokes equations, respectively. From left to right: FPG(18% chord), ZPG (40% chord) and APG (92% chord) zones. Three wall-normal locations are shown: (a,d,g) y^+ 6, (b,e,h) y^+ 24, (c,f,i) y^+ 180. The dashed lines divide the QR-space into 4 sectors which covers respectively a certain flow topology as mentioned in 1.

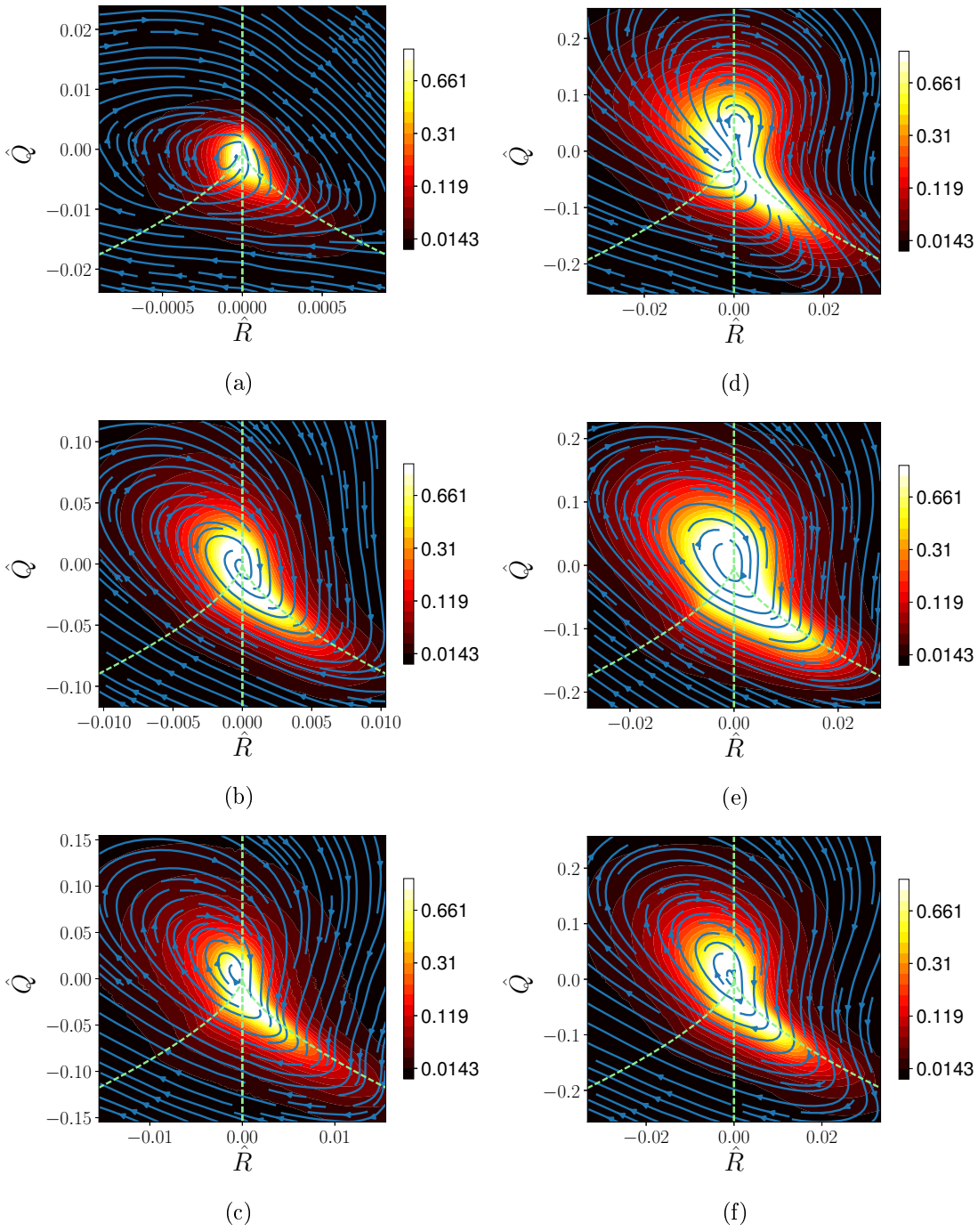

Figure 5.39 The mean QR development with distance to the wall at the trailing-edge and in the near wake: (a)(b)(c), trailing-edge (98% chord);(d)(e)(f), near wake (5% chord from airfoil trailing-edge). The dashed lines divide the QR-space into 4 sectors which covers a certain flow topology respectively as mentioned in 1.

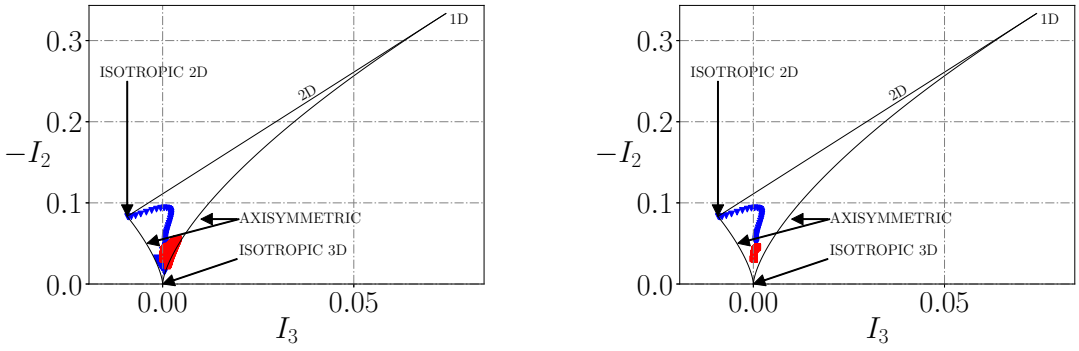

Figure 5.40 Anisotropy invariant map for locations at TE (98% chord) and near wake (x $c = 0\,05$ to TE): (a) entire boundary layer and (b) near wall distribution up to y^+ 6.

Effects of the wall: trailing-edge to near wake flow development

As partly mentioned in the previous sections, the wall has significant effects on the overall QR distribution when compared to HIT flows. This can already be seen from the comparison between the current flow over the airfoil and HIT flow reported in literature, as well as from the comparison between the flow near the airfoil trailing-edge and the flow in the near wake. Figure 5.39 shows the flow at 98% airfoil chord and its adjacent area in the wake 5% airfoil chord downstream of the trailing-edge. More precisely, in Fig. 5.39, each row corresponds to regions in the boundary layer at the TE and in the near wake (left to right) and each column corresponds to either one of these two regions from near the wall (or near the wake centerline) or to locations further from the wall (or further from the wake centerline) (top to bottom). The wall normal locations in the boundary layer at 98% airfoil chord are y^+ 6, y^+ 24 and y^+ 180, respectively. From the horizontal comparisons (trailing-edge flow with their counterparts following the streamlines in the near wake), the QR distribution in the near wake is clearly seen to be more isotropic: all locations exhibit a *teardrop* shape whereas the trailing-edge flow shows significant differences with varying tangential locations. In order to confirm and to quantify the difference on anisotropy levels, the anisotropy invariant map firstly introduced by [Lumley, 1979] is used. Details about the application of such a tool can be found in [Simonsen and Krogstad, 2005] for instance. Figure 5.40 shows the distribution of the second and third invariants

I_2 and I_3 of the Reynolds stress tensor $\boldsymbol{A}_{Re}$ defined as

$$\boldsymbol{A}_{Re} = \begin{matrix} \overline{u_x u_x} - u_x u_x & \overline{u_x u_y} - u_x u_y & \overline{u_x u_z} - u_x u_z \\ \overline{u_y u_x} - u_y u_x & \overline{u_y u_y} - u_y u_y & \overline{u_y u_z} - u_y u_z \\ \overline{u_z u_x} - u_z u_x & \overline{u_z u_y} - u_z u_y & \overline{u_z u_z} - u_z u_z \end{matrix} \tag{5.20}$$

where x, y and z are the streamwise, vertical and spanwise directions, respectively. I_2 and I_3 are defined as

$$I_2 = \frac{1}{2}(trace(\boldsymbol{A}_{Re})^2 \quad trace(\boldsymbol{A}_{Re}^2)) \tag{5.21a}$$

$$I_3 = det(\boldsymbol{A}_{Re}) \tag{5.21b}$$

In Fig. 5.40(a), the distribution of the anisotropy level of wall normal points from the wall to the edge of the boundary layer (up to $_{p99}$) at the TE (98% chord) and their counterparts in the near wake ($x \ c = 0\ 05$ to TE) again clearly shows that in the absence of the wall, the turbulence becomes more isotropic as the values of I_3 and I_2 from the points in the near wake are much closer to the 3D isotropic point where I_3 and I_2 tend to zero. In Fig. 5.40(b), the most severe departure from the 3D isotropy for TE points in Fig. 5.40(a) can be seen to be from the locations closer to the wall (from the wall to y^+ 6) as only the distribution of these near-wall points are plotted in this figure. These near-wall points have a nearly 2D isotropic behaviour. These plots thus further confirm that the trend seen in Figs. 5.39(a) and 5.39(d) comes from the fact that the flow turns more isotropic in the absence of the airfoil surface. Furthermore, the comparison between Figs. 5.39(a) and 5.39(d) shows that the wall greatly suppresses the vortical stretching character of the flow as the left-upper part of the QR plot in the near wake are much bigger and rounder than that from the trailing-edge.

Another aspect worth mentioning, independent of all the flow conditions, for all the investigated regions over the airfoil and the near wake, the general mean lifecycle of turbulent structures stays unchanged in the QR-space. This cycle starts from straining structures and develops to stretching vortical structures and further to contracting vortical structures before the lifecycle continues again in the straining structures. This appears to be an invariant character for all the regions in the current flow under consideration.

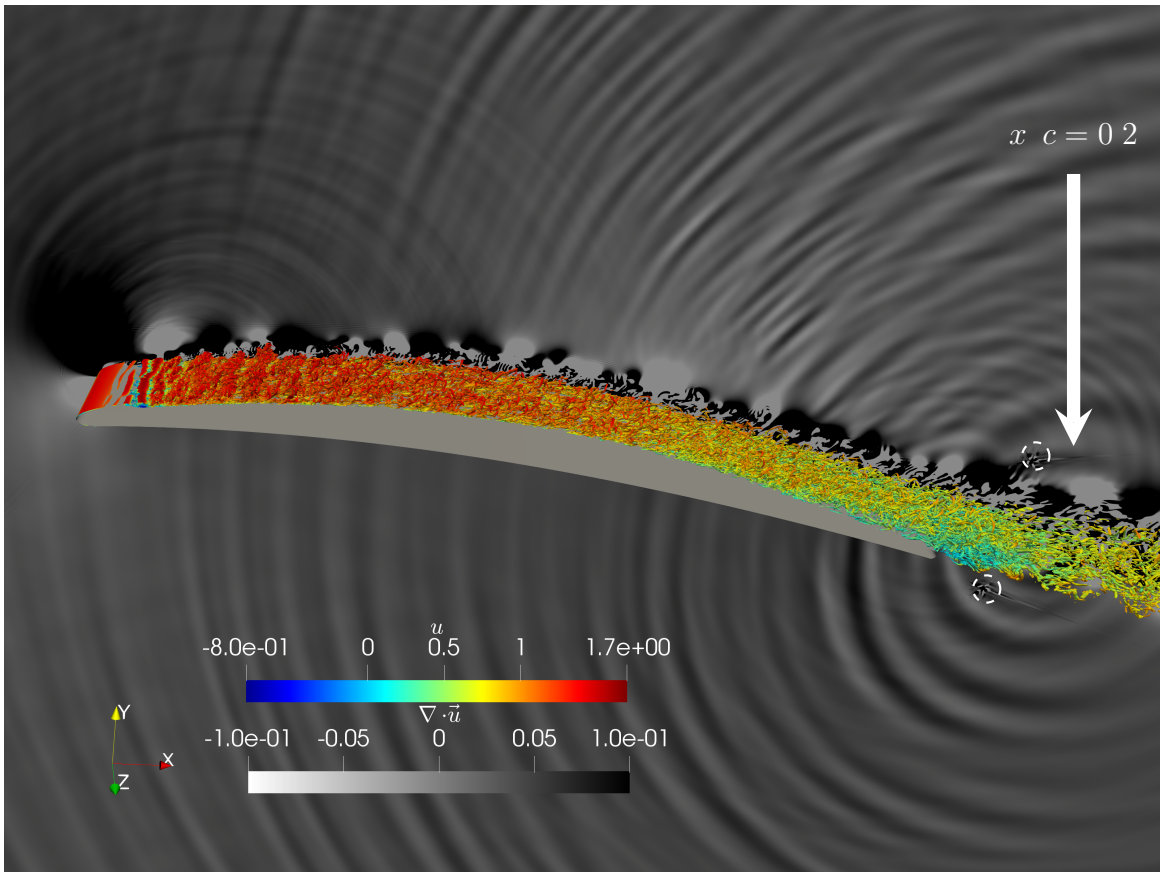

Figure 5.41 Swirling strength criterion $_{ci} = 70$ iso-contours colored by streamwise velocity together with dilatation field (black/white) around CD airfoil.

5.6 Acoustics

5.6.1 Near Field

For the near field, the instantaneous dilatation field (divergence of velocity $\nabla \cdot \boldsymbol{u}$) together with the turbulent structures is presented in Fig. 5.41. In order to exclude spurious effects in the visualization, the dilatation field shown in Fig. 5.41 is computed using the same spatial operator (to compute $\nabla \cdot \boldsymbol{u}$) as in the simulation [Bechlars, 2015]. After reattachment, spanwise coherent rollers appear and then break down in the zero pressure-gradient region and then become turbulent upstream of the TE in the adverse pressure-gradient region. In the near wake, the laminar flow from the pressure side is shed and mixed with the turbulent flow from the suction side and finishes its transition which also involves minor coherent vortex shedding. It can be clearly seen that 3 noise sources exist in this simulation: a weak source from the leading-edge separation bubble, the traditional TE noise from the turbulent attached boundary layer diffracting at the TE and lastly, an extra source in the near wake around $x\ c = 0\ 2$ as indicated by the white arrow in Fig. 5.41. The extra noise source in the near wake seems as strong as or even stronger than the usual TE noise. The distance between 2 consecutive wave fronts as shown in Fig. 5.41 corresponds to a frequency around 6500 Hz. Some slightly spurious numerical artifacts marked by the white dashed circles in Fig. 5.41 can be seen at the 5-block corners in the visualization; yet they are seen to stay immobile and not contribute to the noise production from a series of instantaneous fields at a sampling frequency of 78 kHz for 1 flow-through time.

5.6.2 Far Field

In order to investigate the acoustic radiation from the airfoil trailing-edge, the simulation is coupled with an in-house Ffowcs Williams and Hawkings (FWH) solver *SherFWH* [Fosso-Pouangué *et al.*, 2012, 2014; Fosso Pouangué *et al.*, 2014; Sanjosé *et al.*, 2014a] for the computation of the far-field acoustic pressure from information in the near field recorded during the simulation. A porous FWH formulation and solid wall FWH formulation are used here and are referred to as FWH-Porous and FWH-Solid. Care has been taken to place the porous control surface as close as possible to the airfoil where the mesh has a high resolution, while still including all dominant sources in the flow field. In Fig. 5.42, the FWH-Porous surfaces are illustrated in color: a C-contour shape surface around the airfoil (blue), a connection surface at the TE region and a surface in the wake together with an end-cap (green) surface in the wake where the turbulence intensity is lower than 10%.

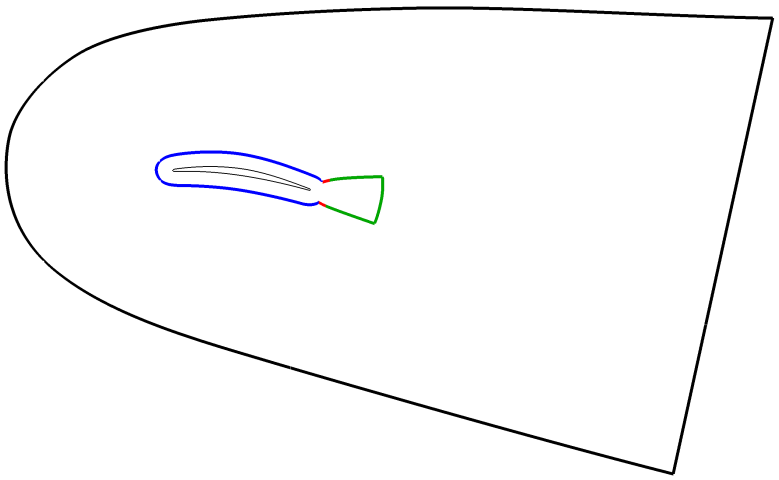

Figure 5.42 Illustration of the location of the FWH-Porous surfaces (colored solid lines).

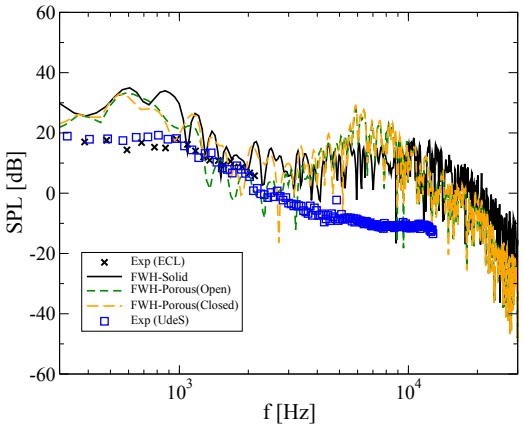

Figure 5.43 Acoustic far-field prediction using porous and solid Ffowcs Williams and Hawkings surfaces of the CD airfoil at $2m$ in the midspan plane at 90 from the trailing-edge.

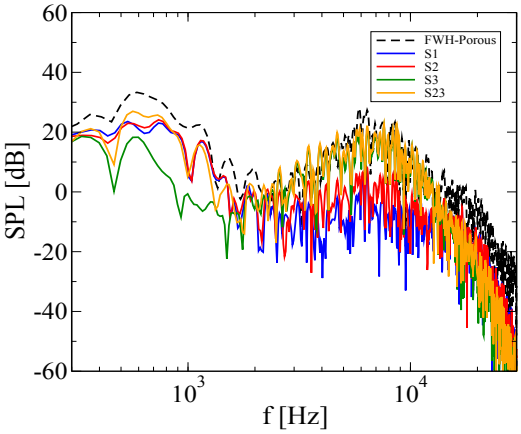

Figure 5.44 Contributions from different patches of the FWH-Porous surfaces to far-field noise.

The FWH-Porous and FWH-Solid surfaces are recorded as instantaneous snapshots during the simulation and then are fed to the *SherFWH* solver. Finally, in order to compare with the experimental data, the predicted far-field PSD for an actual airfoil span L is calculated from the computational slice by

$$S_{pp\,FWH} = \frac{L}{L_{DNS}} \quad S_{pp\,DNS} \tag{5.22}$$

As the spanwise coherence length of the surface pressure is smaller than the computational domain size at nearly all frequencies for this case as shown in Fig. 5.17, such a formulation is valid.

Fig. 5.43 shows the results from the predicted FWH farfield noise level compared with the experimental data from far-field microphones. The two FWH surfaces give good agreement with experimental data for the mid frequency range. In the FWH-Porous case, a secondary hump over the high frequency range is present and is believed to be caused by the secondary noise source in the near wake shown in Fig. 5.41. The contribution to the noise prediction from the end-cap surface can be ignored in this case as the results for FWH-Porous surfaces with and without the end-cap show nearly no difference. In order to locate the source responsible for the extra high-frequency hump, the contribution for different patches of the FWH-Porous surfaces is studied and the results are shown in Fig. 5.44. In this plot, $S1$ the noise from the surfaces in red color in Fig. 5.42, which accounts for the pressure fluctuations inside the boundary layer and part of the TE area; $S2$ the noise from the surfaces in the TE area where the traditional TE noise exists; $S3$ the noise from the surfaces that envelop the near wake region; and finally the $S23$ is a combination of $S2$ and $S3$. From Fig. 5.44, it is clear that:

The source in the near wake is responsible for the high frequency hump;

The noise contribution from the transition bubble at the LE is negligible at the given observer location above the TE;

The traditional TE is mainly responsible for the low-mid frequency range noise.

In the FWH-Solid case, no secondary hump is shown as opposed to the FWH-Porous case. Yet the spectra oscillate over the high frequency range which can be due to the influence from the wake.

As in the pressure spectra and near field results discussed in *Section 5.3*, for the first time, such an extra noise source in the near wake is observed in the far-field noise for such a flow case.

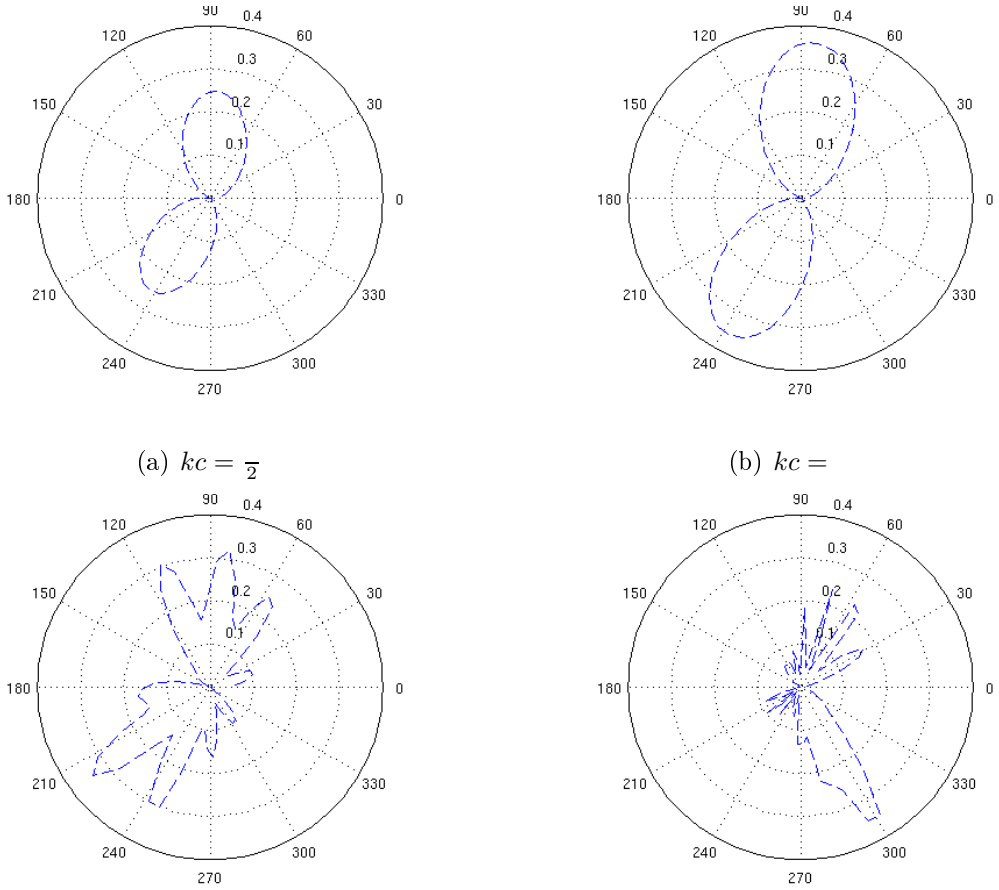

(a) $kc = \frac{}{2}$ (b) $kc =$

(c) $kc = 4$ (d) $kc = 8$

Figure 5.45 Single frequency directivity pattern from FWH-Solid results.

Fig. 5.45 shows the single frequency directivity pattern from the solid wall surfaces. Far field noise data predicted by the $SherFWH$ solver for 72 equi-spaced observers at 1.2 m from the TE in the mid-span plane was used for theses plots. In order to guarantee the synchronization of the signals, the recording interval was chosen so that all 72 observers have peak values which finally give a frequency resolution of 45 Hz. This resolution could be improved by a longer signal length but it is sufficient for the current discussion. As in this case the CD airfoil has an 8 geometric angle of attack, in these directivity plots in Fig. 5.45, the radian coordinates system is set so that the 0 position is aligned with the airfoil chord direction, not the streamwise direction, for better illustration. Fig. 5.45 suggests that quadrupole sources become important with higher kc. For the highest kc value shown here, the directivity pattern is significantly changed by the wake. The effects of the angle of attack and airfoil camber can be seen from the orientation of the lobes and the asymmetry. Compared with the directivity pattern predicted by Amiet's based model [Moreau and Roger, 2009] taking the back-scattering effects into account, the directivity

pattern from the current DNS shows a clear discrepancy in the orientation of the lobes (lobe peak locations in the polar map). For higher kc values ($kc = 4$ and $kc = 8$), there exists a noticeable difference on the contributions respectively from the suction and pressure side of the airfoil. Furthermore, compared with the directivity pattern of a slightly cambered Eppler387 airfoil at 2 angle of attack [Oberai *et al.*, 2002], the camber effects and the effects of the angle of attack of the current DNS are more pronounced because the deviation from the Amiet's directivity [Moreau and Roger, 2009] is larger. Convective effects [Moreau and Roger, 2009; Oberai *et al.*, 2002] were reported from a high fidelity compressible LES [Wolf *et al.*, 2012b] for a similar chord based Reynolds number and for a slightly higher Mach number on a NACA0012 airfoil. In that compressible LES case, effects of the Mach number were shown and the lobes of the directivity plots were oriented towards the LE where the Mach number is higher. Yet such a phenomenon is not observed from the current compressible DNS. This difference is assumed to be caused by the difference of transition mechanism at the LE and consequently its contribution to the radiated noise. On the CD airfoil, the transition at the LE is caused by a short separation bubble yet in the LES of the NACA0012 airfoil the transition is trigged by steady suction and blowing (in the experiment tripping was used) at the LE in order to match the turbulent boundary layer at the TE with experimental data, and this artificial transition can modify the noise contribution from the LE.

As seen above, a high frequency hump is observed in the farfield for the first time for this airfoil case and it is believed it is caused by the additional high frequency noise source in the near wake. This surmise is obtained from previous analysis can be concluded as:
Dilatation field shows a secondary source dominant by a dominant frequency around 6500 Hz;

High frequency hump shown in the wall-pressure PSD for sensor #26 near the TE;

Higher level of correlation from sensors near the TE for high frequency range;

Farfield directivity pattern for high frequencies highly deviated by the wake.

In order to confirm this surmise, further analysis are conducted.

5.6.3 Comparison with a Compressible LES with Complete Geometry

A new compressible LES of CD airfoil using AVBP developed by CERFACS and IFP-EN with high resolution both in space and in time was conducted in order to confirm the source in the wake. In order to distinguish the incompressible LES [Christophe *et al.*,

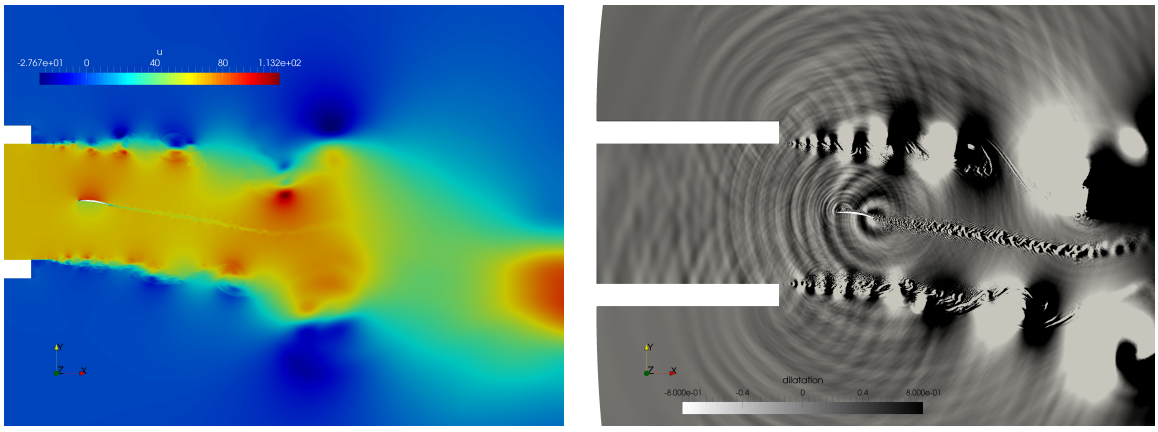

(a) (b)

Figure 5.46 Instantaneous flow field from AVBP LES: (a) velocity magnitude and (b) dilatation.

2009; Wang *et al.*, 2009] mentioned before, this newly produced LES will be referred here and after as AVBP LES.

AVBP solves the three-dimensional compressible Navier-Stokes equations for turbulent reacting flows, using both the DNS and LES approaches on unstructured and hybrid meshes. The filtered compressible Navier-Stokes equations exhibit SGS tensors and vectors describing the interactions between the unresolved and the resolved motions. The influence of SGS on the resolved motion is taken into account in AVBP by a SGS model based on a turbulent kinematic viscosity $_t$. Such an approach assumes that the effect of the SGS field on the resolved field is purely dissipative. Various SGS models are available in AVBP, only differing in the estimation of $_t$. The WALE SGS model [Nicoud and Ducros, 1999] was used for the current LES and a DNS patch at the LE was used to better capture the transition process.

The current AVBP LES was conducted at the same chord based Reynolds number $Re_c =$ 150 000 as in the DNS and the free-stream Mach number was chosen to be $Ma = 0\,2$. Lax-Wendroff [Lax and Wendroff, 1960] was used for initializing the flow field and TTG4A [Donea and Huerta, 2003] (one of the Taylor-Galerkin based schemes [Donea, 1984; Donea and Huerta, 2003; Donea *et al.*, 1987] available in AVBP) was used for the final simulation, which gives a 3^{rd} order accuracy in space and 4^{th} order in time. The mesh containing 11 million points was refined along the jet shear layer line, around the airfoil and as well in the wake center line. It should be mentioned that the mesh between the jet shear layer and the airfoil boundary layer is still coarse in order to avoid extra computational cost from the potential interaction from jet shear layer and the boundary layer. This is a similar

strategy used in a LES using the same code taking the installation effects into account for a high-lift device (HLD) [Salas *et al.*, 2016; Salas and Moreau, 2015]. Yet this is sufficient for giving a proper loading on the airfoil and the study of the noise source region, which are the two most important requirements for the current AVBP LES. The spanwise extent is 0 11c where c is the chord length. The AVBP LES was run in total for 20 flow-through times.

The instantaneous flow field from the AVBP LES is shown in Figs. 5.46(a) and 5.46(b). Big structures are formed in the shear layer from the nozzle but they seem to have minor interactions with the airfoil. No significant refraction from the shear layer is observed as Mach number is low.

The mean flow field is evaluated after the AVBP LES is statistically converged. As can be seen from Fig. 5.47, the mean streamwise velocity field is quite similar to that from the DNS when scaled in the same value range. Fig. 5.48 shows the mean pressure distribution of the AVBP LES compared with previous results on the CD airfoil in Fig. 5.6(a). The AVBP LES predicts the loading over the airfoil quite well.

The wall-pressure fluctuation is then compared with the DNS results. The wall PSD is plotted against the *Strouhal* number defined as $fc\ U_0$ where f is the frequency, c is the chord length and U_0 is the free-stream velocity. In Fig. 5.49, the wall-pressure spectra from sensor #5 and sensor #26 are compared with the DNS results. The match between DNS and AVBP LES is excellent for most of the Strouhal numbers. At very high frequency, the AVBP LES shows a cut-off, which is from the SGS model. The shape of the spectra from sensor #26 seems to be flatter than that from the DNS at low frequencies. This flatter shape is also observed from the LBM-DNS [Sanjosé *et al.*, 2011] with the complete

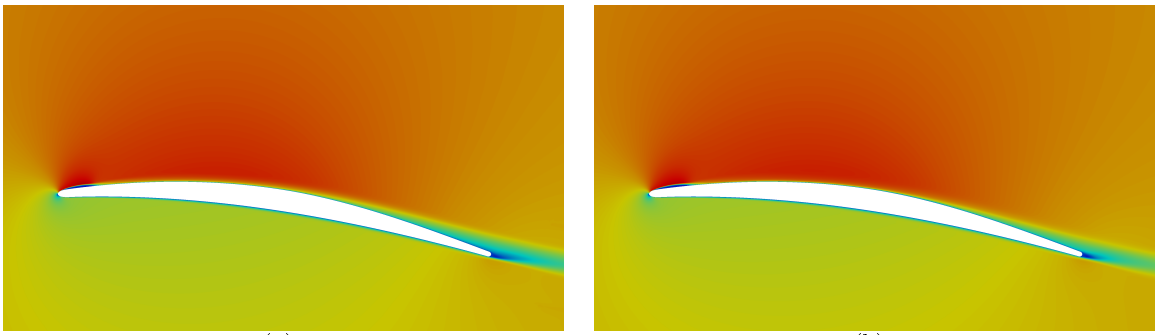

(a) (b)

Figure 5.47 Mean streamwise velocity field comparison between DNS and AVBP LES: (a) DNS and (b) AVBP LES.

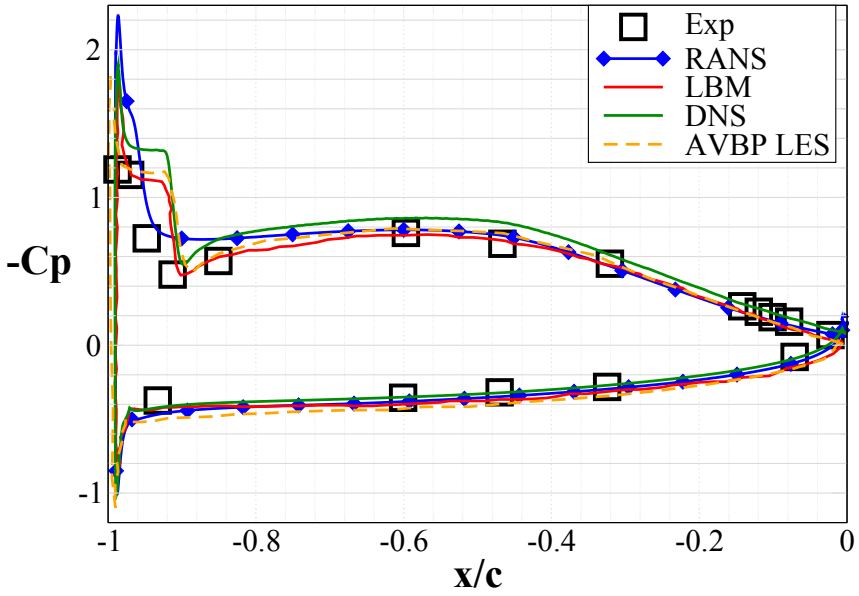

Figure 5.48 Static lift distribution from AVBP LES compared with previous results in Fig. 5.6(a).

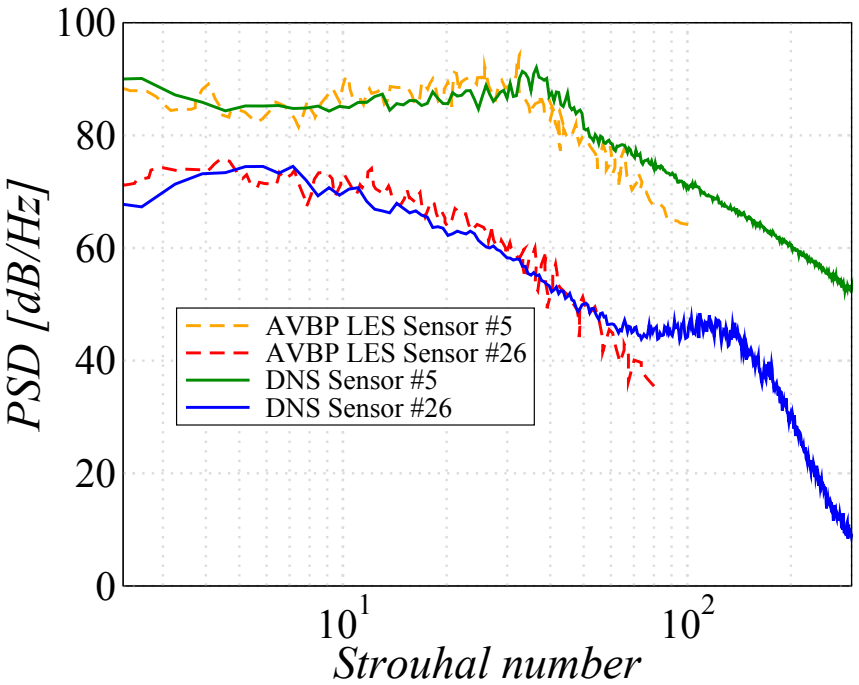

Figure 5.49 Wall-pressure fluctuation spectra comparison between DNS and AVBP LES.

wind tunnel geometry and from experiment (Fig. 5.15). This difference with DNS results is thus assumed to be caused by the jet shear layer.

For the near field, dilatation around the airfoil is shown in Fig. 5.50 both from DNS and AVBP LES. Besides the traditional TE noise, a secondary noise source is present in the near wake both in the DNS and LES, although the location of this secondary noise is slightly different. The one from AVBP LES seems a bit further downstream in the wake compared with DNS. It should be mentioned that the dilatation field from the AVBP LES is calculated by (1)(t) whereas the in the DNS it is calculated by $\cdot \boldsymbol{u}$. They were calculated both using code-based gradient operators to exclude possible visual deviation. At low Mach number such as this case, these two ways of calculating the dilatation gives similar results in the AVBP LES. This is the first time from a compressible high resolution simulation for such a flow case with complete wind tunnel geometry that shows a secondary noise source in the near wake. As shown in Fig. 5.51, it should be mentioned that, the AVBP LES has a very refined mesh resolution both on the airfoil and the near wake which is a prerequisite for the comparison with DNS. Furthermore, it should be noticed that in the AVBP LES, contrary to the DNS mesh, there is no block interface present in the near wake, which indicates again that the extra noise source from the dilatation field from DNS is actually physical.

The FWH analogy is used for the AVBP LES as in the DNS for predicting the farfield sound. Both solid wall from airfoil surface and two porous surfaces around the airfoil are taken as shown in Fig. 5.52(a). In this figure, the solid wall is named as "solid bnd" and the two porous surfaces are named as "close inft" and "further intf". The directivity of the integrated SPL from 500 Hz–12000 Hz from these surfaces are shown in Fig. 5.52(b). The solid wall shows dipole shape while the porous surfaces show more monopole shape.

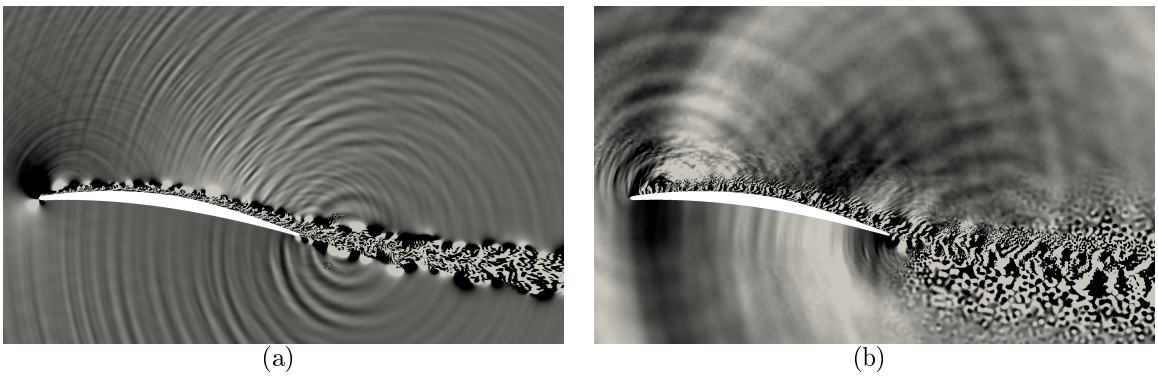

(a) (b)

Figure 5.50 Instantaneous dilatation field comparison between DNS and AVBP LES around the airfoil: (a) DNS and (b) AVBP LES.

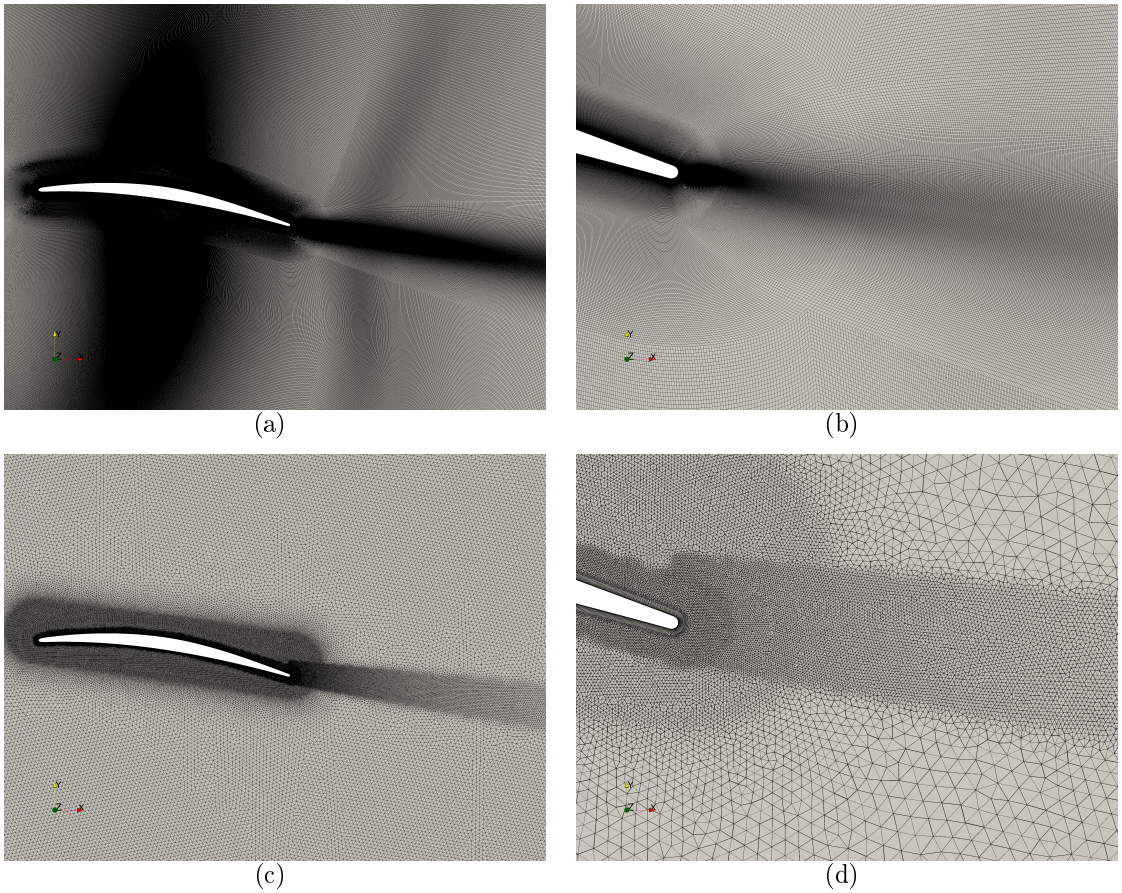

Figure 5.51 Mesh comparison between DNS and AVBP LES: (a)(b) DNS and (c)(d) AVBP LES.

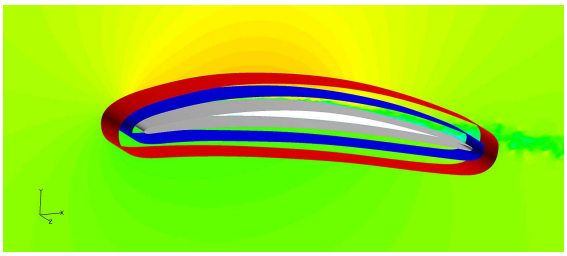

(a)

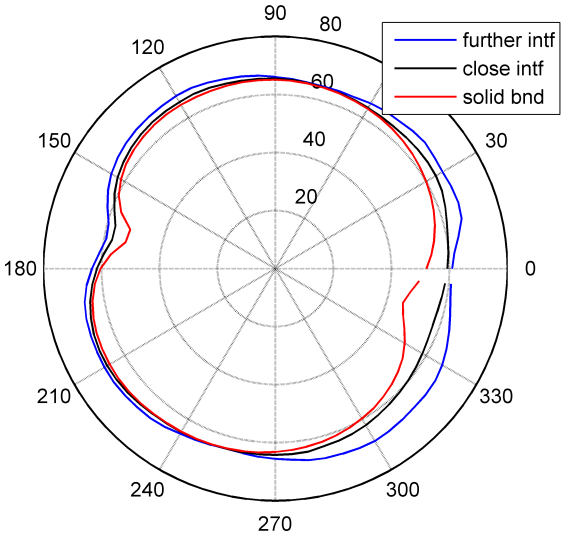

(b)

Figure 5.52 FWH predicted farfield directivity from AVBP LES: (a) illustration of the positions of chosen surfaces and (b) directivity of integrated SPL from 500 Hz–12000 Hz.

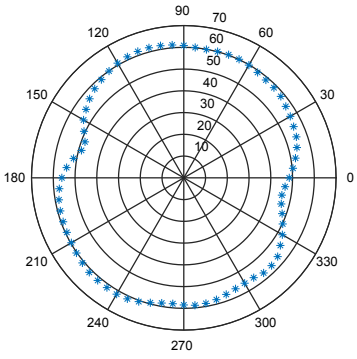

(a)

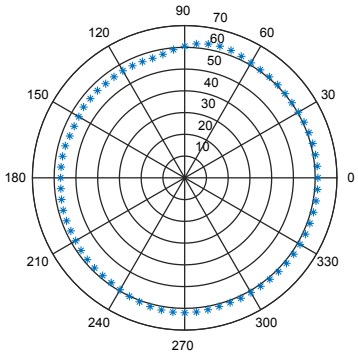

(b)

Figure 5.53 Directivity of integrated SPL from 500 Hz–12000 Hz from FWH-Solid and FWH-Porous (Closed) in Fig. 5.43.

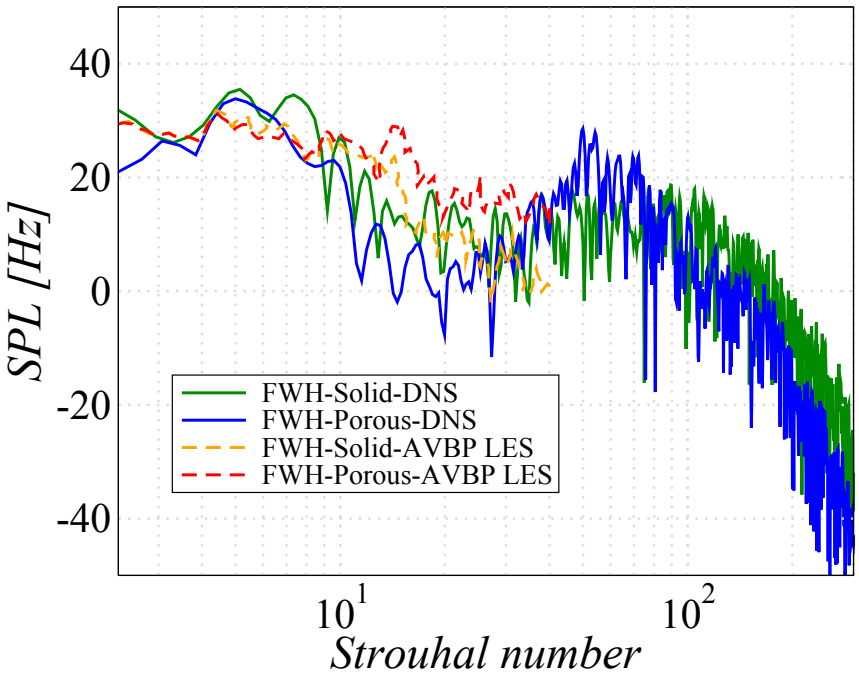

Figure 5.54 Comparison between DNS and AVBP LES: acoustic far-field prediction using porous and solid Ffowcs Williams and Hawkings surfaces.

Furthermore, the porous surfaces have higher SPL level which indicates that more noise sources are included in the porous surfaces. Such a directivity from the DNS is plotted in Fig. 5.53. Same information is observed as in Fig. 5.52. The farfield SPLs predicted from both the DNS and AVBP LES are compared in Fig. 5.54 against the Strouhal numbers. A dip for the mid-frequency in the DNS is not found in the AVBP LES, which is assumed to be caused by the interaction between the jet shear layer and the airfoil. For other frequency range, these two simulations show a good agreement.

In all, despite very different code structures between the DNS and AVBP LES, for the flow at same Re_c and similar Ma, the AVBP LES shows quite a similarity in terms of basic flow patterns over the airfoil compared with the DNS and of acoustics. The extra noise source in the near wake exists also in the AVBP LES.

5.7 Conclusion

A compressible direct numerical simulation was conducted of a controlled-diffusion airfoil at a chord based Reynolds number of $Re_c = 150\ 000$ and a free-stream Mach number of $Ma = 0\ 25$ at 8 angle of attack that is embedded in a wind-tunnel flow. The quality of the simulation was carefully checked and it was ascertained that the mean installation effects was reproduced properly and the DNS was successfully capturing all the relevant flow

features that were known to exist from previous experiments and unsteady simulations. Particularly, the present Navier-Stokes DNS data was in very close agreement with newly produced experimental data in a quieter anechoic chamber at Université de Sherbrooke and previous LBM-DNS. The present results prove that the current DNS can be considered as a high-fidelity database for further analysis for such a flow case.

On the aerodynamic side, the mean pressure gradient effects on the development of the flow in the boundary layer were studied through the evolution of the velocity gradient tensor invariant dynamics. It is the first time such an analysis is conducted on a spatially evolved flow over a blade shape airfoil submitted to various mean pressure gradient conditions. The mean profiles from the turbulent boundary layer at different chordwise positions suggest that pressure gradient greatly changes the topology of the boundary layer. Compared with zero pressure gradient condition, an adverse pressure gradient acts as a reinforcement of the intense momentum exchange by fluctuating velocities, which is extended from viscous-sub-layer to log-layer and even to the edge of the outer-layer. This gradient leads to a platform shape for wall parallel Reynolds stress components and a hump shape connected by two peak values of turbulence production terms.

The mean evolution of the velocity gradient tensor invariant dynamics was found to vary strongly for regions undergoing favorable, zero and adverse pressure gradients. The shape of the QR plots of the log-layer and the outer-layer strongly depends on the mean local pressure gradients while the viscous sub-layer has an invariant character: oval shape independent of the pressure gradient conditions. Furthermore, this evolution changes also greatly with the distance to the wall. Key changes are explained in the context of QR plots with mean trajectories and as well from mean profiles giving both outer and inner scale as reference. The non-linearity and viscous diffusion in the overall evolution of the velocity gradient tensor invariant dynamics maintain their respective invariant characteristic for all investigated regions regardless of the different pressure gradient conditions. The non-linearity drives the global shape of the QR plots. The viscous diffusion drives all structures towards the origin. These two aspects thus do not appear to be the major reasons for the changes of the turbulence evolution for the different investigated regions. In fact, the coupling of the pressure Hessian with the velocity gradient, which is strongly affected by the mean pressure gradient conditions and the wall, is the major factor that drives all the changes of the invariant dynamics in this flow. From a QR-space analysis point of view, this coupling seems to be the most significant feature that affects the turbulence development and is highly influenced by the local mean pressure gradient and wall normal distance. The comparison between previous zero pressure gradient turbulent

boundary layer data and the results from favorable and adverse pressure gradient regions in this airfoil flow shows that the pressure gradients have a significant impact at least in the outer-layer and log-layer of the flow. The adverse pressure gradient leads to more rolling features to the mean trajectories in these two layers and suppresses the vortical stretching regime. The wall effects are contrasted with previous studies, and a comparison between the trailing edge flow and the flow in the near wake is also provided. The wall is observed to mainly suppress the vortical stretching features of the flow and the flow exhibits a uniform feature in QR-space, known as a *teardrop* in the absence of the wall. Lastly, despite different flow conditions for the investigated regions from the current flow case, the general mean lifecycle of turbulent structures stays unchanged in the QR-space.

On the acoustic side, the acoustic near field was obtained directly from the simulation. Besides the previously observed noise source from the leading-edge transition bubble and the trailing-edge noise from the interaction between the convecting turbulent boundary layer and the trailing-edge, an extra noise source appears to exist in the near wake. Such a phenomenon is found for the first time for such a flow case from a compressible DNS approach with a high resolution grid both around the airfoil and in the near wake. The acoustic far field is predicted using a Ffowcs Williams and Hawkings solver both taking the solid wall and porous surface as noise sources. Both of the surfaces show a good agreement with available experimental results. The effect of the end-cap surface from the porous Ffowcs Williams and Hawkings result shows minor influence on the noise prediction. The additional noise source found from the near field contributes to the high frequency hump in the radiated far field.

In order to confirm such a new noise source, a new compressible LES using AVBP, with 3^{rd} order accuracy in space and 4^th order in time, taking the entire wind tunnel nozzle geometry, was conducted. The AVBP LES was run at almost the same flow condition ($Re_c = 150\ 000$, $Ma = 0\ 2$). The hybrid mesh is refined on the jet shear layer, airfoil boundary layer and the wake line. Despite very different code structures between the DNS and AVBP LES, the AVBP LES shows quite a similarity in terms of basic flow patterns over the airfoil compared with the DNS and of acoustics both in the near field and farfield. The extra noise source in the near wake also exists in the AVBP LES. Given that the AVBP mesh is very refined in the wake and has no block connection as in the DNS, this confirms again that the extra noise source in the DNS is actually physical.

Inspired by a recently proposed technique, the wavenumber-frequency spectra is used to understand the contribution from aerodynamics and acoustics from the wall-pressure fluctuation in the boundary layer near the TE. At low frequencies, the acoustic contribution

is hardly seen and is mixed with the convective contribution. With increasing frequencies, the acoustic and convective contributions become separate. At the highest frequencies, the acoustic contribution becomes dominant. The directivity pattern changes gradually from a compact dipole shape to non-compact one with multiple lobes. The direction of propagation seems slightly more pronounced in the upstream direction with highest frequencies. For lower frequencies, no privileged direction of propagation seems noticeable. Finally, it can be concluded that the high frequency wall-pressure fluctuations is almost purely acoustic, which, indicates that the high frequency phenomenon that has been observed in the wall-pressure PSD and wall-pressure coherence, are acoustics induced phenomena.

CHAPTER 6

Conclusion et Perspectives pour les Travaux Futurs

2 SND compressibles de l'écoulement autour d'un profil NACA6512-63 et du profil CD, ont été effectuées, à un nombre de Reynolds de $Re_c = 150\ 000$ basé sur la corde et à un nombre de Mach amont $Ma = 0\,25$, en prenant en compte les effets d'installation de la soufflerie. Dans les deux cas, un calcul 2D RANS de l'écoulement autour du profil a d'abord été réalisé. Ce dernier prend en compte la géométrie complète de la forme de la tuyère utilisée dans les essais. Ensuite, un domaine tronqué pour la SND autour du profil dans le cœur potentiel du jet de la soufflerie est extrait du domaine de 2D RANS sur lequel le maillage est raffiné pour satisfaire les critères de la SND. La distribution de vitesse aux limites du domaine tronqué était été extraite du calcul 2D RANS. Cette distribution définissait l'entrée 2D stable de vitesse pour le domaine de la SND. La SND était d'abord exécutée en 2D d'après les champs de 2D RANS interpolés sur le maillage de la SND, puis est extrudée en 3D pour la simulation finale. Les sources surfaciques et volumiques pour les études de la turbulence et de l'acoustique étaient entregistrées une fois la simulation statistiquement établie. Les sujets principaux dans cette étude comprennent:

Les résultats des SND comparés exhaustivement avec les données existantes des simulations et des expériences sur les champs moyens, les spectres de pression pariétale, les corrélations & les longueurs de cohérence, ainsi que le bruit au champs lointain prédit par les analogies acoustiques;

Des conditions limites stables réussies pour l'écoulement complexe sur le profil NACA6512-63 et un bruit riche capturé;

Une étude détaillée sur l'effet du gradient de pression moyen sur le développement de l'écoulement à l'extrados du profil CD par une analyse QR, couplée avec une analyse sur les profils moyens;

Une investigation complémentaire sur les sources de bruit observées dans la SND du profil CD.

6.1 Découvertes Principales

6.1.1 SND du Profil NACA6512-63 à 0 d'AdA

Même si ce cas est difficile à simuler à cause de l'écoulement étroit du jet de la soufflerie, grâce à des conditions limites bien choisies, les effets d'installation sont généralement bien reproduits en comparant avec les résultats d'essais. A l'intrados, la transition se produit au BA et une couche limite totalement turbulente existe jusqu'au BF. A l'extrados, une couche limite instable et décollée au BF donne une source de bruit supplémentaire par rapport au cas trippé simulé auparavant dans lequel une couche limite turbulente attachée était présente. Il est démontré de plusieurs manières que la couche limite instationnaire au BF à l'extrados du cas non-trippé change la topologie de l'écoulement à l'intrados. Des plus grosses structures sont formées en raison de la couche limite oscillante et la position de transition a changé au BA. Pour le champ acoustique, la prédiction des surfaces poreuses FWH donne un meilleur accord avec les données expérimentales pour le cas non-trippé. Le modèle d'Amiet avec une correction sur l'effet de rétrodiffusion [Roger and Moreau, 2005, 2010] était utilisé pour les cas trippé et non-trippé. Ce modèle donne une bonne prédiction en général pour les deux cas. Pourtant, le choix de l'endroit pour extraire les entrées de ce modèle pour le cas non-trippé est sensible en raison de l'écoulement plus complexe existant au BF. Ce fait peut par conséquence dévier la prédiction. Le couplage acoustique de la bulle de recirculation au BA à l'intrados et la transition au BF à l'extrados doit être examiné plus en détail.

6.1.2 SND du Profil CD à 8 d'AdA

A l'intrados, l'écoulement reste laminaire jusqu'au BF où un échappement tourbillonaire se produit. A l'extrados, l'écoulement transitionne après une fine bulle de recirculation au BA et puis reste turbulent et attaché jusqu'au BF avec successivement un GPF, un GPN et finalement un GPA dans la région au BF. L'effet du gradient de pression moyen sur l'écoulement à l'extrados est discuté en utilisant une analyse QR. L'évolution moyenne de la dynamique de l'invariant du tenseur de gradient de vitesse varie fortement avec les gradients de pression moyens différents (GPF, GPN et GPA). Cette évolution change aussi beaucoup en fonction de la distance à la paroi. Le couplage du Hessien de pression et le gradient de vitesse est l'élément majeur qui provoque tous les changements de la dynamique de l'invariant dans cet écoulement. Le gradient de pression donne un effet important au moins dans la zone externe et dans la zone logarithmique de cet écoulement. Le GPA favorise plus d'enroulements des trajectoires moyennes dans ces deux zones et empêche l'étirement tourbillonaire. La paroi empêche aussi principalement ce régime. Un

caractère universel se présente dans l'espace QR, connu comme la *larme*, sans la présence de la paroi, où l'écoulement est plus isotrope. Du point de vue acoustique, on observe la source liée à la transition de l'écoulement dans la bulle de recirculation comme identifié précédemment à bas nombre de Reynolds, celle liée à l'intéraction de la couche turbulente avec le BF, et une source de bruit supplémentaire dans le proche sillage. C'est la premiére fois que ce phenomène est observé pour cet écoulement. Après plusieurs vérifications numériques, y compris une nouvelle SGE compressible de haute résolution, cette source de bruit supplémentaire dans cette SND apparaît bien physique.

6.2 Les Perspectives pour les Travaux Futurs

Pour le cas de profil NACA6512-63 les effets instationnaires de l'intéraction entre la couche de cisaillement du jet et le profil peuvent influencer la topologie de l'écoulement. Cet aspect demande beaucoup plus de ressources numériques pour être confirmé lorsqu'on prend en compte la géométrie de la tuyère du jet dans la simulation. De plus, comme ce cas est très similaire au cas présenté par [Sanjosé *et al.*, 2017] à l'extrados, on pourrait, avec un signal plus long, constater les évènements *calmes* et *intenses* par Sanjosé *et al.* [2017], ce qui pourrait mettre en lumière le mécanisme de génération du bruit à cause de la séparation et le recollement de l'écoulement au BF. Le couplage du rayonnement de bruit issu de la bulle de décollement au BA à l'intrados et la couche limite oscillante au BF à l'extrados serait aussi intéressant à approfondir. Avec la croissance des ressources informatiques le comportement de l'écoulement lié à l'augmentation du nombre de Reynolds pourrait aussi être étudié.

Comme continuation du travail sur le cas du profil CD, 3 aspects pourraient être examinés. Premièrement, comme il s'agit d'un écoulement variant spatiallement sur un profil de la forme d'une pale, une étude sur les structures turbulentes d'aprés $_{ci}$ liée à l'influence du gradient de pression moyen pourrait être une approche possible pour obtenir plus d'information sur ce cas. L'étude de l'intermmitence et l'analyse quadrant pourraient être réalisées et les résultats pourraient être comparés avec les bases de données accessibles [Jiménez *et al.*, 2010] sur les couches limites des plaques planes et des canaux. Cette étude pourrait être intéressante car aucune comparaison complète n'a été faite comprenant une couche limite de profil avec un GPA considérable au BF. Deuxièmement, la validation et la modification du travail de Panton and Linebarger [1974] en progrès par cette SND peuvent donner plus d'information sur la fiabilité de certaines hypothèses, surtout liées aux effets de la présence de l'APG. Finalement, pour mieux comprendre l'origine de la source du bruit supplémentaire dans le sillage proche, une analyse de stabilité globale, une

analyse de l'instabilité secondaire et un post-traitement du filtrage du signal sont faisables pour une investigation plus profonde.

CHAPTER 7

Conclusion and Perspectives for Future Work

7.1 Summary of Flow Cases

2 compressible DNS of the flow over a NACA6512-63 airfoil and the CD airfoil at a chord based Reynolds number of $Re_c = 150\ 000$ and at a free-stream Mach number $Ma = 0\ 25$ have been conducted, taking mean wind-tunnel installation effects into account. In both cases, firstly a 2D RANS computation of the flow around the airfoil was conducted, taking into account the complete geometrical configuration of the nozzle shape that were used in the experiments. In a second step, a truncated domain for DNS simulation around the airfoil in the jet potential core was extracted from the 2D RANS domain and then the mesh for DNS was refined. The velocity distribution around the boundaries of the truncated domain was taken from the 2D RANS. This data was then used to define a steady 2D inlet velocity profile in the DNS domain. A 2D DNS was then started from the RANS solution interpolated on the DNS mesh and then extended to 3D for the final simulation. The surface and volume sources for turbulent and acoustic studies were recorded at high sampling frequencies after the flow field is statistically converged. Primary topics that have been studied include:

DNS results thoroughly compared with available numerical and experimental data sets on mean flow field, wall-pressure spectra, correlation & coherence length, and far-field noise coupled with acoustic analogies;

A proper stable boundary condition set for simulating a rather complex flow over the NACA6512-63 airfoil and a rich radiated sound field captured;

A detailed study on the effect of the mean pressure gradient on the flow development on the suction side of the CD airfoil through a QR analysis combined with an analysis on the mean profiles;

A further investigation on the noise sources observed in the DNS of CD airfoil case.

7.2 Principle Findings

7.2.1 DNS of NACA6512-63 Untripped Airfoil at 0 AoA

Although it is a difficult case to be simulated because of the narrow stream from the wind-tunnel jet, the mean installation effect is generally well captured when compared with experiments, due to the proper sets of boundary conditions. Transition occurs naturally on both sides of the untripped airfoil. On the pressure side transition occurs at LE and a fully turbulent boundary layer exists close to the trailing edge. On the suction side, a flapping and separated boundary layer at the TE leads to an extra noise source compared with a tripped case previously simulated where an attached turbulent boundary layer is present. Besides, from multiple aspects in this study, the flapping shear layer at the TE on the suction side of the untripped airfoil is shown to change the flow topology on the pressure side. Larger structures at the TE on the pressure side are formed due to the flapping shear layer and such an influence has even modified the transition location at the LE. For the acoustic field, the porous FWH surface shows a better agreement with experimental data for the untripped case. Amiet's model with the correction of the back-scattering effects [Roger and Moreau, 2005, 2010] was used for both the untripped and tripped airfoil to predict the farfield noise. It gives a good overall prediction for both the untripped and tripped cases. However, the chosen location for the inputs of the model is very sensitive because of the more complex flow existing at the TE for the untripped airfoil and can deviate the prediction. The effects from the acoustic coupling of the recirculation bubble at the LE on the pressure side and the transition at the TE on the suction side needs to be further considered.

7.2.2 DNS of CD Airfoil at 8 AoA

On the pressure side, the flow stays laminar until the TE where minor vortex shedding appears. On the suction side, the flow transitions after a short separation bubble at the LE then stays turbulent and attached till the TE. It experiences a mean FPG, a ZPG and finally an APG in the TE region. The mean pressure gradient effects on the flow on the suction side are discussed in detail through a QR analysis. The mean evolution of the velocity gradient tensor invariant dynamics is found to vary strongly for regions undergoing FPG, ZPG and APG. This evolution changes also greatly with the distance to the wall. Key changes are explained in the context of QR plots with mean trajectories and as well from mean profiles giving both outer and inner scale as reference. The coupling of the pressure Hessian with the velocity gradient is the major factor that drives all the changes of the invariant dynamics in this flow. The pressure gradients is shown to have

a significant impact at least in the outer-layer and log-layer of the flow. The adverse pressure gradient leads to more rolling features to the mean trajectories in these two layers and suppresses the vortical stretching regime. The wall is observed to mainly suppress the vortical stretching features of the flow. The flow exhibits a uniform feature in QR-space, known as a *teardrop* in the absence of the wall, where the flow is more isotropic. On the acoustic side, besides the previously observed noise source from the leading-edge transition bubble and the trailing-edge noise from the interaction between the convecting turbulent boundary layer and the trailing-edge, an extra noise source exists in the near wake. Such a phenomenon is found for the first time for such a flow case from a compressible DNS approach. Through several verifications including a newly produced high resolution compressible LES, the extra noise source in the DNS is proved to be actually physical. The wall-pressure fluctuations are finally filtered by a wavenumber-frequency spectra analysis to gain more insight into the contributions from aerodynamics and aeroacoustics.

7.3 Perspectives for Future Work

For the NACA6512-63 airfoil case, the unsteady effects from the interaction from the jet shear layer and the airfoil can have effects on the flow topology and need much more numerical resources to be confirmed by including the jet nozzle geometry. Moreover, as this flow case is very similar to the case reported by Sanjosé *et al.* [2017] on the suction side, with longer simulation time, the quiet and intense events observed in [Sanjosé *et al.*, 2017] may also occur in this case, which can reveal more complex noise generation mechanisms due to the flow separation and reattachment at the TE. The coupling from the radiation from the LE separation bubble on the pressure side and the radiation from the flapping shear layer on the suction side should also be investigated. With the growth of computational resources, the flow behaviour with increasing Reynolds number can also be studied.

As a continuation of the work on the CD airfoil, 3 major aspects can be looked at. Firstly, as this DNS involves a spatially evolved flow on a blade shape airfoil, to gain more information on the flow, the influence of the pressure gradient on the development of the turbulent structures can be studied through the $_{ci}$ criterion. The intermittency and quadrant analysis can be conducted and compared with available data sets such as [Jiménez *et al.*, 2010] on turbulent boundary layer from flat plates and channels. This study will be interesting since no such a complete comparison has ever been achieved on an airfoil that has a severe APG near the TE. Secondly, on noise modeling, the validation and modifica-

tion of Panton [Panton and Linebarger, 1974] and further extension of Rozenberg's model [Rozenberg, 2007] [Rozenberg *et al.*, 2010] [Rozenberg *et al.*, 2012] through the current DNS is currently in progress and will provide more understanding of the validation of certain hypothesis, especially from the influence of the presence of the APG. Lastly, to further understand the origin of the extra noise source in the near wake, a global stability analysis, a secondary instability analysis and a signal filtering process are possible approaches to be investigated.

Appendix

$_{ci}$-criterion

As firstly proposed by [Zhou *et al.*, 1999], $_{ci}$ is the imaginary part of the complex eigenvalue of the velocity gradient tensor $\boldsymbol{A} :=$ $\boldsymbol{u}$ when $\boldsymbol{A}$ is decomposed in Cartesian coordinates as

$$\boldsymbol{A} = \begin{matrix} \boldsymbol{v}_r & \boldsymbol{v}_{cr} & \boldsymbol{v}_{ci} \end{matrix} \begin{matrix} {}_r & & \\ & {}_{cr} & {}_{ci} \\ & {}_{ci} & {}_{cr} \end{matrix} \begin{matrix} \boldsymbol{v}_r & \boldsymbol{v}_{cr} & \boldsymbol{v}_{ci} \end{matrix}^{1} \tag{7.1}$$

where $_r$ is the real eigenvalue corresponding to the eigenvector $\boldsymbol{v}_r$, and $_{cr}$ $_{ci}$i are the conjugate pair of the complex eigenvalues with eigenvectors $\boldsymbol{v}_{cr}$ $\boldsymbol{v}_{ci}$i. In such a decomposition, as explained by [Zhou *et al.*, 1999], the local streamlines can be expressed by the coordinates system defined by ($\boldsymbol{v}_r$ $\boldsymbol{v}_{cr}$ $\boldsymbol{v}_{ci}$) such that the local flow is either stretched or compressed along the axis $\boldsymbol{v}_r$, while on the plane spanned by the vectors $\boldsymbol{v}_{cr}$ and $\boldsymbol{v}_{ci}$, the flow is swirling. The strength of the local swirling motion is then quantified by $_{ci}$.

Equivalent Threshold

There exists a variety of vortex identification methods that can be applied to the current flow cases to show the flow structures. These methods can be categorized as 3 types:

Vorticity based methods;

Velocity gradient tensor based methods;

Others.

The first category includes vorticity magnitude, vorticity lines and kinetic vorticity number. Such a category of method calculates the vorticity and then attempt to visualize the structures in different ways. Major cons come from the inability to distinguish between

	Compressible Flow	Comments
Q	Yes	Can possibly cut a structure
	Yes	Base of $_{ci}$-criterion
$_2$	No	Tailored for incompressible flows
$_{ci}$ and enhanced $_{ci}$	Yes	Clearest explanation on vortex path

Table 7.1 Characteristics of different velocity gradient tensor based criteria.

shear rotation and swirling motion [Kida and Miura, 1998]. It is more adapted for free shear layers and fails in boundary layers. Thus such a method can only be considered as a qualitative approach for the current flow if applied to. The second category is developed based on the velocity gradient tensor $\boldsymbol{A} :=$ $\boldsymbol{u}$ aiming for visualizing the details of the flow structures of wall bounded flows. Major ones in this category developed chronologically are Q-criterion [Hunt *et al.*, 1988], -criterion [Chong *et al.*, 1990], $_2$-criterion [Jeong and Hussain, 1995], $_{ci}$-criterion [Zhou *et al.*, 1999] (shown in Fig. 5.14) and enhanced $_{ci}$-criterion [Chakraborty *et al.*, 2005]. These velocity gradient tensor based criteria usually justify in terms of identifying the most intense structures yet the educed structure should be interpreted with care [Chakraborty *et al.*, 2005]. These criteria are all originally applied to incompressible flows although only $_2$ is tailored for incompressible flow in theory. Their characteristics are summarized in Tab. 7.1. The relationship on equivalent threshold (a certain equivalent value of isocontour for the visualization process) was given by [Chakraborty *et al.*, 2005]. For a certain $_{ci}$ which satisfies $_{ci} >$ $_{th}$ and $_{cr}$ $_{ci}$ $_0$ where $_{th}$ is the threshold value for $_{ci}$ and $_0$ is a given value as a ratio of the real and imaginary part of the complex eigenvalue of the velocity gradient tensor, its equivalent values for Q, and $_2$ (if the flow is incompressible) are

$$\begin{aligned} Q \quad & Q_{th} = {}^{2}_{th} \\ & {}_{th} = \tfrac{1}{27}\,{}^{6}_{th} \\ {}_2 \quad & {}_{2th} = {}^{2}_{th} \quad \text{(if applicable)} \end{aligned} \tag{7.2}$$

Using equivalent threshold, the current flow around mid-chord presented by Q-criterion and $_{ci}$-criterion is shown in Fig. 7.1. The detail of the flow structures indicated by the black circles shows that the $_{ci}$-criterion seems to give more continuous structures than the Q-criterion. Yet the intensive flow structures are qualitatively the same, as expected. The $_{ci}$-criterion [Zhou *et al.*, 1999] and enhanced $_{ci}$-criterion [Chakraborty *et al.*, 2005] are essentially almost the same because they both use $_{ci}$ to describe a flow. The only difference between these two is that the enhanced $_{ci}$-criterion [Chakraborty *et al.*, 2005] introduces an additional ratio $_{cr}$ $_{ci}$ called "inverse spiraling compactness" which can further determine whether the flow is outward/inward spiraling ($_{cr}$ $_{ci} > 0$) or experiencing a perfectly circular path ($_{cr}$ $_{ci} = 0$). Finally the third category includes the methods that are more diverse and simpler such as pressure minima and streamlines, which are also merely qualitative measures to describe the flow. Consequently, the $lambda_{ci}$ is applied to the current flow.

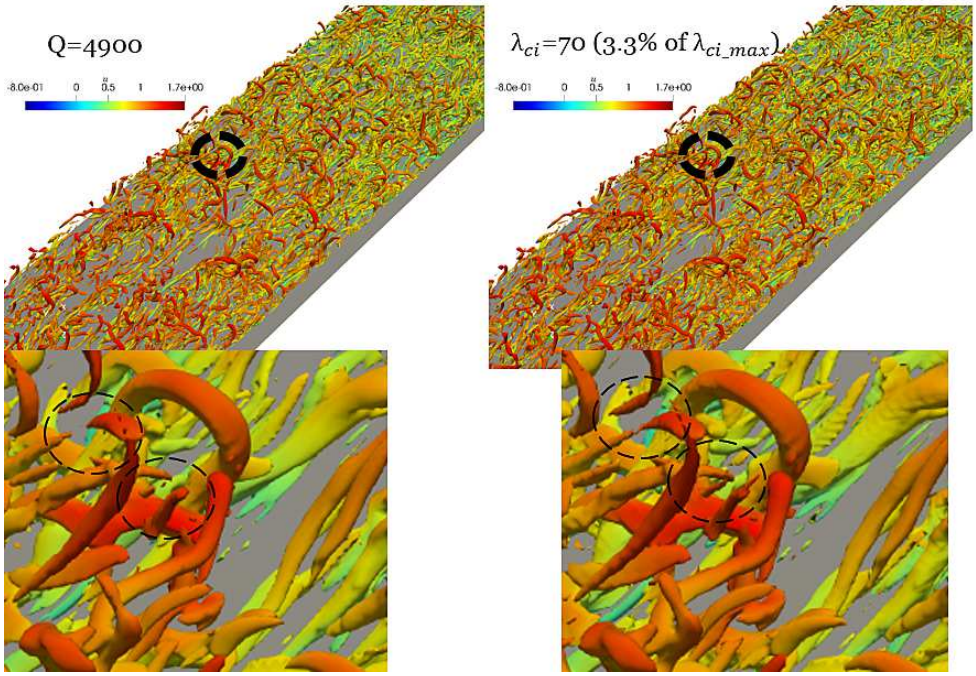

Figure 7.1 Instantaneous flow structures shown by Q-criterion (left) and $_{ci}$-criterion (right) of the flow around mid-chord using equivalent threshold, colored by the streamwise velocity.

List of Publications

Wu, H., Laffay, P., Idier, A., Jaiswal, P., Sanjosé, M. and Moreau S. (2016). Numerical study of the installed Controlled-Diffusion airfoil at transitional Reynolds number. In *Mathematical and Computational Approaches in Advancing Modern Science and Engineering*. Springer, pp. 505-515.

Wu, H., Winkler, J., Moreau, S. and Sandberg, R. D. (2017). Direct numerical simulation of transitional airfoil noise. In *23rd AIAA/CEAS Aeroacoustics Conference, Denver, CO, USA*. p. 3368.

Xia, Y., Wang, G., Loh, C.Y., Ji, T., Zheng, Y. and **Wu, H.** (2017). A NURBS-enhanced treatment of curved boundary integrating for the time-accurate upwind scheme with unstructured grids. In *23rd AIAA Computational Fluid Dynamics Conference*. p. 4298.

Wu, H., Sanjosé, M., Moreau, S. and Sandberg, R. D. (2018). Direct numerical simulation of the self-noise radiated by the installed Controlled-Diffusion airfoil at transitional Reynolds number. *24th AIAA/CEAS Aeroacoustics Conference, Atlanta, GA, USA*. p. 3797.

Wu, H., Moreau, S. and Sandberg, R. D. (2019). Effects of pressure gradient on the evolution of velocity gradient tensor invariant dynamics on a Controlled-Diffusion aerofoil at $Re_c = 150\ 000$. Accepted on 7^{th} Feb., *Journal of Fluid Mechanics*.

Grasso, G., Jaiswal, P., **Wu, H.**, Moreau, S. and Roger, M. (2019). Analytical models of the wall-pressure spectrum under a turbulent boundary layer. Submitted, *Journal of Fluid Mechanics*.

LIST OF REFERENCES

Addad, Y., Prosser, R., Laurence, D., Moreau, S. and Mendonca, F. (2008). On the use of embedded meshes in the les of external flows. *Flow, Turbulence and Combustion*, volume 80, pp. 393–403.

Adrian, R. J. and Westerweel, J. (2011). *Particle image velocimetry*. Cambridge University Press, Cambridge, UK.

Afzal, N. (1983). Analysis of a turbulent boundary layer subjected to a strong adverse pressure gradient. *International Journal of Engineering Science*, volume 21, pp. 563–576.

Amiet, R. K. (1976). Noise due to turbulent flow past a trailing edge. *Journal of Sound and Vibration*, volume 47, pp. 387–393.

Arbey, H. and Bataille, J. (1983). Noise generated by airfoil profiles placed in a uniform laminar flow. *Journal of Fluid Mechanics*, volume 134, pp. 33–47.

Arguillat, B., Ricot, D., Bailly, C. and Robert, G. (2010). Measured wavenumber: Frequency spectrum associated with acoustic and aerodynamic wall pressure fluctuations. *The Journal of the Acoustical Society of America*, volume 128, pp. 1647–1655.

Bardino, J., Ferziger, J. H. and Reynolds, W. C. (1983). *Improved turbulence models based on large eddy simulation of homogeneous, incompressible turbulent flows* (Technical Report TF-19). Stanford Univ. Report.

Bayliss, A. and Turkel, E. (1980). Radiation boundary conditions for wave-like equations. *Communications on Pure and applied Mathematics*, volume 33, pp. 707–725.

Bayliss, A. and Turkel, E. (1982). Far field boundary conditions for compressible flows. *Journal of Computational Physics*, volume 48, pp. 182–199.

Bechlars, P. (2015). *Comprehensive characterisation of turbulence dynamics with emphasis on wall-bounded flows*. Ph.D. thesis, University of Southampton, Southampton, UK.

Bechlars, P. and Sandberg, R. D. (2017a). Evolution of the velocity gradient tensor invariant dynamics in a turbulent boundary layer. *Journal of Fluid Mechanics*, volume 815, pp. 223–242.

Bechlars, P. and Sandberg, R. D. (2017b). Variation of enstrophy production and strain rotation relation in a turbulent boundary layer. *Journal of Fluid Mechanics*, volume 812, pp. 321–348.

Bertagnolio, F., Fischer, A. and Zhu, W. J. (2014). Tuning of turbulent boundary layer anisotropy for improved surface pressure and trailing-edge noise modeling. *Journal of Sound and Vibration*, volume 333, pp. 991–1010.

Bhatnagar, P. L., Gross, E. P. and Krook, M. (1954). Small amplitude processes in charged and neutral one-component systems. *Physical Review*, volume 94, p. 511.

Blackburn, H. M., Mansour, N. N. and Cantwell, B. J. (1996). Topology of fine-scale motions in turbulent channel flow. *Journal of Fluid Mechanics*, volume 310, pp. 269–292.

Blake, W. K. (1975). *A statistical description of pressure and velocity fields at the trailing edges of a flat strut* (Technical Report DTNSRDC-4241). DTIC Document.

Blake, W. K. (1986). *Mechanics of Flow-Induced Sound and Vibration*. Academic Press Inc., Cambridge, MA, USA.

Blazek, J. (2015). *Computational fluid dynamics: principles and applications*. Butterworth-Heinemann, Oxford, UK.

Bogey, C., De Cacqueray, N. and Bailly, C. (2009). A shock-capturing methodology based on adaptative spatial filtering for high-order non-linear computations. *Journal of Computational Physics*, volume 228, pp. 1447–1465.

Bourassa, C. and Thomas, F. O. (2009). An experimental investigation of a highly accelerated turbulent boundary layer. *Journal of Fluid Mechanics*, volume 634, pp. 359–404.

Brooks, T. F. and Hodgson, T. H. (1981). Trailing edge noise prediction from measured surface pressures. *Journal of Sound and Vibration*, volume 78, pp. 69–117.

Brooks, T. F., Pope, D. S. and Marcolini, M. A. (1989). *Airfoil self-noise and prediction*, volume 1218. National Aeronautics and Space Administration, Office of Management, Scientific and Technical Information Division.

Camussi, R. (2013). *Noise sources in turbulent shear flows: fundamentals and applications*, volume 545. Springer Science & Business Media, Berlin, Germany.

Caro, S. and Moreau, S. (2000). Aeroacoustic modelling of low pressure axial flow fans. In *6th Aeroacoustics Conference and Exhibit, Lahaina, Hawaii, USA*. p. 2094.

Caro, S., Ploumhans, P. and Gallez, X. (2004). Implementation of Lighthill's acoustic analogy in a finite/infinite elements framework. *AIAA Paper 2004-2891*.

Carpenter, M. H., Nordström, J. and Gottlieb, D. (1999). A stable and conservative interface treatment of arbitrary spatial accuracy. *Journal of Computational Physics*, volume 148, pp. 341–365.

Casalino, D. (2010). Aeroacoustics research in Europe: the CEAS-ASC report on 2009 highlights. *Journal of Sound and Vibration*, volume 329, number 22, pp. 4810–4828.

Catlett, M. R., Forest, J., Anderson, J. M. and Stewart, D. (2014). Empirical spectral model of surface pressure fluctuations beneath adverse pressure gradients. In *20th AIAA/CEAS Aeroacoustics Conference, Atlanta, GA, USA*. p. 2910.

Cawood, A. F. (2012). *Surface pressure measurements on a rotating controlled diffusion blade*. Master's thesis, RWTH University, Aachen, Germany.

Chacín, J. M., Cantwell, B. J. and Kline, S. J. (1996). Study of turbulent boundary layer structure using the invariants of the velocity gradient tensor. *Experimental Thermal and Fluid Science*, volume 13, pp. 308–317.

Chakraborty, P., Balachandar, S. and Adrian, R. J. (2005). On the relationships between local vortex identification schemes. *Journal of Fluid Mechanics*, volume 535, pp. 189–214.

Chapman, D. K. (1979). Computatisnal aerodynamics development and outlook. *AIAA Journal*, volume 17, pp. 1293–1313.

Chase, D. M. (1972). Sound radiated by turbulent flow off a rigid half-plane as obtained from a wavevector spectrum of hydrodynamic pressure. *The Journal of the Acoustical Society of America*, volume 52, pp. 1011–1023.

Chase, D. M. (1980). Modeling the wavevector-frequency spectrum of turbulent boundary layer wall pressure. *Journal of Sound and Vibration*, volume 70, pp. 29–67.

Choi, H. and Moin, P. (2012). Grid-point requirements for large eddy simulation: Chapman's estimates revisited. *Physics of Fluids*, volume 24, p. 011702.

Chong, M. S., Perry, A. E. and Cantwell, B. J. (1990). A general classification of three-dimensional flow fields. *Physics of Fluids A: Fluid Dynamics*, volume 2, pp. 765–777.

Chong, M. S., Soria, J., Perry, A. E., Chacin, J., Cantwell, B. J. and Na, Y. (1998). Turbulence structures of wall-bounded shear flows found using DNS data. *Journal of Fluid Mechanics*, volume 357, pp. 225–247.

Christophe, J. (2011). *Application of hybrid methods to high frequency aeroacoustics*. Ph.D. thesis, Université Libre de Bruxelles, Bruxelles, Belgium.

Christophe, J., Anthoine, J. and Moreau, S. (2008). Trailing edge noise computation of a fan blade profile. *The Journal of the Acoustical Society of America*, volume 123, pp. 3539–3539.

Christophe, J., Anthoine, J. and Moreau, S. (2009). Trailing edge noise of a controlled-diffusion airfoil at moderate and high angle of attack. In *15th AIAA/CEAS Aeroacoustics Conference, Miami, FL, USA*. p. 3196.

Christophe, J., Moreau, S.and Hamman, C. W., Witteveen, J. A. S. and Iaccarino, G. (2010). Uncertainty quantification for the trailing-edge noise of a controlled-diffusion airfoil. In *Proceedings of the Summer Program, Center for Turbulence Research, Stanford University*. pp. 213–225.

Christophe, J. and Moreau, S. (2008). LES of the trailing-edge flow and noise of a controlled-diffusion airfoil at high angle of attack. In *Center for Turbulence Research, Annual Research Briefs, Stanford University*. pp. 305–316.

Christophe, J., Moreau, S., Hamman, C. W., Witteveen, J. A. S. and Iaccarino, G. (2014). Uncertainty quantification for the trailing-edge noise of a Controlled-Diffusion airfoil. *AIAA Journal*, volume 53, pp. 42–54.

Clarke, J. (1966). A superconducting galvanometer employing josephson tunnelling. *Philosophical Magazine*, volume 13, pp. 115–127.

Clauser, F. H. (1956). *The turbulent boundary layer*. Elsevier, Amsterdam, Netherlands.

Colonius, T. and Lele, S. K. (2004). Computational aeroacoustics: progress on nonlinear problems of sound generation. *Progress in Aerospace sciences*, volume 40, pp. 345–416.

Colonius, T., Lele, S. K. and Moin, P. (1993). Boundary conditions for direct computation of aerodynamic sound generation. *AIAA Journal*, volume 31, pp. 1574–1582.

Corcos, G. M. (1964). The structure of the turbulent pressure field in boundary-layer flows. *Journal of Fluid Mechanics*, volume 18, pp. 353–378.

Crighton, D. G. (1975). Basic principles of aerodynamic noise generation. *Progress in Aerospace Sciences*, volume 16, pp. 31–96.

Curle, N. (1955). The influence of solid boundaries upon aerodynamic sound. In *Proceedings of the Royal Society of London A: Mathematical, Physical and Engineering Sciences*, volume 231. pp. 505–514.

Deniau, H., Dufour, G., Boussuge, J. F., Polacsek, C. and Moreau, S. (2011). Affordable compressible LES of airfoil-turbulence interaction in a free jet. In *17th AIAA/CEAS Aeroacoustics Conference, Portland, OR, USA*. p. 2707.

Desquesnes, G., Terracol, M. and Sagaut, P. (2007). Numerical investigation of the tone noise mechanism over laminar airfoils. *Journal of Fluid Mechanics*, volume 591, pp. 155–182.

Donea, J. (1984). A Taylor–Galerkin method for convective transport problems. *International Journal for Numerical Methods in Engineering*, volume 20, pp. 101–119.

Donea, J. and Huerta, A. (2003). *Finite element methods for flow problems*. John Wiley & Sons, Hoboken, NJ, USA.

Donea, J., Quartapelle, L. and Selmin, V. (1987). An analysis of time discretization in the finite element solution of hyperbolic problems. *Journal of Computational Physics*, volume 70, pp. 463–499.

Escobar, M. (2007). *Finite element simulation of flow-induced noise using Lighthill's acoustic analogy*. Ph.D. thesis, University of Erlangen–Nurnberg, Erlangen, Germany.

Ferziger, J. H. and Peric, M. (2012). *Computational methods for fluid dynamics*. Springer Science & Business Media, Berlin, Germany.

Finez, A., Jondeau, E., Roger, M. and Jacob, M. C. (2010). Broadband noise reduction with trailing edge brushes. In *16th AIAA/CEAS Aeroacoustics Conference, Stockholm, Sweden*. p. 3980.

Fink, M. R. (1977). *Airframe noise prediction method* (Technical Report UTRC/R77-912607-11). DTIC Document.

Fink, M. V. M. (1975). Experimental evaluation of theories for trailing edge and incidence fluctuation noise. *AIAA Journal*, volume 13, pp. 1472–1477.

Fischer, A., Bertagnolio, F. and Madsen, H. A. (2017). Improvement of TNO type trailing edge noise models. *European Journal of Mechanics-B/Fluids*, volume 61, pp. 255–262.

Fosso-Pouangué, A., Sanjosé, M. and Moreau, S. (2012). Jet noise simulation with realistic nozzle geometries using fully unstructured LES solver. In *18th AIAA/CEAS Aeroacoustics Conference, Colorado Springs, CO, USA*. p. 2190.

Fosso-Pouangué, A., Sanjosé, M. and Moreau, S. (2014). Dual-stream jet noise simulations with realistic nozzle geometries using a fully unstructured LES solver. In *20th AIAA/CEAS Aeroacoustics Conference, Atlanta, GA, USA*. p. 2756.

Fosso Pouangué, A., Sanjosé, M., Moreau, S., Daviller, G. and Deniau, H. (2014). Subsonic jet noise simulations using both structured and unstructured grids. *AIAA Journal*, volume 53, pp. 55–69.

Freund, J. B. (1997). Proposed inflow/outflow boundary condition for direct computation of aerodynamic sound. *AIAA Journal*, volume 35, pp. 740–742.

Frisch, U., d'Humieres, D., Hasslacher, B., Lallemand, P., Pomeau, Y. and Rivet, J. P. (1987). Lattice gas hydrodynamics in two and three dimensions. *Complex Systems*, volume 1, pp. 649–707.

Germano, M., Piomelli, U., Moin, P. and Cabot, W. H. (1991). A dynamic subgrid-scale eddy viscosity model. *Physics of Fluids A: Fluid Dynamics (1989-1993)*, volume 3, pp. 1760–1765.

Ghaemi, S., Ragni, D. and Scarano, F. (2012). PIV-based pressure fluctuations in the turbulent boundary layer. *Experiments in Fluids*, volume 53, pp. 1823–1840.

Glegg, S., Baxter, S. M. and Glendinning, A. G. (1987). The prediction of broadband noise from wind turbines. *Journal of Sound and Vibration*, volume 118, pp. 217–239.

Glegg, S., Morin, B., Atassi, O. and Reba, R. (2008). Using RANS calculations of turbulent kinetic energy to provide predictions of trailing edge noise. In *14th AIAA/CEAS Aeroacoustics Conference, Vancouver, BC, Canada*. p. 2993.

Goldstein, M. E. (1976). *Aeroacoustics*, volume 1. New York, McGraw-Hill International Book Co., 1976. 305 p., New York, NY, USA.

Golliard, J., Van Lier, L. and Vedy, E. (2006). Generation of unsteady aeroacoustic source from steady CFD. *Lecture Series von Karman Institute for Fluid Dynamics*, volume 5, p. 8.

Goody, M. (2004). Empirical spectral model of surface pressure fluctuations. *AIAA Journal*, volume 42, pp. 1788–1794.

Gottlieb, D. and Orszag, S. A. (1977). *Numerical analysis of spectral methods: theory and applications*, volume 26. Siam, Philadelphia, PA, USA.

Grasso, G., Jaiswal, P. and Moreau, S. (2018). Monte-carlo computation of wall-pressure spectra under turbulent boundary layers for trailing-edge noise prediction. In *Proceedings of International Conference on Noise and Vibration Engineering, Leuven, Belgium.*

Gungor, A. G., Maciel, Y., Simens, M. P. and Soria, J. (2014). Analysis of a turbulent boundary layer subjected to a strong adverse pressure gradient. *Journal of Physics: Conference Series*, volume 506, p. 012007.

Guo, Y., Adams, N. A. and Kleiser, L. (1994). Direct numerical simulation of transition in a spatially growing compressible boundary layer using a new Fourier method. In *Direct and Large-Eddy Simulation I.* pp. 249–259.

Hayden, R. E., Fox, H. L. and Chanaud, R. C. (1976). *Some factors influencing radiation of sound from flow interaction with edges of finite surfaces* (Technical Report CR-145073). NASA.

He, G. W., Rubinstein, R. and Wang, L. P. (2002). Effects of subgrid-scale modeling on time correlations in large eddy simulation. *Physics of Fluids*, volume 14, pp. 2186–2193.

He, G. W., Wang, M. and Lele, S. K. (2004). On the computation of space-time correlations by large-eddy simulation. *Physics of Fluids*, volume 16, pp. 3859–3867.

He, X. Y. and Luo, L. S. (1997). Theory of the lattice Boltzmann method: From the boltzmann equation to the lattice Boltzmann equation. *Physical Review E*, volume 56, p. 6811.

Herr, M. and Dobrzynski, W. (2005). Experimental investigations in low-noise trailing edge design. *AIAA Journal*, volume 43, pp. 1167–1175.

Hersh, A. S., Sodermant, P. T. and Hayden, R. E. (1974). Investigation of acoustic effects of leading-edge serrations on airfoils. *Journal of Aircraft*, volume 11, pp. 197–202.

Higdon, R. L. (1986). Initial-boundary value problems for linear hyperbolic system. *SIAM Review*, volume 28, pp. 177–217.

Hobbs, D. E. and Weingold, H. D. (1984). Development of controlled diffusion airfoils for multistage compressor application. *Journal of Engineering for Gas Turbines and Power*, volume 106, pp. 271–278.

Hosseini, S. M., Vinuesa, R., Schlatter, P., Hanifi, A. and Henningson, D. S. (2016). Direct numerical simulation of the flow around a wing section at moderate Reynolds number. *International Journal of Heat and Fluid Flow*, volume 61, pp. 117–128.

Howe, M. S. (1978). A review of the theory of trailing edge noise. *Journal of Sound and Vibration*, volume 61, pp. 437–465.

Howe, M. S. (2001). Edge-source acoustic Green's function for an airfoil of arbitrary chord, with application to trailing-edge noise. *The Quarterly Journal of Mechanics and Applied Mathematics*, volume 54, pp. 139–155.

Hower, D. (2012). *Unsteady pressure fluctuations on the surface of a controlled-diffusion airfoil*. Master's thesis, Michigan State University.

Hu, F. Q., Hussaini, M. Y. and Manthey, J. L. (1996). Low-dissipation and low-dispersion runge–kutta schemes for computational acoustics. *Journal of Computational Physics*, volume 124, pp. 177–191.

Hu, N. and Herr, M. (2016). Characteristics of wall pressure fluctuations for a flat plate turbulent boundary layer with pressure gradients. In *22nd AIAA/CEAS Aeroacoustics Conference, Lyon, France*. p. 2749.

Hubbard, H. H. and Shepherd, K. P. (1991). Aeroacoustics of large wind turbines. *The Journal of the Acoustical Society of America*, volume 89, pp. 2495–2508.

Hughes, T. J. R., Mazzei, L., Oberai, A. A. and Wray, A. A. (2001). The multiscale formulation of large eddy simulation: Decay of homogeneous isotropic turbulence. *Physics of Fluids (1994-present)*, volume 13, pp. 505–512.

Hunt, J. C. R., Wray, A. A. and Moin, P. (1988). Eddies, streams, and convergence zones in turbulent flows. In *Proceedings of the Summer Program, Center for Turbulence Research, Stanford University*. pp. 193–207.

Idier, A. (2014). *Réduction du bruit rayonné par un profil de pale par l'implantation de matériaux poreux*. Master's thesis, Université de Sherbrooke, Sherbrooke, QC, Canada.

Ikeda, T., Atobe, T. and Takagi, S. (2012). Direct simulations of trailing-edge noise generation from two-dimensional airfoils at low Reynolds numbers. *Journal of Sound and Vibration*, volume 331, pp. 556–574.

Indinger, T., Buschmann, M. H. and Gad-el Hak, M. (2006). Mean-velocity profile of turbulent boundary layers approaching separation. *AIAA Journal*, volume 44, pp. 2465–2474.

Istvan, M. S., Kurelek, J. W. and Yarusevych, S. (2017). Turbulence intensity effects on laminar separation bubbles formed over an airfoil. *AIAA Journal*, volume 56, pp. 1335–1347.

Jeong, J. and Hussain, F. (1995). On the identification of a vortex. *Journal of Fluid Mechanics*, volume 285, pp. 69–94.

Jiang, M., Li, X.and Bai, B. and Lin, D. (2012). Numerical simulation on the NACA0018 airfoil self-noise generation. *Theoretical and Applied Mechanics Letters*, volume 2, p. 052004.

Jiménez, S. J., Hoyas, S., Simens, M. P. and Mizuno, Y. (2010). Turbulent boundary layers and channels at moderate Reynolds numbers. *Journal of Fluid Mechanics*, volume 657, pp. 335–360.

Jones, L. E. (2008). *Numerical studies of the flow around an airfoil at low Reynolds number*. Ph.D. thesis, University of Southampton, Southampton, UK.

Jones, L. E. and Sandberg, R. D. (2009). Direct numerical simulations of noise generated by the flow over an airfoil with trailing edge serrations. In *15th AIAA/CEAS Aeroacoustics Conference, Miami, FL, USA*. p. 3195.

Jones, L. E. and Sandberg, R. D. (2011). Numerical analysis of tonal airfoil self-noise and acoustic feedback-loops. *Journal of Sound and Vibration*, volume 330, pp. 6137–6152.

Jones, L. E. and Sandberg, R. D. (2012). Acoustic and hydrodynamic analysis of the flow around an aerofoil with trailing-edge serrations. *Journal of Fluid Mechanics*, volume 706, pp. 295–322.

Jones, L. E., Sandberg, R. D. and Sandham, N. D. (2008). Direct numerical simulations of forced and unforced separation bubbles on an airfoil at incidence. *Journal of Fluid Mechanics*, volume 602, pp. 175–207.

Joshi, P., Liu, X. and Katz, J. (2014). Effect of mean and fluctuating pressure gradients on boundary layer turbulence. *Journal of Fluid Mechanics*, volume 748, pp. 36–84.

Kamruzzaman, M., Bekiropoulos, D., Lutz, T., Würz, W. and Krämer, E. (2015). A semi-empirical surface pressure spectrum model for airfoil trailing-edge noise prediction. *International Journal of Aeroacoustics*, volume 14, pp. 833–882.

Karni, S. (1996). Far-field filtering operators for suppression of reflection from artificial boundaries. *SIAM Journal on Numerical Analysis*, volume 33, pp. 1014–1047.

Keith, W. L., Hurdis, D. A. and Abraham, B. M. (1992). A comparison of turbulent boundary layer wall-pressure spectra. *Journal of Fluids Engineering*, volume 114, pp. 338–347.

Kennedy, C. A., Carpenter, M. H. and Lewis, R. M. (1999). Low-storage, explicit Runge-Kutta schemes for the compressible Navier-Stokes equations. *Applied Numerical Mathematics*, volume 35, pp. 177–219.

Kennedy, C. A., Carpenter, M. H. and Lewis, R. M. (2000). Low-storage, explicit Runge–Kutta schemes for the compressible Navier–Stokes equations. *Applied Numerical Mathematics*, volume 35, pp. 177–219.

Kennedy, C. A. and Gruber, A. (2008). Reduced aliasing formulations of the convective terms within the Navier–Stokes equations for a compressible fluid. *Journal of Computational Physics*, volume 227, pp. 1676–1700.

Kida, S. and Miura, H. (1998). Identification and analysis of vortical structures. *European Journal of Mechanics. B, Fluids*, volume 17, pp. 471–488.

Kim, J., Moin, P. and Moser, R. (1987). Turbulence statistics in fully developed channel flow at low Reynolds number. *Journal of Fluid Mechanics*, volume 177, pp. 133–166.

Kim, J. W. (2007). Optimised boundary compact finite difference schemes for computational aeroacoustics. *Journal of Computational Physics*, volume 225, pp. 995–1019.

Kim, J. W. and Lee, D. J. (1996). Optimized compact finite difference schemes with maximum resolution. *AIAA Journal*, volume 34, pp. 887–893.

Kim, J. W. and Lee, D. J. (2000). Generalized characteristic boundary conditions for computational aeroacoustics. *AIAA Journal*, volume 38, pp. 2040–2049.

Kim, J. W. and Lee, D. J. (2003). Characteristic interface conditions for multiblock high-order computation on singular structured grid. *AIAA Journal*, volume 41, pp. 2341–2348.

Kitsios, V., Atkinson, C., Sillero, J. A., Borrell, G., Gungor, A. G., Jiménez, J. and Soria, J. (2016). Direct numerical simulation of a self-similar adverse pressure gradient turbulent boundary layer. *International Journal of Heat and Fluid Flow*, volume 61, pp. 129–136.

Knopp, T., Schanz, D., Schröder, A., Dumitra, M., Cierpka, C., Hain, R. and Kähler, C. J. (2014). Experimental investigation of the log-law for an adverse pressure gradient turbulent boundary layer flow at $Re = 10000$. *Flow, Turbulence and Combustion*, volume 92, pp. 451–471.

Kraichnan, R. H. (1956). Pressure fluctuations in turbulent flow over a flat plate. *The Journal of the Acoustical Society of America*, volume 28, pp. 378–390.

Kreiss, H. O. (1970). Initial boundary value problems for hyperbolic systems. *Communications on Pure and Applied Mathematics*, volume 23, pp. 277–298.

Laffay, P. (2014). *Réduction du bruit propre d'une pale de ventilateur par la mise en place d'une fente de soufflage et de dents de scie sur le bord de fuite de profil*. Master's thesis, Université de Sherbrooke, Sherbrooke, QC, Canada.

Latt, J. (2007). *Hydrodynamic limit of lattice Boltzmann equations*. Ph.D. thesis, University of Geneva, Geneva, Switzerland.

Lax, P. and Wendroff, B. (1960). Systems of conservation laws. *Communications on Pure and Applied mathematics*, volume 13, pp. 217–237.

Lee, J. H. and Sung, H. J. (2008). Effects of an adverse pressure gradient on a turbulent boundary layer. *International Journal of Heat and Fluid Flow*, volume 29, pp. 568–578.

Lee, J. H. and Sung, H. J. (2009). Structures in turbulent boundary layers subjected to adverse pressure gradients. *Journal of Fluid Mechanics*, volume 639, pp. 101–131.

Lee, S. (2018). Empirical wall-pressure spectral modeling for zero and adverse pressure gradient flows. *AIAA Journal*, volume 56, pp. 1818–1829.

Lee, S. and Villaescusa, A. (2017). Comparison and assessment of recent empirical models for turbulent boundary layer wall pressure spectrum. In *23rd AIAA/CEAS Aeroacoustics Conference, Denver, CO, USA*. p. 3688.

Lele, S. K. (1992). Compact finite difference schemes with spectral-like resolution. *Journal of Computational Physics*, volume 103, pp. 16–42.

Lew, P. T., Najafi-Yazdi, A. and Mongeau, L. (2010). Numerical simulation of sound from flow over an airfoil with a blunt trailing edge. In *16th AIAA/CEAS Aeroacoustics Conference, Stockholm, Sweden*. p. 3879.

Lighthill, M. J. (1952a). *On sound generated aerodynamically I*. Royal Society of London, London, UK.

Lighthill, M. J. (1952b). On sound generated aerodynamically. i. general theory. volume 211, pp. 564–587.

Lighthill, M. J. (1952c). *On sound generated aerodynamically II*. Royal Society of London, London, UK.

Lilly, D. K. (1992). A proposed modification of the Germano subgrid-scale closure method. *Physics of Fluids A: Fluid Dynamics (1989-1993)*, volume 4, pp. 633–635.

Lissaman, P. B. S. (1983). Low-Reynolds-number airfoils. *Annual Review of Fluid Mechanics*, volume 15, pp. 223–239.

Longhouse, R. E. (1977). Vortex shedding noise of low tip speed, axial flow fans. *Journal of Sound and Vibration*, volume 53, pp. 25–46.

Lozano-Durán, A., Holzner, M. and Jiménez, J. (2015). Numerically accurate computation of the conditional trajectories of the topological invariants in turbulent flows. *Journal of Computational Physics*, volume 295, pp. 805–814.

Lumley, J. L. (1979). Computational modeling of turbulent flows. In *Advances in Applied Mechanics*, volume 18. pp. 123–176.

Marié, S. (2008). *Etude de la méthode Boltzmann sur Réseau pour les simulations en aéroacoustique*. Ph.D. thesis, Université Pierre et Marie Curie-Paris VI, Paris, France.

Martin, J., Ooi, A., Chong, M. S. and Soria, J. (1998). Dynamics of the velocity gradient tensor invariants in isotropic turbulence. *Physics of Fluids*, volume 10, pp. 2336–2346.

Meneveau, C. (2011). Lagrangian dynamics and models of the velocity gradient tensor in turbulent flows. *Annual Review of Fluid Mechanics*, volume 43, pp. 219–245.

Moin, P.and Mahesh, K. (1998). Direct numerical simulation: a tool in turbulence research. *Annual Review of Fluid Mechanics*, volume 30, pp. 539–578.

Moin, P., Squires, K., Cabot, W. and Lee, S. (1991). A dynamic subgrid-scale model for compressible turbulence and scalar transport. *Physics of Fluids A: Fluid Dynamics (1989-1993)*, volume 3, pp. 2746–2757.

Monty, J. P., Harun, Z. and Marusic, I. (2011). A parametric study of adverse pressure gradient turbulent boundary layers. *International Journal of Heat and Fluid Flow*, volume 32, pp. 575–585.

Moreau, S., Henner, M., Iaccarino, G., Wang, M. and Roger, M. (2003). Analysis of flow conditions in freejet experiments for studying airfoil self-noise. *AIAA Journal*, volume 41, pp. 1895–1905.

Moreau, S., Iaccarino, G., Kang, S., Khalighi, Y. and Wang, M. (2004). Numerical simulation of a low speed fan blade. In *Proceedings of the CTR summer program, Stanford University*. pp. 195–207.

Moreau, S., Laffay, P., Idier, A. and Atalla, N. (2016). Several noise control of the trailing-edge noise of a Controlled-Diffusion airfoil. In *22nd AIAA/CEAS Aeroacoustics Conference, Lyon, France*. p. 2816.

Moreau, S., Mendonca, F., Qazi, O., Prosser, R. and Laurence, D. (2005). Influence of turbulence modeling on airfoil unsteady simulations of broadband noise sources. In *11th AIAA/CEAS Aeroacoustics Conference, Monterey, CA, USA*. p. 2916.

Moreau, S., Neal, D., Khalighi, Y., Wang, M. and Iaccarino, G. (2006a). Validation of unstructured-mesh LES of the trailing-edge flow and noise of a controlled diffusion airfoil. In *Proceedings of the Summer Program, Center for Turbulence Research, Stanford University*. pp. 1–14.

Moreau, S., Neal, D. R. and Foss, J. (2006b). Hot-wire measurements around a Controlled-Diffusion airfoil in an open-jet anechoic wind tunnel. *Journal of Fluids Engineering*, volume 128, pp. 699–706.

Moreau, S. and Roger, M. (2005). Effect of airfoil aerodynamic loading on trailing edge noise sources. *AIAA journal*, volume 43, pp. 41–52.

Moreau, S. and Roger, M. (2009). Back-scattering correction and further extensions of Amiet's trailing-edge noise model. Part ii: Application. *Journal of Sound and Vibration*, volume 323, pp. 397–425.

Moreau, S., Roger, M. and Christophe, J. (2009). Flow features and self-noise of airfoils near stall or in stall. In *15th AIAA/CEAS Aeroacoustics Conference, Miami, FL, USA*. p. 3198.

Morfey, C. L. (2000). Fundamental problems in aeroacoustics. In *Proceedings of the 7th International Congress on Sound and Vibration*. pp. V01AT09A005–V01AT09A005.

Moriarty, P., Guidati, G. and Migliore, P. (2005). Prediction of turbulent inflow and trailing-edge noise for wind turbines. In *11th AIAA/CEAS Aeroacoustics Conference, Monterey, CA, USA*. p. 2881.

Na, Y. (1997). *Direct numerical simulation of turbulent boundary layers with adverse pressure gradient and separation*. Ph.D. thesis, Stanford University, Palo Alto, CA, USA.

Nagano, Y., Tsuji, T. and Houra, T. (1998). Structure of turbulent boundary layer subjected to adverse pressure gradient. *International Journal of Heat and Fluid Flow*, volume 19, pp. 563–572.

Nagib, H. M. and Chauhan, K. A. (2008). Variations of von Kármán coefficient in canonical flows. *Physics of Fluids*, volume 20, p. 101518.

Narasimha, R. and Sreenivasan, K. R. (1973). Relaminarization in highly accelerated turbulent boundary layers. *Journal of Fluid Mechanics*, volume 61, pp. 417–447.

Nash, E. C., Lowson, M. V. and McAlpine, A. (1999). Boundary-layer instability noise on aerofoils. *Journal of Fluid Mechanics*, volume 382, pp. 27–61.

Neal, D. R. (2010). *The effects of rotation on the flow field over a controlled-diffusion airfoil*. Ph.D. thesis, Michigan State University, East Lansing, MI, USA.

Nickels, T. B. (2004). Inner scaling for wall-bounded flows subject to large pressure gradients. *Journal of Fluid Mechanics*, volume 521, pp. 217–239.

Nicoud, F. and Ducros, F. (1999). Subgrid-scale stress modelling based on the square of the velocity gradient tensor. *Flow, Turbulence and Combustion*, volume 62, pp. 183–200.

Node-Langlois, T., Wlassow, F., Languille, V., Colin, Y.and Caruelle, B., Gill, J. R., Chen, X., Zhang, X. and Parry, A. B. (2014). Prediction of contra-rotating open rotor broadband noise in isolated and installed configurations. In *20th AIAA/CEAS Aeroacoustics Conference, Atlanta, GA, USA*. p. 2610.

Nordström, J., Nordin, N. and Henningson, D. (1999). The fringe region technique and the fourier method used in the direct numerical simulation of spatially evolving viscous flows. *SIAM Journal on Scientific Computing*, volume 20, pp. 1365–1393.

Oberai, A. A., Roknaldin, F. and R. Hughes, T. J. (2002). Computation of trailing-edge noise due to turbulent flow over an airfoil. *AIAA Journal*, volume 40, pp. 2206–2216.

Odier, N., Sanjosé, M., Gicquel, L., Poinsot, T., Moreau, S. and Duchaine, F. (2019). A characteristic inlet boundary condition for compressible, turbulent, multispecies turbomachinery flows. *Computers & Fluids*, volume 178, pp. 41–55.

Ooi, A., Martin, J., Soria, J. and Chong, M. S. (1999). A study of the evolution and characteristics of the invariants of the velocity-gradient tensor in isotropic turbulence. *Journal of Fluid Mechanics*, volume 381, pp. 141–174.

Orszag, S. A. and Patterson Jr, G. S. (1972). Numerical simulation of three-dimensional homogeneous isotropic turbulence. *Physical Review Letters*, volume 28, p. 76.

Padois, T., Laffay, P., Idier, A. and Moreau, S. (2015). Detailed experimental investigation of the aeroacoustic field around a Controlled-Diffusion airfoil. In *21st AIAA/CEAS Aeroacoustics Conference, Dallas, TX, USA*. p. 2205.

Panton, R. L. and Linebarger, J. H. (1974). Wall pressure spectra calculations for equilibrium boundary layers. *Journal of Fluid Mechanics*, volume 65, pp. 261–287.

Parchen, R. R. (1998). *Progress report DRAW: a prediction scheme for trailing edge noise based on detailed boundary layer characteristics*. TNO Institute of Applied Physics, The Hague, Netherlands.

Paterson, R. W., Vogt, P. G., Fink, M. R. and Munch, C. L. (1973). Vortex noise of isolated airfoils. *Journal of Aircraft*, volume 10, pp. 296–302.

Perry, A. E. and Chong, M. S. (1987). A description of eddying motions and flow patterns using critical-point concepts. *Annual Review of Fluid Mechanics*, volume 19, pp. 125–155.

Piomelli, U. and Yuan, J. (2013). Numerical simulations of spatially developing, accelerating boundary layers. *Physics of Fluids*, volume 25, p. 101304.

Poinsot, T. J. and Lele, S. K. (1992). Boundary conditions for direct simulations of compressible viscous flows. *Journal of Computational Physics*, volume 101, pp. 104–129.

Pope, S. B. (2000). *Turbulent flows*. Cambridge University Press, Cambridge, UK.

Powell, A. (1959). On the aerodynamic noise of a rigid flat plate moving at zero incidence. *The Journal of the Acoustical Society of America*, volume 31, pp. 1649–1653.

Pröbsting, S. (2015). *Airfoil self-noise investigation with particle image velocimetry*. Ph.D. thesis, Delft University of Technology, Delft, Netherlands.

Pröbsting, S., Scarano, F., Bernardini, M. and Pirozzoli, S. (2013). On the estimation of wall pressure coherence using time-resolved tomographic PIV. *Experiments in Fluids*, volume 54, pp. 1–15.

Pröbsting, S., Scarano, F. and Morris, S. C. (2015). Regimes of tonal noise on an airfoil at moderate Reynolds number. *Journal of Fluid Mechanics*, volume 780, pp. 407–438.

Rai, M. M. and Moin, P. (1991). Direct simulations of turbulent flow using finite-difference schemes. *Journal of Computational Physics*, volume 96, pp. 15–53.

Remmler, S., Christophe, J., Anthoine, J. and Moreau, S. (2010). Computation of wall pressure spectra from steady flow data for noise prediction. *AIAA Journal*, volume 48, pp. 1997–2007.

Roger, M. and Moreau, S. (2004). Broadband self noise from loaded fan blades. *AIAA Journal*, volume 42, pp. 536–544.

Roger, M. and Moreau, S. (2005). Back-scattering correction and further extensions of Amiet's trailing-edge noise model. Part 1: theory. *Journal of Sound and Vibration*, volume 286, pp. 477–506.

Roger, M. and Moreau, S. (2010). Extensions and limitations of analytical airfoil broadband noise models. *International Journal of Aeroacoustics*, volume 9, pp. 273–306.

Roger, M., Moreau, S. and Guédel, A. (2006). Vortex-shedding noise and potential-interaction noise modeling by a reversed Sears' problem. In *12th AIAA/CEAS Aeroacoustics Conference, Cambridge, MA, USA*. p. 2607.

Rozenberg, Y. (2007). *Modélisation analytique du bruit aérodynamique à large bande des machines tournantes: utilisation de calculs moyennés de mécanique des fluides*. Ph.D. thesis, Ecole Centrale de Lyon, Ecully, France.

Rozenberg, Y., Moreau, S., Henner, M. and Morris, S. C. (2010). Fan trailing-edge noise prediction using RANS simulations. In *16th AIAA/CEAS Aeroacoustics Conference, Stockholm, Sweden*. p. 3720.

Rozenberg, Y., Robert, G. and Moreau, S. (2012). Wall-pressure spectral model including the adverse pressure gradient effects. *AIAA Journal*, volume 50, pp. 2168–2179.

Salas, P., Fauquembergue, G. and Moreau, S. (2016). Direct noise simulation of a canonical high lift device and comparison with an analytical model. *The Journal of the Acoustical Society of America*, volume 140, pp. 2091–2100.

Salas, P. and Moreau, S. (2015). Aeroacoustic simulations of a simplified high-lift device accounting for installations effects. In *21st AIAA/CEAS Aeroacoustics Conference, Dallas, TX, USA*. p. 2686.

Salze, E., Bailly, C., Marsden, O., Jondeau, E. and Juvé, D. (2014). An experimental characterisation of wall pressure wavevector-frequency spectra in the presence of pressure gradients. In *20th AIAA/CEAS Aeroacoustics Conference, Atlanta, GA, USA*. p. 2909.

Salze, E., Bailly, C., Marsden, O., Jondeau, E. and Juvé, D. (2015a). An experimental investigation of wall pressure fluctuations beneath pressure gradients. In *21st AIAA/CEAS Aeroacoustics Conference, Dallas, TX, USA*. p. 3148.

Salze, E., Bailly, C., Marsden, O. and Juvé, D. (2015b). Investigation of the wall pressure wavenumber-frequency spectrum beneath a turbulent boundary layer with pressure gradient. In *International Symposium on Turbulence and Shear Flow Phenomena, Melbourne, Australia*.

Sandberg, R. D. (2009). *Generalized cylindrical coordinates for characteristic boundary conditions and characteristic interface conditions* (Technical Report AFM-09/02). School of Engineering Sciences – Aerodynamics & Flight Mechanics Group, University of Southampton.

Sandberg, R. D. (2015). Compressible-flow DNS with application to airfoil noise. *Flow, Turbulence and Combustion*, volume 95, pp. 1–19.

Sandberg, R. D. and Jones, L. E. (2010). Direct numerical simulations of airfoil self-noise. *Procedia Engineering*, volume 6, pp. 274–282.

Sandberg, R. D., Jones, L. E. and Sandham, N. D. (2008). Direct numerical simulations of noise generated by turbulent flow over airfoils. In *14th AIAA/CEAS Aeroacoustics Conference, Vancouver, BC, Canada*. p. 2861.

Sandberg, R. D., Jones, L. E., Sandham, N. D. and Joseph, P. F. (2009). Direct numerical simulations of tonal noise generated by laminar flow past airfoils. *Journal of Sound and Vibration*, volume 320, pp. 838–858.

Sandberg, R. D., Michelassi, V., Pichler, R., Chen, L. and Johnstone, R. (2015). Compressible direct numerical simulation of low-pressure turbines—part i: methodology. *Journal of Turbomachinery*, volume 137, p. 051011.

Sandberg, R. D. and Sandham, N. D. (2006). Nonreflecting zonal characteristic boundary condition for direct numerical simulation of aerodynamic sound. *AIAA Journal*, volume 44, pp. 402–405.

Sandberg, R. D. and Sandham, N. D. (2008). Direct numerical simulation of turbulent flow past a trailing edge and the associated noise generation. *Journal of Fluid Mechanics*, volume 596, pp. 353–385.

Sandberg, R. D., Sandham, N. D. and Joseph, P. F. (2007). Direct numerical simulations of trailing-edge noise generated by boundary-layer instabilities. *Journal of Sound and Vibration*, volume 304, pp. 677–690.

Sandhu, H. S. and Sandham, N. D. (1994). Boundary conditions for spatially growing compressible shear layers. *Rept. QMW-EP-1100, Faculty of Engineering, Queen Mary and Westfield College, Univ. of London, London*.

Sanjosé, M., Fosso-Pouangué, A., Moreau, S., Wang, G. and Padois, T. (2014a). Unstructured LES of the baseline exejet dual-stream jet. In *20th AIAA/CEAS Aeroacoustics Conference, Atlanta, GA, USA*. p. 3037.

Sanjosé, M., Jaiswal, P., Moreau, S., Towne, A., Lele, S. K. and Mann, A. (2017). Laminar boundary layer instability noise. In *23rd AIAA/CEAS Aeroacoustics Conference, Denver, CO, USA*. p. 3190.

Sanjosé, M., Méon, C., Masson, V. and Moreau, S. (2014b). Direct numerical simulation of acoustic reduction using serrated trailing-edge on an isolated airfoil. In *20th AIAA/CEAS Aeroacoustics Conference, Atlanta, GA, USA*. p. 2324.

Sanjosé, M., Moreau, S., Kim, M. S. and Pérot, F. (2011). Direct self-noise simulation of the installed controlled diffusion airfoil. In *17th AIAA/CEAS Aeroacoustics Conference, Portland, OR, USA*. p. 2716.

Sanjosé, M., Moreau, S., Towne, A. and Lele, S. K. (2016). Laminar boundary layer instability noise. In *Proceedings of the Summer Program, Center for Turbulence Research, Stanford University*. pp. 243–252.

Sanjosé, M., Towne, A., Jaiswal, P., Moreau, S., Lele, S. and Mann, A. (2018). Modal analysis of the laminar boundary layer instability and tonal noise of an airfoil at Reynolds number 150,000. *International Journal of Aeroacoustics*, p. 1475472X18812798.

Schlatter, P., Adams, N. A. and Kleiser, L. (2005). A windowing method for periodic inflow/outflow boundary treatment of non-periodic flows. *Journal of Computational Physics*, volume 206, pp. 505–535.

Schloemer, H. H. (1967). Effects of pressure gradients on turbulent-boundary-layer wall-pressure fluctuations. *The Journal of the Acoustical Society of America*, volume 42, pp. 93–113.

Schröder, A., Dierksheide, U., Wolf, J., Herr, M. and Kompenhans, J. (2004). Investigation on trailing-edge noise sources by means of high-speed PIV. In *12th International Symposium on Applications of Laser Techniques to Fluid Mechanics, Lisbon, Portugal*, volume 30.

Seror, C., Sagaut, P., Bailly, C. and Juvé, D. (2000). Subgrid-scale contribution to noise production in decaying isotropic turbulence. *AIAA Journal*, volume 38, pp. 1795–1803.

Simonsen, A. J. and Krogstad, P. Å. (2005). Turbulent stress invariant analysis: Clarification of existing terminology. *Physics of Fluids*, volume 17, p. 088103.

Skaare, P. E. and Krogstad, P. (1994). A turbulent equilibrium boundary layer near separation. *Journal of Fluid Mechanics*, volume 272, pp. 319–348.

Smagorinsky, J. (1963). General circulation experiments with the primitive equations: I. the basic experiment. *Monthly weather review*, volume 91, pp. 99–164.

Soria, J., Sondergaard, R., Cantwell, B., Chong, M. S. and Perry, A. E. (1994). A study of the fine-scale motions of incompressible time-developing mixing layers. *Physics of Fluids*, volume 6, pp. 871–884.

Spalart, P. R. and Strelets, M. K. (2000). Mechanisms of transition and heat transfer in a separation bubble. *Journal of Fluid Mechanics*, volume 403, pp. 329–349.

Spalart, P. R. and Watmuff, J. H. (1993). Experimental and numerical study of a turbulent boundary layer with pressure gradients. *Journal of Fluid Mechanics*, volume 249, pp. 337–371.

Stolz, S. and Adams, N. A. (1999). An approximate deconvolution procedure for large-eddy simulation. *Physics of Fluids (1994-present)*, volume 11, pp. 1699–1701.

Succi, S. (2001). *The lattice Boltzmann equation: for fluid dynamics and beyond*. Oxford University Press, Oxford, UK.

Suman, S. and Girimaji, S. S. (2010). Velocity gradient invariants and local flow-field topology in compressible turbulence. *Journal of Turbulence*, p. N2.

Tam, C. K. W. (1972). On the noise of a nearly ideally expanded supersonic jet. *Journal of Fluid Mechanics*, volume 51, pp. 69–95.

Tam, C. K. W. (2004). Computational aeroacoustics: an overview of computational challenges and applications. *International Journal of Computational Fluid Dynamics*, volume 18, pp. 547–567.

Tam, C. K. W. and Ju, H. (2006). Numerical simulation of the generation of airfoil tones at a moderate Reynolds number. In *12th AIAA/CEAS Aeroacoustics Conference, Cambridge, MA, USA*. p. 2502.

Tam, C. K. W. and Ju, H. (2012). Aerofoil tones at moderate reynolds number. *Journal of Fluid Mechanics*, volume 690, pp. 536–570.

Tam, C. K. W. and Webb, J. C. (1993). Dispersion-relation-preserving finite difference schemes for computational acoustics. *Journal of Computational Physics*, volume 107, pp. 262–281.

Tam, C. K. W. and Webb, J. C. (1994). Radiation boundary condition and anisotropy correction for finite difference solutions of the Helmholtz equation. *Journal of Computational Physics*, volume 113, pp. 122–133.

Tam, C. K. W. and Yu, J. C. (1975). Trailing edge noise. In *2nd Aeroacoustics Conference, Hampton, VA, USA*. p. 489.

Thompson, K. W. (1987). Time dependent boundary conditions for hyperbolic systems. *Journal of Computational Physics*, volume 68, pp. 1–24.

Thompson, K. W. (1990). Time-dependent boundary conditions for hyperbolic systems, II. *Journal of Computational Physics*, volume 89, pp. 439–461.

Vieillefosse, P. (1984). Internal motion of a small element of fluid in an inviscid flow. *Physica A: Statistical Mechanics and its Applications*, volume 125, pp. 150–162.

Vinuesa, R., Örlü, R., Vila, C. S., Ianiro, A., Discetti, S. and Schlatter, P. (2017). Revisiting history effects in adverse-pressure-gradient turbulent boundary layers. *Flow, Turbulence and Combustion*, volume 99, pp. 565–587.

Volkmer, K. and Carolus, T. (2018). Aeroacoustic airfoil shape optimization utilizing semi-empirical models for trailing edge noise prediction. In *25th AIAA/CEAS Aeroacoustics Conference, Atlanta, GA, USA*. p. 3130.

Von Kármán, T. H. (1931). *Mechanical similitude and turbulence* (Technical Report NACA Tech. Mem., No. 611). Washington D.C., USA.

Wang, L. and Lu, X. (2012). Flow topology in compressible turbulent boundary layer. *Journal of Fluid Mechanics*, volume 703, pp. 255–278.

Wang, M., Freund, J. B. and Lele, S. K. (2006). Computational prediction of flow-generated sound. *Annual Review of Fluid Mechanics*, volume 38, pp. 483–512.

Wang, M. and Moin, P. (2000). Computation of trailing-edge flow and noise using large-eddy simulation. *AIAA Journal*, volume 38, pp. 2201–2209.

Wang, M., Moreau, S., Iaccarino, G. and Roger, M. (2004). LES prediction of pressure fluctuations on a low speed airfoil. *Center for Turbulence Research Annual Research Briefs*.

Wang, M., Moreau, S., Iaccarino, G. and Roger, M. (2009). LES prediction of wall-pressure fluctuations and noise of a low-speed airfoil. *International Journal of Aeroacoustics*, volume 8, pp. 177–197.

White, F. M. and Corfield, I. (2006). *Viscous fluid flow*, volume 3. McGraw-Hill, New York City, NY, USA.

Williams, J. E., F. and Hall, L. H. (1970). Aerodynamic sound generation by turbulent flow in the vicinity of a scattering half plane. *Journal of Fluid Mechanics*, volume 40, pp. 657–670.

Williams, J. E. and Hawkings, D. L. (1969). Sound generation by turbulence and surfaces in arbitrary motion. *Philosophical Transactions of the Royal Society of London A: Mathematical, Physical and Engineering Sciences*, volume 264, number 1151, pp. 321–342.

Willmarth, W. W. and Roos, F. W. (1965). Resolution and structure of the wall pressure field beneath a turbulent boundary layer. *Journal of Fluid Mechanics*, volume 22, pp. 81–94.

Winkler, J. and Carolus, T. (2009). Concept, design and characterization of a small aeroacoustic wind tunnel facility with application to airfoil measurements. *Noise Control Engineering Journal*, volume 57, pp. 370–383.

Winkler, J. and Moreau, S. (2008). LES of the trailing-edge flow and noise of a NACA6512-63 airfoil at zero angle of attack. In *Proceedings of the Summer Program, Center for Turbulence Research, Stanford University*. pp. 331–342.

Winkler, J., Moreau, S. and Carolus, T. (2009). Large-eddy simulation and trailing-edge noise prediction of an airfoil with boundary-layer tripping. In *15th AIAA/CEAS Aeroacoustics Conference, Miami, FL, USA*. p. 3197.

Winkler, J., Moreau, S. and Carolus, T. (2010). Airfoil trailing edge noise prediction from large-eddy simulation: influence of grid resolution and noise model formulation. In *16th AIAA/CEAS Aeroacoustics Conference, Stockholm, Sweden*. p. 3704.

Winkler, J., Sandberg, R. D. and Moreau, S. (2012). Direct numerical simulation of the self-noise radiated by an airfoil in a narrow stream. In *18th AIAA/CEAS Aeroacoustics Conference, Colorado Springs, CO, USA*. p. 2059.

Wolf, W. R., Azevedo, J. L. F. and Lele, S. K. (2012a). Compressibility effects on airfoil trailing edge noise generation and propagation. *Blucher Mechanical Engineering Proceedings*, volume 1, pp. 980–994.

Wolf, W. R., Azevedo, J. L. F. and Lele, S. K. (2012b). Convective effects and the role of quadrupole sources for aerofoil aeroacoustics. *Journal of Fluid Mechanics*, volume 708, pp. 502–538.

Wolf, W. R. and Lele, S. K. (2012). Trailing-edge noise predictions using compressible large-eddy simulation and acoustic analogy. *AIAA Journal*, volume 50, pp. 2423–2434.

Wright, S. E. (1976). The acoustic spectrum of axial flow machines. *Journal of Sound and Vibration*, volume 45, pp. 165–223.

Wu, H., Laffay, P., Idier, A., Jaiswal, P., Sanjosé, M. and Moreau, S. (2016). Numerical study of the installed Controlled-Diffusion airfoil at transitional Reynolds number. In *Mathematical and Computational Approaches in Advancing Modern Science and Engineering*. Springer, pp. 505–515.

Wu, H., Sanjosé, M., Moreau, S. and Sandberg, R. D. (2018). Direct numerical simulation of the self-noise radiated by the installed controlled-diffusion airfoil at transitional Reynolds number. In *24th AIAA/CEAS Aeroacoustics Conference, Atlanta, GA, USA*. p. 3797.

Wu, H., Winkler, J. and Sandberg, R. D .and Moreau, S. (2017a). Direct numerical simulation of transitional airfoil noise. In *23rd AIAA/CEAS Aeroacoustics Conference, Denver, CO, USA*. p. 3368.

Wu, X. and Moin, P. (2009). Direct numerical simulation of turbulence in a nominally zero-pressure-gradient flat-plate boundary layer. *Journal of Fluid Mechanics*, volume 630, pp. 5–41.

Wu, X., Moin, P., Wallace, J. M., Skarda, J., Lozano-Durán, A. and Hickey, J. P. (2017b). Transitional–turbulent spots and turbulent–turbulent spots in boundary layers. Volume 114. pp. E5292–E5299.

Yuan, J. and Piomelli, U. (2015). Numerical simulation of a spatially developing accelerating boundary layer over roughness. *Journal of Fluid Mechanics*, volume 780, pp. 192–214.

Zhou, J., Adrian, R. J., Balachandar, S. and Kendall, T. M. (1999). Mechanisms for generating coherent packets of hairpin vortices in channel flow. *Journal of Fluid Mechanics*, volume 387, pp. 353–396.